Theses and Dissertations

12-2012

Design, Fabrication, Testing of CNT Based ISFET and Characterization of Nano/Bio Materials Using AFM

Zhuxin Dong
University of Arkansas, Fayetteville

Recommended Citation

DESIGN, FABRICATION, TESTING OF CNT BASED ISFET AND CHARACTERIZATION OF NANO/BIO MATERIALS USING AFM

DESIGN, FABRICATION, TESTING OF CNT BASED ISFET AND CHARACTERIZATION
OF NANO/BIO MATERIALS USING AFM

A dissertation submitted in partial fulfillment
of the requirements for the degree of
Doctor of Philosophy in Mechanical Engineering

By

Zhuxin Dong
Shenyang University of Technology
Bachelor of Science in Biomedical Engineering, 2005
The Chinese University of Hong Kong
Master of Philosophy in Automation & Computer-Aided Engineering, 2007

December 2012
University of Arkansas

ABSTRACT

A combination of Carbon Nanotubes (CNTs) and Ion Selective Field Effect Transistor (ISFET) is designed and experimentally verified in order to develop the next generation ion concentration sensing system. Micro-Electro-Mechanical System (MEMS) fabrication techniques, such as photolithography, diffusion, evaporation, lift-off, packaging, etc., are required in the fabrication of the CNT-ISFET structure on p-type silicon wafers. In addition, Atomic Force Microscopy (AFM) based surface nanomachining is investigated and used for creating nanochannels on silicon surfaces. Since AFM based nanomanipulation and nanomachining is highly controllable, nanochannels are precisely scratched in the area between the source and drain of the FET where the inversion layer is after the ISFET is activated. Thus, a bundle of CNTs are able to be aligned inside a single nanochannel by Dielectrophoresis (DEP) and the drain current is improved greatly due to CNTs' remarkable and unique electrical properties, for example, high current carrying capacity. ISFET structures with or without CNTs are fabricated and tested with different pH solutions. Besides the CNT-ISFET pH sensing system, this dissertation also presents novel AFM-based nanotechnology for learning the properties of chemical or biomedical samples in micro or nano level. Dimensional and mechanical property behaviors of Vertically-Aligned Carbon Nanofibers (VACNFs) are studied after temperature and humidity treatment using AFM. Furthermore, mechanical property testing of biomedical samples, such as microbubbles and engineered soft tissues, using AFM based nanoindentation is introduced, and the methodology is of great directional value in the area.

This dissertation is approved for recommendation to the Graduate Council.

Dissertation Director:

_____

Dr. Uchechukwu C. Wejinya

Dissertation Committee:

_____

Dr. Chao-Hung Steve Tung

_____

Dr. Po-Hao Adam Huang

_____

Dr. Min Zou

_____

Dr. Kaiming Ye

DISSERTATION DUPLICATION RELEASE

I hereby authorize the University of Arkansas Libraries to duplicate this dissertation when needed for research and/or scholarship.

Agreed   _____

Zhuxin Dong

Refused   _____

Zhuxin Dong

ACKNOWLEDGMENTS

Numerous thanks are due to my dissertation committee members, Dr. Uche Wejinya, Dr. Steve Tung, Dr. Adam Huang, Dr. Min Zou, and Dr. Kaiming Ye. Without their patience and endless instruction and help, I could not imagine how I would be able to complete such a satisfying dissertation. Dr. Wejinya is the special one who is not only an excellent teacher to me, but also a close friend of mine. I really appreciate what Dr. Wejinya has done to take good care of me in both school and life.

Also, I would like to express my special gratitude to HiDEC staff, Mr. Errol Porter and Mr. Michael Glover, who has provided me with precious instruction and advice regarding the usage of fabrication facilities. Lastly, I thank Dr. Husein Rokadia, from whom I had learned a lot on AFM techniques and applications while he was a graduate student in Dr. Tung's group.

DEDICATION

I dedicate this dissertation to my family, especially to my wife Yan Zhao, my parents Zaili Dong and Yingdi Sun, and my grandma Rongfang Zhao who have been providing me with endless support and encouragement.

TABLE OF CONTENTS

LIST OF TABLES

LIST OF FIGURES

Chapter I.   INTRODUCTION

Along with human being's non-stop progress in science and technology, especially in the areas of micro-electro-mechanical systems (MEMS) over the last decade, nano materials are becoming more realistic and popular in engineering, biological, chemical, and medical fields to name a few. Thus, a combination of traditional MEMS fabrication techniques and advanced manipulation in nanoscale level is currently fast-moving in order to satisfy the contemporary research requirement. In this dissertation, a completely novel concept for the next generation ion concentration sensing system is proposed and experimentally verified. In this concept, carbon nanotubes (CNTs) are brought into the design and fabrication of Ion-Sensitive Field Effect Transistor (ISFET). Due to the unique electrical properties of CNTs, such as the excellent conductivity and high current carrying capacity, they possess huge potential to improve the performance of existing ISFETs as a pH sensor. Additionally, Atomic Force Microscopy (AFM) is one of the most famous tools in the nano world. Besides the surface nanomachining involved in developing CNT-ISFET pH sensor, this dissertation also talks about several practical characterizations and manipulations using AFM techniques. The characterization of physical properties of Vertically-Aligned Carbon Nanofibers (VACNFs), which are designed and grown on nanoelectrodes for sensing application, is performed by AFM to study how their physical behaviors change under different environmental conditions. AFM based nanoindentation methodology for mechanical properties testing of nano/bio samples is very critical because conventional methods have met their limits when dealing with these tiny and fragile samples. The dimensional data of VACNFs is not only used for the examination after the growth but also regarded as an important reference for further treatment, for example, temperature, humidity and etchant. Furthermore, the Young's Moduli of some biological samples such as soft tissue

scaffolds and protein microbubbles are obtained, which has a significant value and impact in the field.

1.1 Micro/Nano Materials and Tools

1.1.1 Background of Nanotechnology

Nanotechnology is the engineering of functional systems at the molecular scale. Base on this definition, nanotechnology is quite diverse. It ranges from extensions of conventional device physics to completely new approaches based on molecular self-assembly, from developing new materials with dimensions in the nanoscale to direct control of matter on the atomic scale. Generally, nanotechnology deals with structures sized between 1 to 100 nm (1 nm = 10^{-9} m) in at least one dimension, and involves developing materials or devices possessing at least one dimension within that size. The origins of nanotechnology are traced back to 1980s. During that period, several remarkable research breakthroughs took place, such as the invention of the scanning tunneling microscope in 1981 [1] and the discovery of fullerenes in 1985 [2]. They were the marks that the gate of nano world was opened. Since then, nanotechnology has become extremely important especially in research and development—from academia to industry applications. Researchers have already realized that at present nanotechnology is one of the keys to make the world a better place and devoted themselves into the field, for example nanotechnology in medicine for cancer cure. Researchers from other categories, for instance biology and medicine, have found interactions with and benefited from nanotechnology. In 2006, Dr. Mihail Roco, who is the chair of the US National Science and Technology Council subcommittee on Nanoscale Science, Engineering and Technology and has played a leadership role in the US National Nanotechnology Initiative, described four generations of the development of nanotechnology as shown in Figure 1.1 [3].
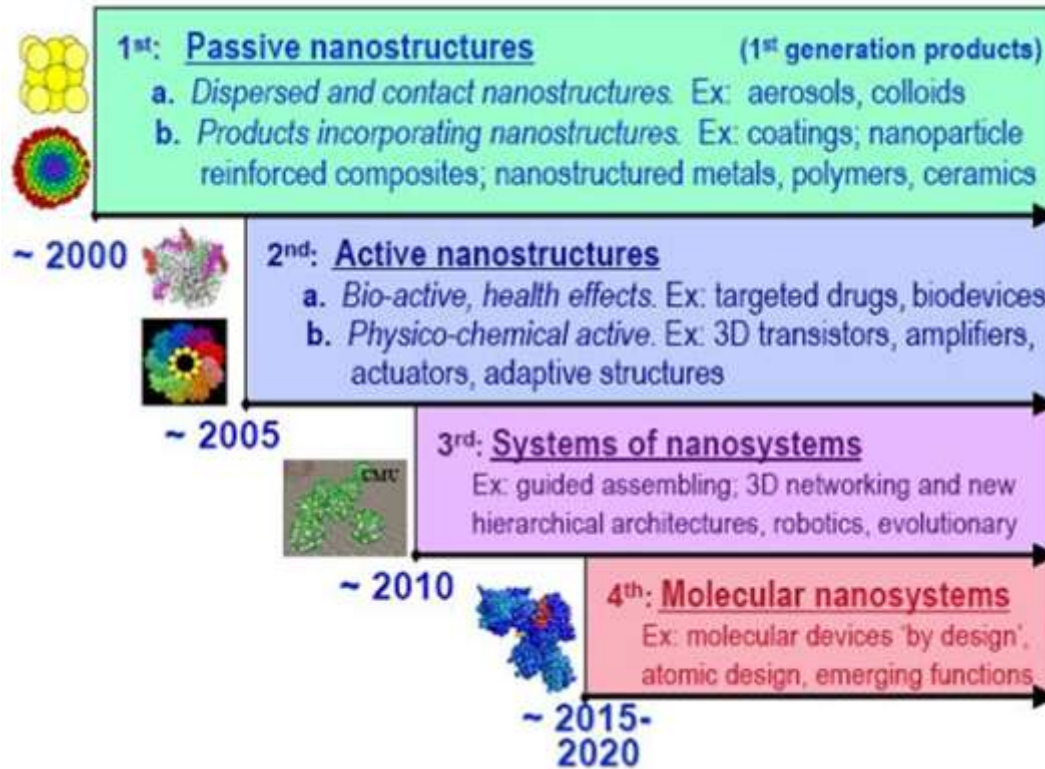
Figure 1.1: Four generations of nanotechnology development.

Nanomaterials and nanotools are the necessary components in nanotechnology. Nanomaterials can be regarded as a field that takes a material science based approach to nanotechnology. It studies materials with morphological features on nanoscale and especially those that have unique properties due to their nano dimensions. In general, nanomaterials are divided into two forms—fullerenes and nanoparticles. In fullerenes, C_{60} is the first discovered, and Carbon Nanotube (CNT) is one of the most famous nanomaterials. Two forms of nanoparticles are quantum dots and chemical catalysts. One of the most important aspects of nanotechnology is the vastly increased ratio of surface area to volume in various nanomaterials. In the rest of this chapter, micro/nano materials, manipulations, devices and tools, which are involved in this dissertation, are introduced.

1.1.2 Vertically Aligned Carbon Nanofibers

With recent increase in pathogen outbreaks in water, food and other media, new methods and technologies for detection and quantification are needed. These devices and systems will need to be fast, reliable, ultrasensitive, portable, and automated. For several decades, detection heavily relied on an indicator organism approach to assess the microbiological quality of drinking water. But an increased understanding of the diversity of waterborne pathogens has concluded that the use of bacterial indicators may not be as universally protective as was once thought [4]. Newer methods involving immunofluorescence techniques and nucleic acid analysis provide valuable opportunities for rapid and more specific analytical methods. Particularly, electrochemical (EC) biosensors are attractive for detecting a wide range of species, including proteins, nucleic acids, small molecules and viruses because of their relative simplicity, portability, low cost and low power requirement. EC biosensors consist of two primary components: a recognition layer containing a biomolecule and an electrochemical signal transducer. They make use of electrochemical reactions or the surface property changes upon target binding. Advances in microfabrication technology have provided electrode configurations such as microelectrode arrays [5] and interdigitated arrays (IDA) [6], but their performance can be further enhanced by miniaturizing to nanoscale. Recent progress in nanofabrication technologies like electron beam lithography and nanoimprinting enable fabrication of one-dimensional nanostructure electrodes, like carbon nanofibers [7][8][9], carbon nanotube bundles [10][11], nanoscale IDA [12], silicon nanowires [13] and diamond nanowires [14], which are capable of high spatial and temporal resolutions, possibly yielding sufficient sensitivity to single molecule detection. Among various types of one-dimensional nanoscale electrodes, Vertically Aligned Carbon Nanofibers (VACNFs) have received tremendous attention because of their attractive properties such as high electrical

and thermal conductivities, superior mechanical strength, a wide electrochemical potential window, flexible surface chemistry and biocompatibility [15][16]. Compared to other carbon materials such as glassy carbon, carbon black, carbon microfibers, and pyrolytic graphite, the open-ended VACNF arrays present well-defined edgeplane structure suitable for selective covalent functionalization of primary amine-terminated oligonucleotide probes. Thus, the microchip, a 3×3 array biosensor using nanopatterned VACNF array for detection of chemical particles, such as *E. coli* O157:H7, has been achieved [17].

Figure 1.2 illustrates the VACNFs through Scanning Electron Microscope (SEM) [17], where (a) as-grown forest-like VACNFs, (b) as-grown patterned VACNF arrays on 100 nm diameter Ni spots using e-beam lithography, (c) the surface of polished VACNFs embedded in SiO_2 matrix, and (d) the surface of polished patterned VACNF array embedded in SiO_2 matrix. (a) and (b) are 30° perspective views while (c) and (d) are top views. The scale bars from (a) to (d) are 3, 1, 2 and 1 μm, respectively.
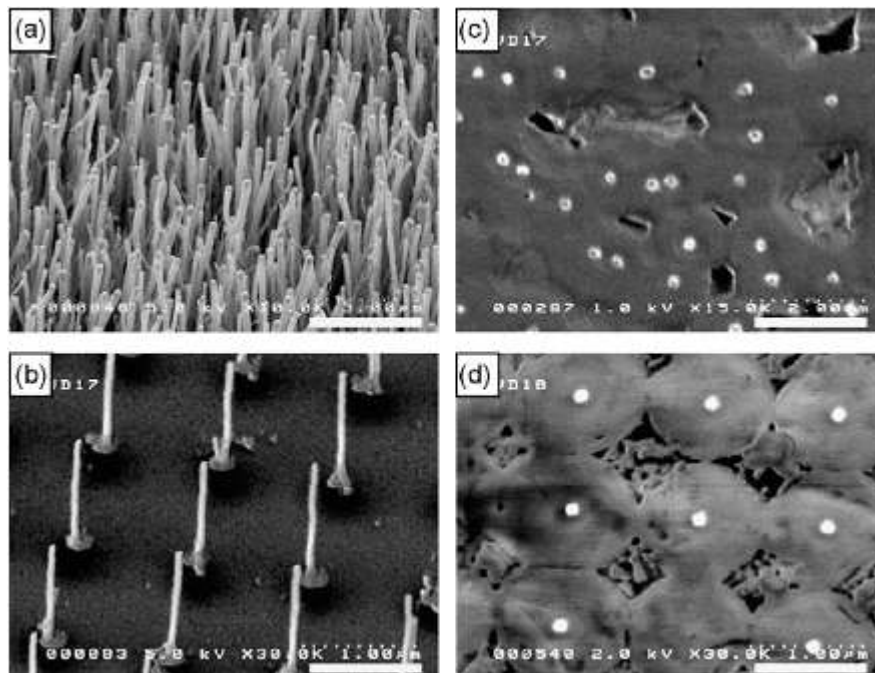
Figure 1.2: SEM images of VACNFs.

1.1.3 Carbon Nanotube

Carbon Nanotubes (CNTs) closely resemble hollow graphite fibers that exist in entangled bundles of tens to hundreds. They come in two different forms: Multi-Walled Carbon Nanotubes (MWCNTs) and Single-Walled carbon nanotubes (SWCNTs). SWCNTs and MWCNTs range in diameter from 1-10 nm and 10-50 nm respectively. About 70-80% of SWCNTs tend to contain semiconducting properties, whereas 70-80% of MWCNTs tend to contain metallic properties [18][19][20]. CNTs have also been known to possess remarkable electrical, mechanical, and thermal properties [21]. Metallic CNTs can be used as connecting wires for Micro-Electro-Mechanical Systems (MEMS) and Nano-Electro-Mechanical Systems (NEMS) because of their size and low resistance, while semiconducting CNTs can be used for nano transistors [22]. Figure 1.3 presents the CNTs with approximate sizes, and Table 1.1 gives their properties.
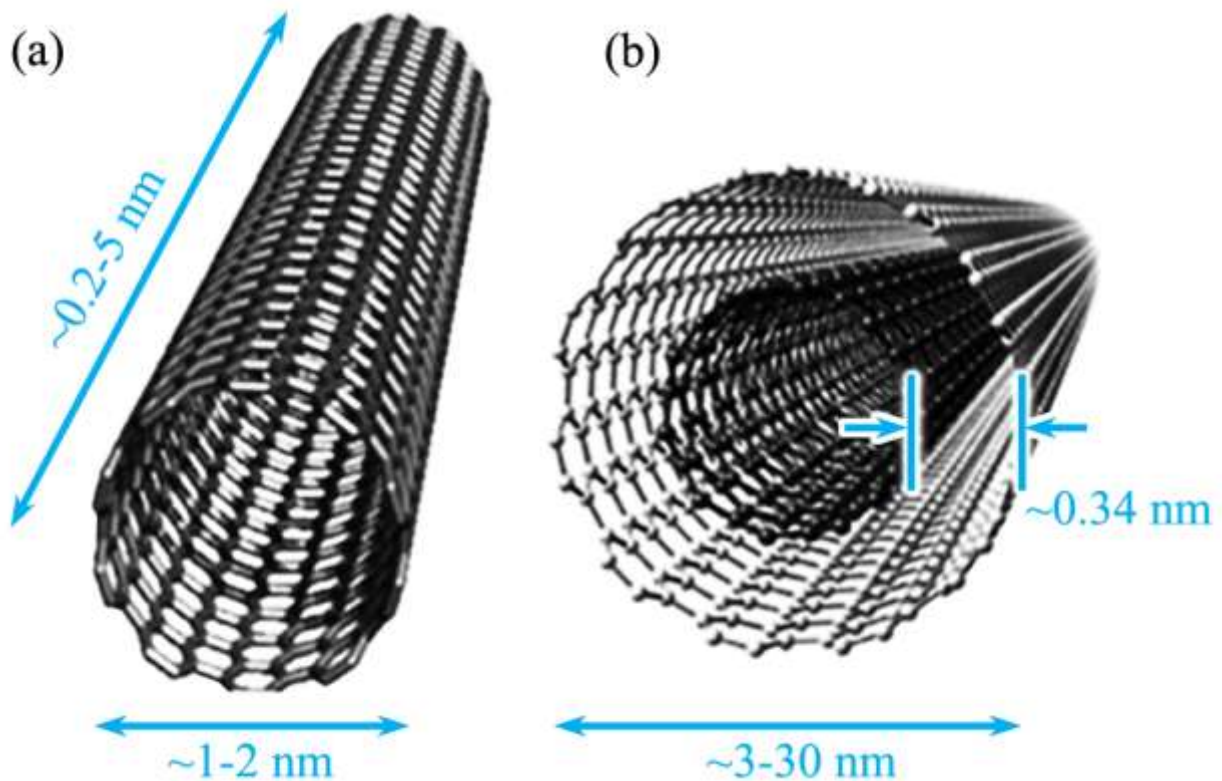
Figure 1.3: Carbon Nanotubes (a) SWCNT and (b) MWCNT.

Property	Item	Data	Potential Application
Geometrical	Layers	Single/multiple	Structures, probes, grippers/tweezers, scissors
	Aspect ratio	10-1000	
	Diameter	~ 0.4nm to 3nm (SW)	
		~ 1.4 nm to >100 nm (MW)	
	Length	Several μm to cm	
Mechanical	Young's Modulus	~ 1TPa (steel: 0.2TPa)	
	Tensile strength	45GPa (steel: 2GPa)	
	Density	~ 1.33-1.4g/cm^3 (Al: 2.7g/cm^3)	
	Interlayer friction	Ultrasmall	Actuators, bearings, syringes, switches, memories
Electronic	Conductivity	Metallic/semiconducting	Diodes, transistors, switches, logic gates
	Current carrying capacity	~ 1TA/cm^3 (Cu: 1GA/cm^3)	Wires/cables
	Field emission	Activate phosphorus at ~ 1-3V	Proximity/position sensors
Electromechanical	Piezoresistivity	Positive/negative	Deformation/displacement sensors
Thermal	Heat transmission	>3kW/mK (diamond: 2kW/mk)	Circuits, sensors, thermal actuators

Table 1.1: Properties of CNTs.

1.1.4 Dielectrophoresis

Electrophoresis is the movement of a particle with a non-zero net charge produced by the Coulomb force. Biological particles generally have a finite surface charge density (usually negative, due to the presence of acid groups on the surface) and observation of the movement of these particles in a uniform electric field is used both to characterize and to separate particles. The Coulomb force F_{EP} on a particle is given by the product of the electric field E and the charge Q on the particle as shown in Equation (1.1):

$$F_{EP} = Q \cdot E = \int \sigma_q dS \cdot E \tag{1.1}$$

where Q is the total charge on the particle which, if the particle has a surface charge density σ_p, is given by the integral of this charge density over the closed surface S of the particle. In an AC electric field, the movement due to this force is oscillatory with zero time-average.

The force on an induced dipole is called Dielectrophoresis (DEP). DEP is the motion of a particle produced by the interaction of a non-uniform electric field with the induced effective dipole moment of the particle. If the field is uniform, the force on each of the two poles of the dipole is equal and opposite and there is no movement. If the field is non-uniform, however, the two forces are not equal and the particle moves. Figure 1.4 shows the principle of DEP force. The DEP force does not require the particle to be charged, and all the particles exhibit dielectrophoretic activity in the presence of the electric fields. The strength of the force strongly depends on the electrical properties of the medium and particle, the shape and size of the particle, as well as the frequency and magnitude of the electric field. For a spherical particle, the full expansion for the time averaged DEP force is [23]:

$$F_{DEP} = \pi \varepsilon_m r^3 Re[f_{CM}] \nabla |E|^2 \tag{1.2}$$

where ε_m is the dielectric constant of the medium, r is the particle radius, E is the root-mean-square (RMS) value of the electric field, and f_{CM} is the Clausius-Mossotti factor. Additionally, Equation (1.3) gives the method how to determine the Clausius-Mossotti factor:

$$f_{CM} = \frac{e_p^* - e_m^*}{e_p^* + 2e_m^*} \tag{1.3}$$

where ε^* is the complex dielectric constant and can be determined by Equation (1.4), e_p and e_m represent the particle and medium , respectively.

$$\varepsilon^* = \varepsilon + \frac{\sigma}{jw} \tag{1.4}$$

where σ is the electrical conductivity, w is the angular frequency, and j is the imaginary unit. Furthermore, DEP forces can be either positive or negative. Positive DEP occurs if the polarisability of the particle is greater than the suspending medium ($Re[f_{CM}]>0$), and the particle moves towards regions of high electric field strength. Negative DEP occurs if the polarisability of the particle is less than the suspending medium ($Re[f_{CM}]<0$), and the particles are repelled from the regions of high filed strength. Consequently, non-uniform electric fields with a particular frequency can manipulate particles with great selectivity, which has allowed the separation of cells, the orientation and manipulation of nanoparticles and nanowire [20][24][25].
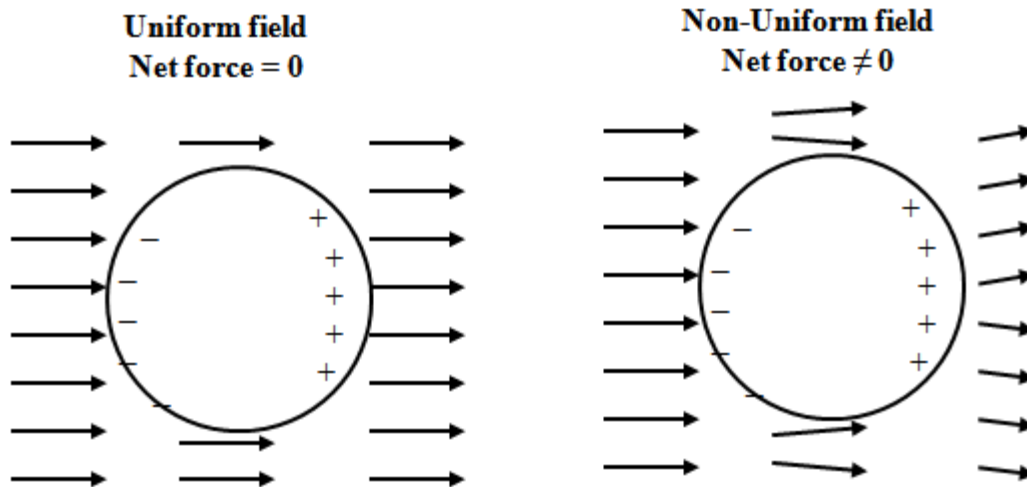
Figure 1.4: Principle of DEP force.

1.1.5   Ion Selective Field Effect Transistor

ISFET has often been used to measure ion concentrations in solutions for more than 30 years. The output signal of the ISFETs is usually a potential difference the magnitude of which varies with the change of logarithm of sensed ion activity or concentration. However, in theory, when the ion concentration, such as pH, changes, the drain current I_D changes due to the effective electrical resistance of the surface inversion layer and the voltage difference V_D between the source and drain. In practice, I_D can be kept as constant by adjusting the gate voltage V_G while

9

V_D is also a constant. Here, the solution is used as the gate electrode instead of the traditional metal gate. The voltage between substrate and oxide surfaces arises due to an ions' sheath. ISFET's source and drain are constructed similar to a Metal-oxide Semiconductor Field-Effect Transistor (MOSFET) [26]. Although an ISFET is similar to a MOSFET, there are still some differences. As shown in Figure 1.5 (1 drain, 2 source, 3 substrate, 4 insulator, 5 metal contacts, 6 reference electrode, 7 solution, 8electroactive membrane, 9 encapsulant, and 10 inversion layer), the metal gate is replaced by the metal of a reference electrode, whilst the target liquid in which this electrode is present makes contact with the bare gate insulator. Both MOSFET and ISFET have the same equivalent circuit. The inversion layer formed at SiO_2-Si interface, and the electrons are supplied by the n$^+$-source region while the n$^+$-drain region is needed to make the electrons flow. Figure 1.6 is a diagram of the complete electrochemical system, together with the relevant electrical potentials. An equivalent ISFET gate voltage difference V_G^* can be defined as the electrical potential difference between the bulk phases of the semiconductor and the gate material as in Equation (1.5):

$$V_G^* = E_I + V_{ref} + V_B \qquad (1.5)$$

where, V_B is an additional series polarizing potential (gate bias potential), E_I is the interfacial membrane-solution potential difference generally given by the Nernst or Eisenmann-Nikolsky equations, and V_{ref} is the reference electrode potential. Thus, the changes at the solution-electroactive material interface are reflected in the changes of I_D after V_B is fixed.
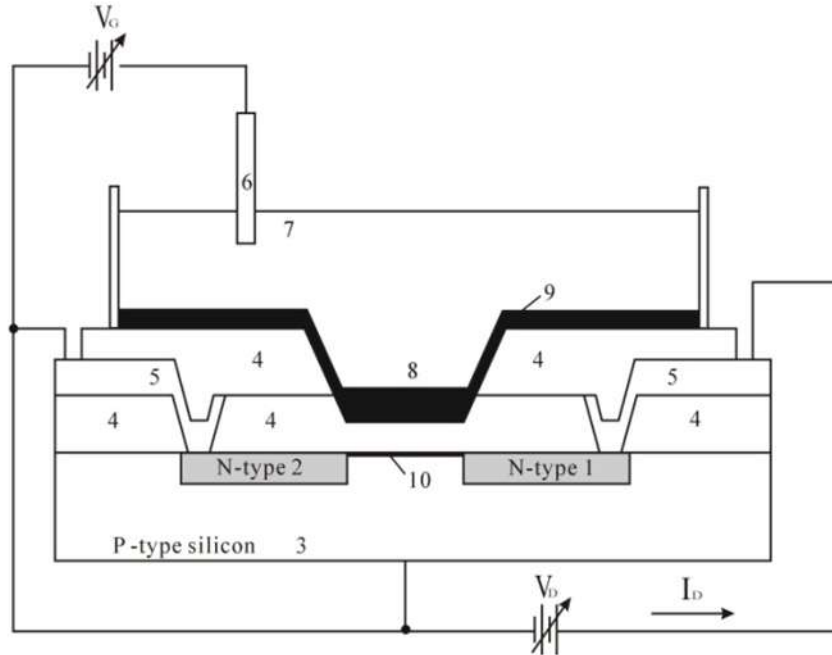
Figure 1.5: Schematic of a composite gate, dual dielectric ISFET.
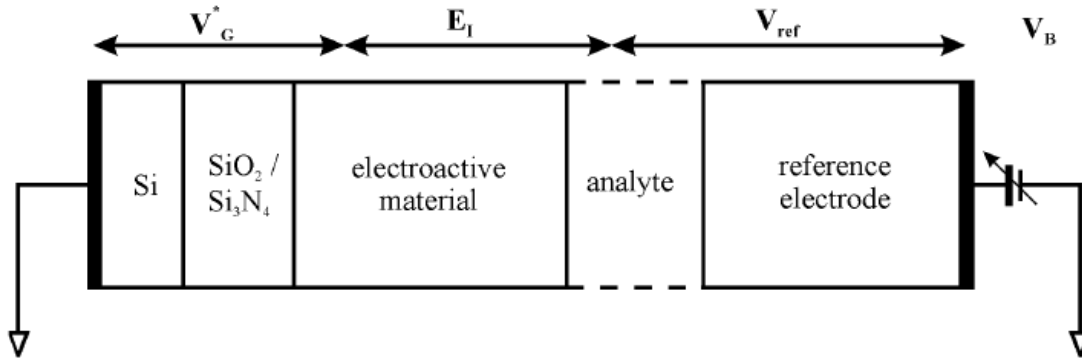
Figure 1.6: Potential difference contributions of composite gate, dual dielectric ISFET.

1.1.6   Nanoindentation

Indentation testing is a simple method that consists essentially of touching the material of interest whose mechanical properties such as elastic modulus and hardness are unknown with another material whose properties are known. The technique has its origin in Mohs' hardness scale of 1822 in which materials that are able to leave a permanent scratch in another were ranked harder material with diamond assigned the maximum value of 10 on the scale. The

establishments of the Brinell, Knoop, Vickers, and Rockwell test all follow from a refinement of the method of indenting one material with another. Nanoindentation is simply an indentation test in which the length scale of the penetration is measured in nanometers (10^{-9} m) rather than microns (10^{-6} m) or millimeters (10^{-3} m) [27], and the nanoindentation technique was developed in the mid-1970s. Apart from the displacement scale involved, the distinguishing feature of most nanoindentation testing is the indirect measurement of the contact area – that is, the area of contact between the indenter and the specimen. In conventional indentation tests, the area of contact is calculated from direct measurements of the dimensions of the residual impression left in the specimen surface upon the removal of load. In nanoindentation tests, the size of the residual impression is of the order of microns and too small to be conveniently measured directly. Thus, it is customary to determine the area of contact by measuring the depth of penetration of the indenter into the specimen surface. This, together with the known geometry of the indenter, provides an indirect measurement of contact area at full load. For this reason, nanoindentation testing can be considered a special case of the more general terms: depth-sensing indentation (DSI) or instrumented indentation testing (IIT).

In a traditional indentation test (macro or micro indentation), a hard tip whose mechanical properties are known (frequently made a very hard material like diamond) is pressed into a sample whose properties are unknown. The load placed on the indenter tip is increased as the tip penetrates further into the specimen and soon reaches a user-defined value. At this point, the load may be held constant for a period or removed. The area of the residual indentation in the sample is measured and the hardness, H, is defined as the maximum load, P_{max}, divided by the residual indentation area, A_r, as in Equation (1.6):

$$H = \frac{P_{max}}{A_r} \tag{1.6}$$

For most cases, the projected area can be measured directly using light microscopy. As can be seen from Equation (1.6), a given load will make a smaller indent in a "hard material than a soft one". This technique is limited due to large and varied tip shapes, with indenter rigs which do not have very good spatial resolution as the location of the area to be indented is very hard to specify accurately. Comparison across experiments, typically done in different laboratories, is difficult and meaningless. Nanoindentation improves on these macro and micro indentation tests by indenting on the nanoscale with a very precise tip shape, high spatial resolutions to place the indents, and by providing real-time load-displacement (into the sample surface) data while the indentation is in progress. Instead of other tools for imaging the indentation, an indenter with a geometry known to high precision (usually a Berkovich tip [28][29], which has a three-sided pyramid geometry) is employed. During the course of the instrumented indentation process, a record of the depth of penetration is made, and then the area of the indent is determined using the known geometry of the indenter. While indenting, various parameters, such as load and depth of penetration, can be measured. A record of these values can be plotted on a graph to create a load-displacement curve such as the one shown in Figure 1.7. These curves can be used to extract mechanical properties of the material [30].

1.1.7 Atomic Force Microscopy

Scanning Probe Microscopy (SPM) is a large and growing collection of techniques for investigating the properties of a sample, at or near the sample surface. The SPM instrument has a sharp probe with radius of curvature typically in the nanometers or tens of nanometers that is in near-contact, intermittent contact, or perpetual contact with the sample surface. Since an SPM is used to investigate sample properties at or near the sample surface, that is immediately beneath the surface (typically several nanometers deep) and immediately above the surface (typically-
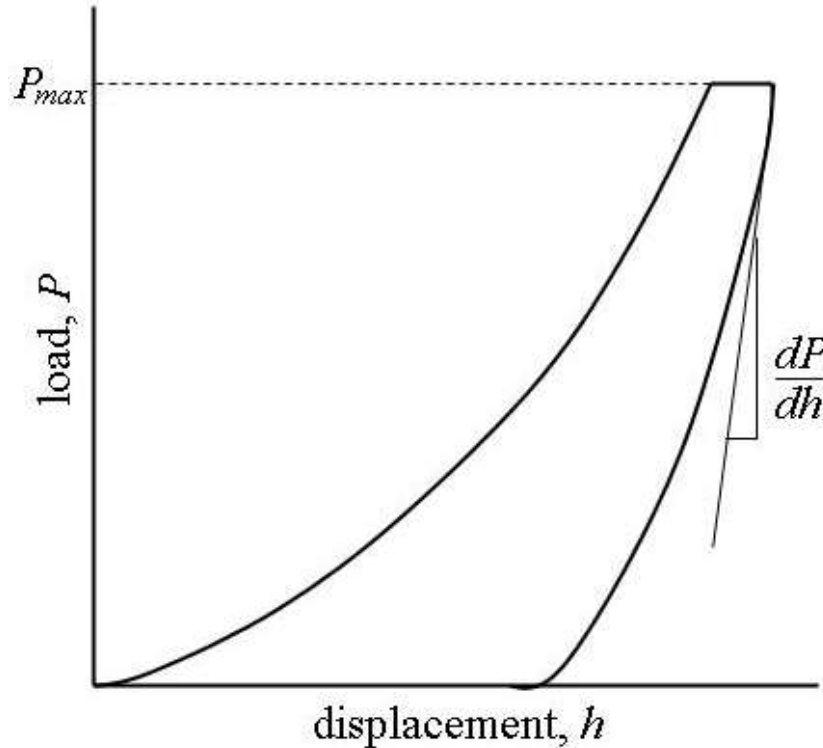
Figure 1.7: Schematic of load-displacement curve for an instrumented indentation.

-several tens of nanometers high). In SPM techniques, the sharp probe (tip) is scanned across a sample surface, or the surface is scanned beneath the tip as shown in Figure 1.8. Interactions between the tip and sample are detected and mapped. Different techniques sense different interactions, which can be used to describe surface topography, adhesion, elasticity, electrostatic charge, etc. The small size of the probe is the key to the SPM's high resolution. The most common SPM images are topography images, in which the third dimension, Z, for any given X/Y coordinates, is the relative height of the sample surface. In other types of SPM images, the third dimension is a measure of the relative strength of a detectable interaction between the probe and sample, such as amplitude and phase. In some instances, the signal from the SPM's detector is mapped directly, for example, the deflection of the probe cantilever, or the current through a conductive tip. SPM also can be used for non-imaging techniques, or nano-manipulation, in which the probe is used to modify the sample surface.

14
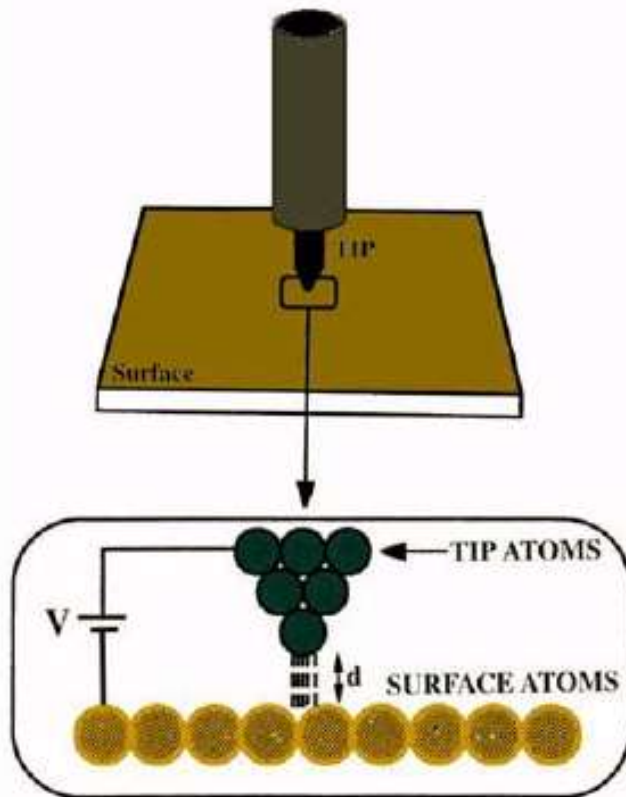
Figure 1.8: SPM diagram.

The earliest, widely-adopted SPM technique was Scanning Tunneling Microscopy (STM). STM was developed by G. Binnig and H. Rohrer in the early 1980s at IBM Research − Zurich, and that was a development which earned them the Nobel Prize for Physics in 1986 [31]. In STM, a bias voltage is applied between a sharp, conducting tip and the sample. When the tip approaches the sample, electrons "tunnel" through the narrow gap, either from the sample to the tip or vice versa, depending on the bias voltage. Changes of only 0.1nm in the separation distance cause an order of magnitude difference in the tunneling current, giving STM remarkably high precision. Figure 1.9 shows the basic STM schematic.
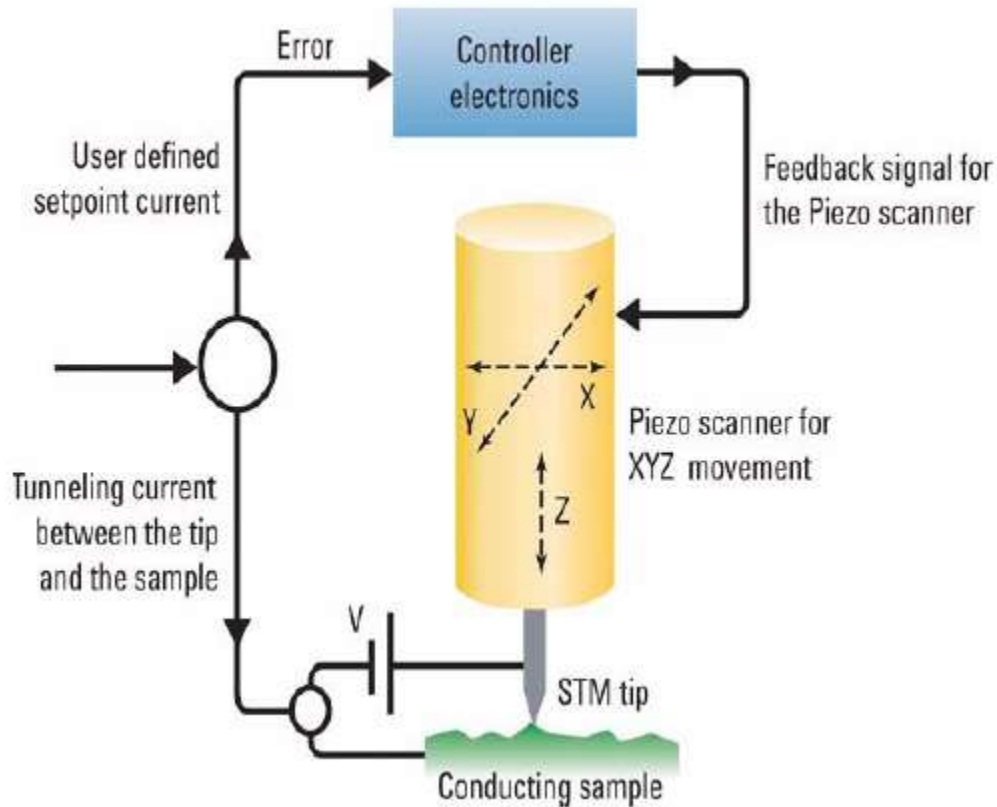
Figure 1.9: STM schematic.

STM can image a sample surface in either constant current or constant height mode. In constant height mode, the tip remains in a constant plane above the sample, and the tunneling current varies depending on topography and local surface properties. The tunneling current measured at each location constitutes the image. The sample surface, however, must be relatively smooth in order for the system to acquire useful information. In constant current mode, a feedback loop is used to adjust the height of the tip in order to hold the tunneling current at a setpoint value. The scanner height measured at each location is then used to map the surface topography. Because the feedback response requires time, constant current mode is typically slower than constant height mode. However, greater variations in height can be accommodated. For electron tunneling to occur, both the sample and tip must be conductive or semi-conductive.

Therefore, STM cannot be used on insulating materials. This is one of the significant limitations of STM, which led to the development of the other SPM methods.

Atomic Force Microscopy (AFM) can resolve features as small as an atomic lattice, for either conductive or non-conductive samples. AFM provides high-resolution and three-dimensional information, with little sample preparation. The technique makes it possible to image in-situ, in fluid, under controlled temperature and in other controlled environments. The first atomic force microscope was invented by G. Binnig, C. F. Quate, and Ch. Gerber in 1986 [32], and the first commercially available atomic force microscope was introduced in 1989. At present, AFM is one of the foremost tools for imaging, measuring, and manipulating matter at the nanoscale. The potential of AFM has already extended to applications in life science, materials science, electrochemistry, polymer science, biophysics, nanotechnology, and biotechnology.

In AFM, as shown in Figure 1.10, a sharp tip at the free end of a cantilever (the "probe") is brought into contact with the sample surface. The tip interacts with the surface, causing the cantilever to bend. A laser spot is reflected from the cantilever onto a position-sensitive photodiode detector. As the cantilever bends, the position of the laser spot changes. The resulting signal from the detector is the deflection, in volts. The difference between the deflection value and the user-specified Setpoint is called the "error signal".

Figure 1.11 shows the force interaction as the tip approaches a sample. At the right side of the curve, the tip and sample are separated by large distance. As they approach, tip and sample atoms first weakly attract each other. This zone of interaction is known as the "non-contact" regime. Closer still, in the "intermittent contact" regime, the repulsive van der Waals force predominates. When the distance between tip and sample is just a few angstroms, the forces balance, and the net force drops to zero. When the total force becomes positive (repulsive), the

17

atoms are in "contact" regime. The various AFM imaging modes can be generally described by their function within these three domains.
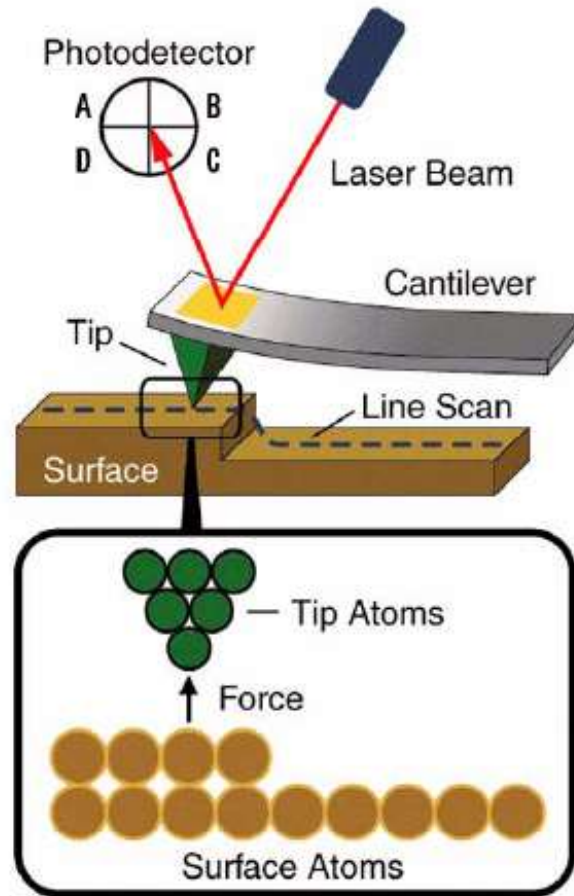
Figure 1.10: AFM principles.

The tip-sample interaction is complicated by additional forces, including strong capillary and adhesive forces that attract the tip and sample. The capillary force arises when water, often present when imaging in the ambient environment, wicks around the tip, holding the tip in contact with the surface. As long as the tip is in contact with the sample, the capillary force should be constant because the fluid between the tip and the sample is virtually incompressible. The total force that the tip exerts on the sample is the sum of the capillary, adhesive and van der Waals forces. The van der Waals force counters almost any force that attempts to push the atoms

closer together. When the cantilever pushes the tip against the sample, the cantilever bends rather than forces the tip closer to the sample atoms. The deflection, therefore, can be used as a reliable indicator of surface topography.
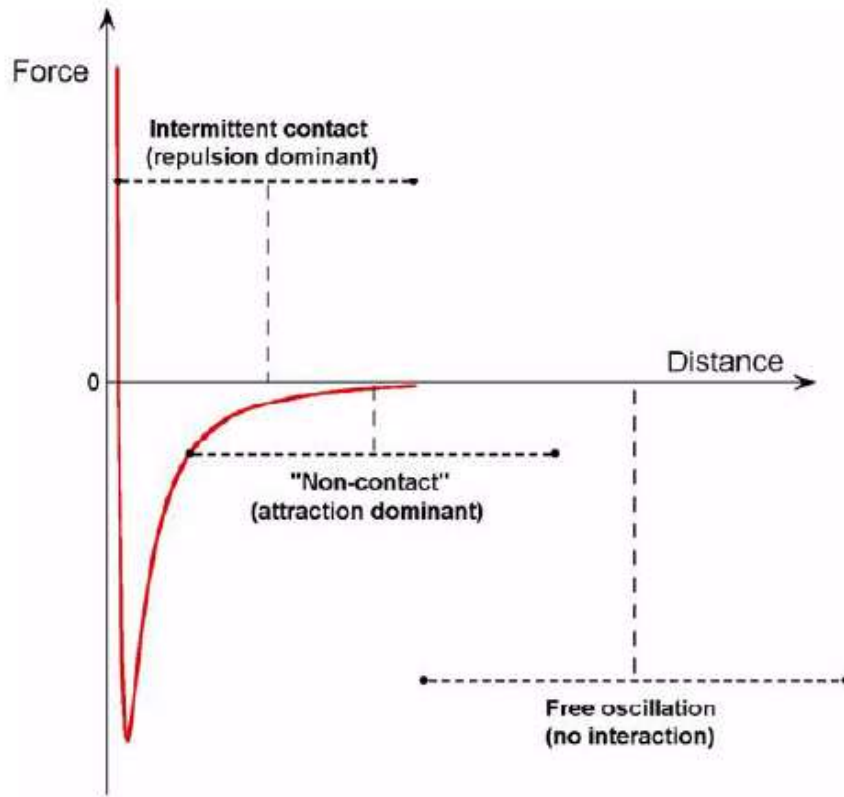
Figure 1.11: Zones of interaction as AFM tip approaches a sample.

In this dissertation, all the AFM-related work is implemented with Agilent 5500 SPM (Agilent Technologies Inc., Santa Clara, CA, USA). Figure 1.12 presents its major components. This system offers multiple AFM operational techniques, including contact AFM, intermittent contact AFM (Acoustic AC, Magnetic AC, Top Magnetic AC), Current Sensing AFM, Force Modulation Microscopy, Lateral Force Microscopy, Dynamic Lateral Force Microscopy, Magnetic Force Microscopy, Electrostatic Force Microscopy, and Kelvin Force Microscopy. There are two A-type scanners, which are most typically used with the Agilent 5500 SPM and need the video system on. The small multi-purpose scanner provides scans up to 9 microns

square and is capable of atomic-level resolution imaging; while the large one provides scans up to 90 microns square and includes closed-loop positioning, in which ultra-precise positioning and more accurate z-position and force control are available. Besides the scan sizes, the large scanner also differs from the small one in the vertical servo range, approximately 6 - 9 µm for the large scanner versus 2.4 µm for the small one. With these system options, users are able to image, measure, and manipulate different samples under various environments, such as vacuum, air, and liquid.

Figure 1.12: Major components of Agilent 5500 SPM.

1.2   Organization of Dissertation

The remaining chapters of the dissertation are organized as follows: In Chapter II, literature reviews will be given to introduce some related work done by other researchers. The methodology of VACNFs' dimensional measurement is introduced and the results are statistically analyzed in Chapter III. Chapter IV describes how to determine the mechanical properties of nano/biomedical samples using AFM-based nanoindentation. The development of CNT-ISFET system for pH sensing is discussed in Chapter V. Then, recommendations for future work are proposed in Chapter VI. At last, a conclusion of the dissertation is given in Chapter VII.

Chapter II.   LITERATURE REVIEW

One of the major limitations in the development of ultra-sensitive electrochemical biosensors based on one-dimensional nanostructures is the difficulty involved with reliably fabricating nanoelectrode arrays (NEAs). P. Arumugam proposed a simple, robust and scalable wafer-scale fabrication method to produce multiplexed biosensors [17]. Each sensor chip consists of nine individually addressable arrays that uses electron beam patterned VACNFs as the sensing element. To ensure nanoelectrode behavior with higher sensitivity, VACNFs were precisely grown on 100 nm Ni dots with 1 μm spacing on each micro pad. Pretreatments by the combination of soaking in 1.0 M HNO_3 and electrochemical etching in 1.0 M NaOH dramatically improved the electrode performance indicated by the decrease of redox peak separation in cyclic voltammogram (ΔE_p) to ~100 mV and an approximately 200% increase in steady-state currents. The electrochemical detection of the hybridization of DNA targets from *E. coli* O157:H7 onto oligonucleotide probes were successfully demonstrated. The 9 arrays within the chip were divided into three groups with triplicate sensors for positive control, negative control and specific hybridization. It has been proved that the proposed method has the potential to be scaled up to 10×10 arrays, which is ideal for detecting a myriad of organisms. In addition, such sensors can be used as a generic platform for many electroanalysis applications. However, although SEM images of VACNF were shown to prove the growth, 3D size information needs to be collected to verify the repeatability of this fabrication method. Furthermore, to learn the dimensional change of VACNFs under different treatments, such as temperature, relative humidity and etchants, is important for various applications. For example, the behavior of dimension and mechanical properties under extreme temperatures will directly determine the performance of VACNFs as sensing elements when used in the outer space.

22

There has been considerable recent interest in the mechanical characterization of thin film systems and small volumes of material using depth-sensing indentation tests with either spherical or pyramidal indenters. Usually, the principal goal of such testing is to extract elastic modulus and hardness of the specimen material from experimental readings of indenter load and depth of penetration. These readings give an indirect measure of the area of contact at full load, from which the mean contact pressure, and thus hardness, may be estimated. The test procedure, for both spheres and pyramidal indenters, usually involves an elastic-plastic loading sequence followed by an unloading. The validity of the results for hardness and modulus depends largely upon the analysis procedure used to process the raw data. Such procedures are concerned not only with the extraction of modulus and hardness, but also with correcting the raw data for various systematic errors that have been identified for this type of testing. The forces involved are usually in the millinewton (10^{-3} N) range and are measured with a resolution of a few nanonewtons (10^{-9} N). The depths of penetration are on the order of microns (10^{-6} m) with a resolution of less than a nanometer (10^{-9} m).

At the beginning of the 20th century, indentation tests were first performed by Brinell, using spherical and smooth balls from ball bearings as indenters to measure the plastic properties of material [33][34]. The Brinell test was quickly adopted as an industrial test method soon after its introduction and prompted the development of various macro and micro indentation tests [35]. Traditional indentation testing involves optical imaging of the indent, which clearly imposes a lower limit on the length scale of the indentation. During the past two decades, the scope of indentation testing has been extended down to the nanometer range. This has been achieved principally through the development of instruments capable of continuously measuring load and displacement throughout an indentation [36][37][38]. In recently developed systems, loads as

23

small as a nano Newton (nN) and displacements of about 0.1 nm can be accurately measured. On the other hand, the recognition in the early 1970s that elastic modulus could potentially be measured from an indentation load-displacement curve [39] greatly promoted the development of instrumented indentation testing methodologies. In recent years, the study of the mechanical properties of materials on the nanoscale has received much attention, as these properties are size-dependent [40][41]. These studies have been motivated partly by the development of nanocomposites and the application of nanometer thick films for miniaturization of engineering and electronic components [42], and partly by newly available methods of probing mechanical properties in small volumes [34][37][38]. The nanoindenter is maturing as an important tool for probing the mechanical properties of small-volume materials. Indentation load-displacement data contains a wealth of information. From the load-displacement data, many mechanical properties such as hardness and elastic modulus can be determined without imaging the indentations [34][37]. The nanoindenter has also been used to estimate the fracture toughness of ultrathin films [43][44][45], which cannot be measured by conventional indentation tests. With a tangential force sensor, nanoscratch and wear tests can be performed at ramping loads [46][47][48][49][50][51][52]. AFM is not only ideal for imaging nanometer-scale indents, providing useful information about nanoindentation deformation and cracking, but also capable to carry out nanoindentation for various biomedical samples [53][54][55][56][57][58][59][60][61][62], many of which are not able to be indented except for using AFM. When an indentation system is used in conjunction with an AFM, *in situ* imaging can be obtained [40]. Therefore, it is believed, with the rapid development of instruments and analytical procedures, more material properties will be measured or estimated by the nanoindentation technique in the near future.

The discovery of C_{60} in 1985 [63] had an impact which extended way beyond the confines of academic chemical physics, and marked the beginning of a new era in carbon science [64][65][66][67]. Carbon nanotubes (CNTs) were discovered by the electron microscopist Sumio Iijima, of the NEC laboratories in Japan, in 1991 [68]. These molecular carbon fibers consist of tiny cylinders of graphite, closed at each end with caps which contain precisely six pentagonal rings. Since then, CNTs have captured the imagination of physicists, chemists and materials scientists alike. Physicists have been attracted to their extraordinary electronic properties, chemists to their potential as 'nanotest-tubes' and materials scientists to their amazing stiffness, strength and resilience. On a more speculative level, nanotechnologists have discussed possible nanotube-based gears and bearings. Nanotubes of the kind described by Iijima in 1991 invariably contain at least two graphitic layers, and generally have inner diameters of around 4 nm. In 1993, Iijima and Toshinari Ichihashi of NEC, and Donald Bethune and colleagues of the IBM Almaden Research Center in California independently reported the synthesisof single-walled nanotubes [69][70]. This proved to be an extremely important development since the single-walled tubes appeared to have structures which approximate to those of the "ideal" nanotubes [71]. CNTs, a type of fullerene, have potential in fields such as nanotechnology, biology, electronics, optics, materials science and architecture. Over the years, new applications have taken advantage of their unique electrical properties, extraordinary strength, and efficiency in heat conduction [72][73][74][75]. Applications of CNTs to which we need pay more attention in this dissertation include interconnects and transistors. Metallic CNTs have aroused research interest for their applicability as very-large-scale integration (VLSI) interconnects because of their high thermal stability, high thermal conductivity and large current carrying capacity [76][77]. Semiconducting CNTs have been used to fabricate field effect transistors (CNTFETs), which shows promise due

to their superior electrical characteristics over silicon based MOSFETS. Since the electron mean free path in SWCNTs can exceed 1 micrometer, long channel CNTFETs exhibit near-ballistic transport characteristics, resulting in high speed devices. CNT devices are projected to operate in the frequency range of hundreds of Gigahertz. Recent work detailing the advantages and disadvantages of various forms of CNTFETs have also shown that tunneling CNTFET offers better characteristics comparing with other CNTFET structures. This device has been found to be superior in terms of sub threshold slope – a very important property for low power applications [78][79][80].

Metal Oxide Semiconductor Field Effect Transistor (MOSFET) is a transistor used for amplifying or switching electronic signals. The basic structure of a MOSFET is formed by adding two heavily doped n^+ regions to the MOS capacitor on p-type Si. MOSFET is also called Insulated Gate FET (IGFET), it is the most commonly used FET. The MOS transistor is also called a surface field effect transistor since it depends on control of current through a thin channel at the surface of the semiconductor. When an inversion region is formed under the gate, current can flow from drain and source. MOSFET began to dominate integrated circuits in both unit volume and sales dollars in the 1970s. Kahng and Atalla demonstrated the first Si MOSFET in 1960 [81]. In 1964, Snow et al. [82] showed that sodium ion drift in thermally grown SiO_2 was the principal cause of the threshold voltage instability, and Kerr et al. [83] found that phosphorus silicate glass getters sodium in SiO_2. Balk suggested in 1965 that hydrogen could anneal out the interface traps by tying up the dangling Si and SiO_2 bonds [84]. Later it was found that HCl added to oxygen during oxidation incorporates chlorine and apparently immobilizes sodium in SiO_2. In 1966, Sarace et al. [85] developed the polycrystalline Si gate which served as a self-aligning diffusion mask for the source and drain. This structure gave a self-aligned gate

26

electrode and greatly simplified manufacturing processes and increased yield. With these technological advances, Intel developed the first large-volume MOS integrated circuit in 1970. This was a three-transistor, Si-gate, 1-kbit dynamic random-access memory (DRAM). Today DRAM chips have hundreds of millions of MOSFETs.

Ion-Sensitive Field Effect Transistor (ISFET) is used for measuring ion concentrations in solution. When the ion concentration (for example, the concentration of H^+) changes, the current through the transistor will change accordingly. The ISFET is in fact nothing else than a MOSFET with the gate connection separated from the chip in the form of a reference electrode inserted in an aqueous solution which is in contact with gate oxide [86][87]. The ISFETs towards pH sensing application have been explored and commercialized [86][87][88][89]. However, CNT-ISFET structures for pH sensing applications have not been reported yet. With the nanomaterials and nanotechnology that we have at present, it is time to develop the next generation CNT-ISFET based ion concentration sensing system.

Chapter III.   DIMENSIONAL CHARACTERIZATION OF VACNFs USING AFM

3.1   Fabrication of VACNFs

The intensively sensitive fabrication process of VACNF NEAs includes six major steps done on a four inch silicon <100> wafer that was previously coated with 500 nm of silicon dioxide. The steps of the fabrication process as well as the corresponding SEM images are shown in Figure 3.1 and Figure 3.2 [17], respectively. The main steps include (a) metal deposition for micro pads, contact pads and electrical interconnects; (b) nanopatterning of Ni catalyst dots; (c) directional growth of CNFs; (d) silicon dioxide deposition for electrical isolation and mechanical support; (e) chemical mechanical polishing (CMP) to expose CNF tips, and (f) a wet etch with 7:1 HF to expose contact pads.
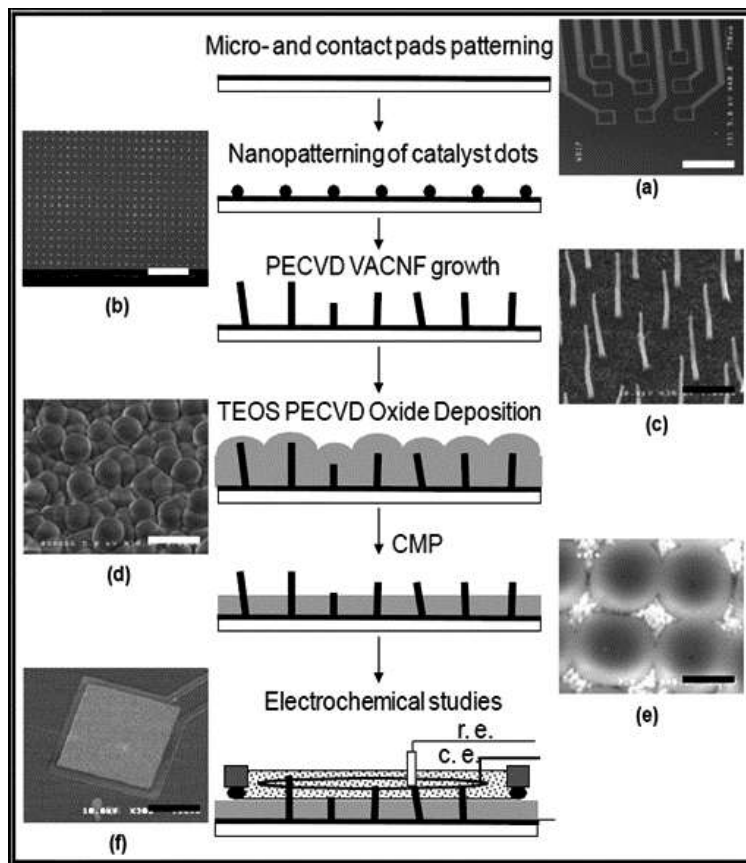
Figure 3.1: Procedures of fabricating VACNFs.
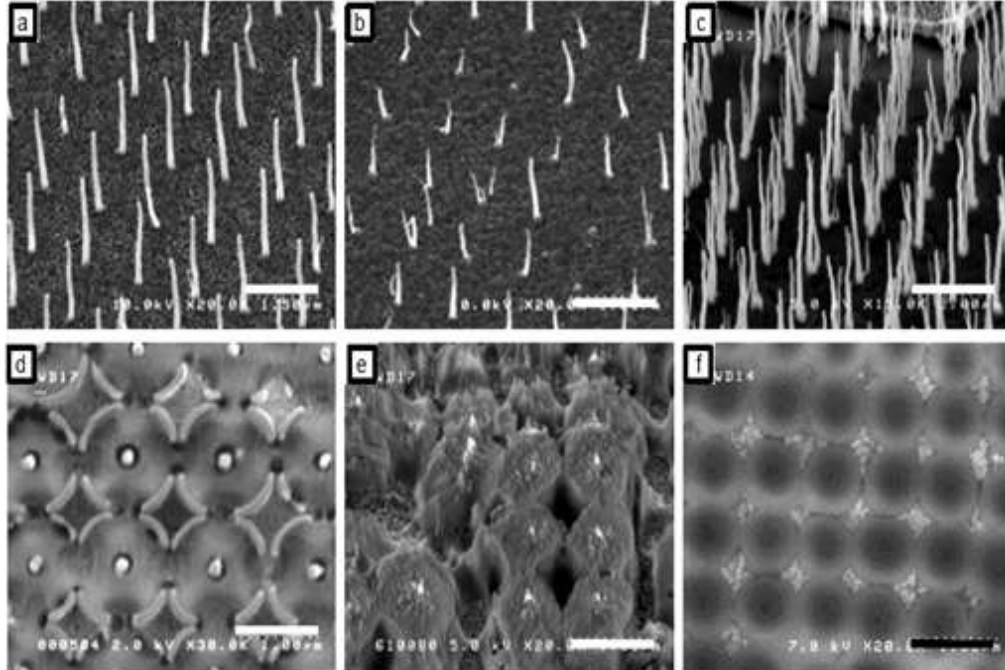
Figure 3.2: SEM images of VACNF fabrication steps.

In Figure 3.2, Top row shows the importance of PECVD chamber conditioning on CNF growth: (a) final run in "warm chamber"; (b) initial run in "cold chamber"; (c) Effect of high thermal ramps (~200 °C/min) resulting in multiple fibers from single nanopot. Bottom row illustrates SEM images of patterned arrays after re-exposing VACNF tips by Reactive Ion Etching (d), (e) and CMP (f). The dots are 100nm in diameter and 1μm in spacing.

3.1.1   Deposition of Metal

Using optical lithography patterning, 30 chips are able to be patterned onto the four inch wafer. Each chip contains nine contact pads that are attached by electrical interconnects to a single 3×3 set of arrays. Each of the nine arrays and the contact pads measures 200 μm × 200 μm and 2 cm × 2 cm respectively. Electrically, the underlying oxide isolates the pads. Using a 1-μm-thick Shipley 3612 resist and microlithography, the pads and interconnects are patterned. An inspection under a microscope is made and then the patterns are metalized using a liftoff technique. The process of electron beam evaporation is then used to deposit a 200-nm-thick Cr

film and then the wafer is immersed in acetone for one hour. Once removed from the acetone, the wafer is sprayed with methanol and isopropyl alcohol and blown dry with N_2.

3.1.2 Nanopatterning

Catalyst dots are then added to the wafer via a process called electron beam lithography patterning. There are approximately 39,000 catalyst dots that measure 100 nm in diameter on each micropad. The process begins with spinning a 400 nm thick layer of poly methyl methacrylate onto the wafer and then baking it at 180 degrees Celsius for 90 seconds and then exposed at 100 keV, 2 nA, 1950 $\mu C/cm^2$. After immersing the exposures into a solution of half methyl isobutyl ketone and half Isopropyl Alcohol (IPA) for two minutes, and then IPA for thirty seconds, the exposures are developed. The wafer is then blown dry with N_2 and examined under a microscope and again the pattern is metalized using a liftoff technique. The process of electron beam evaporation is then used to deposit a 10-nm-thick film of Cr trailing with a 30-nm-thick layer of Ni catalyst. The wafer is then submerged in acetone for one hour. After the time elapsed, the wafer is removed and sprayed with IPA and N_2 to blow dry.

3.1.3 Growth of VACNFs

The next step is to grow the VACNFs on the nickel dots that are created in nanopatterning. The growth is DC-biased Plasma-Enhanced Chemical Vapor Deposition (PECVD) growth. At a processing pressure of 6.3 mbar, plasma power of 180W and 700 degrees Celsius, 125 sccm C_2H_2 feedstock and 444 sccm NH_3 diluent are initiated. Then a five minute thermal annealing at 600 degrees Celsius is carried out following with 250 sccm NH_3. To attain the growth temperatures and thermal anneal needed, a 60 degree Celsius per minute incline is used. Each individual CNF is vertically arranged to freely stand on the surface with Ni catalyst on each tip. To check and affirm the process is done correctly, a fifteen-minute deposition is conducted.

Average results include a height of 1.5 μm, 100 nm base diameter, and 70 nm tip diameter. The uniformity of the growth is then checked by SEM.

3.1.4   Deposition of Silicon Dioxide

PECVD of silicon dioxide is managed next. To passivate the sidewalls of each individual fiber, a 3 micron SiO_2 layer is deposited onto the wafers using a pressure of 3 Torr, temperature of 400 degrees Celsius and RF power of 1000 W. The process includes a parallel plate, dual RF, PECVD using a mixture of 6000 sccm of O_2 and 2-3 ml/min of tetraethlyorthosilicate (TEOS). A highly conformal coating of SiO_2 is created on the newly created fibers and interconnects.

3.1.5   Chemical Mechanical Polishing

By CMP, existing of stock removal and final polish, the overrun oxide and a portion of the VACNF's are removed. This process involves removing the existing material with 0.5 μm alumina (pH 4) at 10 ml/min, 60-rpm platen, 15-rpm carrier, and 15 psig down force at 150 nm/min, re-exposure of VACNF tips and surface planarization. A 0.1 μm alumina (pH 4) at 10 ml/min, 60-rpm platen, 15-rpm carrier, and 25 psig down force is operated for final polish at 20nm/min. The wafer is cleaned by immersing it into a solution composed of water, hydrogen peroxide, and ammonium hydroxide at a ratio of 80:2:1 respectively and then spin-dried. The aim to re-expose the VACNF tips is carried out as well as the planarization of the surface.

3.1.6   Wet Etch

To expose the contact pads, a careful etching using silicon dioxide is achieved. Optical lithography, using 2.5 μm thick Shipley 3012 resist, is again used to remove SiO_2 from the contact pads for electrical connections to the potentiostat. The Shipley resist is baked at 125 degrees Celsius for 120 seconds and immediately immersed in Shipley EC11 to be exposed and developed. The wafer is then rinsed using DI water and inspected via a microscope. Then to set

the resist, the wafer is baked at 125 degrees Celsius for 180 seconds. Then using a 7:1 diluted HF solution, the oxide is carefully etched off of the contact pads at approximately 15 Å per second. For 15 minutes, the resist is then stripped off of the wafer using EKC 830 resist stripper. The wafer is then rinsed with DI water, blown dry with N_2 and diced into 30 individual chips sized approximately 14 mm^2.

3.2   Dimensional Measurement of VACNFs

3.2.1   Experimental Setup

In order to accurately determine the height and diameter of the VACNFs grown on 100 nm Ni dots, an Atomic Force Microscope is employed. The AFM used in the experiment is the Agilent 5500-ILM highly sensitive microscope as shown in Figure 3.3, which illustrates the experimental setup: the scan target is a single chip which contains 1×9 contact pads and a 3×3 set of nanoelectrode arrays. Each of these electrode arrays has a 200 μm $\times$ 200 μm area. The scanning will be done under Acoustic AC imaging mode, which is intermittent contact or non-contact, and the schematic is shown in Figure 3.4. The AFM probe, Tap190Al-G (BudgetSensors, Innovative Solutions Bulgaria Ltd.) has a resonant frequency of 190 kHz and a spring constant of 48 N/m. During intermittent contact, the tip is brought close to the sample so that it lightly contacts the surface at the bottom of its travel, causing the oscillation amplitude to drop. Hence, we may completely ignore the influence of the cantilever tip during the size measurement as it cannot change anything of the target shape without contacting.

In Figure 3.3, (a) shows the main structure for the measurement, (b) shows the sample holder where the chip is attached using a magnetic disk, (c) shows probe properly situated on AFM nose assembly, and (d) uses the video system to align the laser. In Figure 3.4, (a) (1) AC applied to the

nose cone, (2) the base body of the cantilever beam, (3) the cantilever with its probe; (b) & (c) the cantilever driven to oscillate in sinusoidal motion.
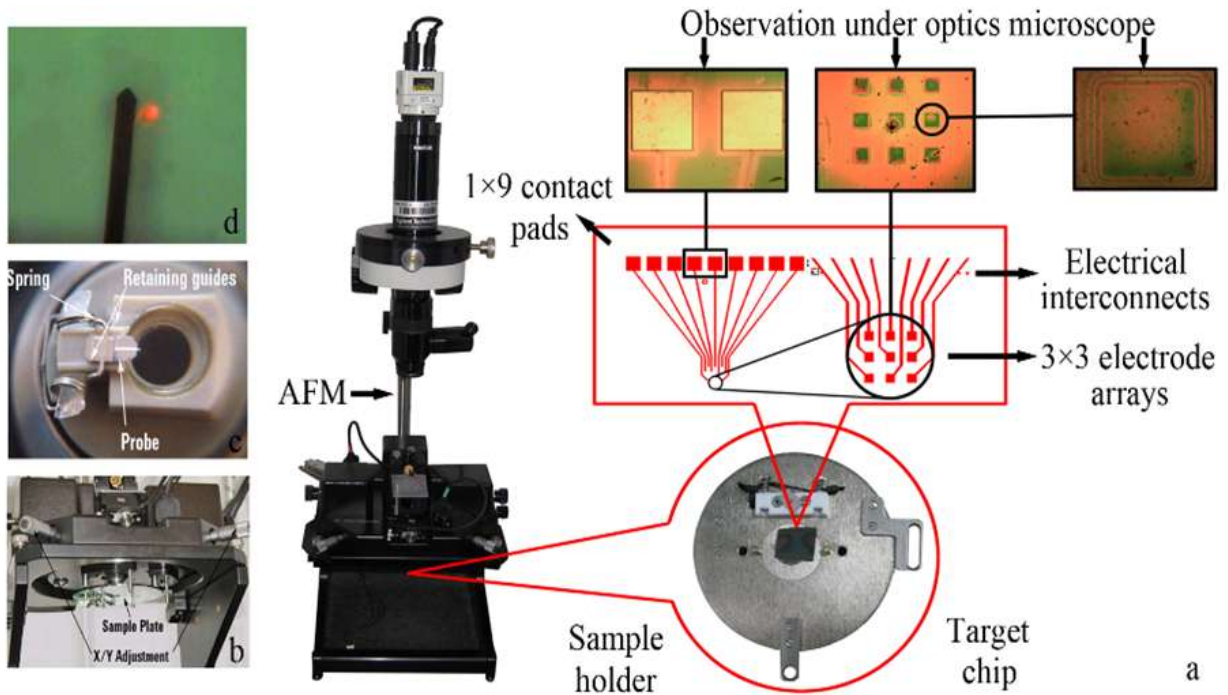
Figure 3.3: Experimental setup for scanning and measuring VACNFs.
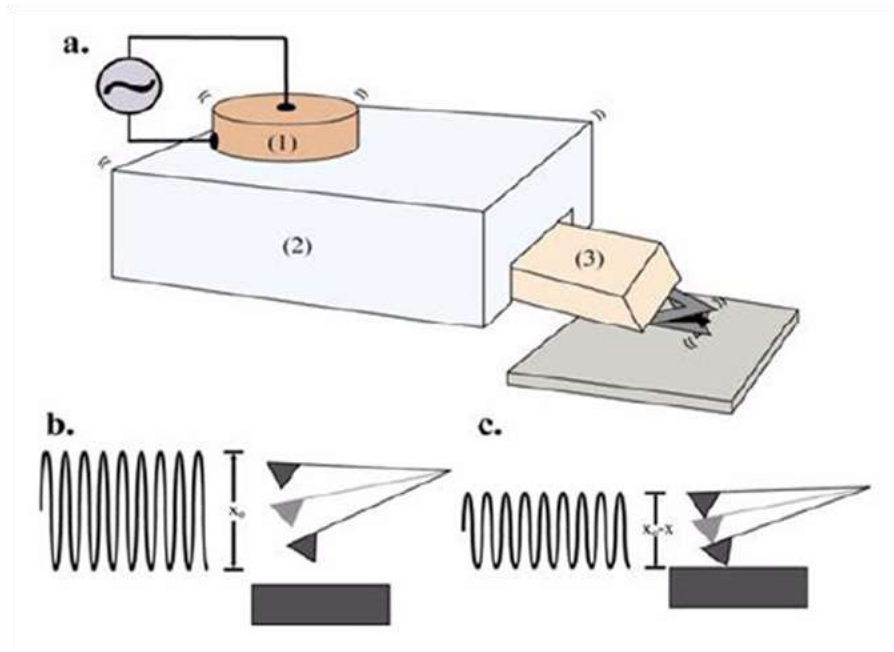
Figure 3.4: AFM probe motion under Acoustic AC mode.

3.2.2   Imaging and Measurement

Before measuring the size of the VACNFs and the cavities on the nanoelectrode arrays, they should be located and observed by the microscope video system. Thus, to scan the arrays in a 9 μm ×9 μm area with the small scanner becomes possible. After locating the fibers and cavities, the image can be zoomed into 2 μm ×2 μm, which encloses the identified fiber tips and cavities to obtain clear scan image and guarantee more accurate measurements. When a fiber or cavity appears clear in a scan topography image, a straight line can be drawn in any direction in topography image to cross the target. At the same time, the vertical information all the way along the line to complete a measurement can be obtained. This procedure is repeated until sufficient data is obtained for a particular array, and then starts on another array. Take Array 1 for instance: Figure 3.5 illustrates a topography scan in a 9 μm × 9 μm area. As we can see, under this scale only cavities are obvious. But it is enough as fiber tips can be found surrounding the cavities after zoom-in. Figure 3.6 (a) shows the zoom-in topography into 2 μm × 2 μm. Besides a cavity, there are four fiber tips surrounding the cavity. For a better view, a 3-Dimensional (3D) image of the zoom-in topography is generated as shown in Figure 3.6 (b). These cavities are caused by the chemical TEOS, which is applied during the step of PECVD oxide deposition. Thus, the measurement can be done by drawing lines crossing the cavities and the fiber tips. Figure 3.7 illustrates how to obtain the height and diameter of a fiber tip and the depth and diameter of a cavity from a cross-section image.
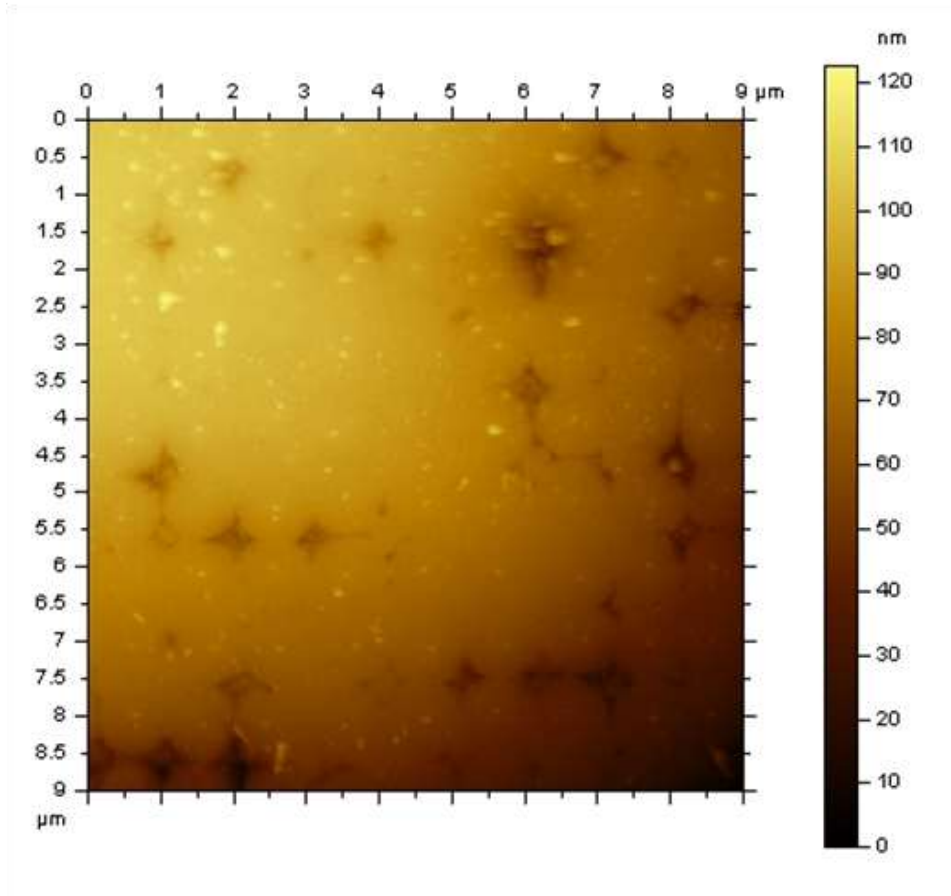
Figure 3.5: A 9 μm × 9 μm topography of Array 1 in Chip 1.
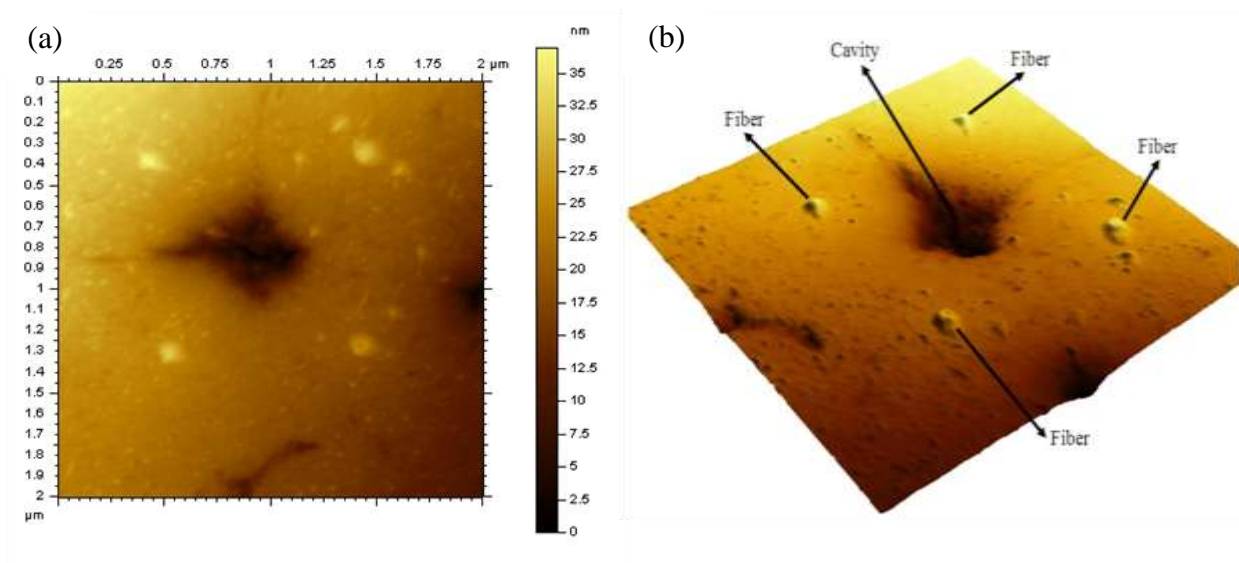
Figure 3.6: Zoom-in topography (a) 2 μm × 2 μm of Array 1 in Chip 1, (b) 3D image.
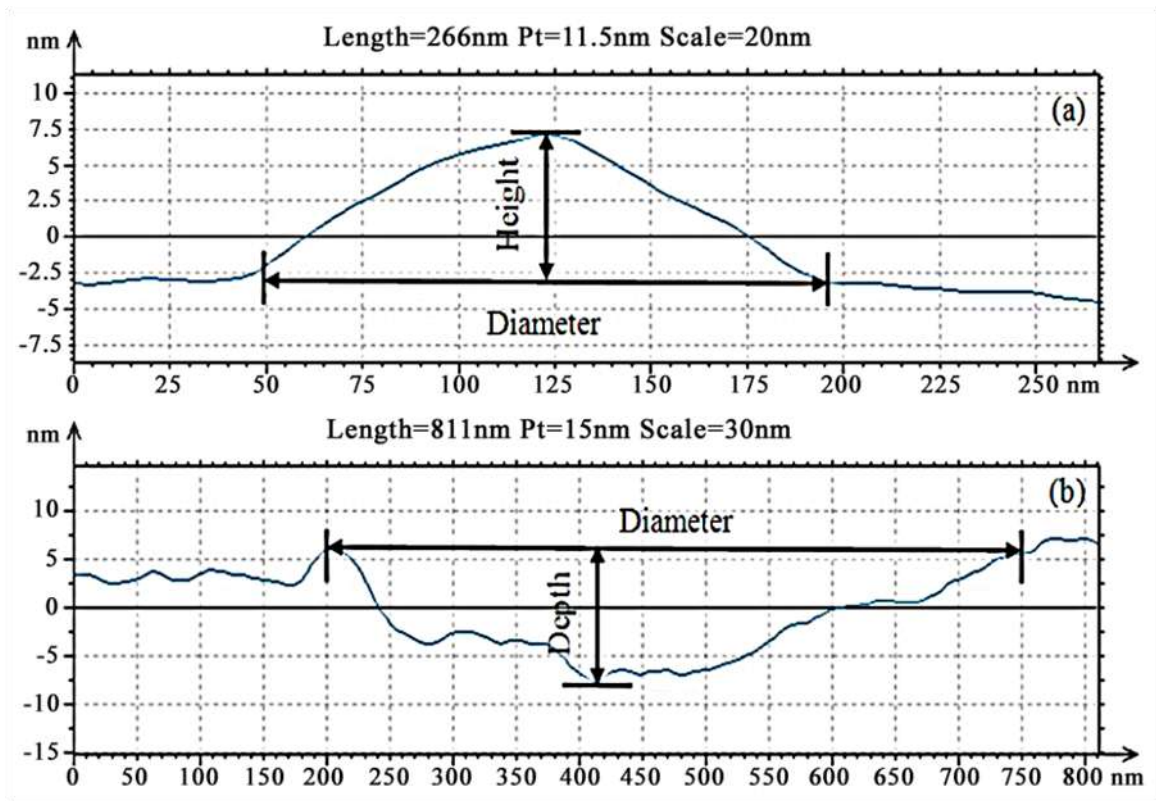
Figure 3.7: Cross-section information for measurement: (a) fiber and (b) cavity.

Table 3.1 gives the measurement results in detail by obtaining 10 measurements of fiber size consisting of diameter (abbreviated as Dia.) and height (abbreviated as Ht.) for each array in Chip 1, and the mean values are shown in Figure 3.8. Besides the fibers, 5 measurements of the cavities for each array in Chip 1 are also completed, and their mean values are shown in Figure 3.9. Additionally, the same measurement procedure is repeated for the fibers in Chip 2, which was fabricated the same way as Chip 1. Table 3.2 gives the measurement results in detail and the mean values are presented in Figure 3.10. After the mean values of the diameter and height of the fibers in each array on both Chip 1 and Chip 2 are obtained, in order to describe the size more accurately and scientifically, statistical analysis is employed.

36

Chip 1	Array 1		Array 2		Array 3	
Measure #	Dia. (nm)	Ht. (nm)	Dia. (nm)	Ht. (nm)	Dia. (nm)	Ht. (nm)
1	121.43	11	159.64	8.2	164.52	6.8
2	133.18	6.3	139.68	8.1	156.68	5.1
3	129.26	10.7	123.72	6.5	141.01	8.1
4	121.43	5.8	123.72	9.6	164.51	5.4
5	137.1	9.6	137.09	8	152.78	9.1
6	144.93	6	160.6	6.2	133.56	8.4
7	125.34	6.7	148.85	7.7	144.93	10.2
8	148.85	7	156.68	7.5	125.34	10.3
9	137.09	10.2	166.72	9.9	144.99	6.3
10	117.51	6.7	146.34	6.6	117.71	6.4
	Array 4		Array 5		Array 6	
Measure #	Dia. (nm)	Ht. (nm)	Dia. (nm)	Ht. (nm)	Dia. (nm)	Ht. (nm)
1	164.53	8.8	144.93	10.9	144.94	7.4
2	168.45	7.6	164.53	8.9	156.75	7.3
3	129.26	6.7	168.44	8.8	148.85	8.4
4	156.68	5.8	160.64	8.4	129.28	8
5	152.53	5.7	161.43	6.1	143.65	6.1
6	155.65	8	153.72	7.5	139.65	7.4
7	163.63	8.2	157.59	7.2	167.59	6.6
8	151.66	6.8	146.06	10	119.72	8.1
9	141.02	9.7	164.54	6.6	152.77	6.8
10	144.93	8.2	148.93	9.3	164.56	6.6
	Array 7		Array 8		Array 9	
Measure #	Dia. (nm)	Ht. (nm)	Dia. (nm)	Ht. (nm)	Dia. (nm)	Ht. (nm)
1	135.69	8	139.7	7.6	141.02	7.4
2	143.7	9.1	143.74	7.8	141.02	5.6
3	127.71	6.4	147.67	9.7	129.28	7.1
4	119.75	7.3	151.67	10.9	125.34	7.4
5	121.43	8.2	141.01	9.3	148.85	6
6	117.54	7.8	144.93	7.1	137.12	6.4
7	129.26	6.2	145.04	7.7	133.18	6.6
8	134.29	7.5	133.18	10.2	141.03	6.4
9	117.51	6.4	129.37	7.3	143.69	7.7
10	137.12	5.8	129.35	9.2	135.69	7.2
Overall Mean	Diameter: 142.87 nm				Height: 7.7 nm	

Table 3.1: Measurement results of VACNFs in Chip 1.
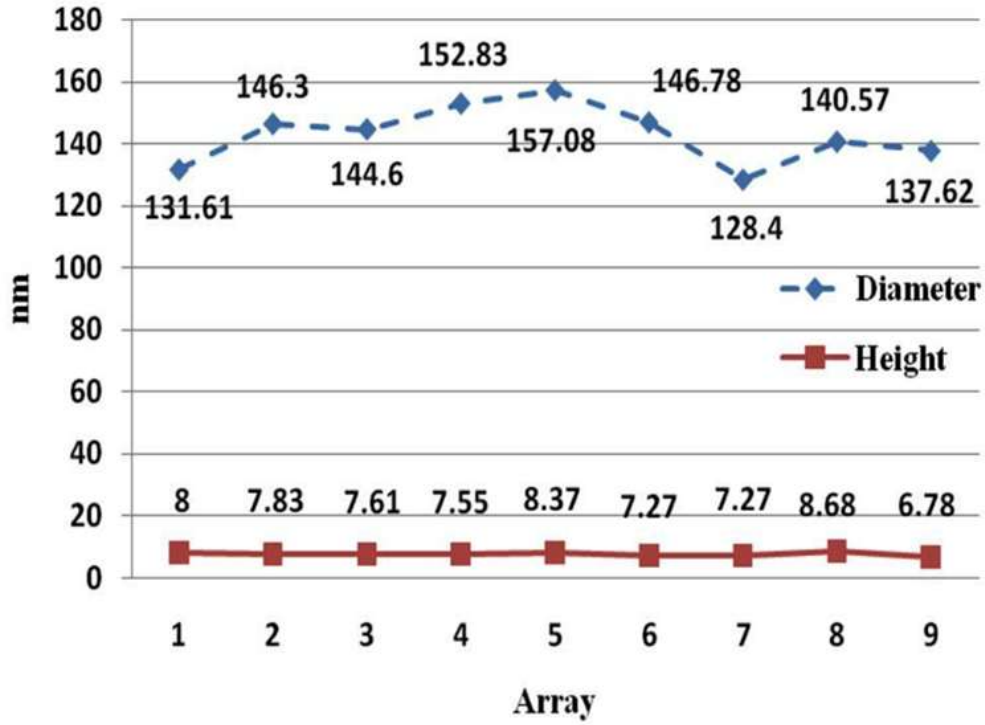
Figure 3.8: Measurement result of fibers in Chip 1 presented by mean values.
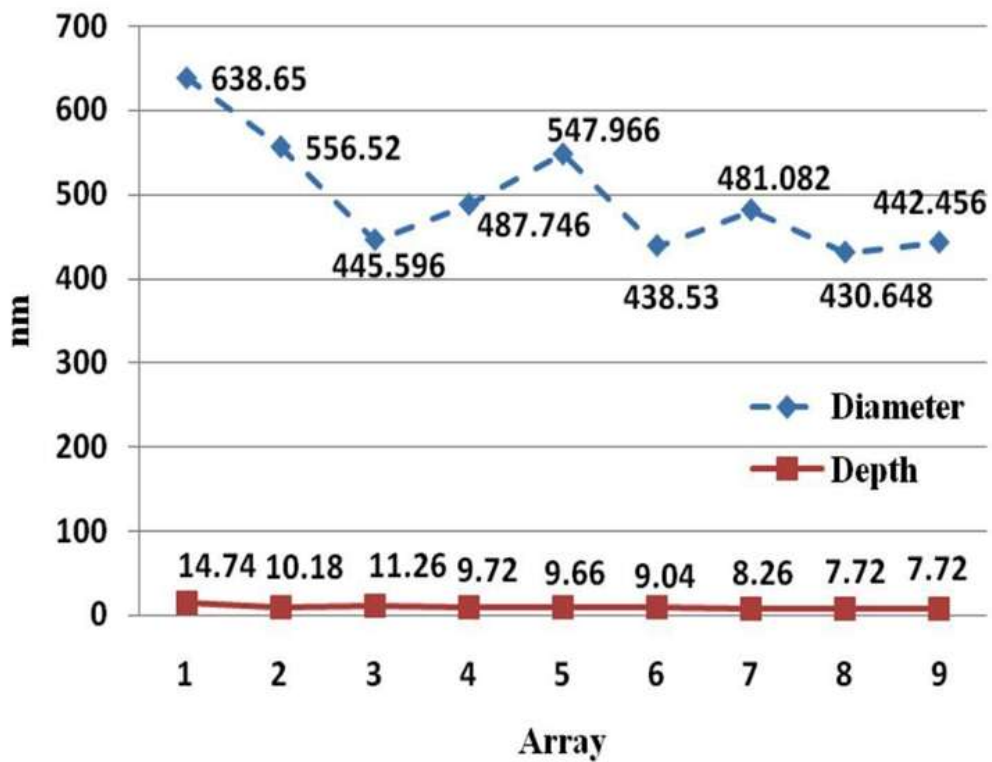
Figure 3.9: Measurement result of cavities in Chip 1 presented by mean values.

Chip 2	Array 1		Array 2		Array 3	
Measure #	Dia. (nm)	Ht. (nm)	Dia. (nm)	Ht. (nm)	Dia. (nm)	Ht. (nm)
1	132.92	6.5	187.58	4.8	160.60	4.3
2	156.40	6.5	171.74	6.8	160.60	10.4
3	172.02	6.7	159.64	4.6	141.02	7
4	140.74	5.5	175.60	7	144.93	6.1
5	125.10	5.8	179.60	5.8	137.10	8.9
6	125.15	7.6	140.74	7.1	152.77	8.9
7	140.74	7.5	164.19	7.4	148.81	10.8
8	164.20	7.1	140.74	5.4	137.06	8.6
9	172.08	6.5	132.92	6	143.68	7.4
10	140.74	7.5	179.90	10.2	147.68	11.9
	Array 4		Array 5		Array 6	
Measure #	Dia. (nm)	Ht. (nm)	Dia. (nm)	Ht. (nm)	Dia. (nm)	Ht. (nm)
1	148.85	7.1	171.61	9.1	151.36	8.5
2	141.01	6.1	123.74	14.8	143.47	7.7
3	168.44	6.3	111.74	13.5	151.36	6.9
4	156.68	5.8	126.01	6.6	159.33	6.1
5	172.35	14.4	150.40	6.6	129.82	6.5
6	176.27	8.7	121.94	8.2	129.88	9
7	105.89	13.2	138.20	7	129.82	5.7
8	144.93	6.6	123.74	8.4	137.93	6.3
9	156.68	6.9	139.71	7	167.30	7.7
10	115.32	11.6	152.76	9.9	143.39	7.4
	Array 7		Array 8		Array 9	
Measure #	Dia. (nm)	Ht. (nm)	Dia. (nm)	Ht. (nm)	Dia. (nm)	Ht. (nm)
1	127.46	6.8	122.74	7.2	125.23	11.7
2	135.43	7	145.76	8.5	172.02	13
3	135.54	8.2	168.87	6.3	156.33	7.4
4	151.36	8.7	145.76	6.1	164.20	7.9
5	148.56	8.3	133.00	6.7	191.19	8.1
6	164.19	6.9	148.56	6.2	143.40	6.6
7	140.83	7.1	140.74	7.3	143.40	10.9
8	140.74	10.3	140.74	7.7	127.46	10.4
9	140.74	7	143.56	6.3	184.11	10.2
10	148.56	7.2	159.48	6.6	176.44	12.5
Overall Mean	Diameter: 148.15 (nm)				Height: 7.9 (nm)	

Table 3.2: Measurement results of VACNFs in Chip 2.
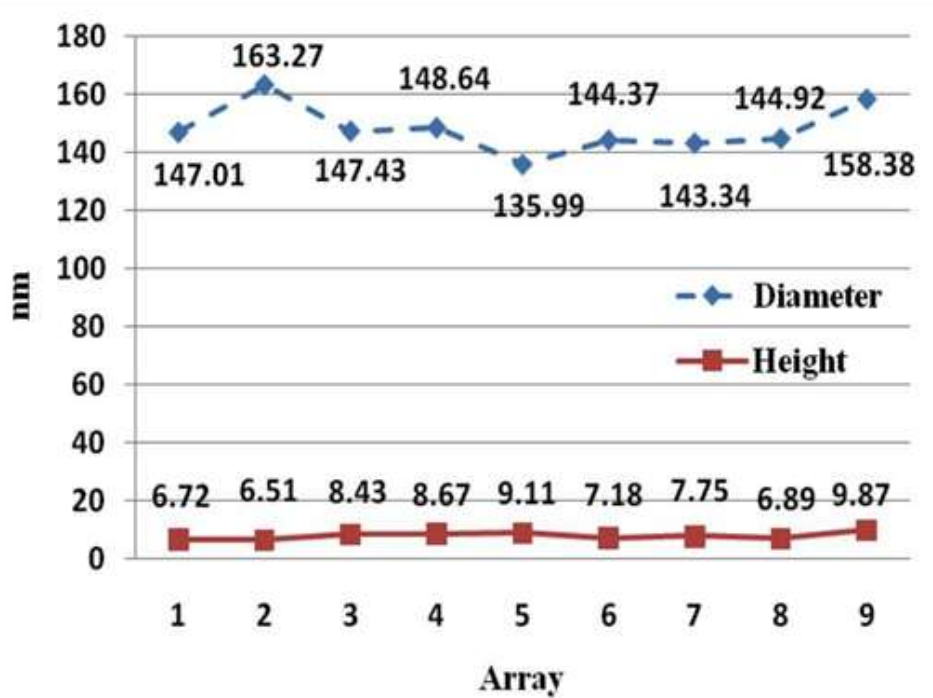
Figure 3.10: Measurement result of fibers in Chip 2 presented by mean values.

3.3 Statistical Analysis

3.3.1 Confidence Interval

In statistics, a confidence interval (CI) is an interval estimate of a population parameter [90]. Instead of estimating the parameter by a single value, an interval likely to include the parameter is given. Thus, confidence intervals are used to indicate the reliability of an estimate. How likely the interval is to contain the parameter is determined by the confidence level or confidence coefficient.

Therefore, this statistical method is applied for our experimental data in order to obtain the intervals to describe the size of fibers. Take the fibers in Chip 1 for instance, from [90] and Figure 3.8, the mean values for each array are obtained, and we put the value as the first element in a 1×9 matrix as follows: {131.61 146.3 144.6 152.83 157.08 146.78 128.4 140.57 137.62}, and then we substitute these samples into the calculation of a 95% confidence interval. The mean

of the matrix is 142.87 nm and the standard deviation is 8.82 nm. Thus, the CI is determined as

[137.11nm 148.63nm]. For the height, the matrix is as follows: {8 7.83 7.61 7.55 8.37 7.27 7.27

8.68 6.78}, the mean is equal to 7.7 nm and the standard deviation is 0.554 nm. Thus, the CI can

be determined as [7.338 nm 8.062 nm]. Furthermore, based on the data in Figure 3.9, the

standard deviations are 66.65 nm and 2.07 nm for cavity diameter and depth (abbreviated as Dp.)

respectively. Thus, the 95% CIs can be calculated to describe the diameter and depth as [453.03

nm 540.12 nm] and [8.46 nm 11.16 nm] respectively. Lastly, from Figure 3.10, another two CIs

with same confidence level are computed, [143.13 nm 153.17 nm] and [7.18 nm 8.62 nm] for

diameter and height respectively. Their standard deviations are 7.68 nm and 1.11 nm respectively.

Hence, the accurate size of the fibers and cavities can be determined with the intervals as stated.

The CI result details are given in Table 3.3, and Equation (3.1) shows how to calculate the

interval.

$$CI = [\overline{X} - Z \times \frac{\sigma}{\sqrt{N}}, \overline{X} + Z \times \frac{\sigma}{\sqrt{N}}]$$
(3.1)

where, $\overline{X}$ is the mean values of the samples; Z, the critical value, is equal to 1.96 in a 95% CI; σ

is the standard deviation, and N is the number of the samples.

Chip 1		Confidence Interval	Mean	Standard Deviation
Fiber	Dia. (nm)	[137.11 148.63]	142.87	8.82
	Ht. (nm)	[7.338 8.062]	7.7	0.554
Cavity	Dia. (nm)	[453.03 540.12]	496.58	66.65
	Dp. (nm)	[8.46 11.16]	9.81	2.07
Chip 2		Confidence Interval	Mean	STD. Dev.
Fiber	Dia. (nm)	[143.13 153.17]	148.15	7.68
	Ht. (nm)	[7.18 8.62]	7.9	1.11

Table 3.3: Calculation results of CIs for fibers and cavities.

3.3.2   P-Value

Besides CI, another statistical method is employed to help, P-Value. In statistical hypothesis testing, the P-Value is the probability of obtaining a test statistic at least as extreme as the one that was actually observed, assuming that the null hypothesis is true. The fact that P-Values are based on this assumption is crucial to their correct interpretation. The lower the P-Value is, the less likely the result is, assuming the null hypothesis, the more "significant" the result, in the sense of statistical significance. One often rejects a null hypothesis if the P-Value is less than 0.05 or 0.01, corresponding to a 5% or 1% chance respectively of an outcome at least that extreme, given the null hypothesis [90].

Therefore, the P-Value can be used to judge if a new group of measurements is reliable enough to confirm the fibers dimension but not some other "dirty" particles on the surface. Take measurements for Arrays 3 & 5 in Chip 1 and Arrays 3 & 7 in Chip 2 for example, Table 3.4 gives the results of the fibers for us to tell if the measurement for each array should be accepted or rejected. In Table 3.4, the standard is the mean of entire 90 measurements on each chip of diameter and height, respectively (see Table 3.1 Table 3.2); the mean is the averaged value of 10 measurement for each array; the critical value Z is calculated as in Equation (3.2); $\Phi(abs(Z))$ is the corresponding cumulative area, whose value can be determined; P-Value is obtained as in Equation (3.3) and the significance level is 0.05. Thus, the rejection is able to be confirmed after comparing P-Value with the significance level. If P-Value is less than or equal to 0.05, this group of data is rejected.

			Standard	Mean	Std.Dev.	Z	ϕ(abs(Z))	P-Value	Sig. Lv.	Reject
Chip 1	Array 3	Dia. (nm)	142.866	144.603	14.95	0.367	0.6736	0.6528	0.05	No
		Ht. (nm)	7.707	7.61	1.79	-0.171	0.5987	0.8026	0.05	No
	Array 5	Dia. (nm)	142.866	157.081	7.867	5.714	0.9997	0.0006	0.05	Yes
		Ht. (nm)	7.707	8.37	1.442	1.454	0.9394	0.1212	0.05	No
Chip 2	Array 3	Dia. (nm)	148.148	147.425	8.081	1.784	0.9678	0.0644	0.05	No

		Ht. (nm)	7.903	8.43	2.182	1.048	0.8531	0.2938	0.05	No
	Array 7	Dia. (nm)	148.148	143.341	9.741	0.244	0.5987	0.8026	0.05	No
		Ht. (nm)	7.903	7.75	1.067	0.203	0.5987	0.8026	0.05	No

Table 3.4: Calculation and application of P-Value.

$$Z = \frac{(Mean - Standard) \times \sqrt{N}}{Stdev.}, N = 10 \tag{3.2}$$

$$P - Value = 2 \times (1 - \Phi(abs(Z))) \tag{3.3}$$

3.3.3   Discussion

The calculations above show relatively large variations to the measurement of the same objective. For example, in Table 3.1, the fourth measurement of fiber diameter in Array 2 is 123.72 nm, which is quite different from the sixth measurement of 160.6 nm. Similarly, the measurement of fiber height is 5.1 nm versus 10.3nm in Array 9. This phenomenon is not caused by an incorrect measurement but by the non-uniform growth of the VACNFs on Ni dot nanoelectrodes. Similarly, in Figure 3.5, the upper-left differs from the bottom-right owing to an uneven distribution of the cavities generated in CMP procedure, which matters very little. The cavities in the arrays will not influence the performance of the nanofibers on the nanoelectrodes as long as the VACNFs growth is not impeded. Furthermore, as introduced in 3.1.3, the bare VACNF tips we originally incubated by PECVD are supposed to have a diameter of 70 nm while our AFM measurement combined with a statistical analysis shows an almost double size after the deposition of SiO_2 and CMP steps as given in Table 3.3. Based on this phenomenon, it may be concluded that there could be some SiO_2 residual still covering these VACNF tips after CMP. Thus, there would be an obstacle to the electrical connection with outside circuit through the contact pads. This is also verified by our attempt at electrical property testing of VACNF tips using Current Sensing AFM. In the future, since tetraethlyorthosilicate (TEOS) causes the cavities on the surface of the nanoelectrodes, it could essentially be used as a method to create

nanochannels for other potential applications such as chemical sensor and pH sensor Lab-on-Chip (LOC) system development using the VACNFs.

3.4 Summary

Microchips with multiplexed 3×3 biosensing arrays employing patterned VACNFs are ready to work. However, when researchers want to examine the quality of the fabrication, a tool with nano-level ability is needed. In this chapter, measurements of the VACNFs are carried out using AFM, and the results are presented. Consequently, their accurate sizes are indicated statistically by confidence interval. Furthermore, P-Value is introduced as a tool for the judgment of the possibility of correct measure target in the future measurement. The work is a proof of the feasibility to examine the growth of carbon nanofibers using the nano tool, AFM. With proper statistical analysis, the experimental results become more scientific and reliable for other researchers to refer to.

Chapter IV.   MECHANICAL PROPERTY TESTING OF NANO/BIO SAMPLES

USING AFM BASED NANOINDENTATION

4.1   Methodology of AFM Based Nanoindentation

The mechanical properties of linear, isotropic, elastic materials considered here may be completely described by two intrinsic parameters, the Young's Modulus E (Pa) and the Poisson's Ratio v (dimensionless). Through the AFM-based nanoindentation, it is able to obtain the raw data Amplitude (V) versus distance (μm), similar to Figure 1.7. The raw data indirectly gives the relationship of the force (nN) versus indentation (nm), which is the pre-condition to calculate the Young's modulus of the sample. Force curves can be collected by monitoring the cantilever deflection while users ramp the piezo scanner in z direction (vertical), with the x, y scanning disabled, resulting in a plot of Amplitude versus the distance that the piezo scanner changes vertically. Figure 4.1 illustrates the schematic for indenting a soft flat surface with a rigid conical indenter. As we can see, Δz is the piezo-actuator vertical displacement under user's control, Δd is the deflection of the cantilever, and δ is the indentation distance on the sample. The relationship of these three parameters can be described as in Equation (4.1). Furthermore, according to Newton's third law, the magnitude of the force acting on the sample is equal to the force exerting on the cantilever, which is able to be calculated as in Equation (4.2), where k_c is the spring constant of the cantilever. Thus, the force curve can be obtained.

$$\Delta z = \Delta d + \delta \tag{4.1}$$

$$F = k_c \cdot \Delta d \tag{4.2}$$

Before it is able to convert the raw data of amplitude versus distance into the relationship of force versus indentation of the sample, a calibration is necessary as the AFM software provides the deflection information of the cantilever through amplitude in volt. The sensitivity (nm/V) is

necessary in order to obtain the deflection of the cantilever in nm during the indentation. For the calibration, we usually indent a mica surface with the same tip as the one that is going to indent a sample. The mica surface is hard enough to work as a rigid substrate, which means there will not be a deformation of the mica surface and the translation distance is equal to the deflection of the cantilever (imagine there is no sample and δ is 0 in Figure 4.1). Hereby, the sensitivity is able to be determined with this method. Figure 4.2 illustrate how to extract force vs. indentation data based on AFM indentation raw data after the sensitivity is known.
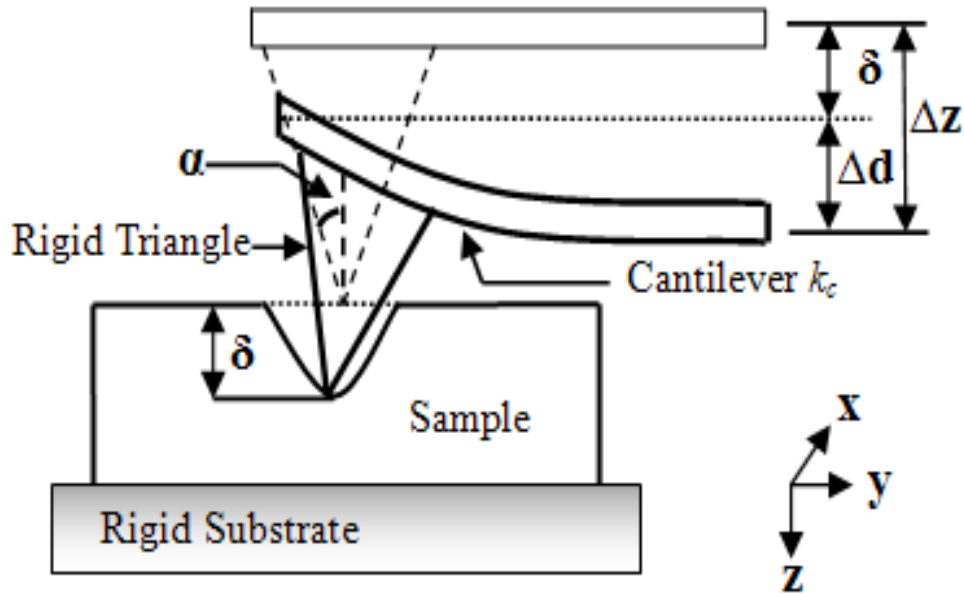
Figure 4.1: Schematic of AFM-based nanoindentation for thin sample with conic tip.

The slope of a force curve describes the elastic properties of a sample in a qualitative way. On an infinitely stiff sample, the deflection Δd of the cantilever is identical to the movement of the piezo in Δz direction. In the case of a soft sample, the cantilever tip will indent the sample. This indentation distance δ leads to a smaller deflection Δd, resulting in a flatter force curve with a smaller slope. Also the loading force can be determined as in Equation (4.2) according to Hooke's law.
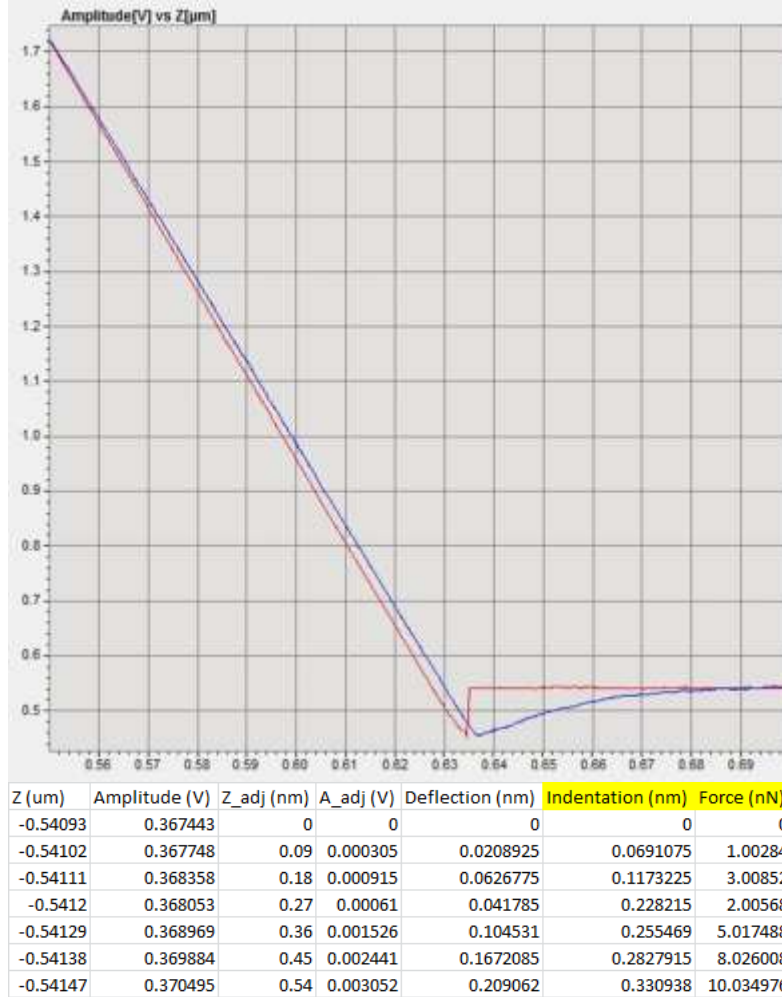
Figure 4.2: A typical AFM based nanoindentation force curve and corresponding data extraction.

Z (um)	Amplitude (V)	Z_adj (nm)	A_adj (V)	Deflection (nm)	Indentation (nm)	Force (nN)
-0.54093	0.367443	0	0	0	0	0
-0.54102	0.367748	0.09	0.000305	0.0208925	0.0691075	1.00284
-0.54111	0.368358	0.18	0.000915	0.0626775	0.1173225	3.00852
-0.5412	0.368053	0.27	0.00061	0.041785	0.228215	2.00568
-0.54129	0.368969	0.36	0.001526	0.104531	0.255469	5.017488
-0.54138	0.369884	0.45	0.002441	0.1672085	0.2827915	8.026008
-0.54147	0.370495	0.54	0.003052	0.209062	0.330938	10.034976

The elastic deformation of two spherical surfaces touching under load was calculated theoretically in 1882 by H. Hertz. Sneddon extended the calculation to other geometries [91], like a rigid cone pushing onto a flat thin sample as used in this chapter. We will call this model the Sneddon model to distinguish it from others. The Sneddon model gives the following relation between the indentation δ and the loading force F:

$$F = \left(\frac{2}{\pi}\right)\left[\frac{E}{(1-v^2)}\right]\delta^2 \cot\alpha \qquad (4.3)$$

where, F is the loading force on the sample, E is Young's Modulus of sample, v is the Poisson's Ratio (assumed to be 0.06 and 0.5 for VACNFs and scaffolds respectively [92][93][94]), δ is the

indentation distance, and α is the half-opening angle of indenter (AFM tip). Therefore, E can be determined once the relationship between the force and the indentation is obtained. For the Sneddon model, the indentation distance δ needs to be so large that the cone apex can be considered infinitely sharp.

4.2   Dimensional and Mechanical Behavior of VACNFs at Subzero Temperatures

4.2.1   Background

A major concern for the space organizations is to adjust the space and resources available on a space mission. Extraordinary electro mechanical properties of carbon nanomaterials had attracted the attention of researchers [95][96][97]. Ever since discovery of carbon nanotubes in 1991, researchers have effectively used them as sensory materials, storage materials, hardening materials and so on. With the advancement in MEMS technologies and understanding about carbon nanomaterials integration, today it is possible to detect molecules down to parts per billion (ppb) with carbon nanomaterials sensors [98][99]. More exciting are their response time in seconds and the resources in millivolts. Thus, many space research organizations, for example NASA, are exploring the possibility of integration of sensors made of carbon nanomaterials.

NASA took the initiative and established a research organization called NASA Ames research center with a mission *"To develop Nanotechnology based chemical sensors that can provide high sensitivity, low power and low cost portable tools for in-situ chemical analysis in space and terrestrial applications"* [100]. Based on their current sensor development results, NASA has proven that *the carbon nanotube sensors can offer very high sensitivity for NO_2 , ammonia, methane, acetone, benzene and toluene detection, with detection limits in the lower ppm to ppb level and response time in seconds to minutes"* [100]. Each sensor draws the power in microwatts to milliwatts. The size of the detector is designed to be $5´\times 5´\times 1´$ for 32 sensing

48

elements detection system. The weight of this detector is estimated to be less than 2 kg. All these factors are encouraging scientists to use them in space applications.

In 2003, the Nuclear Regulatory Committee (NRC) Decadal Survey for Solar System Exploration recommended that "NASA commit to significant new investments in advanced technology so that future high–priority flight missions can succeed." In a 2007 report released by NASA on its failure of flight missions [101], it concluded that extreme environments of temperature, pressure and extreme radiations are the primary causes for the failure of the missions. The report also emphasizes on the need for investment on extreme environment technology needs. In the near future, there will be many more outer space missions, and this pose a greater challenge to the scientific community for development of materials that can cater the needs of these missions.

The fact that most of our planetary system is engulfed in negative temperature convinced us to characterize the nanofibers at subzero temperatures. Furthermore, since the mechanical properties of materials change widely with temperatures, the measurement of Young's Moduli for VACNFs is targeted.

4.2.2   Extreme Environment Treatment

In this experiment, the same VACNF chip as shown in Figure 3.3 is used. Additionally, a Microclimate Benchtop Test Chamber (Cincinnati Sub Zero, MCBH-1.2) as shown in Figure 4.3, which possesses an error of $\pm 0.5\%$ in the range of -73 ^{o}C – 190 ^{o}C, is employed to realize extreme environment treatment. Thus, the environmental chamber is set to a fixed temperature. After the attainment of a specified temperature, the chip with nanofibers is placed in the Environmental Chamber for 30 minutes at the specified temperature in order to facilitate response to temperature. Then, the substrate is transferred into a dry box (McDry MCU-201,

49

Seika Machinery Inc., USA) as shown in Figure 4.4 for about 90 seconds to eliminate water vapor. The relative humidity of dry box normally remains as low as 1% in normal operation. After loading the sample from the subzero temperature treatment chamber, the percentage can resume to less 3% in 90 seconds. Then, the sample can be transferred to the AFM for imaging to measure the dimensions and analyze the mechanical properties of treated fibers. In general, it takes about 255 seconds to complete a single frame scan for 5 μm × 5 μm when the scan speed is set at 5.021 μm/s, which means 1.004 lines/s, and the image resolution is 256 × 256.

Figure 4.3: Microclimate benchtop test chamber for subzero temperature treatment.

Figure 4.4: Dry box for anhydrating chip after each subzero temperature treatment.

4.2.3   Imaging and Measurement Using AFM

Agilent 5500 ILM is used for accurate measurement of VACNF dimensions after the treatment in the test chamber. Dimensional measurement is carried out in Acoustic AC (Tapping) mode with a Tap190DLC (BudgetSensors, Innovative Solutions Bulgaria Ltd.) probe, which has a resonant frequency of 190 KHz and force constant of 48 N/m. In Atomic Force Microscopy, a large area of 5 μm × 5 μm is scanned initially in order to locate the nanofibers. As mentioned in the fabrication methodology, the nanofibers are grown on a patterned Ni dots with a spacing of 1 μm. AFM and SEM images of VACNF before temperature treatment are shown in Figure 4.5. Standing carbon nanofibers at spacing of 1 μm are clearly seen in the figure. Once the nanofibers are identified, substrate is rescanned to shrink the area to 2 μm × 2 μm in order to accurately

measure the nanofiber dimensions. Figure 4.5 (b) shows the SEM image of the nanofibers scanned using a Philips SEM at 30 KeV. Nanofibers are clearly seen as the white dots in the black background.
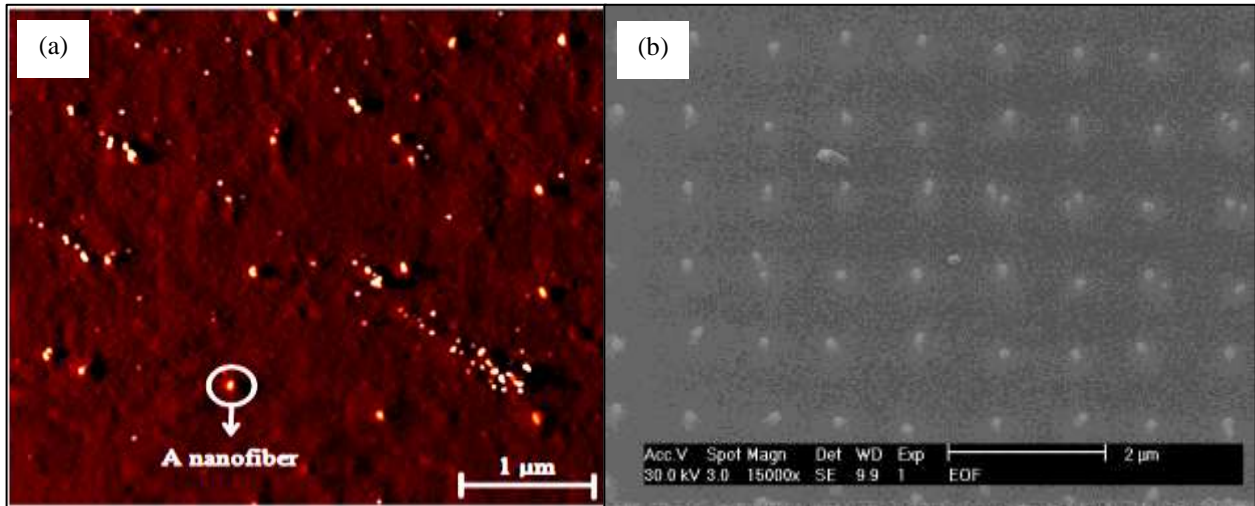
Figure 4.5: Scan images of VACNFs (a) AFM and (b) SEM.

Figure 4.6 shows 3D AFM images after VACNFs are exposed to different subzero temperatures. As seen from the 3D images, there is no obvious change to the shape of the nanofibers before and after the treatment. For reliability, 20 measurements for both height and diameter are recorded and averaged at each temperature treatment. Table 4.1 gives the mean and standard deviation of nanofibers after treated in the extreme environments. From the Table 4.1, it is clear that the nanofibers become smaller as the temperature decreases.
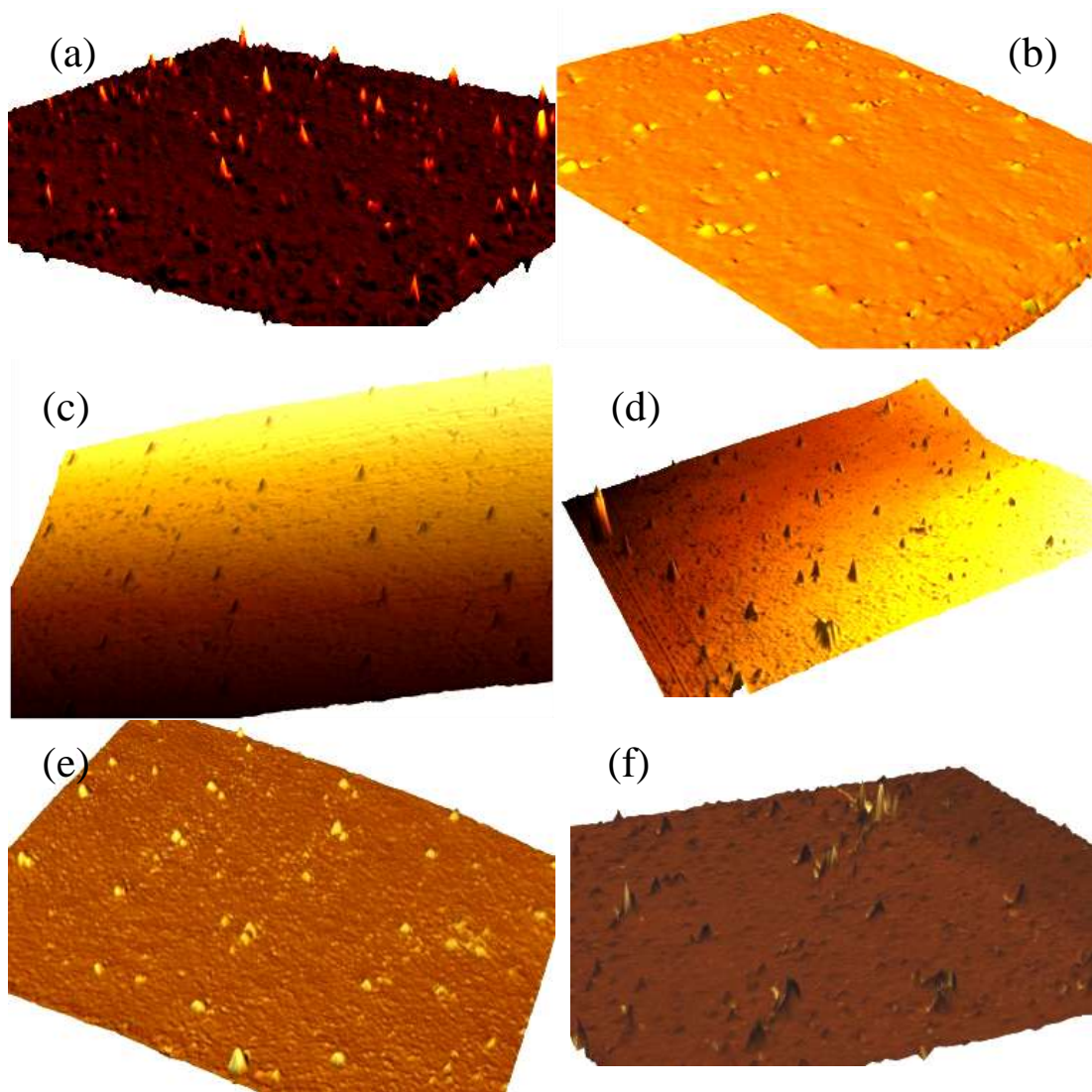
Figure 4.6: AFM 3D images of VACNFs at (a) -20, (b) -30, (c) -40, (d) -50, (e) -60, and (f) -70 °C.

Temp (oC)	Average Height (nm)	Average Diameter (nm)	Standard Deviation of Height (nm)	Standard Deviation of Diameter (nm)
25	8.86	254	1.321	36.4
-20	5.25	189.5	0.939	27.5
-30	6.71	136.75	2.35	21.83
-40	5.44	112.77	1.28	15.36
-50	6.53	118.58	2.27	22.29
-60	5.99	173.2	1.172	17.03
-70	6.63	120.50	1.58	19.95

Table 4.1: Average dimensions of VACNFs exposed to extreme temperatures.

4.2.4　Nanoindentation on Treated VACNFs

The nanoelectrode arrays are scanned to locate VACNFs, and Figure 4.6 (f) shows the VACNFs that are treated in the test chamber at -70 ºC for 30 minutes. The tip is then positioned on the top of a located fiber followed by a sweep of amplitude versus distance in vertical direction. Thus, the raw data of indenting a treated nanofiber is obtained as shown in Figure 4.7, where "Amplitude" describes Δd and "z" presents Δz. In order to convert the amplitude in V into the cantilever deflection in nanometer (nm), to calibrate the sensitivity (S_Z in nm/V) of the cantilever deflection for Position Sensitive Detector (PSD) on the AFM is necessary. Before scanning the nanoelectrode arrays, the same tip is used to indent a mica disc surface 5 times. During this indentation period, the mica surface is assumed to be rigid, which indicates $\delta = 0$. Hence, the deflection of the cantilever Δd equals to the vertical displacement Δz, which is controlled by user when an indentation sweep is engaged. Therefore, the sensitivity is obtained, and its mean value is calculated to be 68.5 nm/V with a standard deviation of 0.55 nm/V. With this sensitivity, the relation between the force and the indentation distance is obtained. Furthermore, the slope of force versus δ^2 is approximated by a linear fit as shown in Figure 4.8. The linear fit provides the slope approximation, which is 34.078 nN/nm^2. Finally, this slope is substituted in Equation (4.3) to compute value of the Young's Modulus, $E_{VACNF} = 23.9628$ GPa. Table 4.2 shows the detailed results of E_{VACNFs} at different temperature treatments.

Temp (^{o}C)	E_{VACNF} 1 (GPa)	E_{VACNF} 2 (GPa)	E_{VACNF} 3 (GPa)	Mean (GPa)	Stdev. (GPa)
25	511.82	1240.43	1010.68	920.98	372.50
-20	44.03	124.80	50.76	73.19	44.82
-30	70.36	64.41	80.86	71.88	8.33
-40	59.18	50.89	40.53	50.20	9.35
-50	37.66	34.22	55.07	42.32	11.17
-60	41.01	40.67	30.22	37.30	6.13
-70	23.54	20.84	26.86	25.09	1.67

Table 4.2: Young's Moduli of VACNFs after exposed to subzero temperatures.
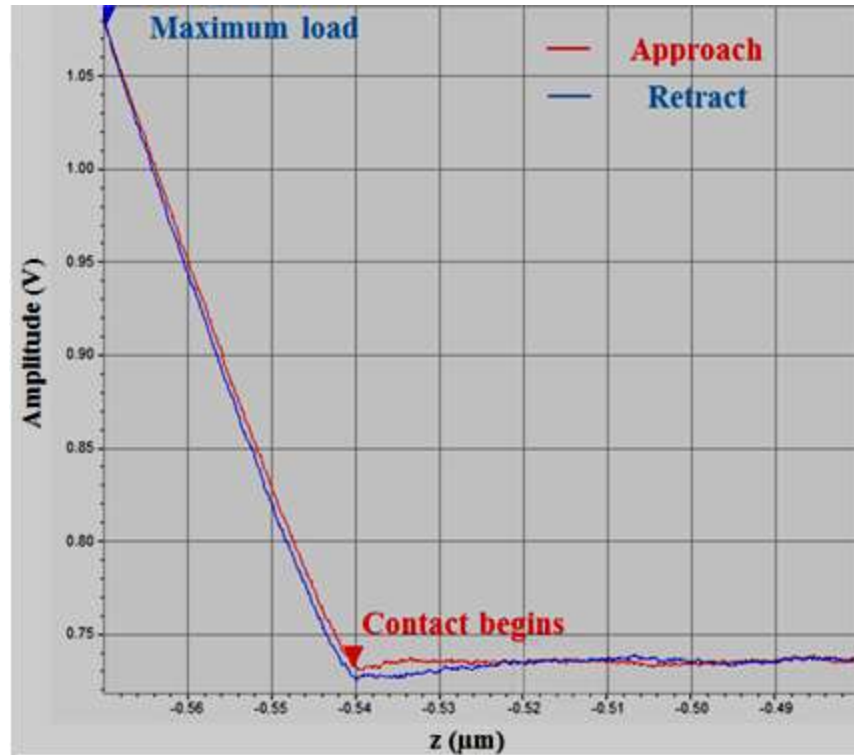
Figure 4.7: Raw data of AFM based nanoindentation on a treated fiber.
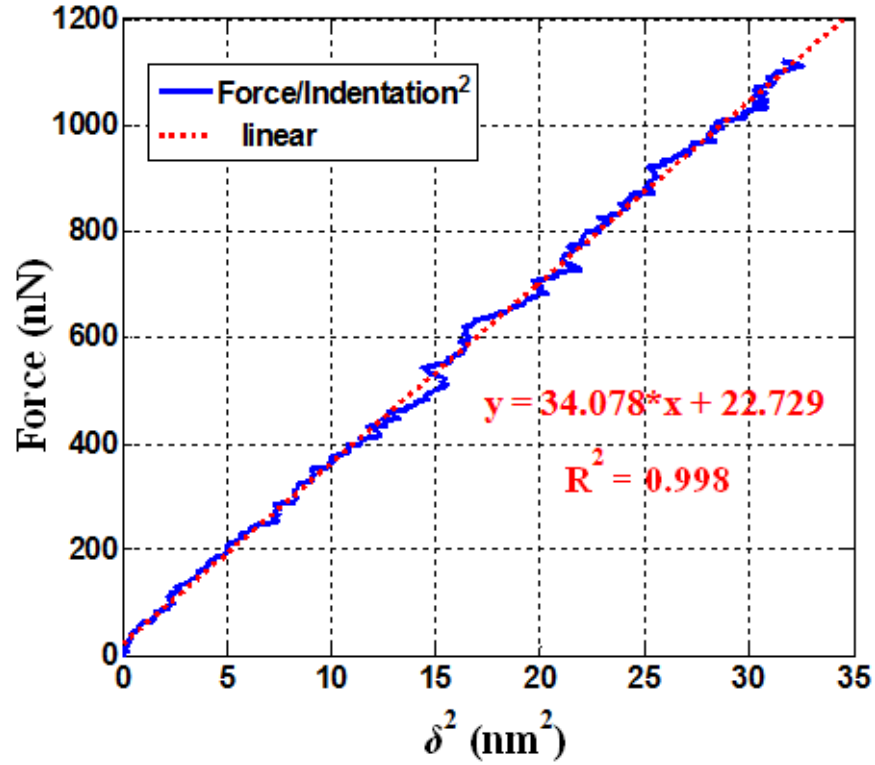
Figure 4.8: Force vs. indentation squared with linear fit.

55

4.2.5 Discussion

From the current dimensional results, it is imperative that the dimensions of VACNFs are widely affected by the changes in temperatures. This is critically important because of the fact that most material properties at nanoscale depend on the dimensions. Our particular interest lies in the changes of the height of VACNFs rather than their diameter as the side walls of the nanofibers are passivated by SiO_2, which leads to much more complex material behavior. Furthermore, it has been reported that the main problem with VACNF based sensor is that large variations in fiber height and overall fiber density will fluctuate the sensitivity of the sensor [17], which is the key to the reproducibility of sensor. From the current dimensional results, it is observed that the nanofiber height decreases with the temperature when compared with the original room temperature. But in the subzero range, the height almost remained constant near to 6 nm.

Besides the height of VACNFs, the other critical factor regarding the sensing ability is the density of fibers. Materials usually become more vulnerable at low temperatures. To investigate the mechanical properties of VACNFs at extreme temperatures become necessary as fibers are promising to work in space. Fibers, that lose their stiffness significantly, may no longer be functional as sensing elements. Mechanical properties of the nanofibers exposed to extreme environments are studied in detail. Young's moduli of the nanofibers are calculated at different temperatures. It is obtained that the Young's modulus of VACNFs at room temperature approximately equals 920 ± 372.5 GPa. These values are in accordance with the Young's modulus of MWCNTs reported in previous research works [102][103]. However, the Young's moduli of the VACNFs fall drastically as they are exposed to subzero temperatures. It is also imperative from Table 4.2 that the Young's Moduli of VACNFs are reduced approximately by

20 fold at subzero temperature range. Moreover, the Young's moduli decrease linearly as temperature changes in the subzero range. Figure 4.9 shows the plot of Young's Moduli against subzero temperatures. With linear curve fit, a regression line equation is obtained and included in Figure 4.9. In statistics, coefficient of determination, R^2, is used to evaluate the quality of curve fit. R^2 varies between 0 and 1 with 1 being the best fit and 0 being the worst fit. As depicted in Figure 4.9, Young's Moduli vs. subzero temperatures linear fit curve (the red dashed line) has an R^2 of 0.9537 proving that the linear fit is the best one for the collected data when -70 $^{\circ}$C $\leq$ T $\leq$ -20°C. Thus, VACNFs will lose their complete stiffness at a temperature lower than -93.68 $^{\circ}$C accordingly.
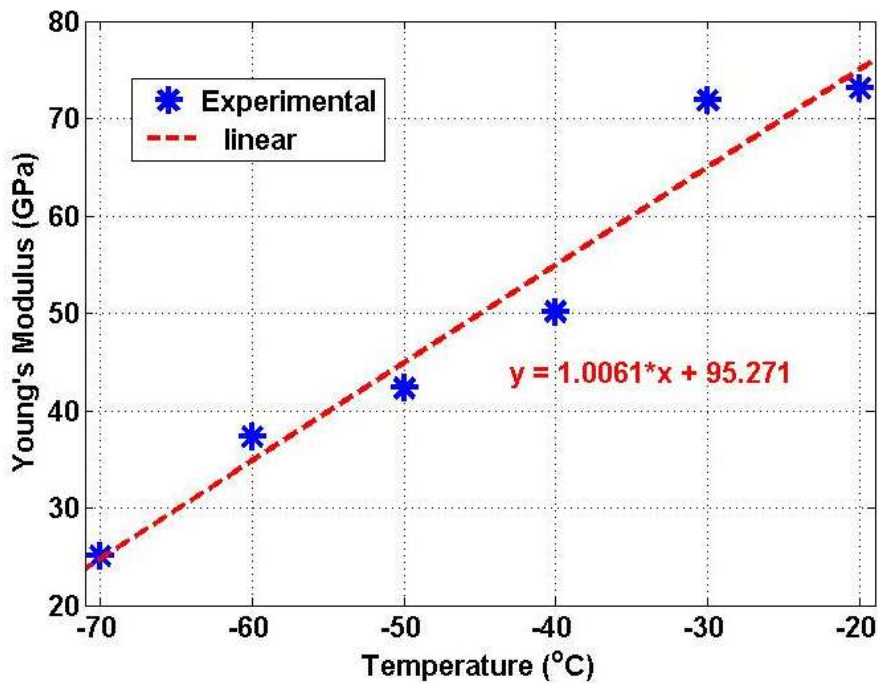
Figure 4.9: Yong's Moduli of VACNFs at subzero temperatures.

4.3   Determination of Mechanical Properties of Soft Tissue Scaffolds

4.3.1   Background

Cells *in vivo* interact with various surrounding cells through cell-cell and cell-extracellular matrix (ECM) interaction in a three dimensional (3D) fashion. It has become clear recently that

cell fate is regulated by not only soluble signaling molecules but also physicochemical cues such as mechanical properties of the ECM. Thus, the determination of mechanical properties of *in vitro* constructed ECM, i.e., tissue scaffolds, becomes more critical for cell growth and differentiation in 3D cultures. A variety of biomaterials have been developed and adopted for fabricating various types of scaffolds for 3D cultures. Among those biomaterials, collagen and chitosan are two of widely used natural biomaterials for 3D cultures [104][105][106][107]. Collagen and chitosan can be readily crosslinked to form hydrogels for growing soft tissues [108][109][110]. Compared to scaffolds made from hard materials, cells grown inside soft scaffolds respond more significantly to mechanical properties of a scaffold. For example, cells grown inside a hydrogel scaffold have been found to respond considerably different to the stiffness of a scaffold [111][112][113][114]. In addition, the elasticity of a soft scaffold can be altered by cells through their secreted ECM [115]. A body of evidence suggests that cells can alter substrate's stiffness hundreds of micrometers away from their edges [116]. The traction forces that cells apply to their matrix can also refashion matrix stiffness of a hydrogel scaffold that exhibit strain-stiffening behaviors.

Different from hard materials, the characterization of mechanical properties of soft scaffolds is quite challenging due to their fragility. They usually can only tolerate nN stress, making it difficult to measure. One way to overcome this difficulty is to determine the elastic modulus of these scaffolds through the nanoindentation technique. Nanoindentation has been developed for investigating mechanical properties of many soft materials [117][118]. In a nanoindentation test, small loads and small tip size can be achieved using an AFM [119]. AFM is a powerful tool for determining various biological processes in nanometer scale. It can not only image the topography of a surface but also measure forces at nN level. It has been employed as a

nanoindenter for characterizing elastic properties of soft materials [120][121][122]. For example, AFM nanoindentation has recently been applied to quantify quasi-static mechanical properties of newly synthesized cell-associated matrices of individual chondrocytes [59][62].

Although AFM nanoindentation shows tremendous potentials for characterizing soft tissues, its application in determining mechanical properties of hydrogel scaffolds in liquid has not been explored yet. Here, the dissertation presents an approach to quantify mechanical elastic stiffness of soft tissue scaffolds through AFM-based nanoindentation. A mathematical model is developed for determining the stiffness and elastic modulus of a collagen-chitosan hydrogel scaffold. The effect of cell growth on the mechanical tensile strength of a collagen-chitosan scaffold is also investigated

4.3.2   Scaffold Fabrication and Cell Growth

Cell-based tissue engineering holds great potential for therapies involving regeneration and/or replacement of damaged tissue. Such approaches typically involve seeding cells within scaffolds and subjecting them to stimulatory biochemical and/or mechanical factors in vitro or in vivo to promote the development of engineered tissue. The ultimate goal and challenge is to develop a graft with structural, biochemical and biomechanical properties similar enough to healthy tissue so that upon maturation in vivo it can restore physiological function. To achieve this objective, it is important to know the mechanical property of engineered tissue.

Details regarding how to fabricate collagen-chitosan scaffolds can be found in [123]. In brief, 0.5% (w/v) rat tail type I collagen and 2% chitosan were dissioved in 0.1 M acetic acid, followed by freezing at -80 $^{\circ}$C for 2 hours and then lyophilized for 24 hours. After lyophilization, the scaffolds were crosslinked by cutting them into small sizes (15 mm in diameter and 2 mm in thickness) and immersing into 2 ml 40% (v/v) ethanol containing 50 mM MES (ethanesulfonate)

59

(pH 5.0), 33 mM EDC (carbodiimide) and 8 mM NHS (N-hydroxyl succinimide) for 10 hours. After crosslinking, the scaffolds were neutralized with 0.1 M Na_2HPO_4 (pH 9.1) for 1 hour, followed by repeatedly washing with 40% ethanol and Milli-Q water to remove excess base until the pH reached between 7.0-7.4. The scaffolds were then lyophilized for 24 hours and sterilized under UV.

A human foreskin fibroblast cell line, HFF-1 (ATCC SCRC-1041) was routinely maintained in 20% defined fetal bovine serum, 2 mM L-glutamine, 1% nonessential amino acids, 0.1% mM β-Mercaptoethanol, and 80% DMEM at 37 ^{o}C in a 5% CO_2 incubator. Single suspended cells were prepared by trypsinizing with 0.05% trypsin/0.53 mM EDTA (Mediatech, Inc. VA) and seeded into collagen-chitosan scaffolds at a density of 1×10^5 cells/scaffold. The scaffolds were prewashed with Phosphate Buffered Saline (PBS) solution and pre-equilibrated with the aforementioned culture medium.

Collagen is one of the major ECM components that support cell growth. It has been widely used in constructing 3D tissue scaffolds [124][125]. Chitosan is another biomaterial that has been extensively used to endow scaffolds with sufficient mechanical strengths required for cell growth. A number of studies suggest that the mixing of chitosan with collagen can significantly improve cell proliferation and attachment [126][127]. Studies further indicate that physicochemical cues of a collagen-chitosan scaffold are significantly different depending upon the collagen content in the scaffolds [128]. We find that a ratio of 8:2 (collagen versus chitosan, v/v) or 7:3 of collagen-chitosan scaffolds are suitable enough for cell growth [123][128]. Thus, in this experiment, the ratios of 8:2 (refer to scaf1) and 7:3 (refer to scaf2) are chosen for fabricating the scaffolds. These interconnected porous structures are suitable for cell growth [129].

Scaffolds were mounted on stubs with a double-stick carbon tape and sputter coated with gold-palladium, and examined using a Joel Field Emission SEM (JSM-6335F, JOEL) at an accelerating voltage of 5 kV. Distinct sections from each sample were imaged (4 images per sample), and the pore size was determined using the Image-Pro Plus software. At least 90 pores were assessed for each sample. Data are presented by the mean pore size ± Standard Deviation (SD). The SEM images of these two scaffolds are shown in Figure 4.10. Both scaffolds exhibit interconnected network structures with a high porosity. The average pore size of high collagen content scaffolds, scaf1 (8:2), is about 150±67 μm. It is 100±48 μm for low collagen content scaffolds, scaf2 (7:3).
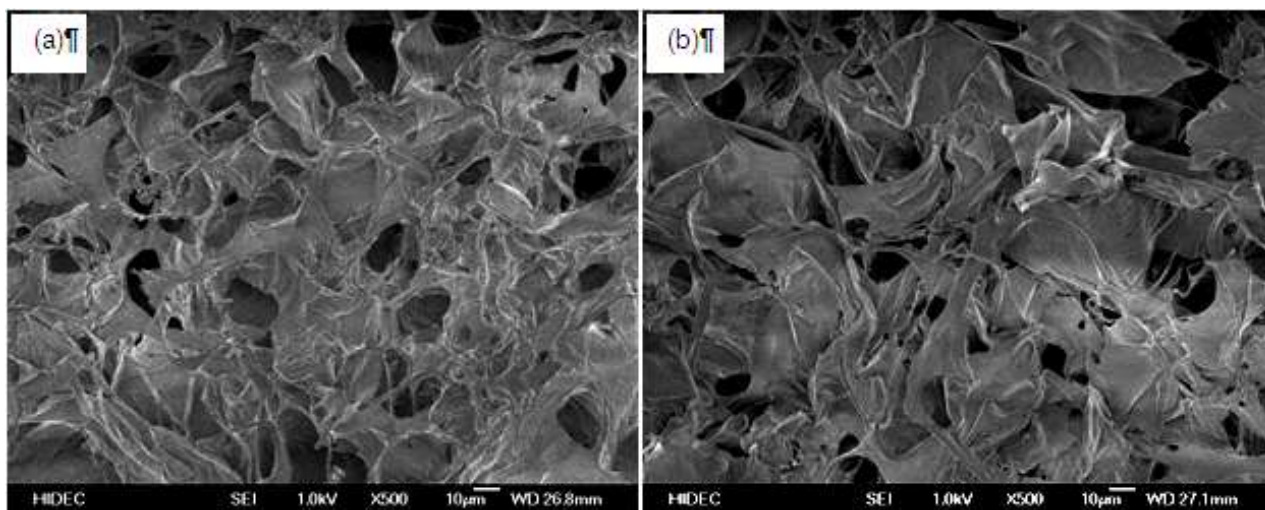
Figure 4.10: SEM images of collagen-chitosan (v/v) scaffolds (a) 8:2 and (b) 7:3.

4.3.3   Nanoindenter and Conditions

The Agilent 5500 ILM AFM is used to perform the nanoindentation. A rotated monolithic silicon probe ContAl (BudgetSensors, Innovative Solutions Bulgaria Ltd.) with a spring constant of 0.2 N/m is adopted for AFM AC mode imaging and nanoindenting test. The probe employs an "on scan angle" symmetric triangle tip to provide a more symmetric representation of features over 200 nm and its resonance frequency is 13 kHz in air, which could vary accordingly in liquid.

The tip radius is less than 10 nm and its half cone angle α is 25°. A typical indentation distance is approximately 1000 nm, 200 nm and 65 nm for the scaffolds, 3µm bubble, and 1µm bubbles, respectively. The nanoindentation test needs to be done in liquid. For liquid imaging, the laser is originally aligned in air mode after a tip is assembled. This is critical to the controlling of the distance by which the tip is withdrawn from the sample plate, as the tip and the sample will be invisible after the liquid cell is mounted on the sample plate. After alignment, a liquid cell is mounted on the sample plate as shown in Figure 4.11 to create a liquid-sealed space where the sample is immersed in PBS. In case the sample floats, a transparent tape can be used to fix the sample to the bottom of the plate to guarantee the stability. The assembled sample plate is then moved back to AFM for scanning or indenting. Since liquid will cause laser refraction, the position of the detector needs a second adjustment in order to keep receiving the laser signal. The indentation is very much straightforward as the distance between the tip and the sample can be controlled by user.

Figure 4.11: Liquid cell for imaging and indenting samples in liquid.

Before the indentation process, the surface information of the scaffold is obtained under liquid environment using Acoustic AC imaging mode. Scaffold samples are immersed in PBS buffer to simulate the same surroundings as they are inside human body. The topography image obtained during scanning is depicted in Figure 4.12 for the engineered Collagen-Chitosan scaffold. The scan is suspended right after it starts, and no valuable information about the sample surface is obtained. The reason for this is that the position of the AFM tip varies fiercely than it does for a normal scan because of the liquid environment which affects the stability of the scanning motion. Moreover, this happens because of the extreme softness of the engineered collagen-chitosan scaffold. Additionally, approaching is always hard to complete as the scaffold sample is so soft that it is very unstable while sitting on the sample plate in PBS. Furthermore, a small ladder-like surface would have the tip stuck as the scan range of the AFM scanner is in microns. Despite these particular setbacks, the nanoindentation of the engineered Collagen-Chitosan scaffold will not be affected.
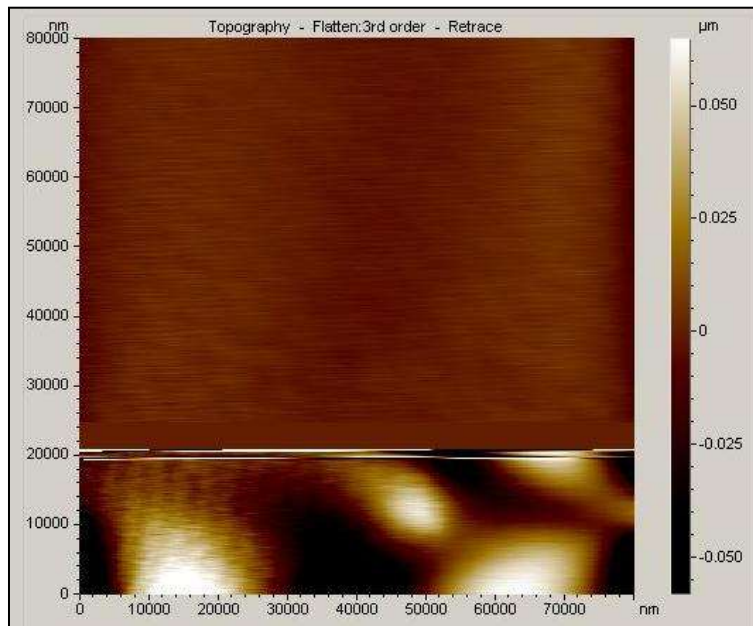
Figure 4.12: A suspended scan of scaffold in liquid.

The mean elastic modulus of a scaffold can be determined from its force curve. Data from each group will be expressed as the mean ± SD by frequency analysis. The Levene homogeneity test indicates unequal variances ($p<$ 0.05). Therefore, the means are analyzed by one-way analysis of variance with a Brown Forsythe test to account for unequal variances, followed by Bonferroni post-hoc tests using SPSS to evaluate differences between regions. A P-Value $<$ 0.05 is considered statistically significant.

4.3.4 Results of Nanoindenting Scaffolds

Before indenting the scaffolds, a mica disk is indented for the sensitivity calibration with the same tip as well as in the same condition, and it is resolved that the sensitivity of the cantilever deflection for PSD (S_Z) on the AFM is approximately 89.0 nm/V. Besides E, there are another two variables to be determined, the nanoindentation force (F) and distance (δ). They are the precondition and will be indicated in the force curve of force (nN) versus indentation (nm). The curve can be obtained indirectly from the indentation raw data in the AFM control software PicoVIEW. Eventually, the Young's Modulus (E) can be computed by selecting six points from the force versus indentation curve and averaging the values. Equations below will better explain how to extract the indentation force and distance from a group of indentation raw data, where the information of Δz and amplitude A can be read from the raw data. A_0 and z_0 are the amplitude and z-axis piezo sensor when the cantilever begins to bend, while A and z the corresponding values of an indentation status that user select.

$$\Delta z = |z - z_0| \tag{4.4}$$

$$\Delta d = d - d_0 = (A - A_0) \times S_Z \tag{4.5}$$

$$\delta = |z - z_0| - (d - d_0) \tag{4.6}$$

$$F = (A - A_0) \times S \times K_C \tag{4.7}$$

Figure 4.13 shows a typical set of AFM raw data after indenting a collagen-chitosan scaffold at a ratio of 7:3 (a. piezo movement starts in z-axis; b. cantilever begins to contact the sample; c. z-axis movement stops; d. cantilever departs from the sample during unloading; and e. piezo movements stops). It appears that the approach and the retrace curves are not completely overlapped. There is a 0.4 μm offset between the start and end height. The effect of this offset, however, is minor, as the indenting curves are linear. This offset should be mainly due to the water layer on the sample. As the measurements are performed in PBS buffer, the liquid layer exerts a capillary force that is strong and attractive. As the scanner pulls away from the surface, the water holds the tip in contact with the surface, bending the cantilever strongly towards the surface (Amplitude difference between point b and d in Figure 4.13). At some point, depending upon the thickness of the water layer, the scanner retracts enough that the tip springs free (point d in Figure 4.13). This is known as the snap-back point. As the scanner continues to retract beyond the snap-back point, the cantilever remains straight as the scanner moves it away from the surface in free space [130]. Moreover, it is assumed that the deformation during indentation is elastic and the indenter is a rigid body. Only the approach data is used for obtaining force curves of a sample.
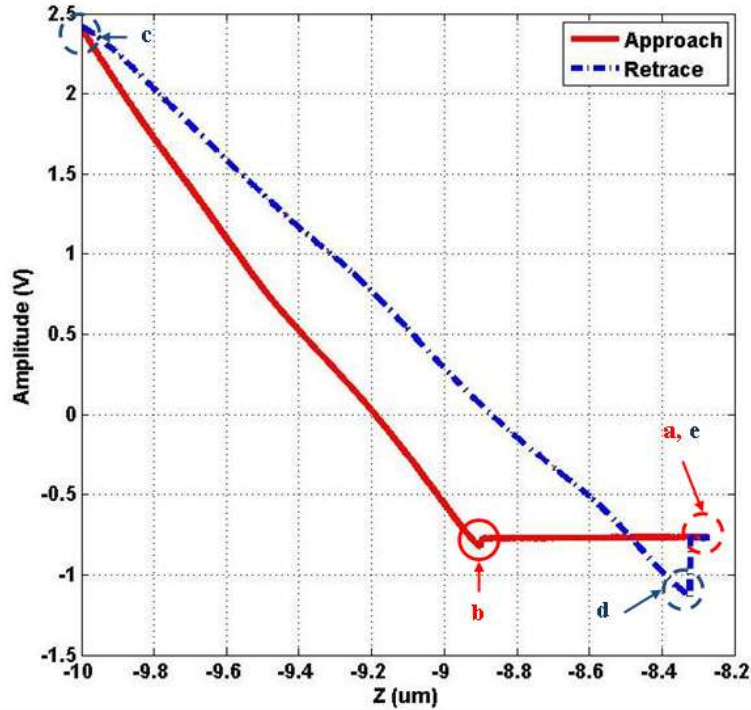
Figure 4.13: Raw data of indenting a collagen-chitosan scaffold.

Because the AFM tips used are rather sharp cones, the induced shear stress is on the order of the sample's elastic modulus with the danger of producing plastic deformation. Although the cone could penetrate the surface of a scaffold, resulting in plastic and/or irreproducible deformations, such effect can be minimized by taking a reading on one spot a time. It is believed that as long as the indentation approach and retrace plots are the same for one and the other, and the force curves obtained are linear, the elastic state would be guaranteed. Figure 4.14 presents the force curves from 4 indentations on a scaf1 sample at 4 locations within a small neighboring area of the sample surface. Only one indentation is done at each location. The slopes (nN/nm) are 0.01058, 0.008055, 0.02341, and 0.01845 for Indent #1, 2, 3, and 4, respectively. They appear to be within a reasonable range.
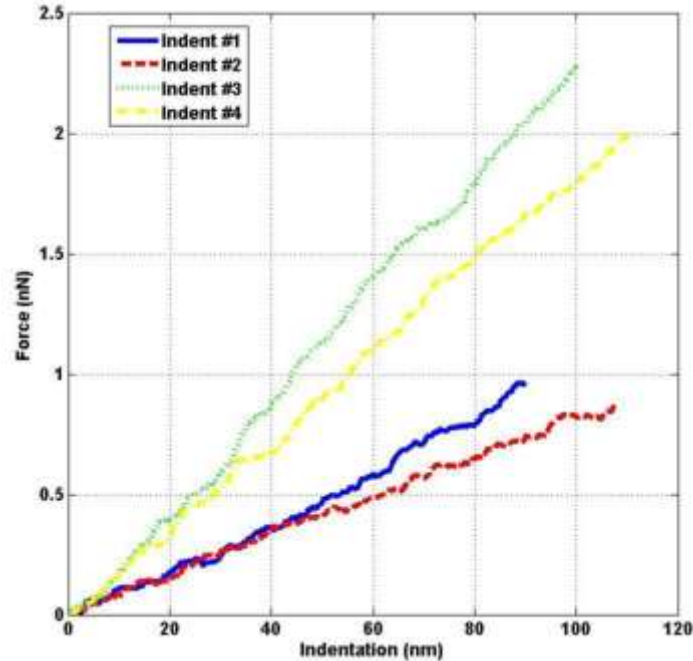
Figure 4.14: Force curves obtained from indenting a scaf1 sample multiple times.

On the other hand, since the radius of the tip for the indentation is less than 10 nm and the features on the scaffolds tested are in the dimension of 10 μm level, the conditions are satisfied to apply the schematic in Figure 4.1 and Equation (4.3) for the estimation of the Young's Modulus of the scaffolds. While indenting, there is no speed control, but the z distance and the total number of data points along that distance are controlled. For example, the indentation distance is 2 μm, and the number of data points, which possess the indenting raw data, is 10,000. ~50% of the approaching curve from the point where the cantilever begins to deflect is selected to analyze the indentation, as the use of the retracting curve might lead to an incorrect measurement of indentation. With this method, two force curves for a scaf1 sample and a scaf2 sample are obtained and plotted in Figure 4.15 in order to estimate the Young's Modulus. From linear curve fitting, the slopes are 0.00974 and 0.01368 (nN/nm) for scaf1 and scaf2, respectively. Then, six points in each force curve in Figure 4.15 are adopted and substituted into Equation (4.3) to calculate the Young's Modulus. The results are showed in Figure 4.16. The Young's Moduli

are 1.8 kPa and 10.4 kPa for the scaf1 and scaf2 sample respectively, which suggests the addition of chitosan to a collagen scaffold helps enhance its stiffness.
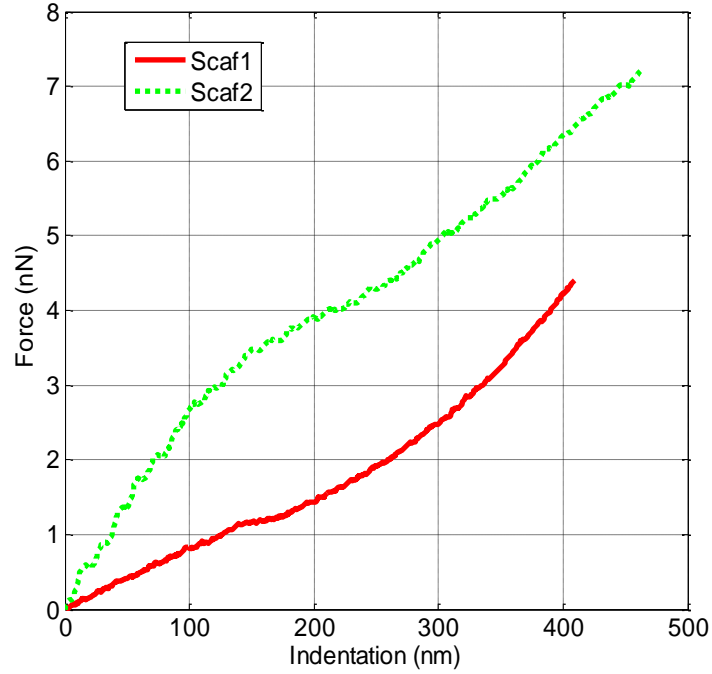
Figure 4.15: Force curve comparison between scaf1 and scaf2 samples.
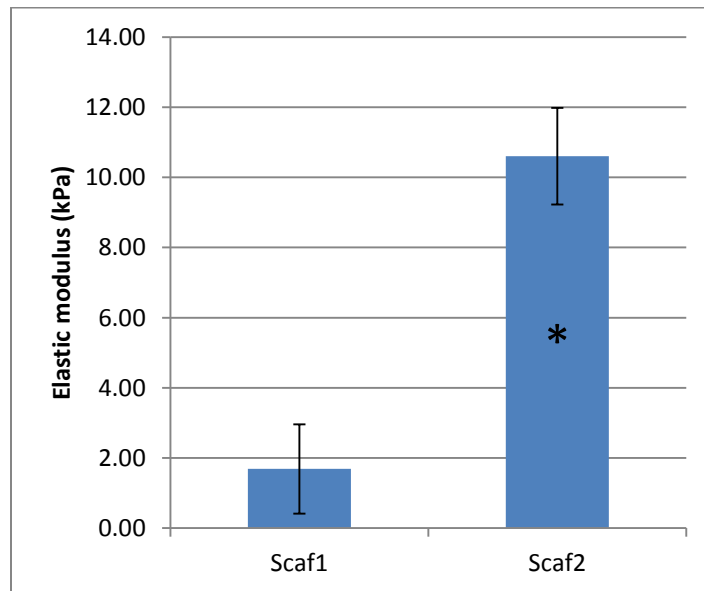
Figure 4.16: The averaged Young's Modulus for scaf1 and scaf2 samples.

To validate these tests, we ascertain the Young's Modulus of mouse pancreas and heart tissues prepared from 3 mice in the same way. Figure 4.17 gives the force curve comparison with the slopes (nN/nm) of 0.00329:0.00908 through linear fitting, and Figure 4.18 shows that the averaged Young's Modulus is 8.25 kPa and 47.4 kPa for the mouse pancreas and heart tissues, respectively. The estimation result of the Young's Modulus for the mouse heart tissues is in agreement with others' work. For example, one study has reported that the average stiffness of a mouse heart sample is about 49.6 kPa [131]. Therefore, the estimation of the Young's Moduli for the scaffolds is reliable.
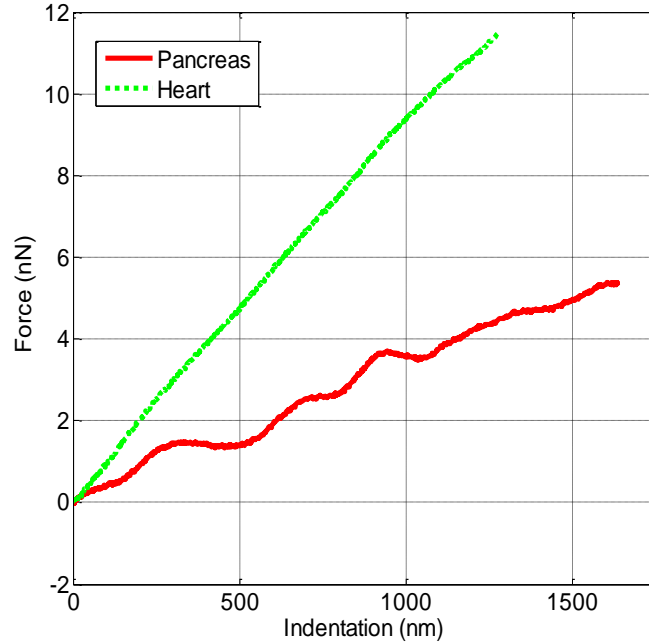
Figure 4.17: Force curve comparison between mouse pancreas and heart tissues.
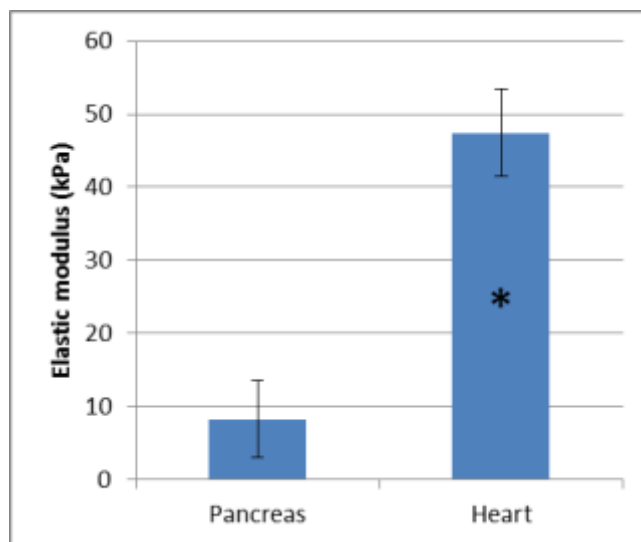
Figure 4.18: The averaged Young's Modulus of mouse pancreas and heart tissues.

4.3.5 Results of Nanoindenting Scaffolds with Cell Cultures

Next, whether or not the tensile strength of a collagen-chitosan scaffold is altered by ECM deposited from cells grown inside a scaffold is investigated. The human foreskin fibroblasts are seeded into both scaf1 and scaf2 the way as in [128][132]. The elastic moduli of the two scaffolds are determined at different time points within 10 days of cultures. As shown in Figure 4.19 (a) and (b), their elastic moduli decrease gradually when they are immersed in a cell culture medium for 10 days. The scaf1's elastic modulus drops from 3.69 to 2.63 kPa, while scaf2's elastic modulus declines from 11.6 to 5.19 kPa after 10 days incubation. It appears that a high content collagen in the scaffolds helps delay their deterioration. As documented in literatures, collagen tends to degrade in culture medium [124][132]. In contrast, the tensile strength of collagen-chitosan scaffolds increase when cells are grown inside them. The elastic modulus of scaf1 is elevated from 10.5 kPa on day 3 to 63.4 kPa on day 10 when the human foreskin fibroblasts are cultured inside the scaffolds as shown in Figure 4.19 (c). The deposition of ECM from cells might contribute to this increase. Although the cellular deposition of ECM is not directly observed here, related early works using similar scaffolds demonstrated the ECM

deposition from cells grown inside the scaffolds [123][128][133]. It is also found out that the tensile strength of a collagen-chitosan scaffold is less affected by the cellular deposition of ECM if a higher content chitosan is used for fabricating scaffolds as shown in Figure 4.19 (d). The elastic modulus of scaf2 is increased only slightly from 3.64 kPa on day 3 to 8.72 kPa on day 10 with cells grown inside.

The cellular enhancement of mechanical properties of a collagen scaffold has been observed by other groups as well [134]. The transition of mechanical property has also been found in other scaffolds [135]. The effect of scaffold stiffness on cells has also been characterized extensively [136]. It is also noteworthy to point out that large variation in elastic modulus measurements is observed in our experiment. These variations might be due to the nature of porous scaffolds or due to the different positions where a tip touches the scaffolds during the measurements. Thus, the procedure needs to be further optimized in order to generate more consistent measurements.
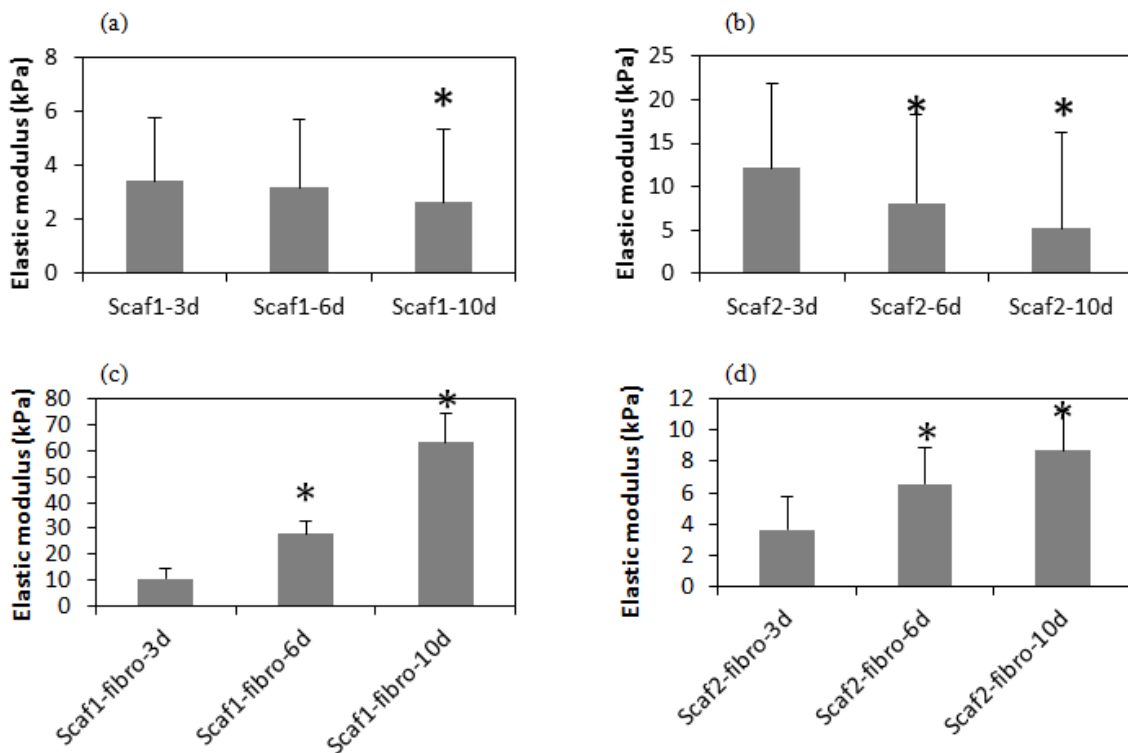
Figure 4.19: Changes in elastic moduli of scaffolds during 3D cell cultures.

4.4 Estimation of Mechanical Properties of Protein Microbubbles

4.4.1 Background

Over the last decade, there has been significant progress towards the development of microbubbles as theranostics for a wide variety of biomedical applications. The unique ability of microbubbles to respond to ultrasound makes them useful agents for contrast ultrasound imaging [137] and targeted drug and gene delivery [138]. The general composition of a microbubble is a gas core stabilized by a shell comprised of proteins, lipids or polymers. Each type of microbubble has its own unique advantages and can be tailored for specialized functions.

Microbubbles work by resonating in an ultrasound beam, rapidly contracting and expanding in response to the pressure changes of the sound wave. By a fortunate coincidence, they vibrate particularly strongly at the high frequencies used for diagnostic ultrasound imaging. This makes them several thousand times more reflective than normal body tissues. In this way they enhance both grey scale images and flow mediated Doppler signals. As well as being useful in itself, the resonance that microbubbles produce has several special properties that can be exploited to improve diagnoses. Just as with a musical instrument, multiple harmonic signals, or overtones, are produced. Ultrasound scanners can be tuned to "listen" to these harmonics, producing strong preferential imaging of the microbubbles in an image. The selective excitation produced can also destroy microbubbles relatively easily, an effect that can be useful both in imaging and in emerging therapeutic applications. The use of microbubbles in treatments may eventually be even more important than there diagnostic uses [139]. Microbubbles can aid drug delivery in themselves and as agents to carry drugs for site-specific treatment. Their most exciting application is in the emerging area of gene therapy, where delivery of genetic material to a chosen site is difficult [140].

Microbubbles used for biomedical purposes are typically between 0.5 and 10 μm diameter, which is the upper limit for passage through the lung capillaries. The gas core is a single chamber and comprises a large majority of the total particle volume. The shell acts as a barrier between the encapsulated gas and the surrounding aqueous medium. Different shell materials may be used, including lipid (~3 nm thick), protein (15-20 nm thick) and polymer (100-200 nm thick). Figure 4.20 shows the structure of a typical microbubble with different shell compositions [138]. The unique ability of microbubbles to respond to ultrasound energy and to potentially cause a physiological response makes them ideally suited for targeted delivery applications.
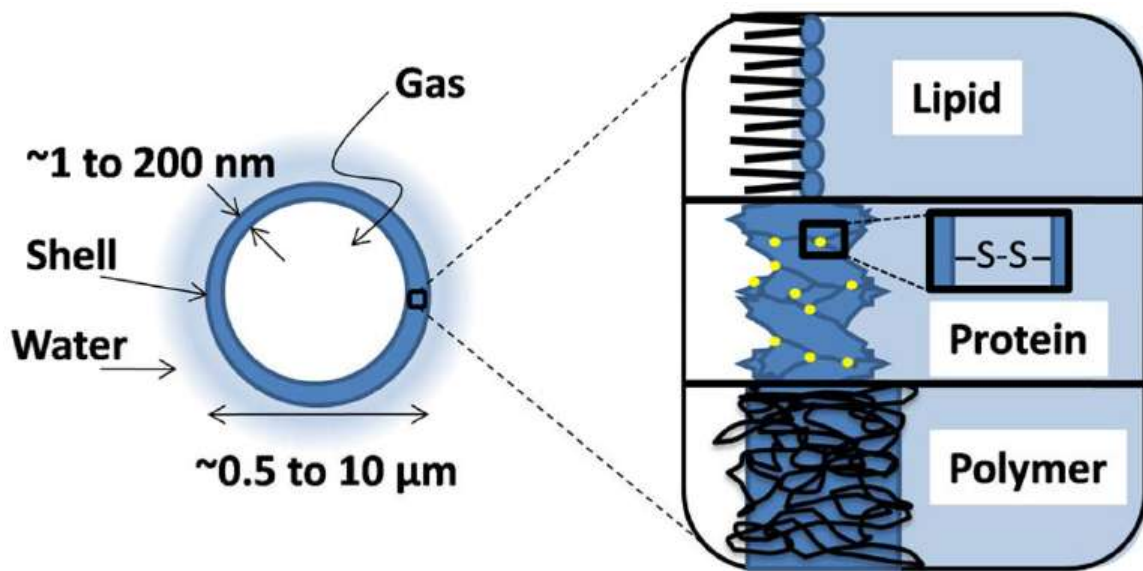
Figure 4.20: Structure of a typical microbubble with different shell compositions.

The microbubbles involved in this dissertation are designated for gene /drug delivery and ultrasound contrast diagnostic with protein shells. The University of Arkansas Medical Science (UAMS) provides the microbubble samples with two different diameters, 1 μm and 3 μm. Figure 4.21 is a schematic of microbubbles for a potential drug delivery application towards brain thrombus treatment. Assume a patient, who is suffering from a brain thrombus issue, swallows a number of microbubbles, and the protein shells encapsulate particular pills for delivery. The

microbubbles normally survive in a liquid environment for about 2 hours. During this time, the microbubbles are able to be led to a chosen site (affected area) and release the pills after they burst through ultrasound-mediated effects of microbubbles, such as acoustic backscatter, streaming, fragmentation, dissolution, cavitation and radiation force. Thus, the thrombus will be eliminated after the pills take effective. However, before microbubbles can be applied into various biomedical applications, some mechanical properties of the microbubbles need to be known in order to make use of them properly and accurately. The mechanical properties are also among important parameters of microbubbles for quality control purpose. The Young's Modulus of the microbubbles is one of their major mechanical properties to be estimated. Owing to the particularities of the microbubbles and the constraints of the experimental condition, it is not straightforward, or even not feasible to implement the measurement until advanced techniques in nano level become mature. Now, the AFM-based nanoindentation technique is one of the potential solutions to carry out the task as AFM imaging in liquid will examine the microbubbles size-wise and nanoindentation will offer the information for mechanical properties at the same time. Our experimental results show the proof of the methodology. Although there is still distance to be perfect by this means, the current results are encouraging and significant as no one has reported such an AFM-based nanoindentation attempt for estimating the mechanical properties of protein microbubbles.
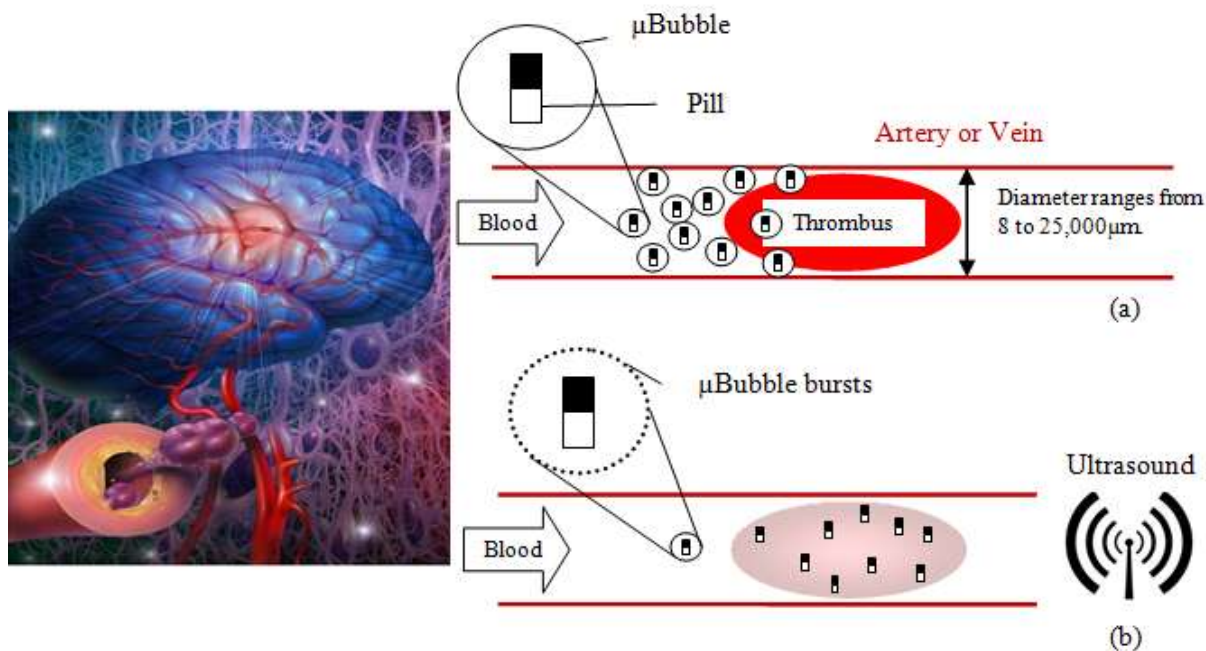
Figure 4.21: Schematic of microbubbles for drug delivery.

4.4.2   Immobilization of Microbubbles

The microbubble samples are stored in syringes with PBS and need to be kept refrigerated (do not freeze). It is recommended that freshly prepared microbubbles or ones that are stored concentrated at 5 °C be used for AFM application. Before bringing the microbubbles to AFM, the immobilization is necessary. Figure 4.22 shows the procedures that are used for immobilizing the microbubbles on a 10-mm-diameter mica disk. Firstly, a Polydimethylsiloxane (PDMS) mask with four round wells is made. Each well has a diameter of 6 mm. Secondly, fill one of the wells with 6% poly-l-lysine solution. Make sure the poly-l-lysine solution is a little above the PDMS mask surface, which secures the contact after a mica disk covers the well. Then keep the mica disk and the poly-l-lysine solution in contact for 15 minutes, remove the mica disk, let it air-dry overnight, and a poly-l-lysine layer is coated on the mica disk. Poly-l-lysine is a synthetic amino acid chain that is positively charged and widely used as a coating to enhance cell attachment and adhesion to both plasticware and glass surfaces. Poly-l-lysine is also a charge enhancer, and it

75

can be used for coating many surfaces. Coated surfaces will often improve cell attachment in reduced or serum-free conditions. It is recommended that poly-l-lysine be stored at or below 2 to 10 ℃. Therefore, poly-l-lysine is adopted to immobilize the microbubbles on the mica surface. Thirdly, the microbubbles are attached to the poly-l-lysine coated mica disk. The syringes are kept vertical with the nozzle facing down in a fridge so that the microbubbles gather in the top of the syringe owing to the smaller density. In order to guarantee that a large number of bubbles can be filled in the well, PBS in the bottom part of the syringe is pushed out immediately after taking the syringe out of the fridge. Then, after lightly shaking the syringe for a few minutes, the microbubbles are suspending everywhere in the rest of PBS. Fill a well on the PDMS mask with the PBS with a great number of microbubbles, and also make sure the PBS level is a little above the mask surface. Cover the well with the mica disk with the poly-l-lysine coated side facing down, and keep it in contact with PBS for about 15 minutes. During that time, all the microbubbles rise to the top and are attached to the poly-l-lysine coated surface. The poly-l-lysine layer provides the bubble-immobilization, and multilayer of microbubbles will not happen. Finally, the mica disk is moved to a petri dish and flipped over with the bubble-attached side facing up. Flood the disk slowly with PBS, and let the microbubbles, which are the extra ones and not able to be attached, be suspending in the PBS. Then the mica disk with the immobilized microbubbles is taken out of the petri dish and attached to an AFM metal specimen disc using a Lift-N-Press tab. Transfer the disc to the AFM sample plate with the liquid cell mounted, and fill the cell with PBS. Since there is a magnetic area at the center of the sample plate, everything is stable. The microbubbles are ready to be scanned and imaged.
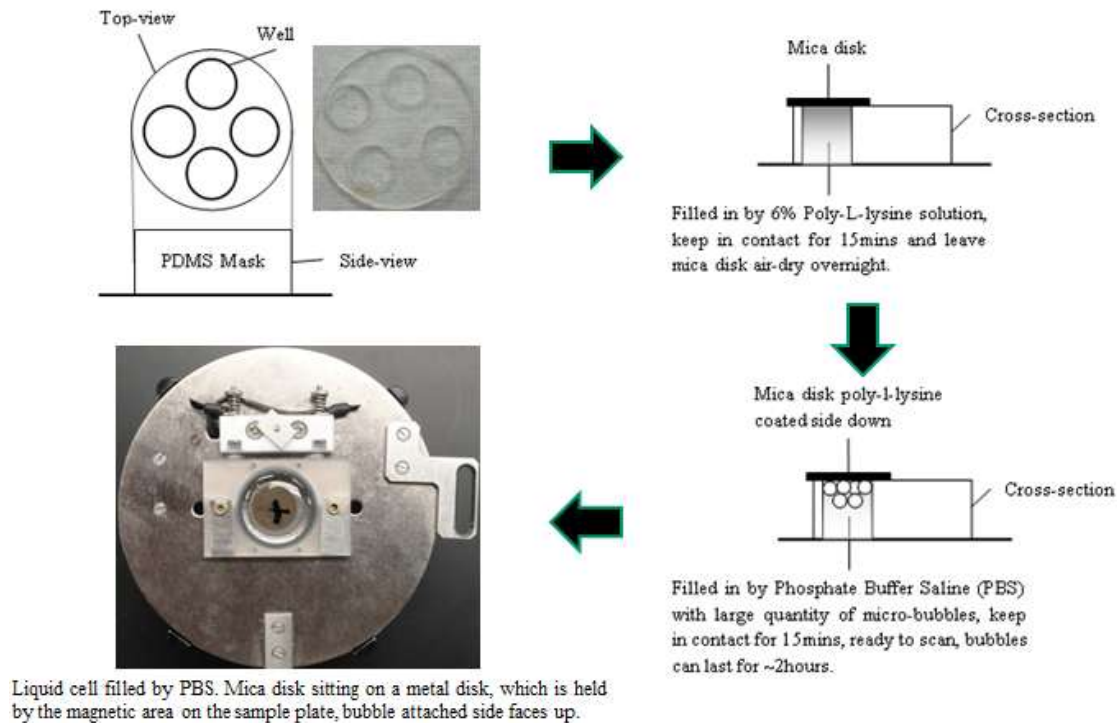
Figure 4.22: Immobilization procedures of microbubbles.

As introduced in **1.1.7**, the large multi-purpose AFM scanner has a scan size of 90 μm × 90 μm, which is 0.0081 mm². However, that is still tiny comparing to the surface area of the mica disk, which is about 78.54 mm². Therefore, the surface density of the immobilized microbubbles becomes quite critical to determine the success of AFM imaging. After the failure to image the microbubbles at the first beginning, to examine the density of immobilized microbubbles using an optical microscope becomes necessary. Olympus BX51 is then used to observe the immobilized microbubbles under phase contrast mode before we take them to the AFM. Figure 4.23 presents a comparison between good and bad 3 μm-bubble attachments, which lead to a success and failure AFM scan, respectively. With a high surface immobilizing density, AFM users spend much less time in locating the microbubbles than they do with a low surface-attachment density. Sometimes, a low surface-attachment density may take an AFM user too long (~a few hours) to image the microbubbles as these microbubbles will be gone after about 2

77

hours in PBS. The bubbles will burst immediately when they are exposed to the air. Since imaging these microbubbles is implemented in liquid, nothing can be seen from the AFM real-time video system except for the AFM tip and laser even though microbubbles are visible for both high and low surface-attachment density. So, it is recommended that the examination of the attachment should be always performed before the samples are taken to the AFM. Otherwise, there exists possibility that pains trade no gains.
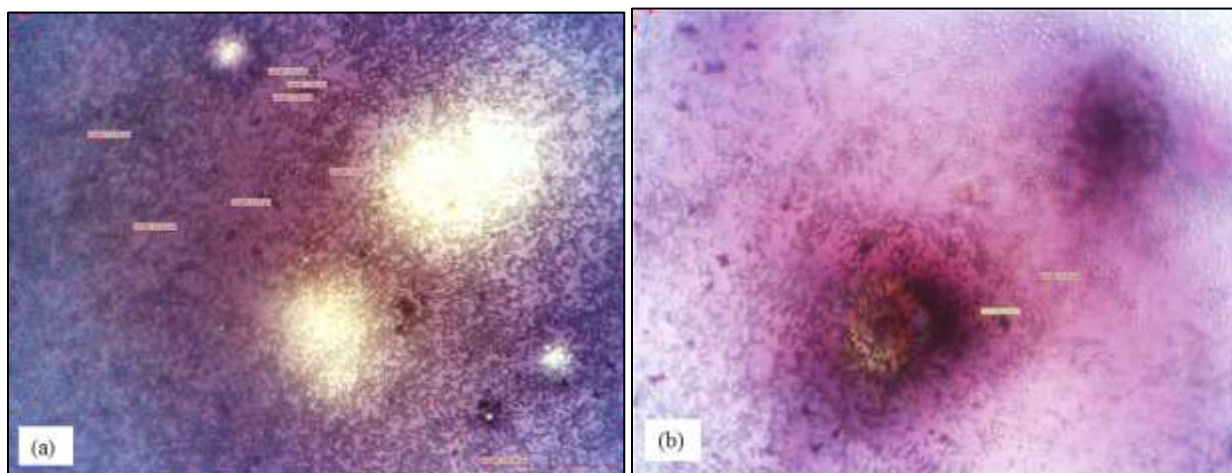
Figure 4.23: Optical microscope images of immobilized 3 µm bubbles (a) success and (b) failure to scan.

4.4.3   AFM Imaging of Microbubbles

After 3 µm bubbles are immobilized with a high surface density, the sample plate is brought back to the AFM for imaging. The same AFM probes (ContAl) as the ones used for indenting the scaffolds are adopted mainly because of their low cantilever force constant, 0.2 N/m. A dummy approach should be executed with a bare metal specimen disc on the sample plate in advance in order to control the distance between the tip and the sample. Once the dummy approach is done, the tip is lifted from the metal specimen disc by 3,000 µm. Then, it is safe to mount the sample plate with the microbubbles attached mica disc in the liquid cell. Next, manually approach while observing the distance change. In general, the cantilever will be immersed by the PBS in the

liquid cell after the distance is decreased from 3000 μm to 1000 μm, and the position of the AFM detector needs to be adjusted to receive the deflected laser signal. Resume the manual approach until the distance is decreased within 300 μm and 400 μm, which indicates the AFM tip is very close to the microbubbles as the mica disc is 210 μm thick. Manual tune to determine the resonance frequency of the cantilever, and it is about 27 kHz in PBS. The force setpoint is set at about 1.0 V by controlling the drive percentage. Thus, it is ready to implement auto approach to let the AFM tip reach the sample.

Once the auto approach is completed, a 50 μm × 50 μm square area near the center of the sample plate is scanned in tapping mode. Figure 4.24 shows that a pack of microbubbles are found and imaged. It is often the truth that the phase and amplitude images offer better visual performance than the topographies when imaging samples in liquid. Since to indent a deflated microbubble currently does not provide us with much valuable information for the future application, it is necessary to examine the bubble size before indenting it. Figure 4.25 gives the measurement results on microbubbles' diameter. The measurement profiles verify they are 3-μm-diameter bubbles. Figure 4.26 shows five microbubbles located within 20 μm × 20 μm and the height of microbubbles are measured. The second scan is also completed followed by the third scan for the same area, and the microbubbles are becoming smaller and smaller as the scan number goes up as shown in Figure 4.27 and Figure 4.28. Table 4.3 records the height measurement information, and it suggests that the indentation should be carried out immediately after a target bubble is located at the first time although the microbubbles are imaged under intermittent contact mode. Additionally, another area of 50 μm × 50 μm on the same mica disc is scanned an hour and a half later. Figure 4.29 shows that the microbubbles are still able to be

imaged, but they are already weak. So, once the immobilization of the microbubbles is finished, to locate the microbubbles quickly using AFM becomes critical and decisive for indenting.
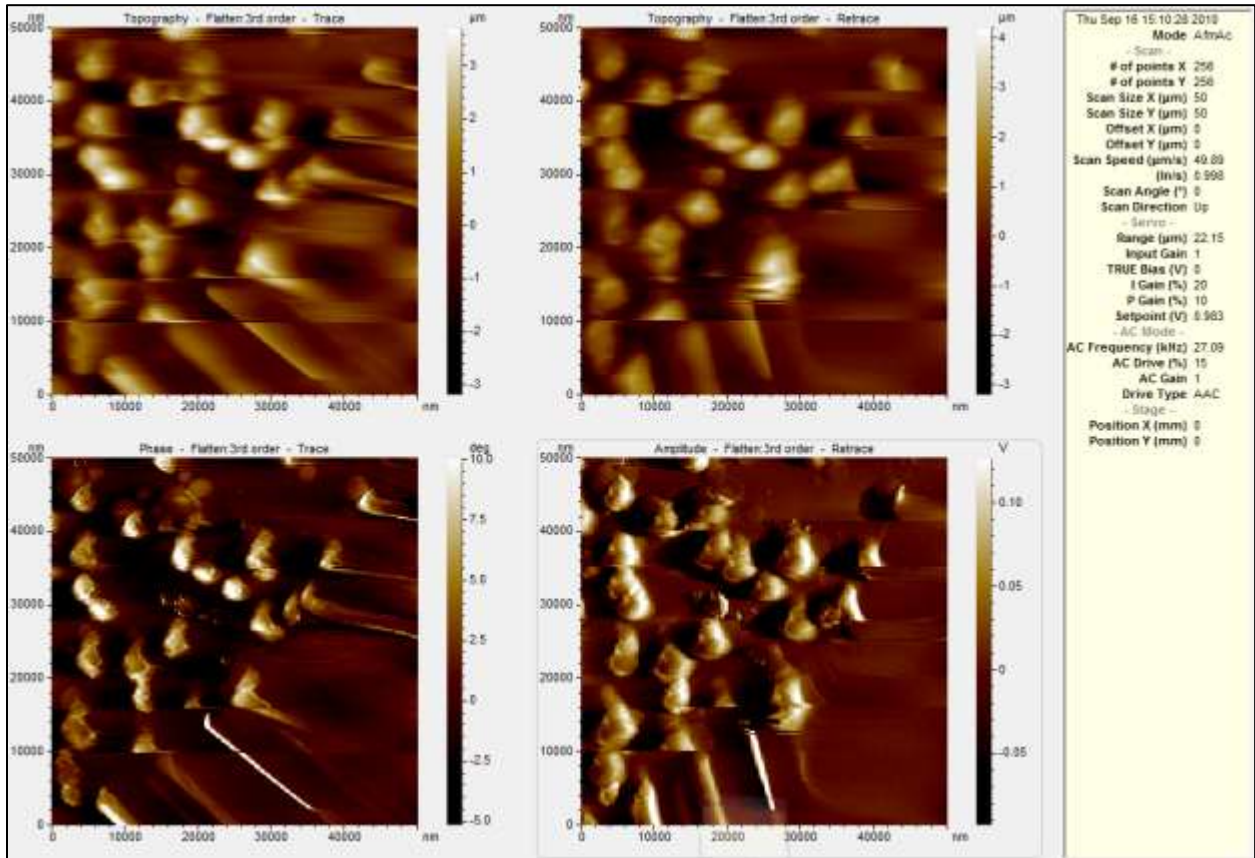
Figure 4.24: AFM image of 3 μm bubbles immediately after immobilization.
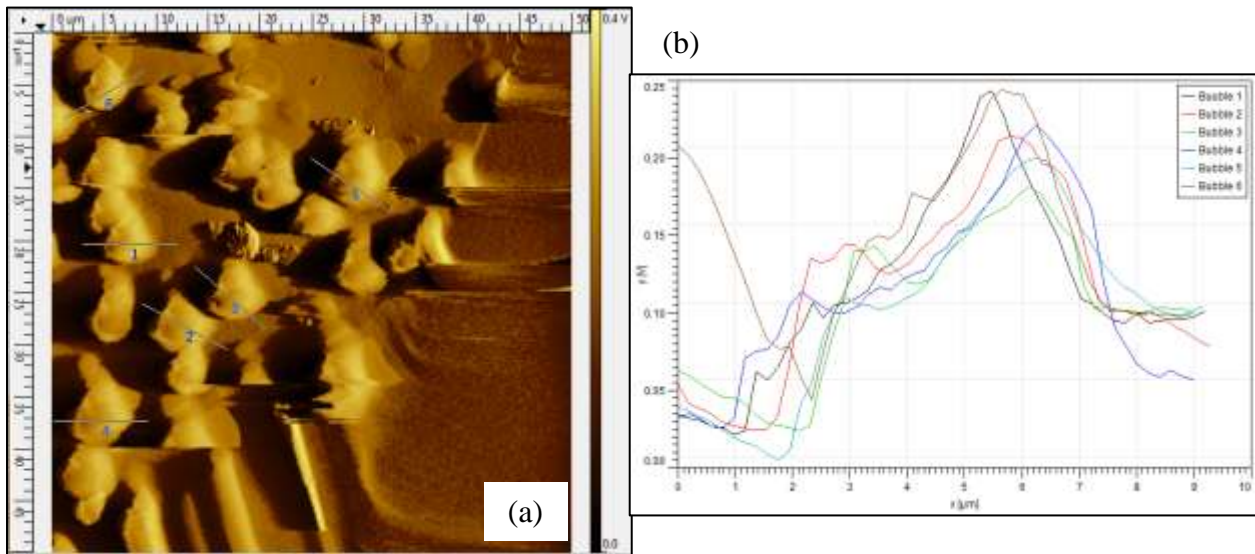
Figure 4.25: Diameter measurement of 3 µm bubbles (a) selected bubbles and (b) profiles.
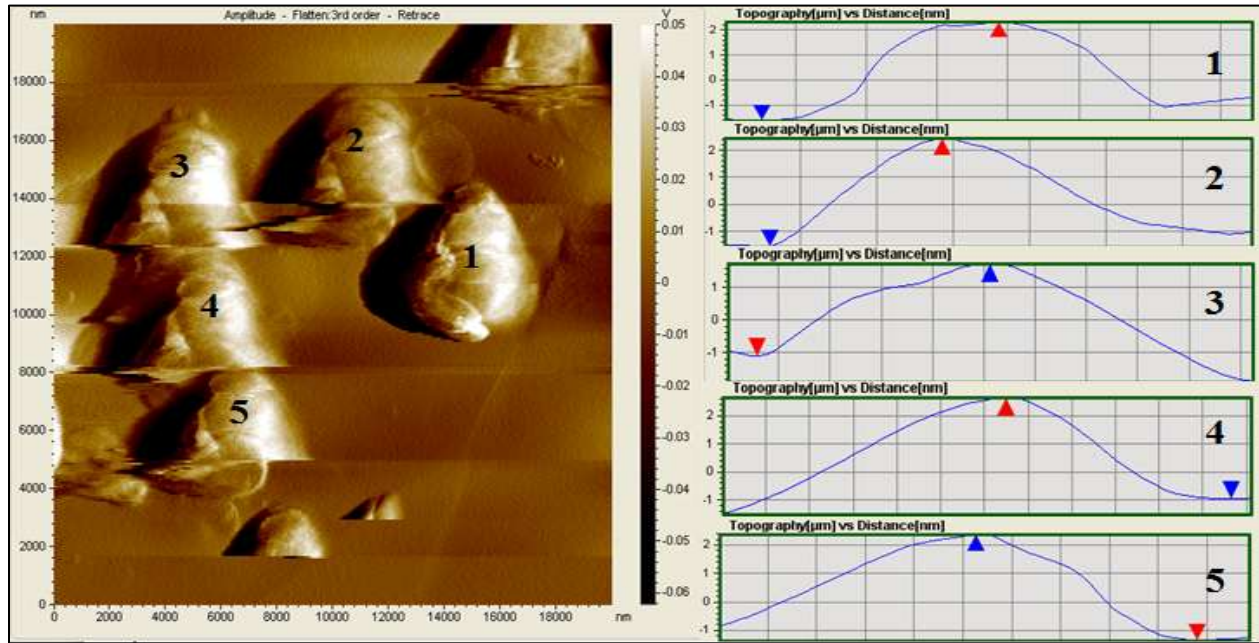
Figure 4.26: The first scan of five 3 µm bubbles for height measurement.
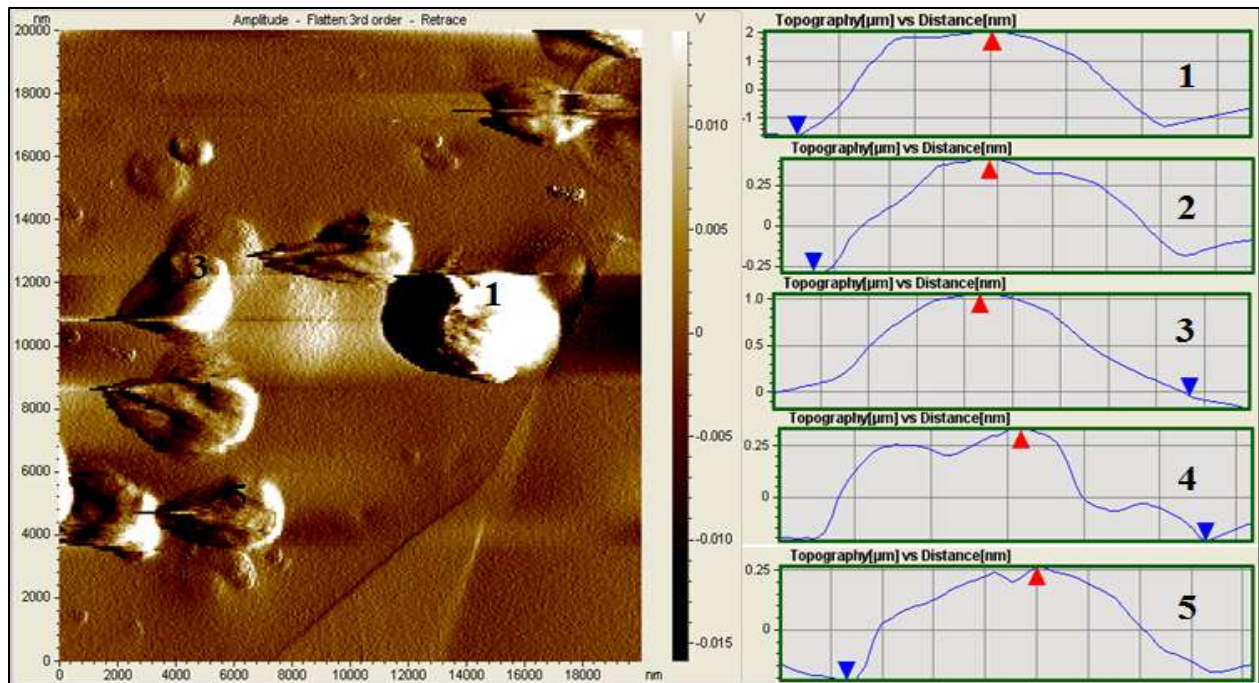
Figure 4.27: The second scan of the same 3 µm bubbles as in Figure 4.26.
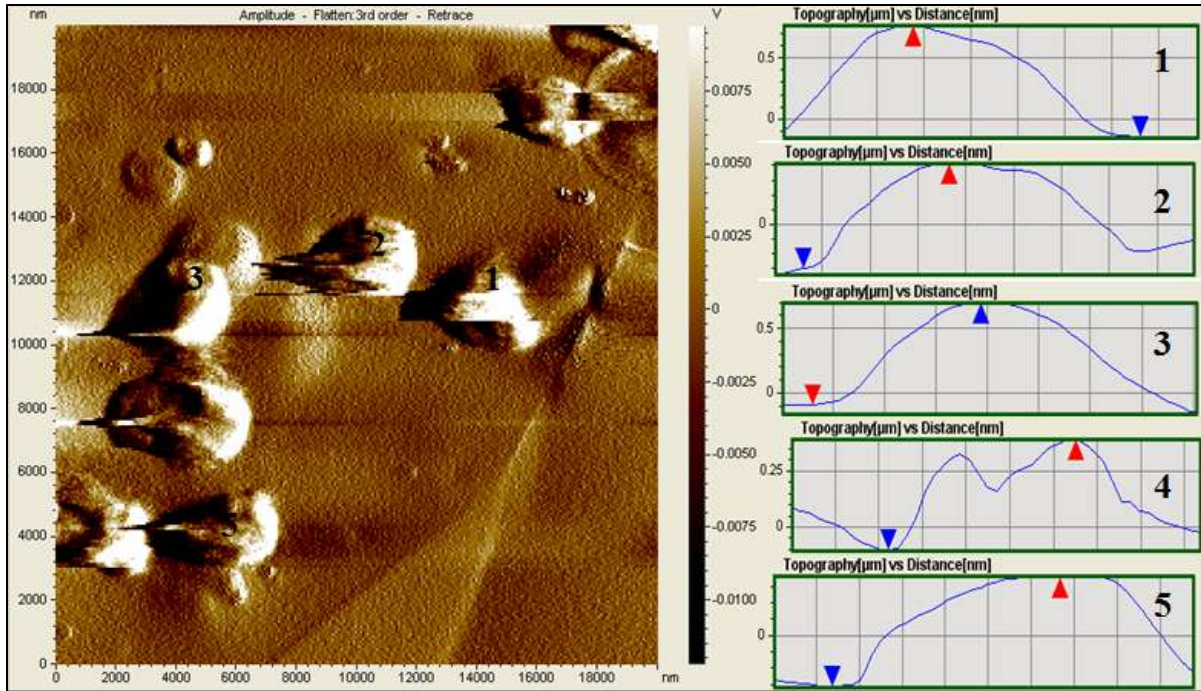
Figure 4.28: The third scan of the same 3 µm bubbles as in Figure 4.26.
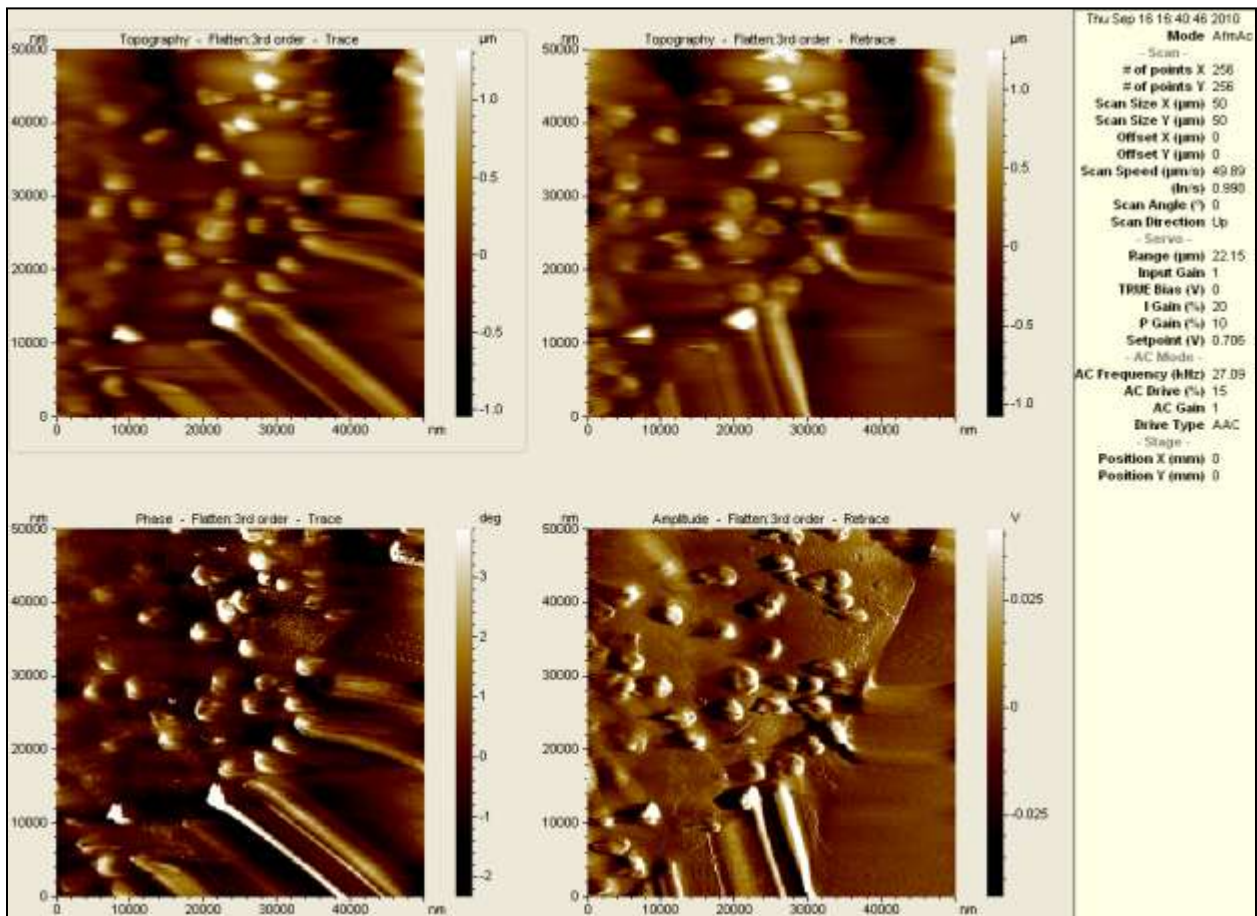
Figure 4.29: Another scan of 3 μm bubbles an hour and a half later than in Figure 4.24

# of Scan	Bubble 1 (μm)	Bubble 2 (μm)	Bubble 3 (μm)	Bubble 4 (μm)	Bubble 5 (μm)
1	3.8651	3.9373	2.8081	3.5733	3.6624
2	3.6022	0.6803	1.0866	0.5389	0.4679
3	0.8992	0.7028	0.7794	0.4822	0.6575

Table 4.3: Height measurement of 3 μm bubbles after multiple scans.

To image the bubbles with 1 μm diameter share the same procedures except for the AFM scanner. The small scanner is adopted for these smaller microbubbles as it offers better images for the samples which suffice for the scan limitations. For example, the vertical servo range of the small scanner, about 2.4 μm, is obviously capable to image samples that are supposed to be around 1 μm high. Figure 4.30 shows a 9 μm × 9 μm scan area that includes a number of microbubbles. According to Figure 4.31, these microbubbles are all approximately 1 μm wide.
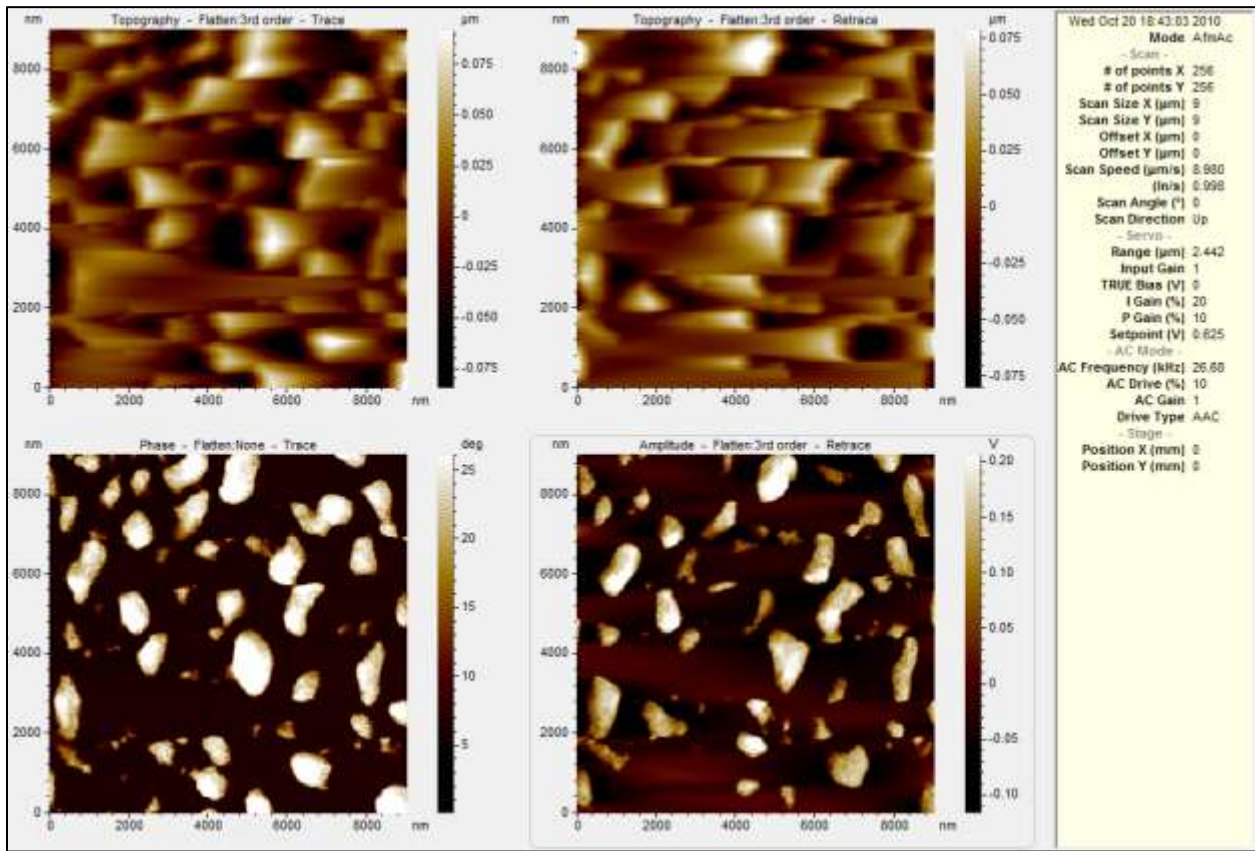
Figure 4.30: AFM image of 1 μm bubbles.

83
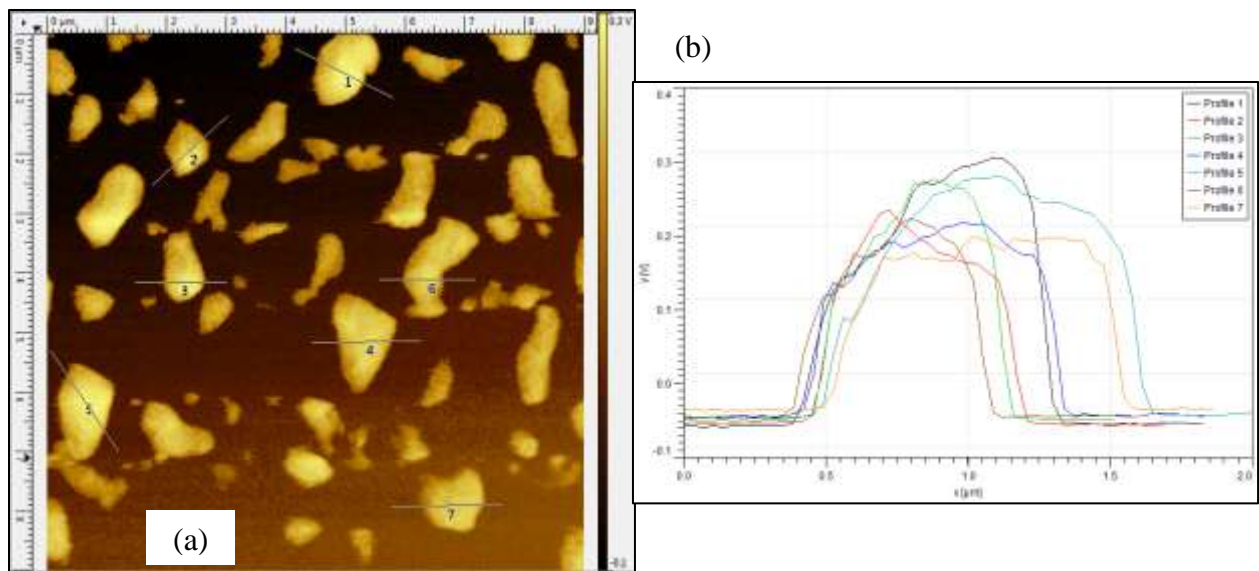
Figure 4.31: Diameter measurement of 1 µm bubbles (a) selected bubbles and (b) profiles.

In fact, it is very challenging for us to precisely measure the height of these microbubbles. During the entire experiment, there are issues regarding the height verification. Although 3-µm-high bubbles are verified as shown in Figure 4.24 and Figure 4.25, it still may be inaccurate. The sensitivity in z-axis of the large AFM scanner was adjusted based on a calibration with a grating sample. However, when the sensitivity was changed based on the height of the grating feature, the deflection range of AFM cantilever increased to 22.15 µm from the original 7.826 µm, which is strange and suspicious. Moreover, it is unable to obtain correct height information after imaging 1 µm bubbles using the small scanner. The height of bubbles in Figure 4.30 is much less than 1 µm even if their diameter measured on x-y surface is satisfying. The two scanners have separate calibration files, and the parameters on the small scanner file remained the same as factory calibration, which is reliable. Thus, this height issue becomes one of the major challenges for us to face. It is possible for the microbubbles to deform and lose their sphere shape due to the water pressure when the microbubbles are immobilized at the bottom level of PBS in the liquid

cell. Therefore, it could be a major reason why the diameter and height of a microbubble is no longer identical.

4.4.4   Results of Nanoindentating Microbubbles

Since the conical indenter is regarded to be rigid and has a tip radius less than 10 nm while the bubbles are in micro scale, the Sneddon mode in Equation (4.3) is also applicable to approximate the relationship among force, indentation distance and Young's Modulus during indenting the microbubbles. The Poisson's Ratio υ of microbubbles is assumed to 0.5 [141][142], and the AFM probe ContAl is employed to carry out nanoindentation. Therefore, to estimate the Young's Modulus of the microbubbles becomes feasible after the force curves are obtained. There are four major steps in order to calculate the Young's Modulus for microbubbles. Firstly, experimental raw data of nanoindentation on mica surface and microbubbles needs to be obtained. Secondly, the raw data of indenting on mica surface will be used to obtain the PSD sensitivity (S_Z in nm/V). This sensitivity needs to be calibrated each time right before indenting a sample as the value would change under different conditions even if the same kind of AFM probe is used and pre-calibrated. With this sensitivity, the raw data of indenting microbubbles will be used to obtain the relationship between the indentation force and distance according. The nanoindenting raw data reflects the relationship between Δz vertical displacement of AFM piezo in μm and the cantilever deflection in V, which indirectly gives the relation between the indentation force and distance on a sample as indicated in Equations from (4.4) to (4.7). Thirdly, the relation between nanoindentation force and distance squared can be extracted. With a proper curve fitting, the slope of nanoindentation force over distance squared is known. Lastly, this slope will be substituted into the Sneddon Model together with the Poisson's Ratio and the half

cone angle of the AFM tip, which is 0.5 and 25° respectively. Thus, the Young's Modulus is able to be calculated as it becomes the only unknown variable in Equation (4.3).

Figure 4.32 illustrates an AFM image with four 3-µm-diameter bubbles to nanoindent. In order to obtain S_Z, the AFM tip is first used to complete three dummy nanoindentations at the positions without any microbubbles. Figure 4.33 illustrates the AFM raw data of indenting mica while Figure 4.34 illustrates the AFM raw data of indenting a microbubble. These AFM files can be imported into Microsoft Excel to extract the raw data as long as the files are saved in ASCII format. Thus, the mean of S_Z is obtained at 192.8 nm/V with a standard deviation of 26.3 nm/V. With this sensitivity, the deflection of the cantilever during nanoindentation process can be known by obtaining the product of the amplitude from the raw data and this sensitivity, which also enables us to calculate the corresponding force and indentation distance on the sample. Next, the force curve of nanoindenting a microbubble is obtained as shown in Figure 4.35, from which the relation between force and indentation squared is obtained as shown in Figure 4.36. With a proper curve fitting, the slope of force over indentation squared is known, which is 0.0019 nN/nm^2, and this value is substituted into Equation (4.3) together with $\upsilon = 0.5$ and $\alpha = 25°$. Finally, the Young's modulus of the indented microbubble is calculated, $E = 1.044$MPa.
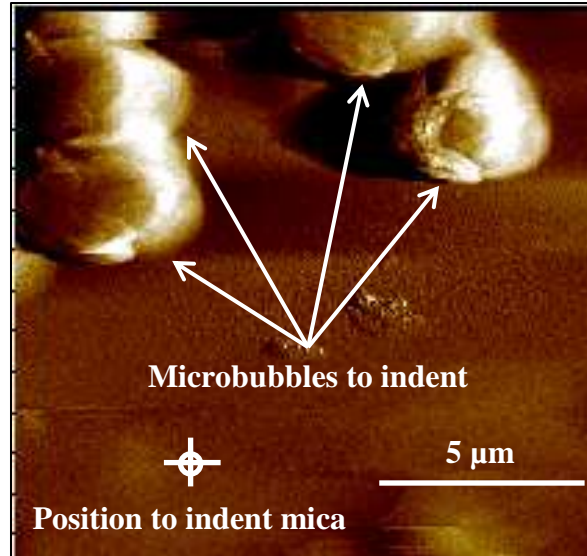
Figure 4.32: AFM image of four 3 µm bubbles for nanoindentation.
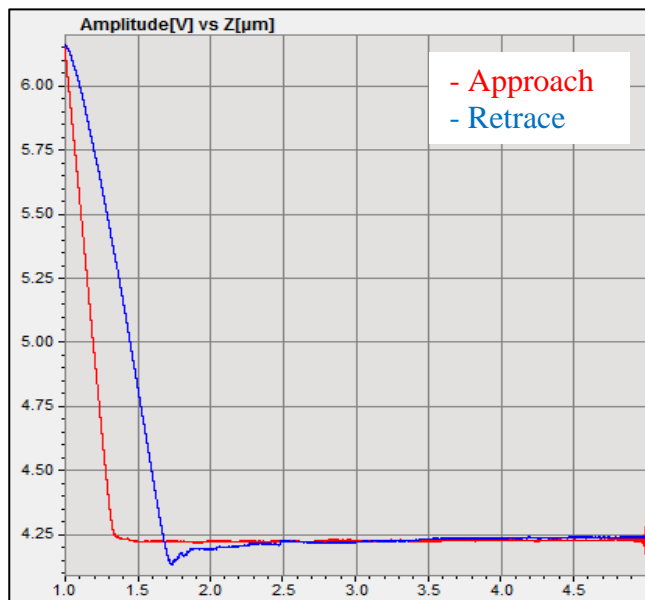
Figure 4.33: AFM raw data of nanoindenting mica before 3 µm bubbles.
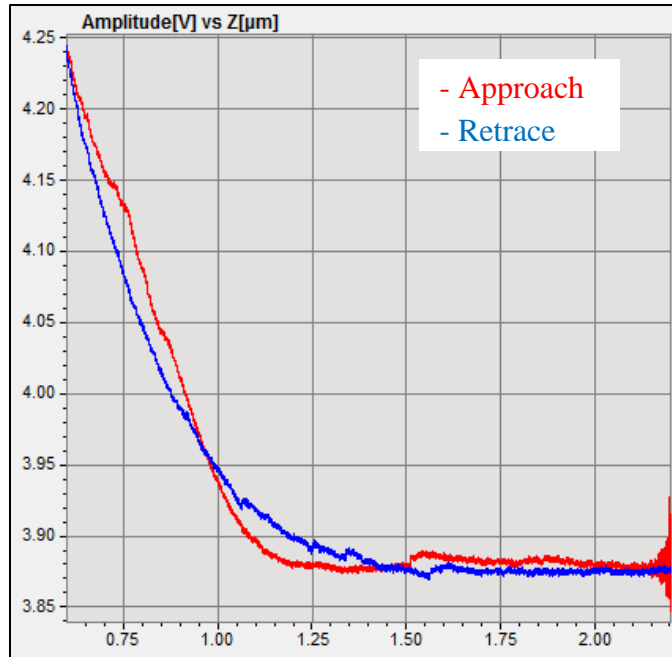
Figure 4.34: AFM raw data of nanoindenting a 3 µm bubble.
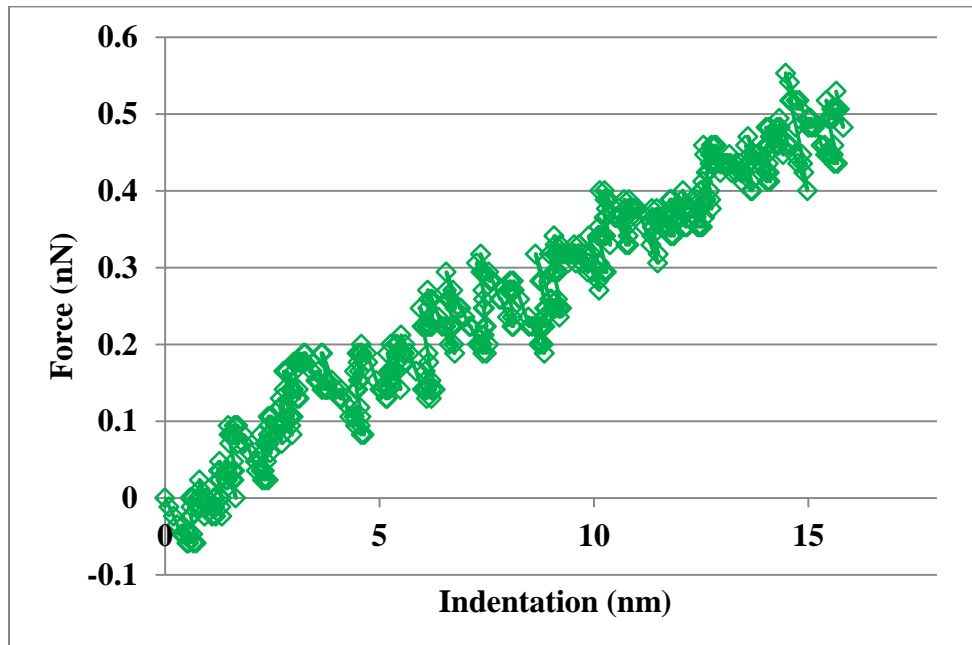
Figure 4.35: Force curve of nanoindenting a 3 µm bubble based on Figure 4.34.
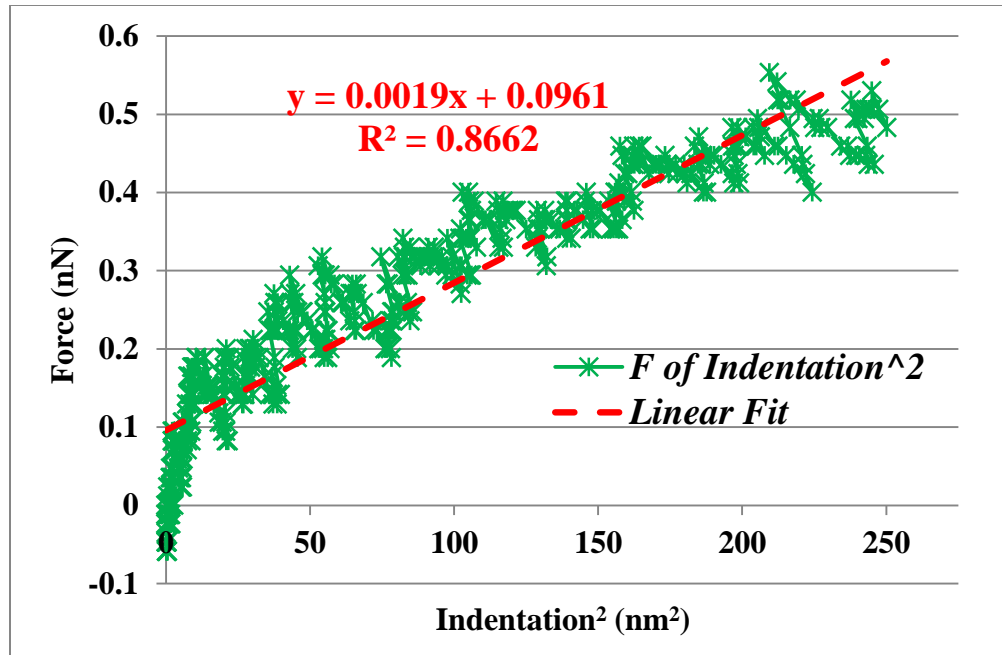
Figure 4.36: Force vs. indentation squared curve based on Figure 4.35.

Table 4.4 records the results of calculated Young's Moduli for the four 3 µm bubbles. As we can see, the mean Young's Modulus equals about 0.824 MPa with a standard deviation at 0.273 MPa. Thus, we have succeeded in quantifying the Young's Modulus of 3 µm bubbles through AFM based nanoindentation.

ν	α (°)	S_Z (nm/V)	Microbubble 1		Microbubble 2		Microbubble 3		Microbubble 4	
			F/δ^2 (nN/nm^2)	E (MPa)	F/δ^2 (nN/nm^2)	E (MPa)	F/δ^2 (nN/nm^2)	E (MPa)	F/δ^2 (nN/nm^2)	E (MPa)
0.5	25	192.8	0.0019	1.04378	0.0015	0.82403	0.0018	0.98884	0.0008	0.43948
Overall		**Mean (MPa)**		0.8240325		**Stdev. (MPa)**		0.272843729		

Table 4.4: Results of calculated Young's Moduli for 3 µm bubbles.

The procedures are repeated in order to obtain the Young's Moduli of 1 µm bubbles. Figure 4.37 contains two AFM images of 1 µm bubbles. Two bubbles in the left image and three bubbles in the right one are indented. Figure 4.38 is one of the AFM raw data of nanoindenting mica, and the sensitivity S_Z is 86.0 nm/V and 80.1 nm/V for the left and right image respectively. Figure 4.39 shows the AFM raw data of nanoindenting one of the microbubbles in the left image

of Figure 4.37. Thus, the corresponding force curve and correlation between force and nanoindentation squared are obtained as shown in Figure 4.40 and Figure 4.41 respectively. Through linear curve fit on the force vs. indentation squared data, the slope is determined at 0.0105 and substituted into Equation (4.3) together with υ = 0.5 and α = 25°. Finally, the Young's Moduli of the indented 1 µm bubbles are obtained as recorded in Table 4.5.
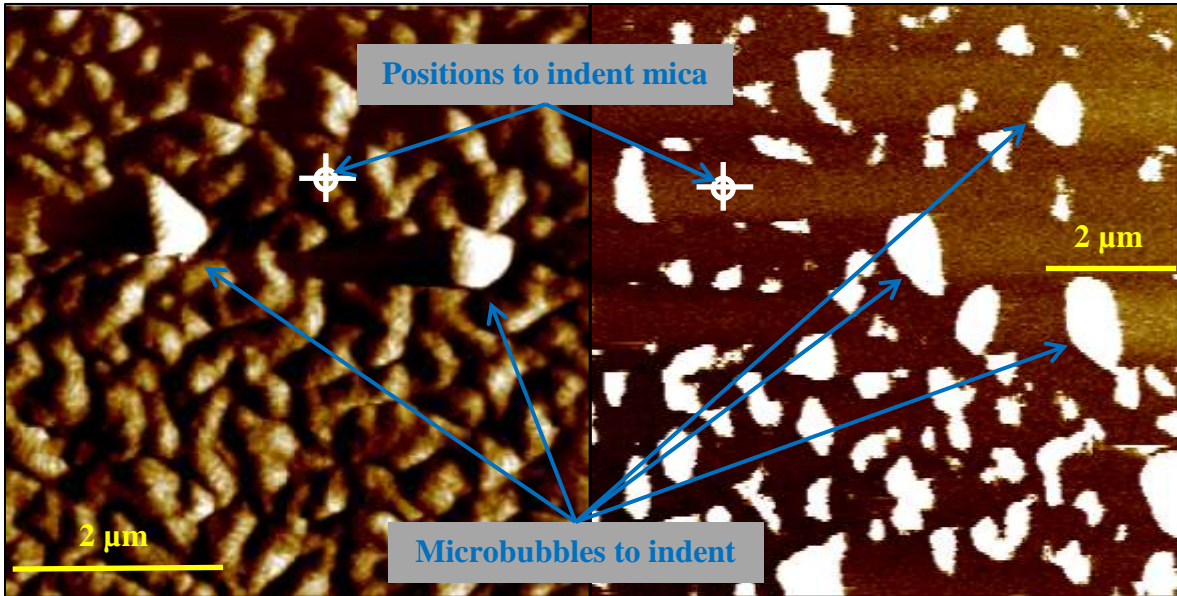
Figure 4.37: AFM images of five 1 µm bubbles for nanoindentation.
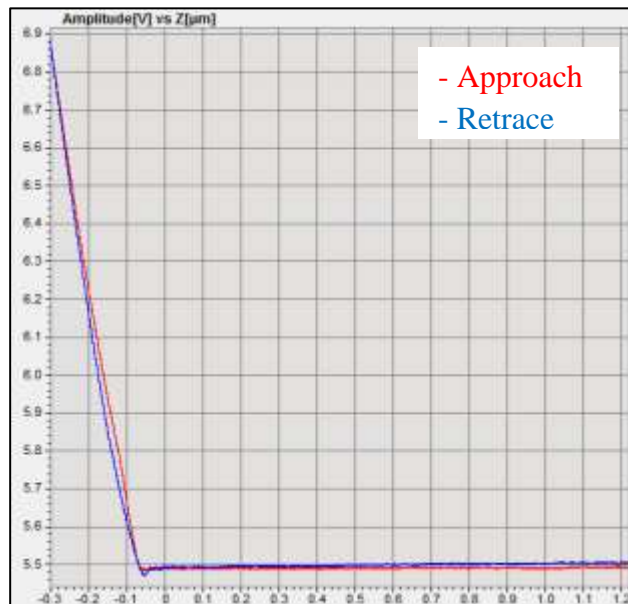
Figure 4.38: AFM raw data of nanoindenting mica before 1 μm bubbles.
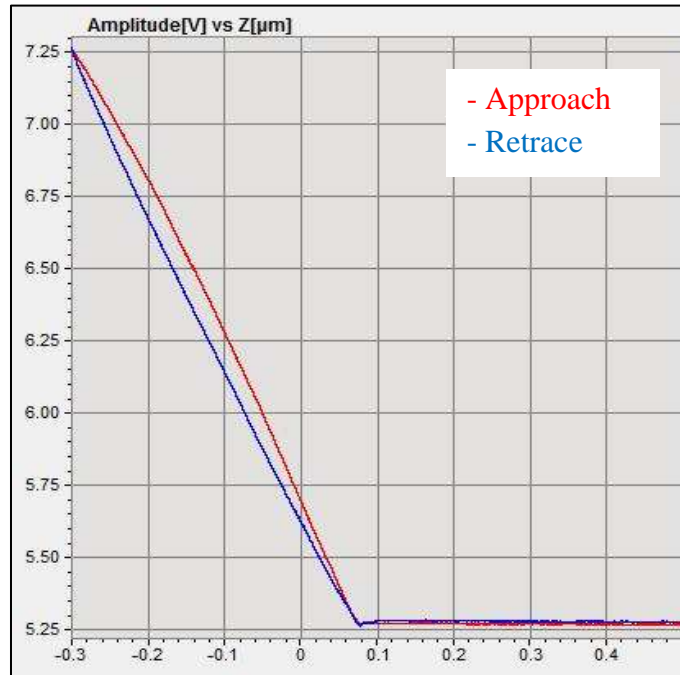
Figure 4.39: AFM raw data of nanoindenting a 1 μm bubble.
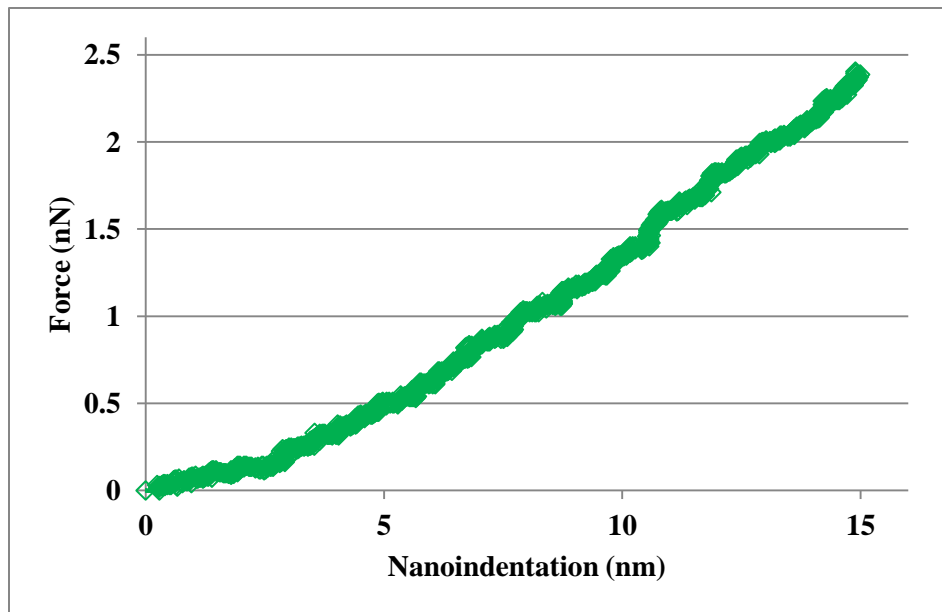
Figure 4.40: Force curve of nanoindenting a 3 μm bubble based on Figure 4.39.
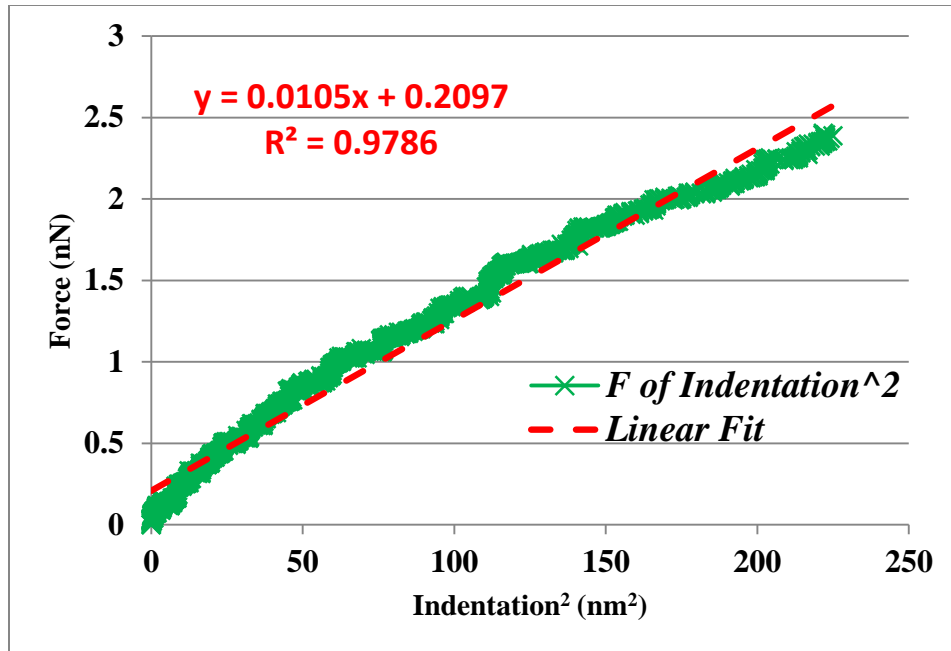
Figure 4.41: Force vs. indentation squared curve based on Figure 4.40.

ν	α (°)	S_Z (nm/V)	Microbubble 1		Microbubble 2		**Overall**	
			F/δ^2 (nN/nm^2)	E (MPa)	F/δ^2 (nN/nm^2)	E (MPa)	**Mean (MPa)**	**Stdev. (MPa)**
0.5	25	85.9521	0.0105	5.768235	0.0079	4.33991	**4.8672918**	**0.876045835**
ν	α (°)	S_Z (nm/V)	Microbubble 3		Microbubble 4		Microbubble 5	
			F/δ^2 (nN/nm^2)	E (MPa)	F/δ^2 (nN/nm^2)	E (MPa)	F/δ^2 (nN/nm^2)	E (MPa)
0.5	25	80.0729	0.0071	3.900426	0.0082	4.504717	0.0106	5.823171

Table 4.5: Results of calculated Young's Moduli for 1 μm bubbles.

4.5   Summary

The methodology of AFM based nanoindentation is introduced in this chapter. With AFM's assistance, it becomes feasible to characterize the mechanical properties of some nano/bio samples which used to be impossible due to their unique characteristics and the limited testing conditions. The Sneddon Model is employed to approximate the contact correlation between AFM tip and samples. By this means, we have investigated the mechanical properties of VACNFs at subzero temperatures, soft tissue scaffolds with cell cultures, and protein

microbubbles. Based on the experimental results, it is found that the Young's Modulus of VACNFs drops significantly when they are treated at subzero temperatures comparing to what it is at room temperature. Also, their Young's Modulus keeps decreasing in a linear manner when the temperature varies from -20 °C to -70 °C. This information is of great value for the potential usage of VACNFs as sensing element in outer space missions. The results on the mechanical properties of collagen-chitosan scaffolds reveal that addition of chitosan to collagen in the scaffold ingredients enhances the stiffness. Also, the Young's Modulus of the scaffolds decreases gradually when they are immersed in a cell culture medium for 10 days, and it appears that a high content of collagen in scaffolds helps delay their deterioration. On the other hand, it is interesting that the Young's Modulus increases when human embryonic fibroblast cells are cultured. Furthermore, the AFM-based nanoindentation has successfully realized imaging and indenting microbubbles in PBS, and the results on the mechanical properties reveal that 1 µm bubbles are stiffer than 3 µm ones. This mechanical property of microbubbles is precious information for quality control objective and as pre-condition of proper applications.

Chapter V.   DESIGN, FABRICATION, TESTING OF CNT BASED ISFET

5.1   Design of CNT Integrated ISFET

As introduced in **1.1.5**, an ISFET is generally used to measure ion concentrations in solutions. When the ion concentration, such as pH, changes, the current through the transistor will change accordingly. Researchers have reported ISFET development for sensing ion concentration in solutions for more than 30 years. Solution is used as the gate electrode instead of the traditional metal gate. The voltage between substrate and oxide surfaces arises due to an ions' sheath. An ISFET's source and drain are constructed similar to a Metal-oxide Semiconductor Field-Effect Transistor (MOSFET). Although an ISFET is similar to a MOSFET, there are still some differences. As shown in Figure 1.5, the metal gate is replaced by the metal of a reference electrode, whilst the target liquid in which this electrode is present makes contact with the bare gate insulator. Both have the same equivalent circuit. Devices with this structure can be applied to pH measurement. However, the final objective of our work on the nano-pH sensor is to enhance the inversion layer with CNTs as "nano-bridge" to conduct electrons between the drain and source. The drain current might be much greater under the same condition. When an ISFET device is active, ions will flow between the source and drain through the inversion layer and form the drain current, whose magnitude depends on the ion concentration of solution. CNT-ISFET structure intends to make use of CNTs' extremely high current carrying capacity ($\sim$1TA/cm^3) to improve the performance. There will be a "highway" for the ions after CNTs are aligned properly inside a nanochannel that is fabricated in the location of the inversion layer. Figure 5.1 illustrates the design for CNT-ISFET structure with nanochannel. If all of these conditions are satisfied, the device will be able to measure targets solutions in microliter or even smaller scale comparing to at least milliliter scale of conventional pH sensors. It would be a

revolution of measuring ion concentration in solutions if the sensitivity can be remained while sample volume significantly decreases. Therefore, in order to achieve CNT integrated ISFET, it is needed to fabricate common ISFET structure using MEMS techniques except for the inversion layer where nanochannels and CNT alignment are involved.
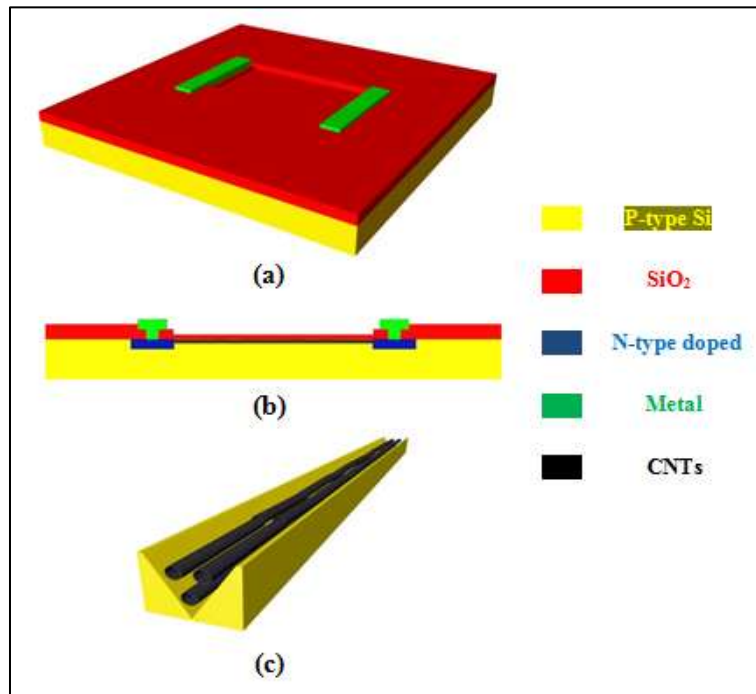
Figure 5.1: Design of CNT-ISFET structure: (a) perspective view, (b) side view and (c) CNTs in nanochannel.

5.2   Fabrication of ISFET

The fabrication process of our ISFET consists of eight major steps, all of which were completed using the cleanroom thin film facilities in High Density Electronics Center (HiDEC) of University of Arkansas. The fabrication started with a 5-inch p-type boron diffused silicon wafer with orientation of <1-1-1> and thickness of 625 μm. The major fabrication steps are Field Oxidation, Phosphorus Source Preparation, Pre-Deposition, Drive-in, Gate Oxide, Backside Oxide Etch, Lift-off Patterning, and Metallization as shown in Figure 5.2, where a) silicon b) first mask photolithography c) oxide etching d) phosphorus pre-deposition e) deglaze f) drive-in

g) second mask photolithography and gate oxide etching h) gate oxidation i) backside oxide etch j) strip off resist k) third mask photolithography l) oxide etching m) apply and pattern 5214 photoresist n) evaporation o) lift-off.
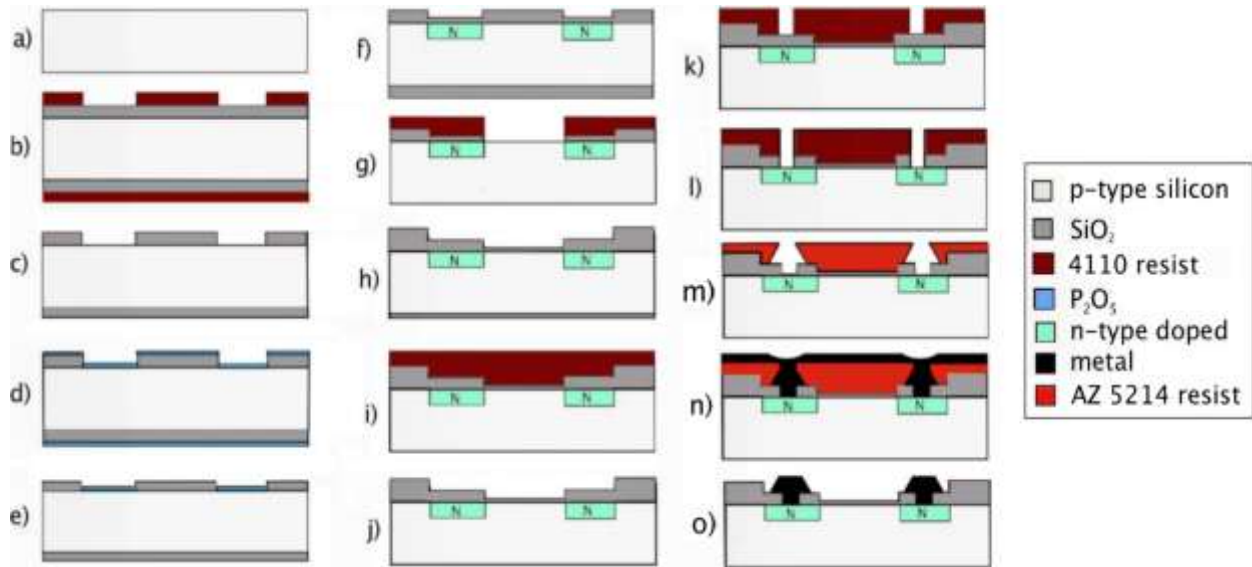
Figure 5.2: ISFET fabrication flowchart.

5.2.1   Mask Design

Before the fabrication, the mask for photolithography needs to be designed and produced. Since the ISFET is a multilayer structure, the mask also should contain multilayer. This multilayer mask is designed using AutoCAD as shown in Figure 5.3. According to the demand of photolithography during the entire process, four layers are necessary and they are named NDIFF (in red), GATE (in green), MET (in blue) and CNT (in yellow) respectively. There are 60 × 40 ISFET chips in the design, and each is sized of 1.4 mm × 0.9 mm, and the classification is given in Table 5.1. Actually, all these ISFET chips are based on a fundamental design which has a 40 μm × 300 μm gate area, and the CNT area exactly overlaps the gate area. The only major difference between the chips is the metal electrode as shown in Figure 5.4. The chips without electrodes can only be tested as an ISFET, while CNTs can be integrated to the ones with

96

electrodes. Finally, the masks are produced on transparency films with both clear field and dark

filed polarities.
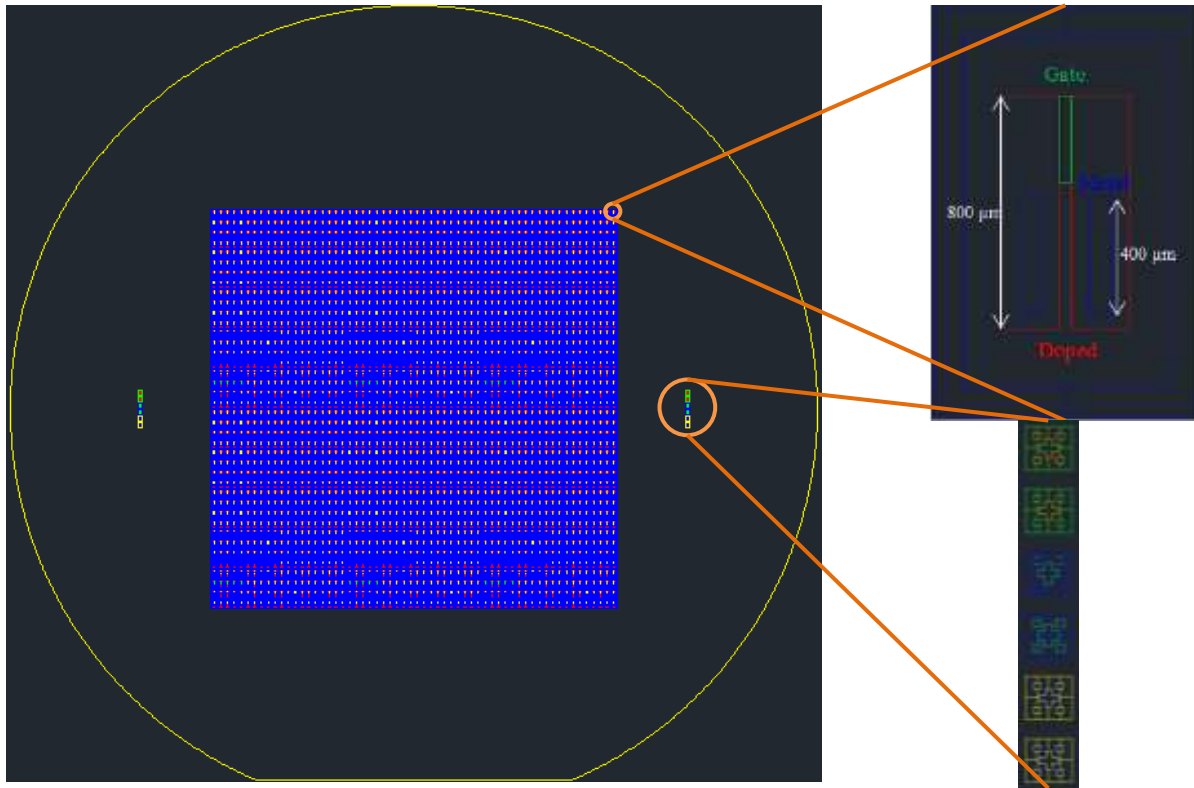
Figure 5.3: Multilayer mask design for fabricating ISFETs.
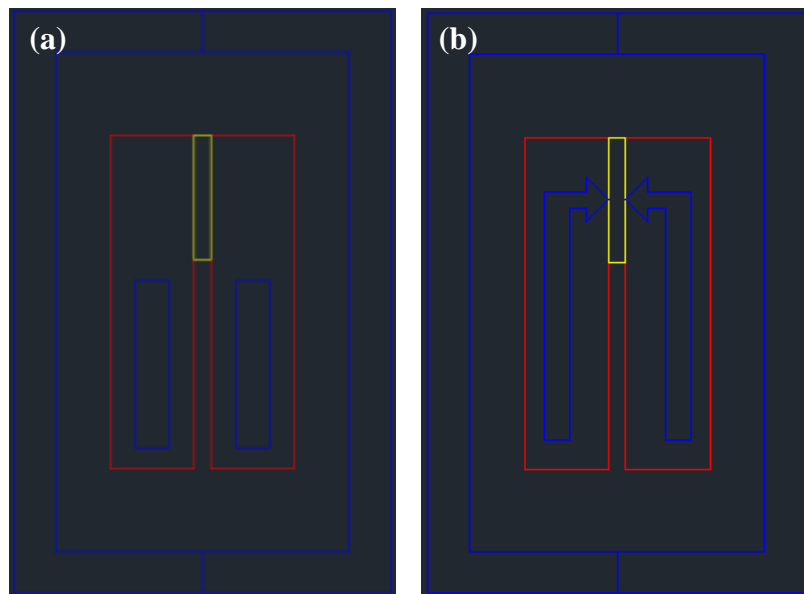
Figure 5.4: Comparison of (a) ISFET and (b) ISFET with triangle electrodes.

Gap of Source/Drain (μm)	Electrode Shape	Expanded Gate (μm)	Shrunk Gate (μm)	Gate Length (μm)
40				300
40		1		300
40		2.5		300
40		5		300
40			1	300
40			2.5	300
40			5	300
40				380
40		1		380
40		2.5		380
40		5		380
40			1	380
40			2.5	380
40			5	380
40	Triangle 90°			300
30	Triangle 90°			300
40	Triangle 90°	1		300
40	Triangle 90°	5		300
30	Triangle 90°	1		300
30	Triangle 90°	5		300
40	Triangle 90°		1	300
40	Triangle 90°		5	300
30	Triangle 90°		1	300
30	Triangle 90°		5	300
40	Triangle 60°			300
30	Triangle 60°			300
40	Triangle 60°	1		300
40	Triangle 60°	5		300
30	Triangle 60°	1		300
30	Triangle 60°	5		300
40	Triangle 60°		1	300
40	Triangle 60°		5	300
30	Triangle 60°		1	300
30	Triangle 60°		5	300
40	Triangle 30°			300
30	Triangle 30°			300
40	Triangle 30°	1		300
40	Triangle 30°	5		300
30	Triangle 30°	1		300
30	Triangle 30°	5		300
40	Triangle 30°		1	300
40	Triangle 30°		5	300
30	Triangle 30°		1	300
30	Triangle 30°		5	300

Table 5.1: Classification of ISFET chips in the mask design.

5.2.2   Field Oxidation

During the fabrication, a diffusion furnace (Bruce BDF4, Bruce Technologies Inc., USA) as shown in Figure 5.5 is used for oxidation and phosphorus diffusion. In filed oxidation, multiple bare silicon wafers are loaded into the furnace for oxidizing, one of which would be used as the process wafer. The objective of field oxidation is to grow a silicon dioxide layer of about 500 nm thick on wafer's polished side. After loading the wafers and heating inside the oxidation tube of the furnace at 750 °C for 50 minutes, the process wafer underwent a DCE clean, which helps the wafer trap or remove metal substances or other impurities. Then, the temperature is increased to 1100 °C to complete dry oxidation and wet oxidation for 40 minutes and 34 minutes respectively. Finally, the tube is cooled to 750 °C for 55 minutes. Then, the field oxidation process is complete. Through Nanospec microscopy as shown in Figure 5.6, the thickness of oxidation layer is obtained as recorded in Table 5.2. An average of 5430 Å thick SiO2 on the polished side is achieved. The oxidation on both sides of the process wafer will work as a protection layer during the following diffusion process.

Figure 5.5: Diffusion furnace for oxidation and diffusion.

Figure 5.6: Nanospec reflectometer for SiO_2 thickness measurement.

Center	Left	Top	Right	Bottom	Average
5425 Å	5410 Å	5422 Å	5457 Å	5440 Å	5430.8 Å

Table 5.2: SiO_2 thickness measurement after field oxidation.

5.2.3   Phosphorus Source Preparation

The phosphorus source preparation is done in a specific phosphorus tube (tube #4) which is different from the oxidation one (tube #1). The source wafer is a PH-950 n-type 5-inch wafer with active component of SiP_2O_7. The source wafer is loaded into the tube on a boat with 2 dummy wafers located on its edges as shown in Figure 5.7. The tube is first dried in N_2 at 400 °C for 1 hour. Then, the temperature rises to 885 °C in 50 minutes, and it is followed by maintaining the temperature at 885 °C for 18 hours with both N_2 and O_2 valves on. Then, the tube temperature is decreased to 400 °C for 1 hour before loading the process wafer. After this process, the tube is filled with the dopant vapor P_2O_5 from the source by direct volatilization.

Figure 5.7: Phosphorus source wafers on boat.

5.2.4   Pre-Deposition

It is necessary to open windows in order to diffuse the silicon wafer by etching the oxidation layer using photolithography before the pre-deposition process really starts. The process wafer is first coated by AZ 4110 positive Photoresist (PR) by a desktop spin coater at maximum rpm of 3000 for 30 seconds. Figure 5.8 shows two desktop spin coaters available in the HiDEC photolithography room, where the left spin coater is specified for Poly(Methyl methacrylate) (PMMA) coating towards electron beam lithography while the right one is particular for other PRs, such as AZ4000/5000 series resist. Before coating, a hexamethyldisilazane (HMDS) process is implemented for the silicon wafers in order to provide an adhesion promoter for PR. Figure 5.9 shows the HMDS oven where HMDS can be applied to wafers in vapor form. Thus, the coating process gives a 1.25 μm thick PR layer. Then, the coated wafer is baked on the hot plates of Eaton Spin Coater (Eaton 6000HX Spin Coater) at 110 °C for 2 minutes and transferred to the mask aligner (SUSS Microtec MA 150 Contact Aligner) as shown in Figure 5.10 and Figure 5.11, respectively. The first mask (NDIFF, darkfield) is attached onto a blank glass substrate by double-sided tape with ink facing up as shown in Figure 5.12, and it is used to

101

pattern the applied PR by exposing the process wafer under UV for 6 seconds, and the exposed PR is developed at a caustic wet bench as shown in Figure 5.13. In order to prevent the silicon dioxide layer on the backside from being etched during etching the frontside, the backside is also coated by a layer of PR and baked inside a Blue M Oven at 110 °C for 20 minutes as shown in Figure 5.14. Next, the openings are ready to be etched by Buffered Oxide Etch (BOE, Baker) 5:1, the etching rate of which is about 1000 Å/min. After etching at an acid wet bench as shown in Figure 5.15, the rest of PR is completely stripped off by immersing the wafer into a positive resist stripper (Baker PRS-1000) solution at 85 °C for 10 minutes using another caustic wet bench as shown in Figure 5.16. Eventually, the wafer is loaded to the phosphorus tube. The deposition begins at 700 °C for 30 minutes, and then the temperature is increased to 885 °C for 65 minutes. The deposition ends with another 35 minutes treatment at 700 °C. Thus, the wafer is uniformly covered by the dopant. During the entire furnace process, N_2 is the only gas needed.

Figure 5.8: Photoresist desktop spin coaters.

Besides the process wafer, a control wafer C1, a bare silicon wafer of the same kind as the process wafer, is also loaded in this process in order to investigate the diffusion quality. After

unloading, the both wafers need a deglaze process by immersing them into a mixture solution of 1000 mL DI water and 100 mL HF at room temperature for 2 minutes. The deglaze is used to remove the excess un-reacted dopant. The mixture solution is contained in a 5000-ml-volume plastic beaker, and the two wafers are loaded in a wafer cassette which enables us to deglaze both simultaneously.

Figure 5.9: HMDS oven to generate HMDS adhesion layer in vapor form.

Figure 5.10: Eaton 6000HX spin coater with hotplates.
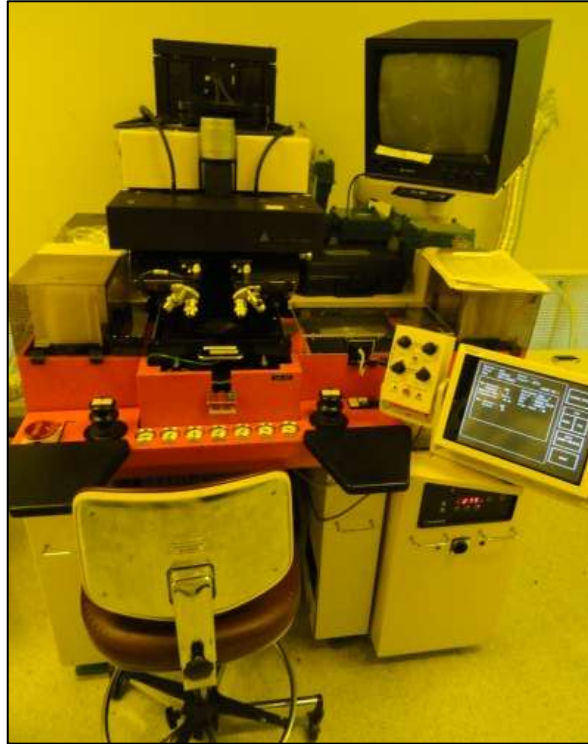
Figure 5.11: Suss microtec MA 150 aligner.
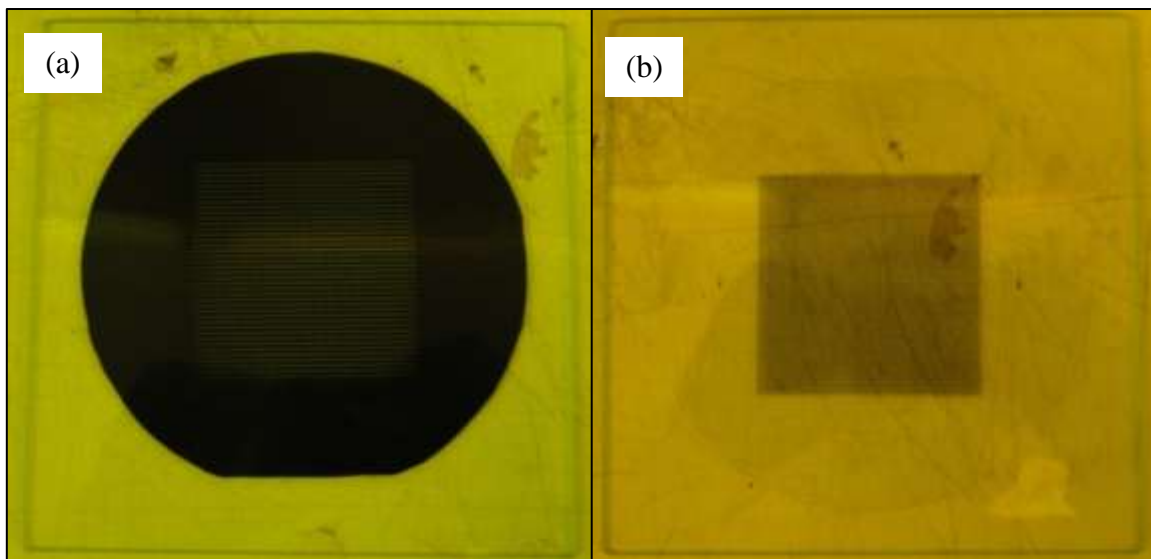
Figure 5.12: Transparency masks attached on glass (a) dark field and (b) clear field.

Figure 5.13: Caustic wet bench for developing PR.

Figure 5.14: Blue M Oven for baking PR applied to wafer backside.

Figure 5.15: Acid wet bench for etching SiO$_2$.

Figure 5.16: Caustic wet bench for stripping off PR.

5.2.5   Drive-In

The dopant deposited on Si will diffuse into Si substrate by loading the control wafer C1 and the process wafer into the phosphorus tube at high temperatures with N_2 and O_2 gas flow as shown in Figure 5.17. The wafers are first heated at 1000 °C for 30 minutes with N_2 and another 30 minutes with O_2. After the dry oxidation, a wet oxidation with steam flow is done for 20 minutes at the same temperature. Finally, the temperature is decreased to 750 °C for 35 minutes with N_2. After drive-in, the wafers are covered by a thin SiO_2 layer. Thickness of SiO_2 on C1 and the process wafer are 924 Å and 4009 Å respectively after the completion of diffusion. The SiO_2 thickness on C1 is supposed to be the same as the one on the diffused areas on the process wafer.
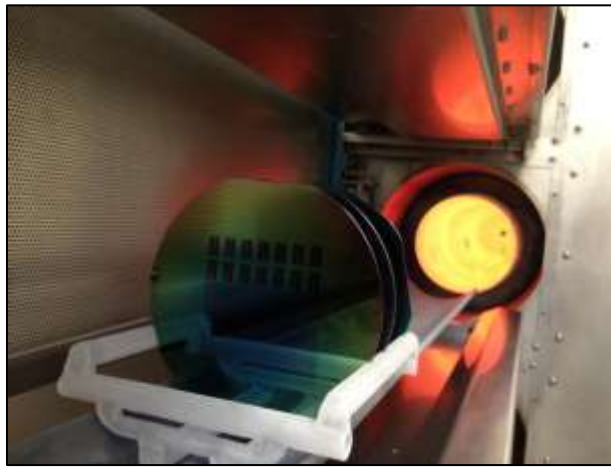
Figure 5.17: Loading process and control wafers into phosphorus tube for drive-in.

Besides measuring the thickness of SiO_2, C1 can also be used to calculate the junction depth in order to verify the diffusion, for which a groove is need on the doped silicon surface. The junction sectioning geometry is illustrated in Figure 5.18. The oxidation layer on C1 is firstly removed by BOE 5:1 wet etching, and a groove is fabricated by using a wafer groover as shown in Figure 5.19. The blade of wafer groover has a radius of 19,885 μm, and 5 minutes grooving gives a 16-μm-deep groove measured by Dektak 3030 as shown in Figure 5.20 and Figure 5.21. The solution of $CuSO_4*5H_2O$ with HF is prepared as the n-type stain. A stain droplet is applied

107

to the grooved area on C1, and it is taken to the Suss aligner to be exposed for 390 seconds. Then, the stain is removed by dipping into DI water and blow-dry with N_2. The copper plating on the doped area can be inspected by microscopy. As shown in Figure 5.22, the copper plating is obvious to present the outline of the groove after the stain is exposed and rinsed off. Next, a microscope with micro-measure function as shown in Figure 5.23 is employed to determine W_1 and W_2, which are 1692.4 µm and 1442.7 µm respectively. According to the geometry, the junction depth x_j was able to be calculated using Equation (5.1). Ultimately, the junction depth on C1 is obtained, $x_j = 4.9$ µm. Detailed measurement results are given in Table 5.3.

$$x_j = d_2 - d_1 = \sqrt{r^2 - \left(\frac{W_2}{2}\right)^2} - \sqrt{r^2 - \left(\frac{W_1}{2}\right)^2} \qquad (5.1)$$

	r	Units	W_1	Units	W_2	Units
	19885	um	**1692.4**	um	**1442.7**	um
	r^2	Units	$(W_1/2)^2$	Units	$(W_2/2)^2$	Units
Depth	395413225	um	716054.44	um	520346	um
	SQRT $(r^2 - (W_2/2)^2)$		SQRT $(r^2 - (W_1/2)^2)$			Units
Depth	19871.91181		19866.98695			um
	SQRT $(r^2 - (W_2/2)^2)$ - SQRT $(r^2 - (W_1/2)^2)$					Units
Junction Depth		**4.9**			**µm**	

Table 5.3: Result of junction depth measurement.
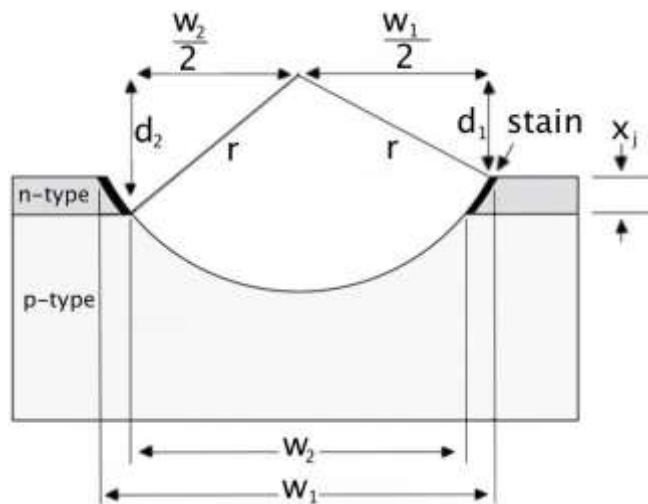
Figure 5.18: Junction sectioning geometry.

108

Figure 5.19: Wafer groover to fabricate groove on diffused Si substrate.

Figure 5.20: Dektak 3030 surface profiling measuring system.
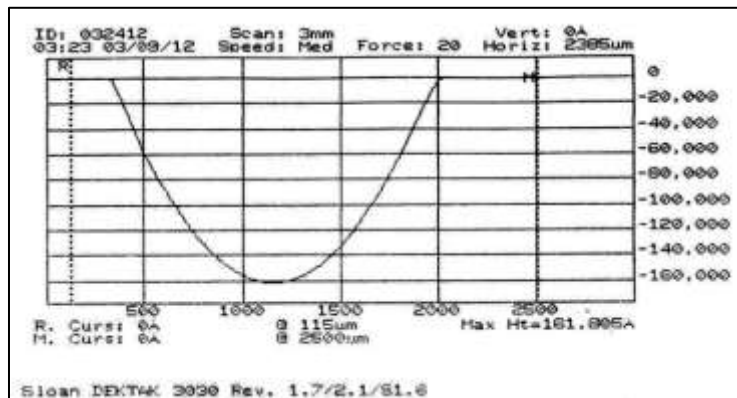
Figure 5.21: Surface profile of grooved Si substrate.
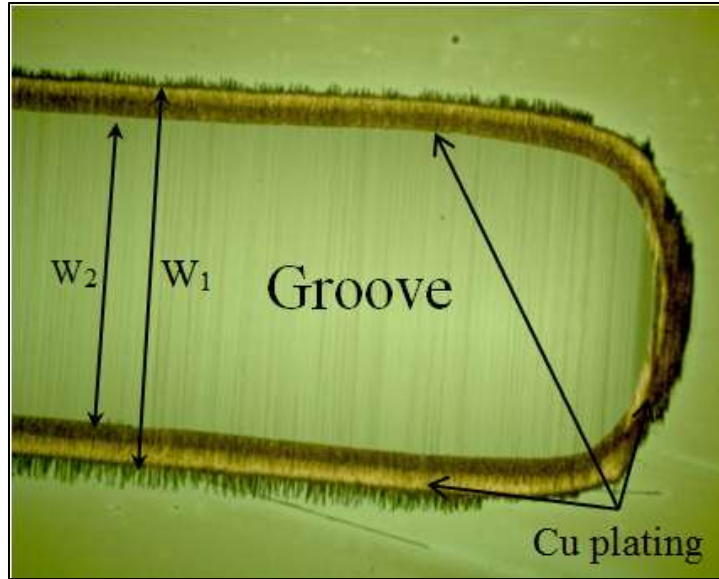
Figure 5.22: Inspection (top-view) of Cu plating on groove after stain exposed and rinsed.

Figure 5.23: Micro measure system to measure groove dimensions.

5.2.6   Gate Oxide

After completing the diffusion, the thickness of oxidation layer on the process wafer is about

4009.4 Å except for those doped areas where the thickness is about 923.6 Å. Since the direct

contact between target solutions and the transistor happens on the gate area, a fine thin oxide

layer is needed instead of the current one. Thus, the second mask (GATE, dark field) is used to pattern the PR 4110 after coating and exposing on the frontside. HMDS and soft baking are done before and after coating respectively. After exposing the PR with the GATE mask for 6 seconds, the PR is developed for 45 seconds. Before etching, the backside is again coated by PR the same way as in **5.2.4**. During etching, the process wafer is immersed into 1000 ml BOE 5:1 solution for 5 minutes to remove the uncovered SiO_2. Then, the PR is completely removed by PRS-1000 at the caustic wet bench, and the wafer is ready to go back to the furnace for oxidation with a second control wafer C2, another bare silicon wafer. Besides DCE clean, the gate oxidation process only involves dry oxidation with O_2 flow at 1100 °C for 40 minutes. Then, the temperature is decreased to 400 °C for 3 hours. Based on the oxidation thickness measurement through Nanospec microscopy, the thickness of SiO_2 layer on C2 is about 560 Å as given in Table 5.4, which reflects the oxide thickness at the gate areas on the process wafer, while the thickness of oxidation layer on the diffused areas is about 1310 Å. In fact, C1 is also involved in the gate oxide process before it is etched and grooved to measure the junction depth. Therefore, the oxide thickness on the doped areas of the process wafer is obtained by measuring C1, and Table 5.5 presents the measurement result on C1.

Center	Left	Top	Right	Bottom	Average
558 Å	556 Å	557 Å	559 Å	556 Å	557.2 Å

Table 5.4: SiO_2 thickness measurement for gate area after gate oxide.

Center	Left	Top	Right	Bottom	Average
1304 Å	1272 Å	1434 Å	1282 Å	1254 Å	1309.2 Å

Table 5.5: SiO_2 thickness measurement for doped area after gate oxide.

5.2.7 Backside Oxide Etch

In order to protect the oxidation layer on the front side during etching the oxidation off the backside of the process wafer, the frontside is coated with PR4110 by desktop spin coater after going through HMDS process. The coated wafer is baked at 110 °C for 2 minutes, and then immersed into 1000 ml BOE 5:1 solution for 7 minutes to remove the backside oxidation completely. At last, the frontside of the process wafer is applied to flood UV exposure using a black glass for 24 seconds and 3 minutes developing to strip off the PR.

5.2.8 Lift-off Patterning

In order to pattern the metal layer by lift-off, an image reversal photoresist AZ 5214E [143] is employed. This special photoresist is intended for lift-off technique, which calls for a negative wall profile. Although AZ 5214E is still a positive photoresist comprised of a novolak resin and naphthoquinone diazide as Photo Active Compound (PAC), it is capable of Image Reversal (IR) resulting in an opposite pattern of mask. Actually, AZ 5214E is almost exclusively used in the IR-mode. The IR-mode can be activated by baking and exposing the PR twice, and at the same time the IR-mode can cause a lower dissolution rate at the top a higher rate at the bottom. Consequently, there will be a negative wall profile ideally suited for lift-off while AZ 4000 series PR such as 4110 and 4330 will create a positive wall profile as shown in Figure 5.24.

Before coating the process wafer with 5214E, it is cleaned using acetone on a spin coater and undergoes an HMDS process. Then, 5214E is applied to the wafer using spin coater at 4000 rpm for 30 seconds which gives a 2 μm thickness. Then, the coated wafer is baked at 88 °C for 45 seconds before the first exposure. The third mask (MET, clear field) is used to expose the PR for 6 seconds. It is followed by the IR baking, where the wafer is baked at 106 °C for 45 seconds. Next, the second exposure, a flood exposure with a blank glass, is completed for 45 seconds to

turn on IR-mode of 5214E. Then, the PR is developed using MF CD-26 developer for 45 seconds. Eventually, the area that is exposed only once is developed leaving a negative wall profile, and the process wafer is ready for metallization.
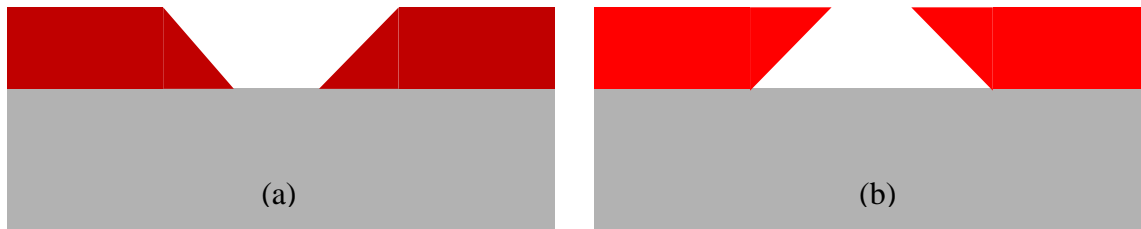
Figure 5.24: PR wall profile after developing (a) positive and (b) negative.

5.2.9 Metallization

Metallization is realized through evaporation using Edwards Auto 306 Turbo as shown in Figure 5.25. Chromium and gold are deposited onto the process wafer using a chromium rod and four highly pure gold pellets as the source. In this process, the four gold pellets are evaporated in two times, and two pellets are fed each time. Generally, each gold pellet generates a 50-nm-thick layer. Finally, the chromium as an adhesion layer is 15-nm-thick and the gold layer is about 233.8-nm-thick. One of the major advantages of evaporation over other deposition methods, for example sputtering, is that the PR can survive during evaporation process and be used for lift-off. To lift off the metal, an ultrasonic cleaner is used. The process wafer is put into a crystallizing dish which is filled with acetone. Then the dish is moved into the water-filled ultrasonic cleaner and floated on the top of water as shown in Figure 5.26. The ultrasonic is turned on for 5 minutes, and the metal starts to be lifted off. Figure 5.27 illustrates the process wafer in the middle of lift-off. The ultrasonic process may last longer until the metal is no longer lifted off, and the acetone in crystallizing dish should be replaced if necessary. Next, the wafer is rinsed with acetone and isopropyl alcohol (IPA). Finally, the ISFET structure is completed as shown in Figure 5.28. The

thickness of metal layer is also measured using Dektak 3030, and the metal is about 2000 Å above the oxide layer on the doped area as shown in Figure 5.29.
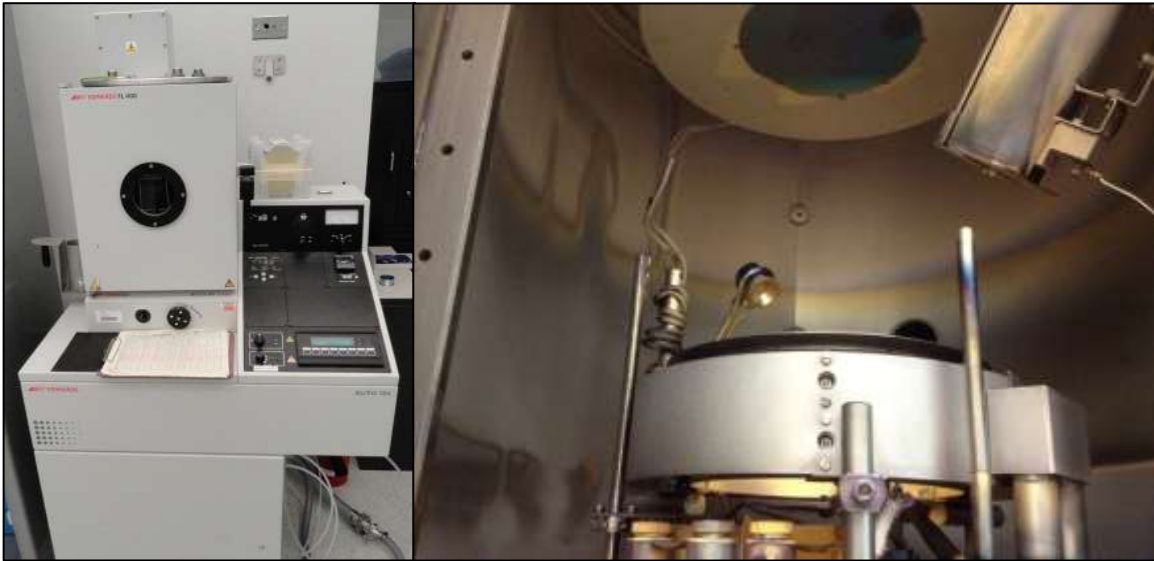
Figure 5.25: Evaporator for chromium and gold deposition.
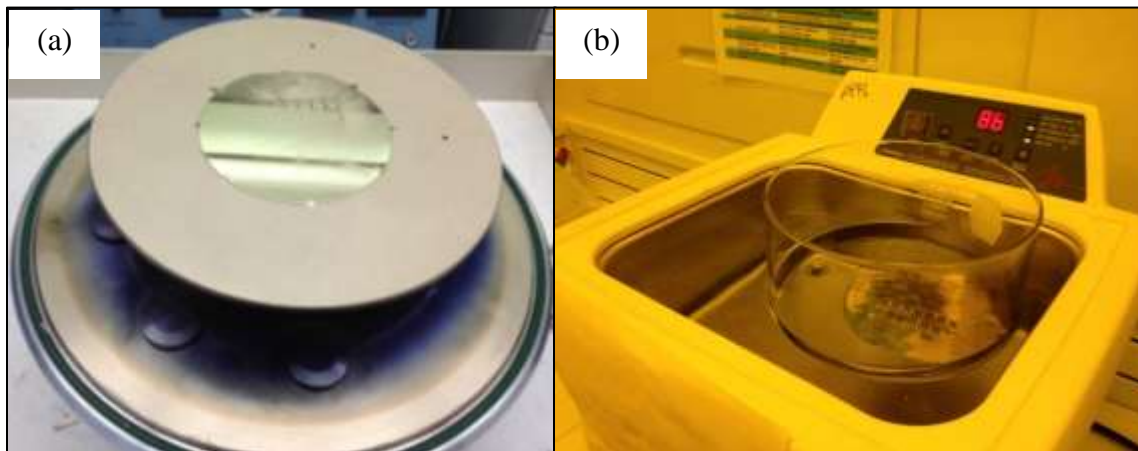
Figure 5.26: Metallized wafer (a) in acetone to lift-off ultrasonically (b).
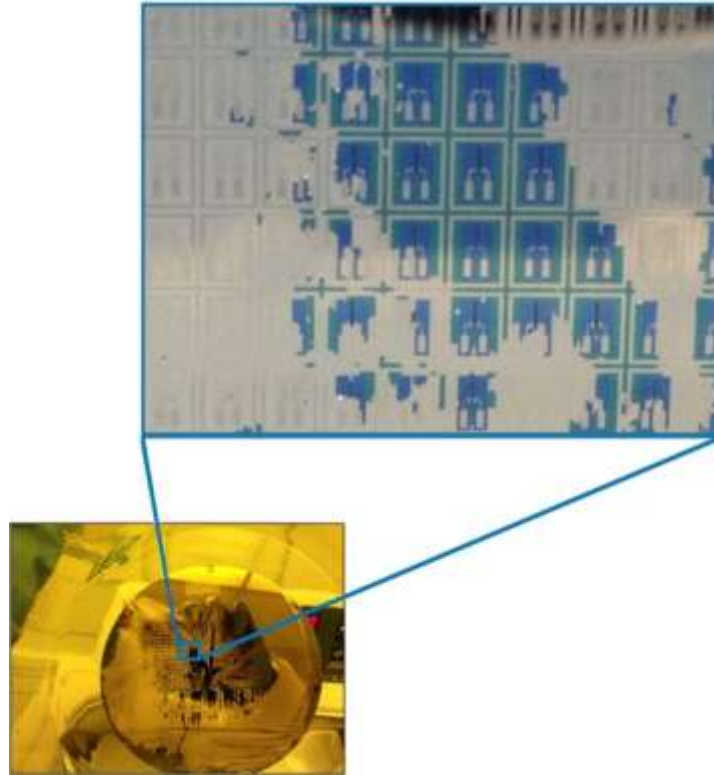
Figure 5.27: Process wafer in the middle of lift-off.
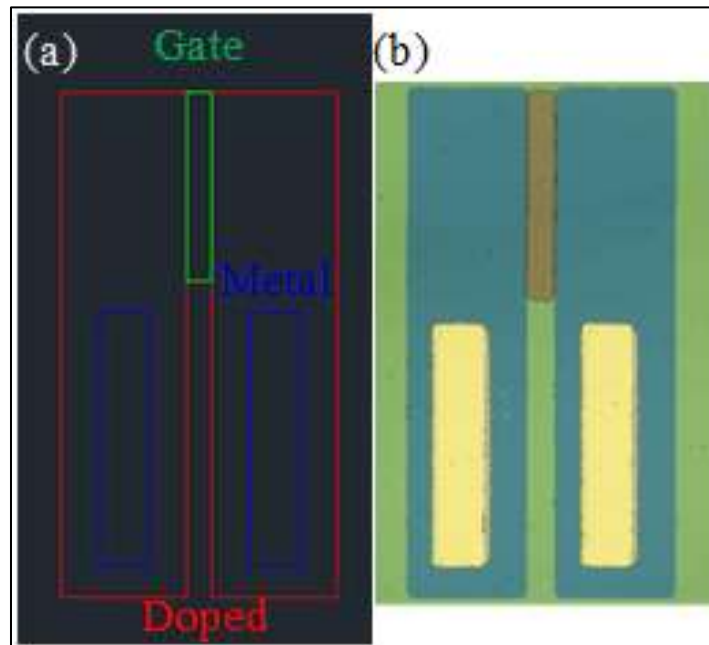
Figure 5.28: Structure of ISFET: (a) desired and (b) fabricated.
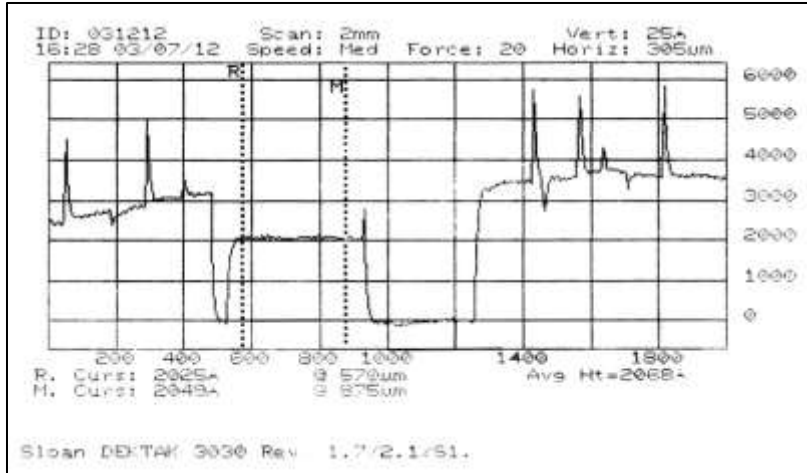
Figure 5.29: Metal layer thickness measurement above doped area.

5.3 Experimental Setup for pH Measurement

After cutting the process wafer into pieces of ISFET chip using a dicing saw (MicroAutomation Model 1100) as shown in Figure 5.30, a small outline integrated circuit package (CSO00802, Spectrum Semiconductor Materials Inc., USA) as shown in Figure 5.31 is employed in order to establish reliable electrical connections through which outer electronic devices can be applied. Figure 5.32 shows both the schematics and reality of setup. There is a metal layer on top of the package cavity, and the chip substrates are attached onto the cavity surface by conductive epoxy. The epoxy works as glue after cured by heating at 150 °C for 10 hours in a vacuum oven (Fisher Isotemp Oven 282) as shown in Figure 5.33. Then, the gold on the doped areas and the package cavity surface are bonded to different pins through a wire bonder (Model 4123, Kulicke & Soffa, Singapore) as shown in Figure 5.34, which provides 25.4 µm diameter aluminum wire bonding. During the pH measurement, this structure employs a discrete null-balancing method and the output of ISFET, drain current I_d, will be held constant by adjusting the gate voltage V_{gs}. When gate area of the ISFET chip is exposed to various target solutions, the external bias voltage V_{gs} in series with the reference electrode should be adjusted to

116

secure zero change of I_d. Therefore, the change of V_{gs} depends directly on the ionic activity/concentration. In this experiment, the drain voltage V_{ds} is constant at 1 V provided by a DC power supply (Model XP-760, Elenco Electronics Inc., USA), and I_d is measured by a picoammeter (Model 6485, Keithley, USA). A second DC power supply (Model N5748A, Agilent, USA) with a fine adjustable function at 0.01 V is employed to adjust V_{gs}. A copper wire in diameter of 250 μm (Model 93-2972, Strem Chemicals, USA) is used to sense target solutions.
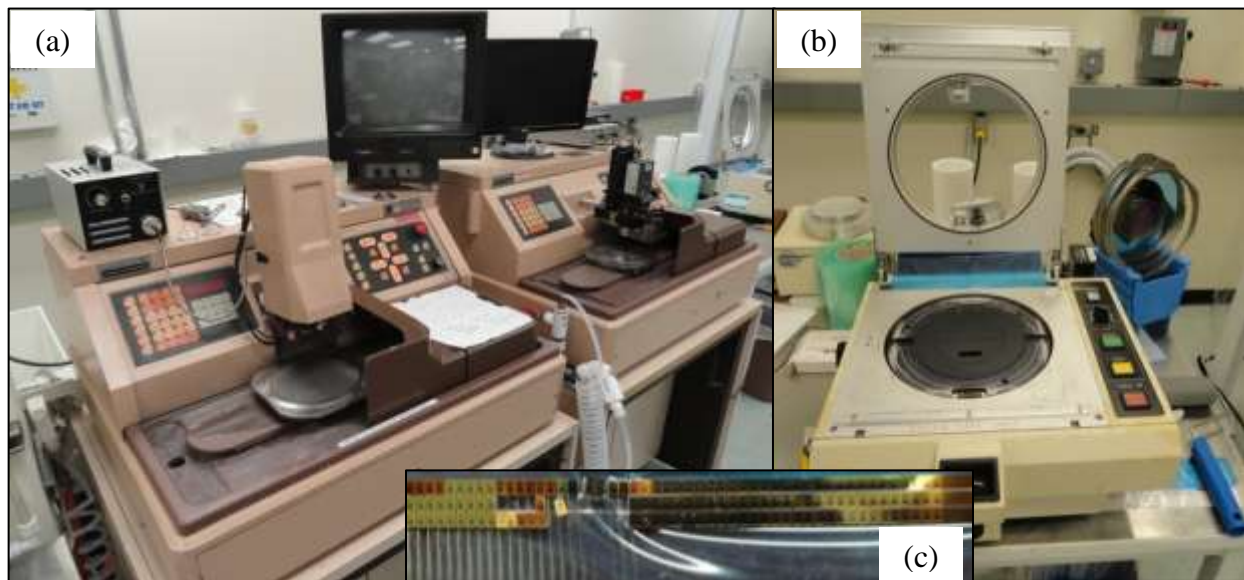
Figure 5.30: Dicing saw system (a) automatic saw, (b) wafer taper and (c) diced chips.
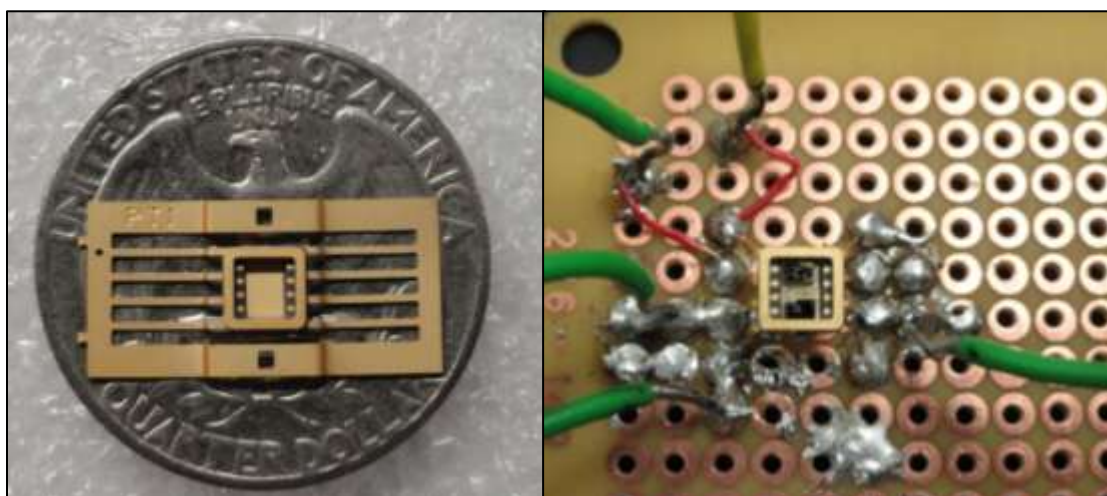
Figure 5.31: Small outline integrated circuit package.
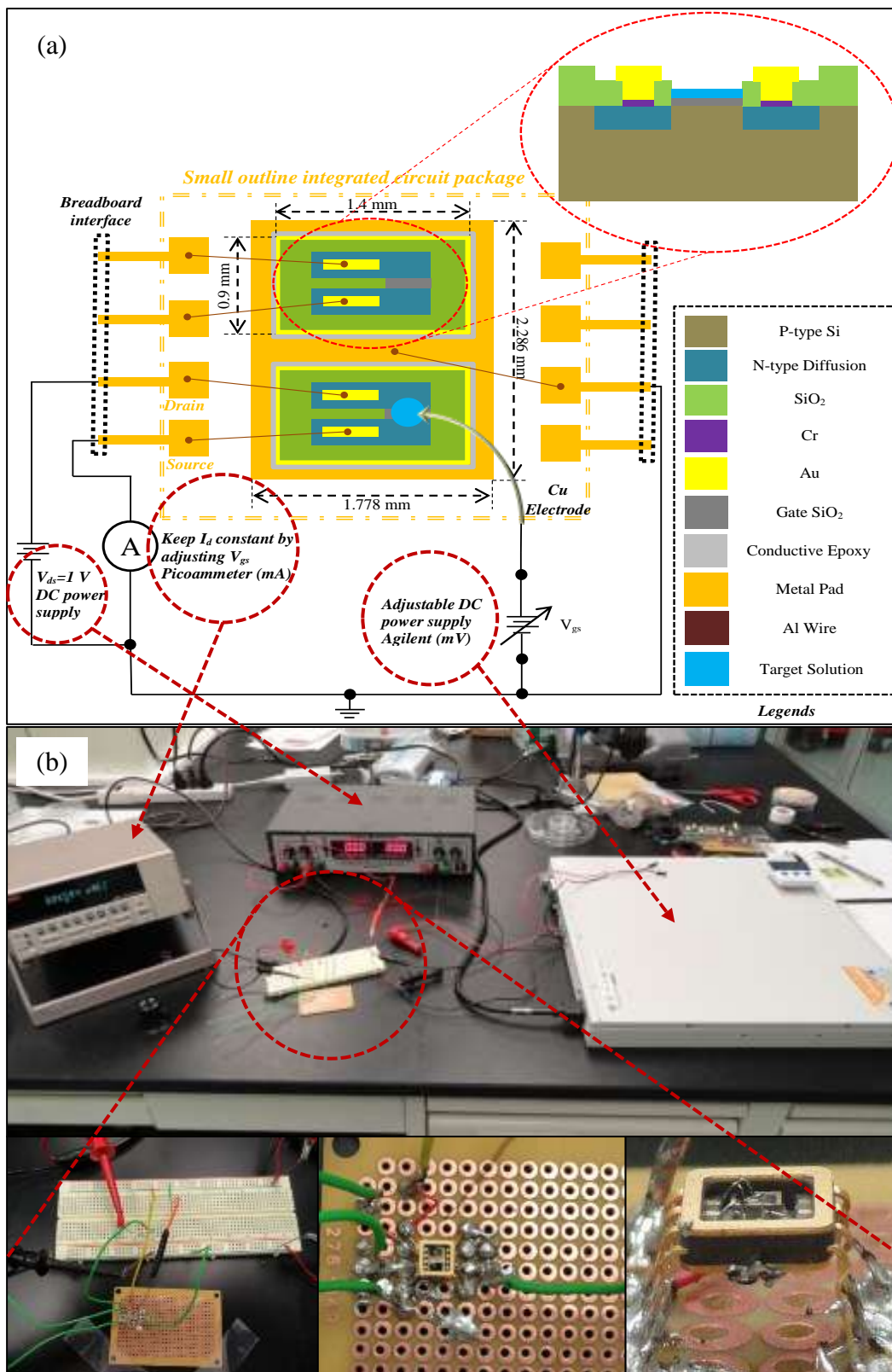
Figure 5.32: Experimental setup for pH measurement (a) schematic and (b) real.

Figure 5.33: Vacuum curing oven for conductive epoxy bonding.

Figure 5.34: Wire bonding machine.

5.4   Current Results on pH Measurement

Before testing, six target solutions are prepared. Their pH values are checked using a pH tester (pH55, Milwaukee Instruments, USA) and are 4.1, 5, 6, 7.1, 8.5, and 9.5 respectively. Figure 5.35 shows the pH tester and pipette (Eppendorf Research Pipette) that are involved during the pH measurement. In order to test the ISFET, five droplets of 2.5 µL from each target solution are dropped onto the gate area and measured. For instance, a 2.5 µL droplet from pH 4.1

solution is located onto the gate area using a pipette while the drain voltage is applied at 1 V.

Then, the copper wire as reference electrode is inserted into the droplet while the gate voltage is

applied and adjusted to keep the drain current constant at 5.475 mA. When the drain current is

stabilized, the gate voltage is recorded. The droplet evaporates quickly after the gate voltage is

applied. Thus, the testing continues until five data are recorded for each pH. Then, the ISFET

chip is stored overnight in the dry box (McDry MCU-201, Seika Machinery Inc., USA), where

the relative humidity can be as low as 1 %. Then, the measurement for next pH solution could be

carried out next day. Eventually, the complete results for pH detections between 4.1 and 9.5 are

given in Table 5.6 and Figure 5.36. Furthermore, the corresponding ΔV_{gs} at each pH is collected

to apply a linear fit in order to study the sensitivity of the ISFET as shown in Figure 5.37.

According to the linear fit, the slope is 0.0107, which means the sensitivity is 10.7 mV/pH.

Additionally, the ISFET has an instant response. During the measurement, the reading of I_d

varies simultaneously when the electrode is in contact with the target solution.

pH	V_{gs} (V)							
	#1	#2	#3	#4	#5	Mean	Stdev.	ΔV_{gs}
4.1	0.52	0.51	0.5	0.53	0.53	0.518	0.01304	-0.042
5	0.54	0.54	0.56	0.56	0.56	0.552	0.01095	-0.008
6	0.56	0.57	0.56	0.57	0.56	0.564	0.00548	0.004
7.1	0.56	0.56	0.55	0.57	0.56	0.56	0.00707	0
8.5	0.58	0.58	0.59	0.58	0.57	0.58	0.00707	0.02
9.5	0.6	0.59	0.58	0.58	0.58	0.586	0.00894	0.026

Table 5.6: Results of pH measurement at V_{dc} = 1V and I_d = 5.475 mA.
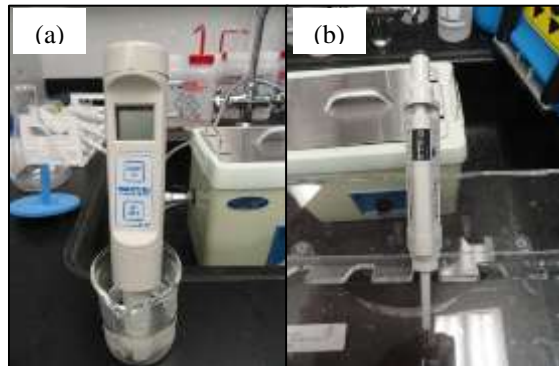
Figure 5.35: (a) pH tester and (b) 0-2.5 µL pipette involved in pH measurement.
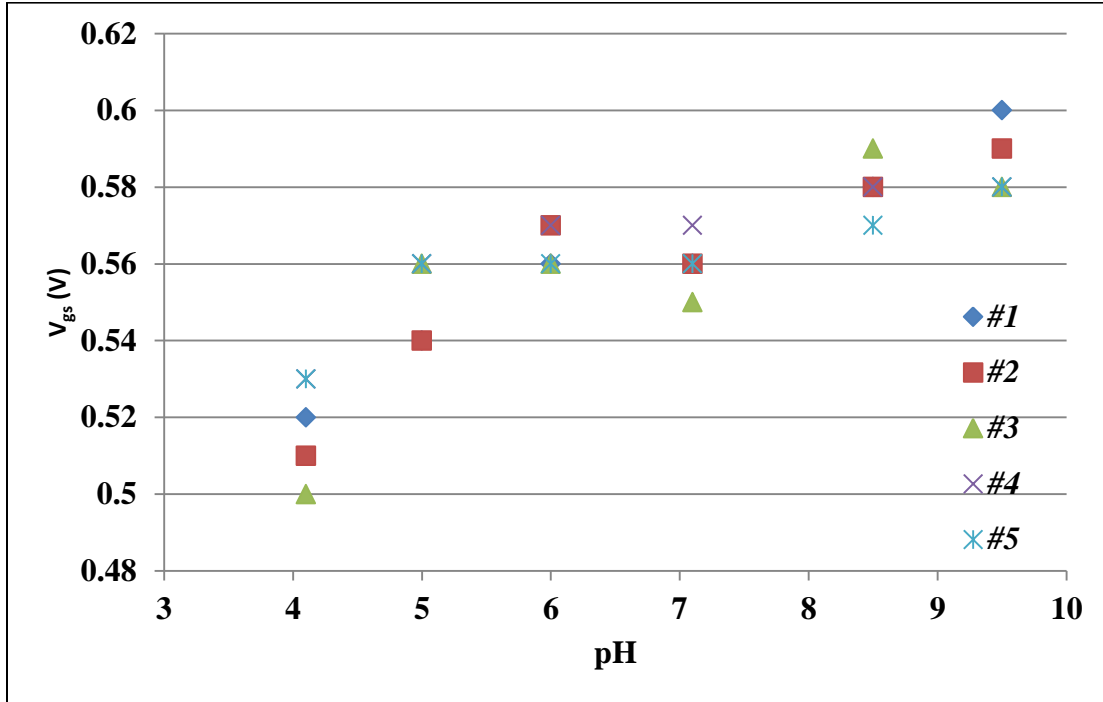
Figure 5.36: Results of pH measurement at V_{dc} = 1V and I_d = 5.475 mA.
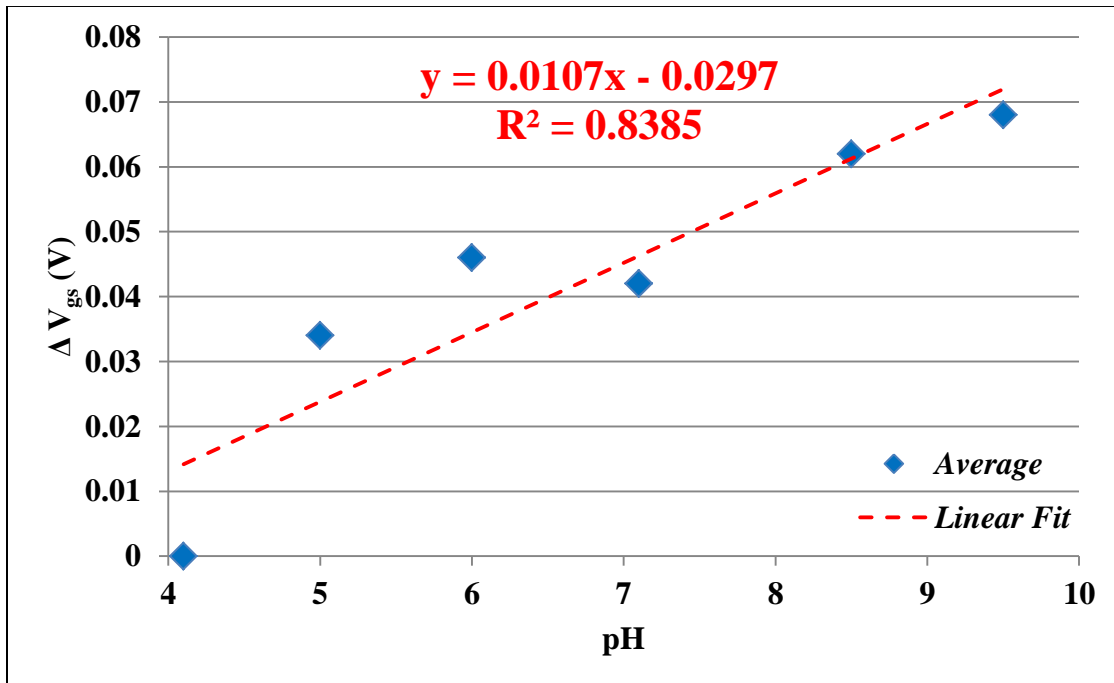
Figure 5.37: Sensitivity of ISFET for pH measurement.

5.5 Modeling – Nernst Potential

As known, pH is defined as the decimal logarithm of the reciprocal of the hydrogen ion activity a_{H+} in a solution as in Equation (5.2). As a matter of fact, hydrogen ion activity is always approximated to the free hydrogen ion concentration $[H^+]$. Thus, we can use Equation (5.3) to describe the definition of pH in solution instead. Furthermore, the pH measurement using ISFET is based on the principle of Nernst Potential, which has a physiological application when it is used to determine the potential of an ion of charge z across a membrane. This potential is calculated using the concentration of the ion both inside and outside the cell. Equation (5.4) expresses the meaning of the Nernst Potential, where E is the Nernst Potential in voltage, R is the ideal gas constant in joules per kelvin per mole, T the is temperature in kelvin, F is the Faraday's constant in coulombs per mole, z is the valence of the ion ($z = 1$ for hydrogen ion), and $[H_1^+]$ and $[H_2^+]$ are the hydrogen ion concentration outside cell and inside cell respectively, which, in our case, are the ion activity I_d and the hydrogen ion concentration in the target solution. Therefore, if the ion activity/concentration in either side of the membrane is kept constant, the Nernst Potential only depends on the ion activity/concentration in the other side of the membrane and the Nernst Potential can be used as output to reflect the ion activity/concentration of target solution. In the experiment, both I_D and V_{ds} are held constant during the pH measurement while the measured potential V_{gs} indicates the pH of the target solution. Equation (5.5) and (5.6) reveal the relation between the measured Nernst Potential and the pH, where E^0 is the standard membrane potential at the temperature of interest and a constant due to constant I_d and V_{ds}.

$$pH = -\log_{10}(a_{H+}) = \log_{10}(\frac{1}{a_{H+}}) \qquad (5.2)$$

$$pH = -\log_{10}[H^+] = \log_{10}(\frac{1}{[H^+]}) \qquad (5.3)$$

$$E = \frac{RT}{zF} \ln\left(\frac{a_{1H+}}{a_{2H+}}\right) = 2.303 \frac{RT}{zF} \log_{10}\left(\frac{[H_1^+]}{[H_2^+]}\right) \qquad (5.4)$$

$$E = 2.303 \frac{RT}{zF} (\log_{10}[H_1^+] - \log_{10}[H_2^+]) = E^0 - 2.303 \frac{RT}{zF} \log_{10}[H_2^+] \qquad (5.5)$$

$$E = E^0 + 2.303 \frac{RT}{zF} pH \qquad (5.6)$$

$$E = E^0 + 0.059172 pH \qquad (5.7)$$

After substituting the constants, $R = 8.314472 \text{ JK}^{-1}\text{mol}^{-1}$, T at room temperature 25 °C which is 298.16 K, $z = 1$ and $F = 96485.3 \text{ Cmol}^{-1}$, Equation (5.6) is rewritten as in Equation (5.7). As we can see, the slope of the relation between Nernst Potential and the pH of target solution is 0.059172 V/pH or 59.2 mV/pH. Apparently, the Nernst Equation is a mathematical description of an ideal pH electrode behavior. Therefore, the slope of 59.2 mV/pH is an ideal sensitivity of ISFET based pH sensor when pH is measured by the means of Nernst Potential. Figure 5.38 presents the comparison between the pH sensitivity of current ISFET and the ideal Nernst slope.
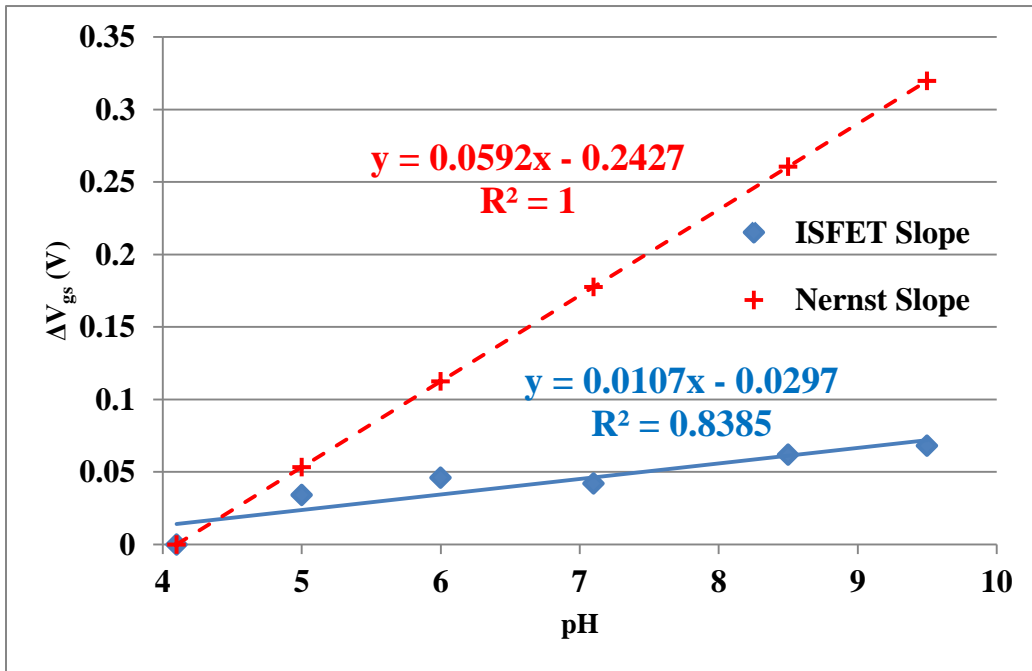
Figure 5.38: pH sensitivity of ISFET chip vs. ideal Nernst slope.

One of the major factors that cause a low sensitivity in the current pH measurement is the volume of target solution is scaled down to microliter while conventional pH sensors generally require the target solution in at least milliliter scale. As shown in Figure 5.39, the quantity of ions decreases significantly while the volume is reduced even if the corresponding concentration is kept the same. To measure the pH value for solutions in microliter or molecule level is one of the significant novelties for this project. However, the sensitivity has to be affected owing to the largely reduced volumes. It has been reported [88] that an ISFET fabricated similarly but with extra p-type stop channel using boron diffusion reached a sensitivity of 40 mV/pH. Their ISFET device was also equipped with an optimized reference electrode. However, the device was totally immersed into the target solution for measuring pH, which means relatively large volume of target solution was necessary to reach the sensitivity. Furthermore, it was mentioned in [144] that a layer of silicon nitride on the top of gate oxide as the ion sensing material might be able to improve the ISFET performance. Unfortunately, so far it has not been reported any research work regarding an effective compensation for measuring solutions in microliter or molecule level. Therefore, we propose CNT integrated ISFET as a promising solution.
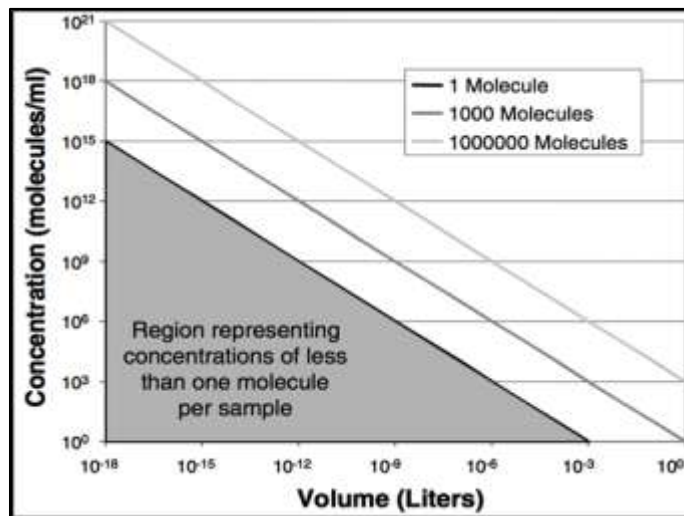
Figure 5.39: Relation between quantity of molecules/ions and volume/concentration.

5.6   CNT Alignment

5.6.1   Fabrication of FET

As introduced in **1.1.4**, a non-uniform electric field is the precondition in order to generate DEP forces, which can be used to align polarizable particles such as CNTs. So, FET structures are needed in order to produce non-uniform electric field. Figure 5.40 illustrates the mask designed using AutoCAD. The FET structure consists of four layers: Si wafer, 300 Å of SiO_2, 200 Å of chromium and 5000 Å of gold. The fabrication flowchart using MEMS surface micromachining techniques is illustrated in Figure 5.41, where we have (a) Si substrate, (b) 300 Å SiO_2 by thermal oxidation, (c) chromium and gold are deposited by evaporation and electro plating, (d) apply photoresist, (e) photolithography, and (f) the metals are etched as patterned and the rest of photoresist is stripped off completely. Triangular electrodes of 30, 60 and 90 degree angles, with various electrode gaps are designed. 24 microelectrode chips are fitted on a 5-inch Si wafer. The reason why triangular variation is selected is that it provides a wider zone of stronger DEP force and weaker hydrodynamic force than other variations, such as square and semicircular-shaped ones, which do not allow particles to be easily released [145].
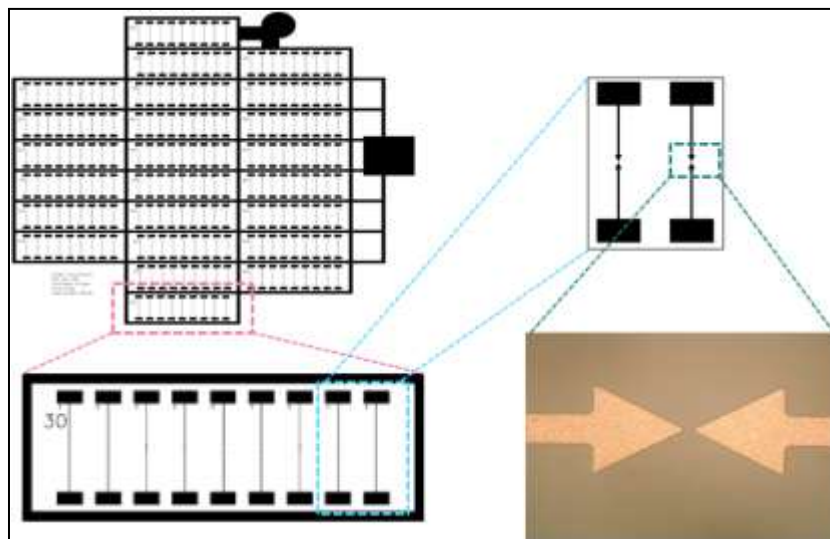
Figure 5.40: Mask design for Au microelectrodes on silicon as FET.
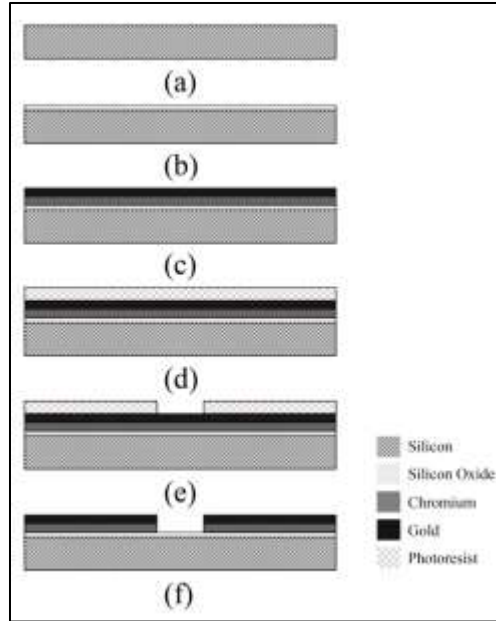
Figure 5.41: MEMS fabrication process for FET structure.

5.6.2   Experimental Setup

Two CNT stocks are prepared: 1.37mg SWCNTs dissolved in 1ml Deionized (DI) water with 2μl Triton; and 2.69mg MWCNTs dissolved in 1ml DI water with 5μl Nanosperse. Then both samples are sonicated for 1 hour. After the stocks are available, 5X, 10X and 20X dilutions are also prepared for each kind CNT.

For wire bonding, since the traditional method of soldering can damage microchips easily, conductive epoxy is used to stick wires onto the gold pads in order to interface the outer environment. In the experiment, the two parts of conductive epoxy are equally mixed, and then a little of the mixture is deposited on the pads. The epoxy becomes firm enough to bond stably between wires and pads after it is heated at 130ºC for about 1 hour on a heat plate. Eventually, the FET chip is to apply DEP forces in between the electrodes.

5.6.3   Alignment by DEP

Figure 5.42 illustrates the experimental setup for CNT alignment by generating DEP forces. A function/arbitrary waveform generator (33220A, Agilent Technologies) provides an AC power

of 20V p-p and 1.5MHz, which will be verified by the oscilloscope (MSO6012A, Agilent Technologies). Then, the chip is real-time observed by the optical microscope (BX51, Olympus) during the alignment. 1.5µl of 10X SWCNT dilution is dropped on the gap of the electrode pairs 1-4 while 1.5µl of 10X MWCNT dilution for the pairs 6-9. Then by connecting the electrodes to the function generator, DEP forces are generated in the gaps and the electrodes are bridged by the CNTs. Figure 5.43 shows the observations of the electrode gaps, where we have a. gap measure, b. covered by CNT droplet, c & d. bridged by SWCNTs and MWCNTs respectively.
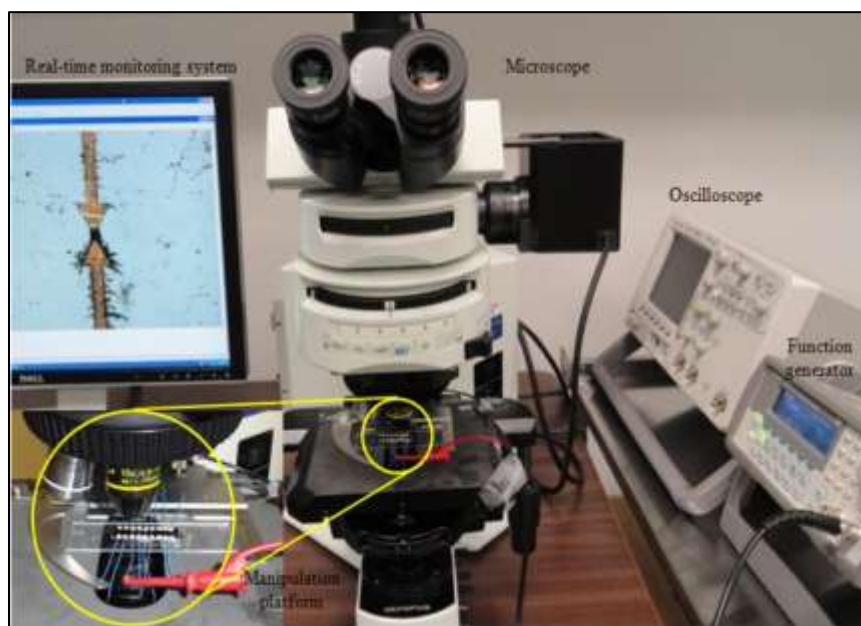
Figure 5.42: Experimental setup for CNT alignment using DEP.
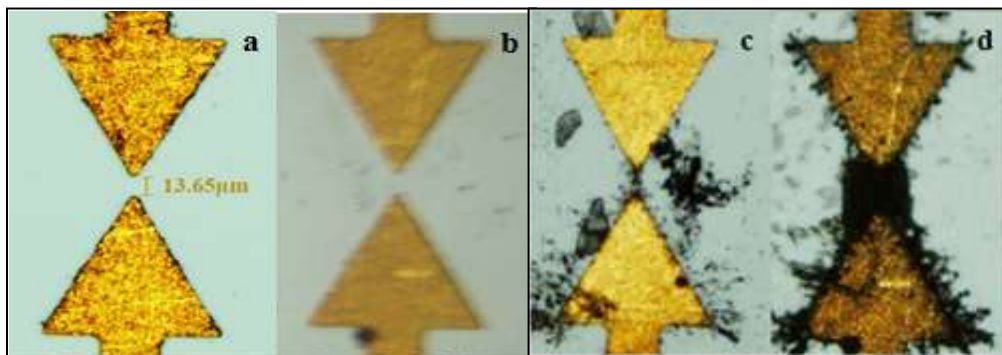
Figure 5.43: Pairs of Au electrodes observed by optical microscope.

5.6.4   Verification of Aligned CNT

Figure 5.44 shows I-V curve measurement results of all the nine pairs of electrodes. As we can see, both SWNTs and MWNTs aligned between the gaps possess a linear I-V curve. This linear relationship reveals that these CNTs are metallic and possessing very excellent ion conductive properties. Additionally, the I-V characteristic reveals that the source and drain of each pair of electrode are connected by the aligned CNTs after DEP is applied. Otherwise, all the I-V curves are supposed the same as the one for Pair 5, which has no CNT applied.
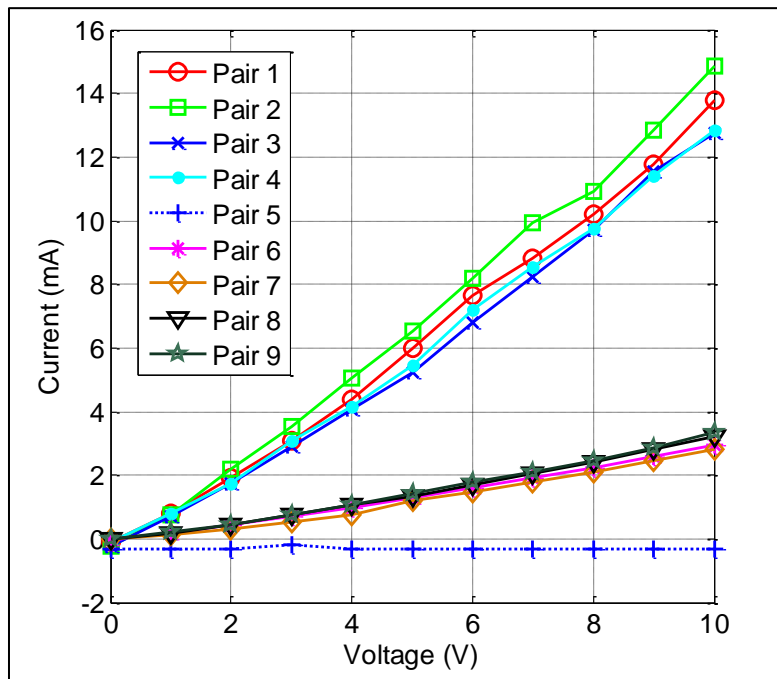
Figure 5.44: I-V characteristics with SWCNTs alignment (Pair 1-4), MWCNTs alignment (Pair 6-9) in the scratched gaps and Pair 5 for the bare electrode.

5.7   Electrical Characterization of CNT Using Conductive AFM

5.7.1   Current Sensing AFM

Generally, electrical characterization based on DEP alignment is suitable for bundle of CNTs. However, it is feasible to study the electrical property of single CNT through a conductive AFM technique – current sensing. To set up the experiment, we need a conductive surface to sustain

the nanotubes. A glass slide coated by an indium tin oxide (ITO) layer on the top guarantees the surface conductivity. A droplet of CNT solution is on the ITO surface, and surface is dried by heating. Then the CNT sample is ready for scanning. Agilent 5500-ILM supplies a Current Sensing AFM (CSAFM) capability, where an ultra-sharp AFM cantilever, coated with conductive film, probes the conductivity and topography of the sample surface simultaneously. CSAFM requires a special 10˚ nose cone containing a preamplifier. A bias voltage is applied to the sample while the cantilever is kept as virtual ground. During scanning, the tip force is held constant and the current is used to construct the conductivity image of the surface. It has proven useful in joint I-V spectroscopy and contact force experiments as well as contact potential studies. Figure 1 illustrates the schematic. This novel technique offers a simple and effective method with which electrical properties of single nano particle, like nanotubes, are able to be investigated.

The resonant frequency and spring constant of the conductive Si AFM probes (ElectriCont-G, BudgetSensors) are 13 kHz and 0.2 N/m respectively. These probes are coated by Cr/Pt conductively on both sides. The special nose cone assembled has a sensitivity of 10nA/V.
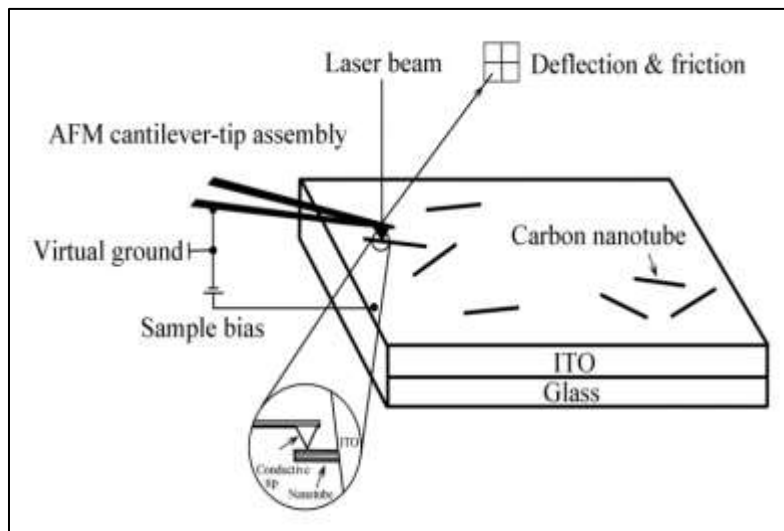
Figure 5.45: Schematic of measuring electrical property of single CNT using CSAFM.

5.7.2   Preamp

Before measuring the I-V curve, the electrical environment in the AFM should be examined by the process called preamp. A test resistor is employed to construct a connection by placing one end directly on the CSAFM nose cone, held by a spring clip, and the other to the 3-wire-EC cable that normally connects to the sample plate. Thus the test assembly takes the places of the sample and AFM probe. Then, a current versus bias sweep needs to be run to see whether or not the preamp is operational. The plot should of course present a linear relationship running from -1 nA to +1 nA as the voltage sweeps from -10V and +10V. As shown in Figure 5.46, it can be concluded the electrical circuit is reliable to carry on electrical property measurement. The plot is linear enough to validate the preamplifier. However, there is a tiny offset as current in pA level is measured at 0V. This phenomenon may be caused by imprecise parameter setting for the preamplifier and can be eliminated by further calibration. The offset is negligible as the experiment is to determine CNT is either metallic or semiconducting rather than extract exact resistance.

Figure 5.46: Preamp plot for electrical circuit examination.

5.7.3   Testing of SWCNT

Figure 5.47 shows the topography image of the surface in 10 µm × 10 µm square where it is clear to find a single SWCNT in the middle separating from the others. After the scanning is stopped, the tip is moved to contact with the nanotube at one point of its body, and the setpoint, which controls the force of the probe acting on its target, is increased to confirm the electric connection. Next, the sample bias is modified and input in terms of range from -3V to 3V to obtain the I-V characteristic. Figure 5.48 illustrates the SWCNT has a non-linear curve of CSAFM/Aux BNC vs. Sample Bias. In CSAFM, the system has a current output range from -10nA to 10nA. The platform indicates the current is out of range when the bias belongs to the intervals of (-3, -1) and (1, 3). Eventually, a conclusion that the nanotube is semiconducting is established.
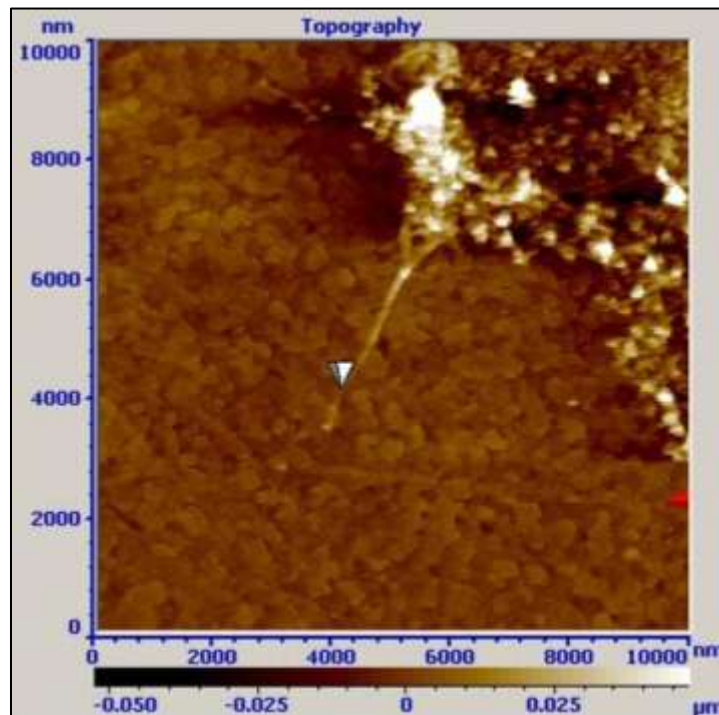
Figure 5.47: Topography of ITO surface with SWCNT: the cursor is where to measure I-V.

131
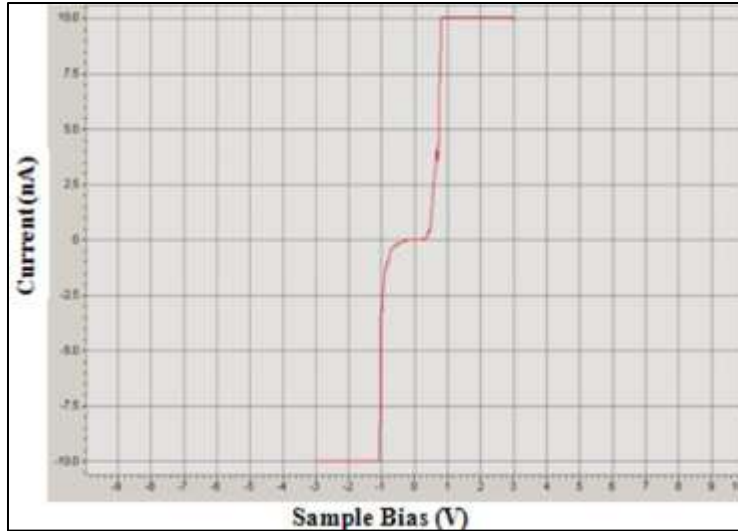
Figure 5.48: I-V sweep on SWCNT with range from -3 to +3V.

5.7.4 Testing of MWCNT

The MWCNTs are about 0.5~2 µm long and 30~50 nm in diameter. Figure 5.49 illustrates the AFM images of the sample surface in 1 µm × 1 µm, in the middle of which a multi-walled nanotube is forming an "island". While scanning the surface, a conductivity map of the same area is also generated with a bias of 200mV as shown in Figure 5.49 (b). This potential bias is applied from the microscope sample plate, which is connected to the ITO surface through a Cu wire. In conductivity map, larger current flows into the AFM tip in brighter area, which suggests ITO has a lower resistance than the MWCNT does. After the scanning is stopped, the tip is moved to contact with the nanotube body. The setpoint, which controls the force of the probe acting on its target, is increased to confirm the electric connection. Then the cross-section information is measured at the location as shown in Figure 5.50. Figure 5.51 gives the nanotube's diameter is 40 nm, which further convinces us it is a MWCNT. Finally, a potential range from -10V to 10V is applied to draw the I-V curve. Figure 5.52 illustrates that the MWCNT has an approximately linear relationship of CSAFM/Aux BNC vs. Sample Bias. Eventually, a conclusion that the MWCNT is metallic is established.

132
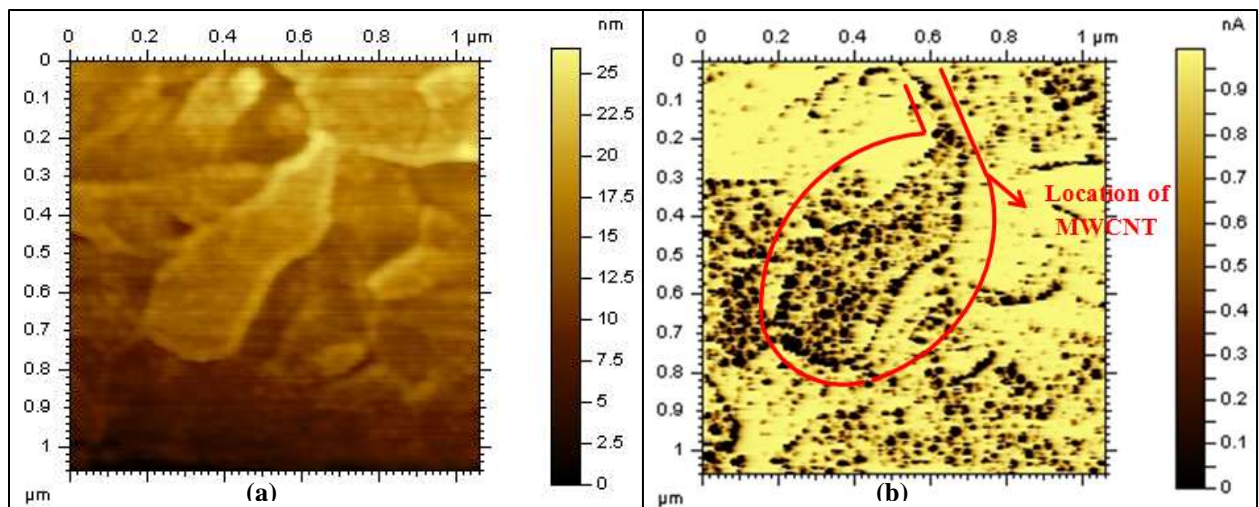
Figure 5.49: AFM images of MWCNT on ITO (a) topography and (b) conductivity map.
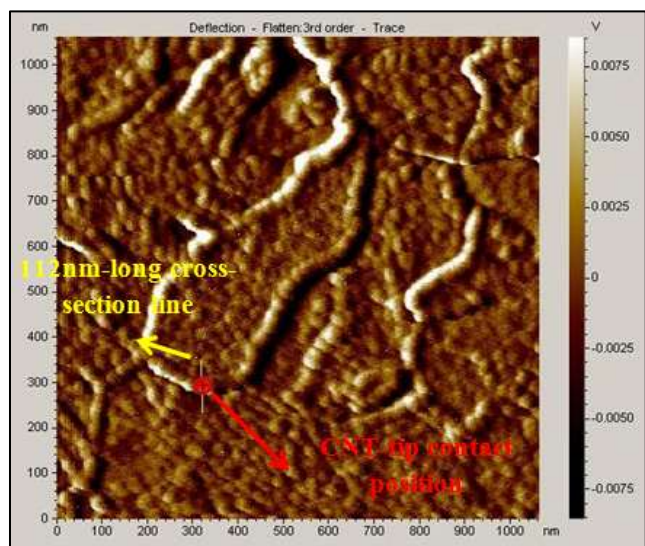
Figure 5.50: Deflection image shows the contact position on the CNT body.
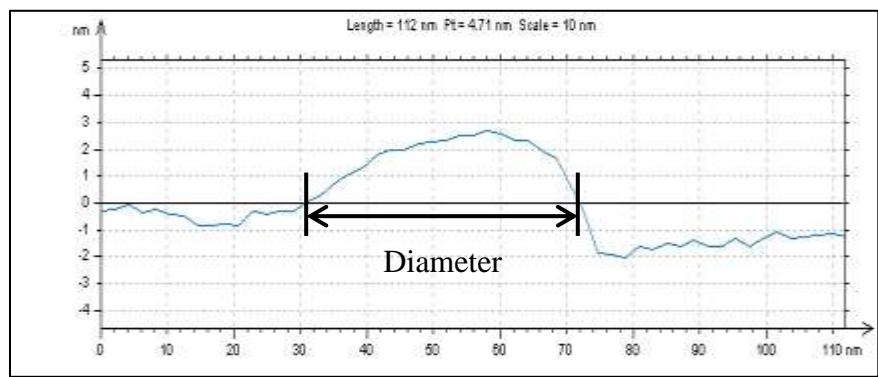
Figure 5.51: 112-nm-long cross-section line for CNT diameter measurement.

133
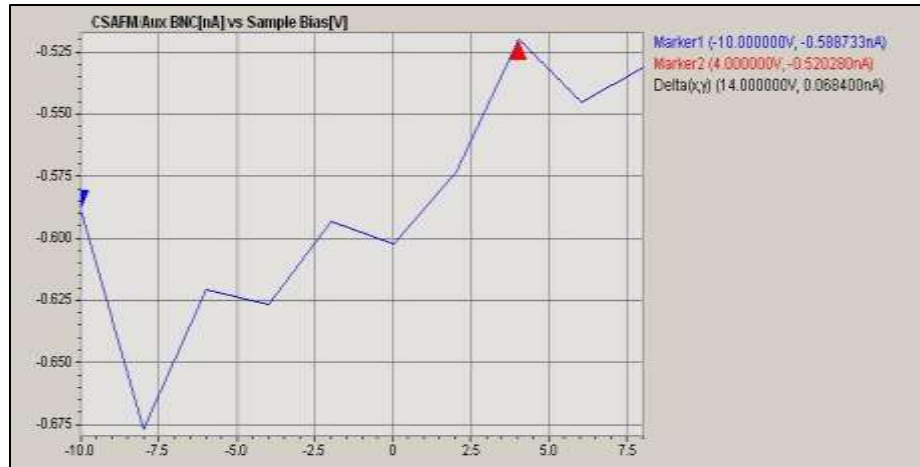
Figure 5.52: I-V sweep on MWCNT with range from -7.5 to +7.5 V.

5.8 AFM Based Surface Nanoscratching for Nanochannels

5.8.1 Background

Among current nanotechnology applications, the design and fabrication of nanochannels are one of the major challenges. To date, the methods for fabricating nanochannels have included bulk nanomachining and wafer-bonding [146][147], surface nanomachining [148], buried channel technology [149] and nanoimprint lithography [150][151][152]. Nanochannels that are 50 nm deep and 5 μm wide, 20-100 nm deep and 0.5-20 μm wide and 10 nm deep and 50 nm wide have been demonstrated. Although nanoimprint lithography can fabricate 2-dimensional nanochannels, these channels are all fabricated by complex processing methods that require sophisticated masking and etching. Thus, a means by which nanochannels are able to be fabricated without complex processing and reach to nano level in 3-dimension becomes necessary. AFM-based nanolithography [153] offers a simple and reliable technique for mechanically machining nanochannels on substrates such as polymer [154][155][156], metal [157], semiconductor [158][159][160], and insulator [161]. So, we are inspired to create nanochannels using AFM based surface nanoscratching in the inversion layer of ISFET where CNTs will be aligned to seek for improvement of the device. However, nanochannels on a bare

134

silicon substrate produced by AFM have not been reported yet. Thus, a calibration is needed for several promising AFM tips when they are used to scratch surfaces. Eventually, the AFM based nanoscratching technique will be employed to achieve the integration of CNTs and ISFET.

5.8.2 Calibration of Nanoscratching with Two Ordinary Tips

The calibration is used to specify the effect of two kinds of AFM probes when they are used to create nanochannels on Si, SiO_2 and glass surfaces. The AFM probes are Tap190DLC (BudgetSensors) and PPP-NCH (Nanosensors), both of which are recommended by the manufacturers for nanoscratching. In the experiment, the scratching is completed under the close-loop mode in order to guarantee precise control of tip position. The results can help us to judge preliminarily whether these probes are capable of creating nanochannels in the CNT-ISFET system.

As introduced previously, Tap190DLC has a 48N/m force constant and a 190 kHz resonant frequency. In general, a 48N/m probe is almost among the stiffest ones available in the current market. Two channels are made in different settings on Si, SiO_2, and glass respectively. Five measurements are taken on each channel for the width and depth. Table 5.7, where NA represents no channel, provides the parameters and measurements of the nanochannels, which tells Tap190DLC is able to create nanochannels on all the three materials (M.). However, it is inefficient, especially when scratching on the Si surface. For example, 150 times for an 11.7188 μm channel at 1.5 μm/s speed (Sp.) takes about 45 minutes and only provides a 5-nm-deep channel. Table 5.7 also proves that the setpoint (S_T) and time (T) are the two key factors that determine the depth of the channel. Figure 5.53 presents a precise control of the channel location: the real channel is right underneath the red line that shows the desired channel after scratching under the close-loop mode.

135

M.	S_T(V)	Sp.(um/s)	Time	Ave. W.(nm)	Stdev. W	Ave. D.(nm)	Stdev. D.
Si	7.5	1.5	150	233	0.632	4.94	2.88
Si	7.5	1.5	100	NA	NA	NA	NA
SiO$_2$	7.5	1.5	100	350	0	39.5	6.85
SiO$_2$	7.5	1.5	50	362	150	0.446	0.101
SiO$_2$	5	1.5	100	NA	NA	NA	NA
G	7.5	1.5	100	362	66.4	7.76	2.29
G	7.5	1.5	50	280	60.5	0.912	0.354
G	5	1.5	100	NA	NA	NA	NA

Table 5.7: Calibration Results of Tap190DLC on Si, SiO$_2$ and Glass.
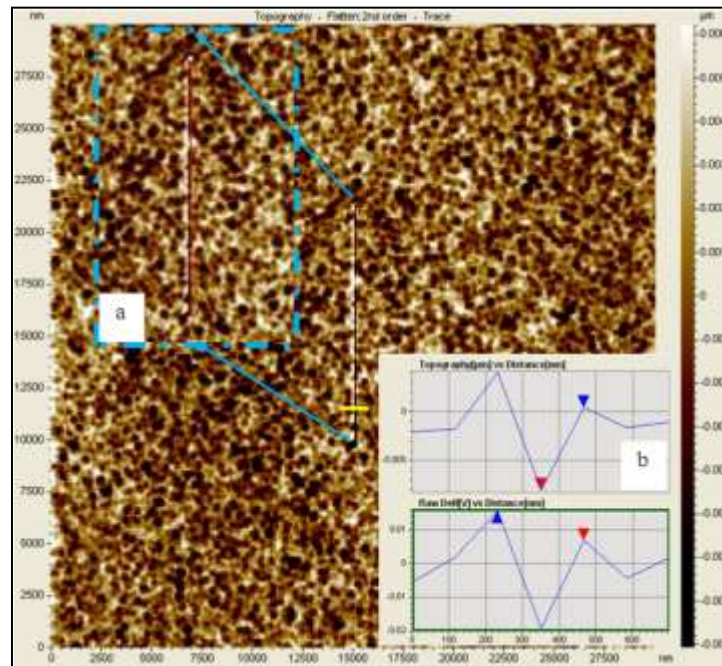
Figure 5.53: Re-image topography of a nanochannel on Si substrate (a) the real channel locally

overlaps the desired one in red and (b) channel dimension.

PPP-NCH has a lower force constant of 42 N/m, and as recorded in Table 5.8, it is unable to

create nanochannels on any of the three samples even though the setpoint is increased to 8 V.

Additionally, the glass surface heaves in the track that the tip scratches as shown in Figure 5.54.

During all the attempts with PPP-NCH, there is no channel, but the heaving phenomenon also

appears on Si substrate. Besides the force constant and the resonant frequency, another important

difference between the two tips is that Tap190DLC has a 15-nm-thick diamond-like-carbon

coating to protect the tip while PPP-NCH does not, which means scratching with PPP-NCH will leave some residuals of the tip on the surface, and scratching with Tap190DLC leaves nothing. Therefore, neither of Tap190DLC or PPP-NCH is suitable to create nanochannels on Si due to their defects including inefficiency, time consuming, unstable, and unpredictable.

M.	S_T (V)	Sp.(um/s)	Time	Ave. W.(nm)	Stdev. W	Ave. D.(nm)	Stdev. D.
Si	8	2	150	NA	NA	NA	NA
SiO$_2$	7.5	1.5	100	NA	NA	NA	NA
G	7.5	1.5	100	1576	420	-40.5	16.9

Table 5.8: Calibration Results of PPP-NCH on Si, SiO2 and Glass.
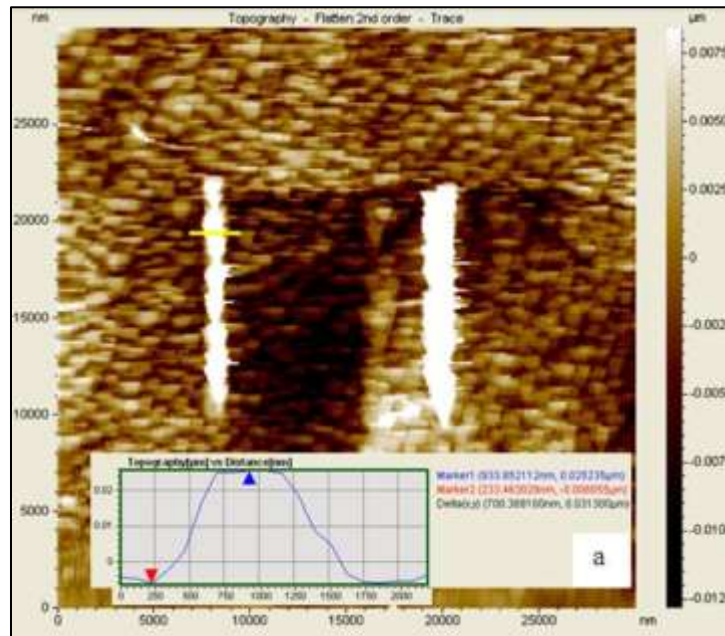
Figure 5.54: "Nanochannels" are created but above glass surface (a) channel dimension.

5.8.3   Calibration of Nanoscratching with Diamond Tip on Silicon

The experiment is performed using Agilent 5500 SPM with the Head Electronics Box that provides an oscillating voltage for AC (tapping) Mode imaging. A hand-crafted high force cantilever with a diamond tip for nanoindentation/nanoscratching is used to produce the nanochannels (DNISP, Bruker Corporation). The cantilever is pre-calibrated with a normal spring constant (K_C) of 244 N/m. The radius of the diamond tip is 40 nm. The diamond tip apex

is similar to the corner of cube so that three right angle planes form an "A"-shape apex. This is used for all nanolithography-related operations. The cantilever is made of stainless steel with a normal elastic modulus (E) of 193 GPa and a shear modulus (G) of 80 GPa. The sensitivity (S_Z) of position-sensitive-detector (PSD) is 255 nm/V.

Figure 5.55 illustrates the schematic of the experimental setup for creating nanochannels on a polished silicon layer (625-μm-thick), where we have (1) piezo scanner for XYZ movement; (2) cantilever; (3) diamond tip; (4) silicon; (5) nanochannel; (6) laser; and (7) four-quadrant PSD.. The topographies are scanned under AC Mode, while nanoscratching is completed under Contact Mode where the vertical deflection of the cantilever is kept constant and controlled by the setpoint (S_T in V). Therefore, once the setpoint is specified, the scratching normal force (F_N) can be computed as in Equation (5.8) [162].

$$F_N = K_C \times S_Z \times S_T \tag{5.8}$$
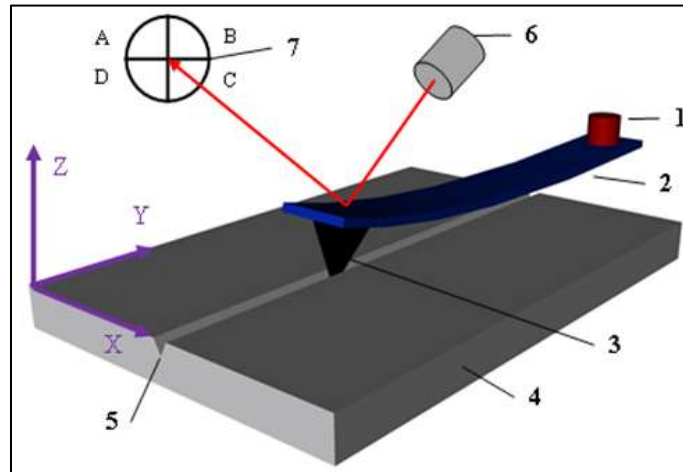
Figure 5.55: Schematic of AFM based nanoscratching.

Before scratching, three user-controllable parameters that may affect the dimensions of the nanochannels need to be determined. These parameters are the scratching velocity, the scratching normal force (the setpoint) and the number of times that the tip scratches. Through single nanomachining experiment, it is observed that the variation of scratching velocity is negligible

for predicting the dimensions. Figure 5.56 presents 25 5-µm-long nanochannels that are fabricated by single-scratch, but with different F_N from (a) to (e), at different scratching velocities from I to V. Take Figure 5.56 (a) for example: it has five channels, all of which are fabricated under $F_N = 31.11$ µN, but the scratching velocity varies from 0.1 µm/s, 0.25 µm/s, 0.5 µm/s, 0.75 µm/s and 1 µm/s for nanochannel I, II, III, IV, and V, respectively. No trends about significant dimensional changes are observed either from the vision of figure or the measurement of nanochannel dimension as the scratching velocity varies.
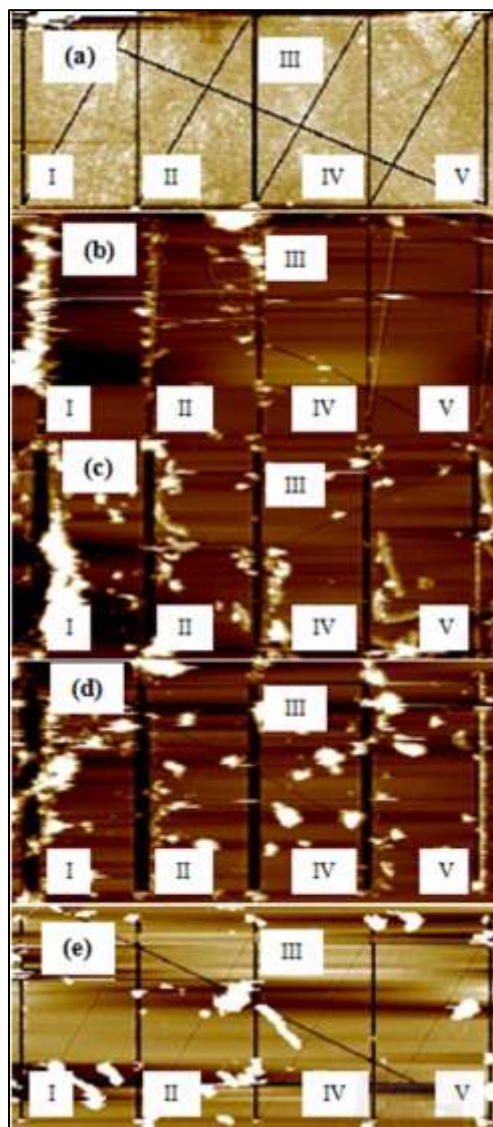
Figure 5.56: AFM topographies of nanochannels scratched at different forces and velocities.

In Figure 5.56, nanochannels in part (a), (b), (c), (d), and (e) are fabricated in different locations. However, every five nanochannels (I, II, III, IV, and V) in each part are fabricated continuously. Take part (a) for instance as shown in Figure 5.57, the AFM tip starts scratching at Point 1 with a normal force of 31.11 µN until it reaches Point 2. After this process, the normal force should return to an original value when it moves from Point 2 to 3. This normal force is caused by the setpoint used after switching from AC to Contact mode, and it has to be positive in order to maintain the contact between the tip and the sample. During scratching from Point 3 to 4, a normal force of 62.22 µN is applied. After repeating the scratching procedure, i.e., 1-2, 3-4, 5-6, 7-8, 9-10 and moving from 2-3, 4-5, 6-7,8-9, 10-1, the tip moves back to the origin position Point 1 by system default. Due to the setpoint in Contact mode, there are diagonals left when the tip moves from an end point to a start point. We also measure and analyze these diagonals and find they are much smaller than the nanochannels next to them. In addition, the reason why there are a lot of scratching residuals in the topographies is that five deep nanochannels are fabricated in 7 µm × 7 µm square and imaged immediately after the fabrication. The issues are only caused by automatically fabricating multiple nanochannels at a time. In the future application, we can fabricate single nanochannel at a time, so these issues will no longer exist. Furthermore, if multiple channels need to be fabricated simultaneously in certain application, the setpoint can be set as low as 0.1 V which will maintain the contact and lead negligible diagonal depths.
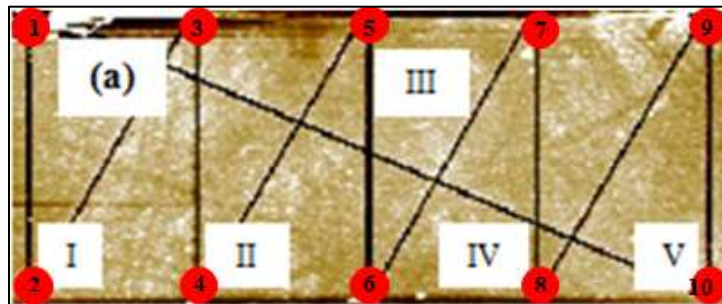
Figure 5.57: Route for continuous fabrication of five nanochannels at different settings.

In order to investigate the relationship between the dimension of nanochannels and the scratching normal force, single surface nanoscratching is implemented. In this test, the scratching velocity is kept constant at 0.1 μm/s, and five 5-μm-long nanochannels are fabricated at different normal forces of 31.11 μN, 62.22 μN, 93.33 μN, 124.44 μN and 155.55 μN. Then, five measurements for each nanochannel are recorded in Table 5.9. Figure 5.58 presents the topography for the nanochannels. Furthermore, Figure 5.59 shows how to take the dimensional measurement by drawing arbitrary cross-section line over target. Finally, the linear relationship between the depth of nanochannels and the scratching normal force for single surface nanomachining is obtained as shown in Figure 5.60.

Channel (left to right)	Force (μN)	Depth (nm)					Mean (nm)	St. Dev. (nm)
1	31.11	5.32	4.55	7.90	6.42	6.29	6.09	1.26
2	62.22	16.2	17.4	18.2	18.8	15.3	17.2	1.42
3	93.33	28.0	22.3	25.3	23.0	25.8	24.9	2.28
4	124.44	30.3	28.0	33.5	29.5	31.8	30.6	2.11
5	155.55	32.3	35.0	35.5	36.7	40.7	36.1	3.04

Table 5.9: Nanochannel depth for single nanoscratching with diamond tip on silicon.
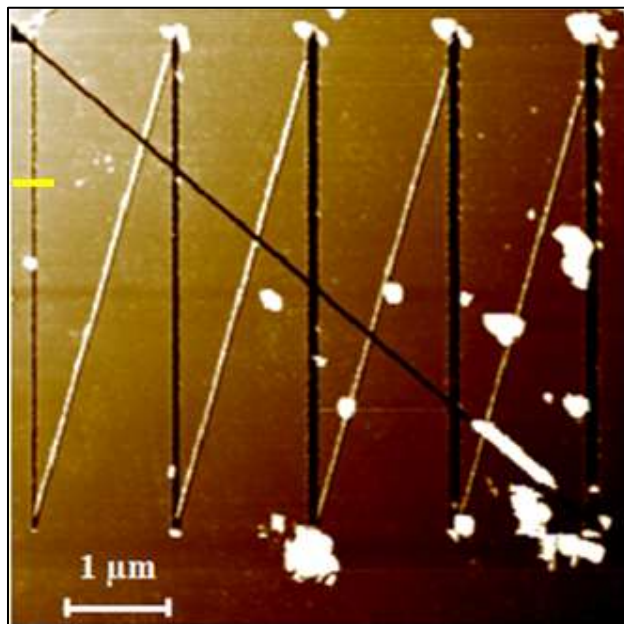
Figure 5.58: Topography of single nanoscratching at different normal forces.
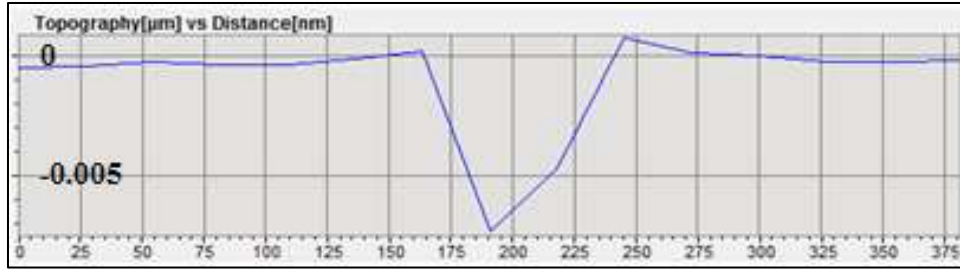
Figure 5.59: Nanochannel dimensional by the yellow cross-section line in Figure 5.58.
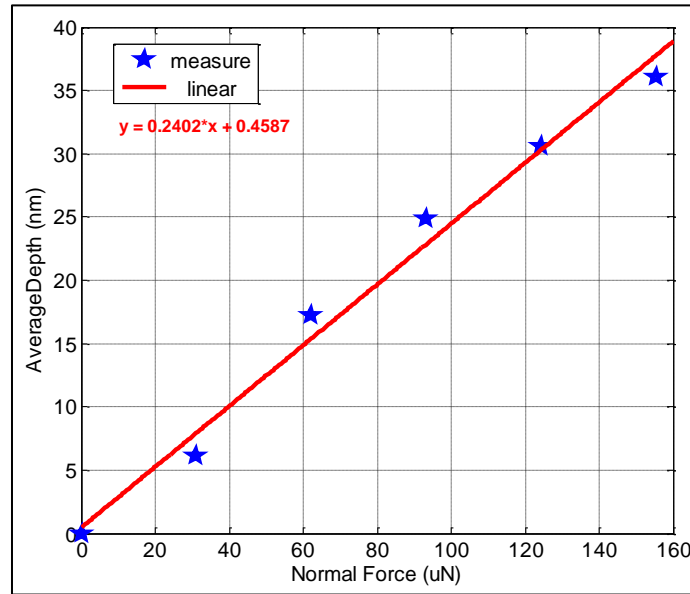
Figure 5.60: Linear relationship between depth and force for single-scratching.

Furthermore, the relationship between the depth of nanochannel and the normal force in repeatable nanoscratching is also studied. The scratching velocity is kept at 0.1 µm/s, but the surface will be scratched twice by the diamond tip to fabricate each 5-µm-long channel at different normal forces of 31.11 µN, 62.22 µN, 93.33 µN, 124.44 µN and 155.55 µN. Figure 5.61 shows the topography of the channels, and their depth information is recorded in Table 5.10. In addition, the linear relationship between the depth of nanochannels and the scratching normal force for double surface nanomachining is shown in Figure 5.62.
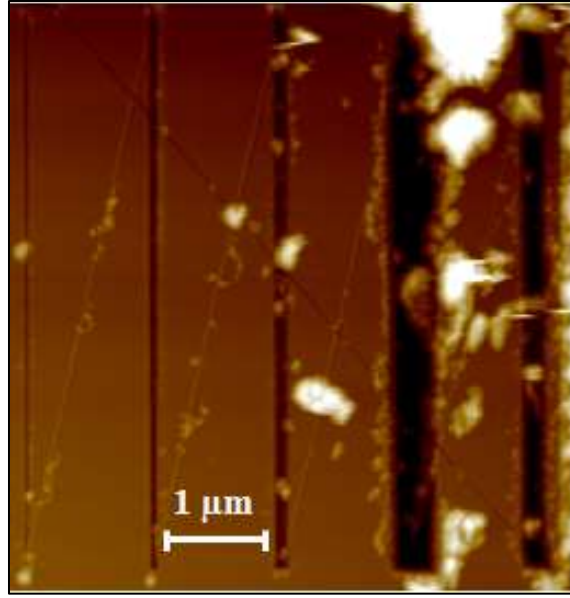
Figure 5.61: Topography of double nanoscratching at different normal forces.

Channel (left to right)	Force (µN)	Depth (nm)					Mean (nm)	St. Dev. (nm)
1	31.11	7.55	16.5	10.3	13.9	14.6	12.6	3.60
2	62.22	35.7	32.4	35.0	37.4	34.3	35.0	1.82
3	93.33	49.0	45.2	48.7	44.9	36.3	44.8	5.12
4	124.44	136	141	91.0	130	148	129	22.4
5	155.55	107	113	101	92.2	106	104	7.67

Table 5.10: Nanochannel depth for double nanoscratching with diamond tip on silicon.
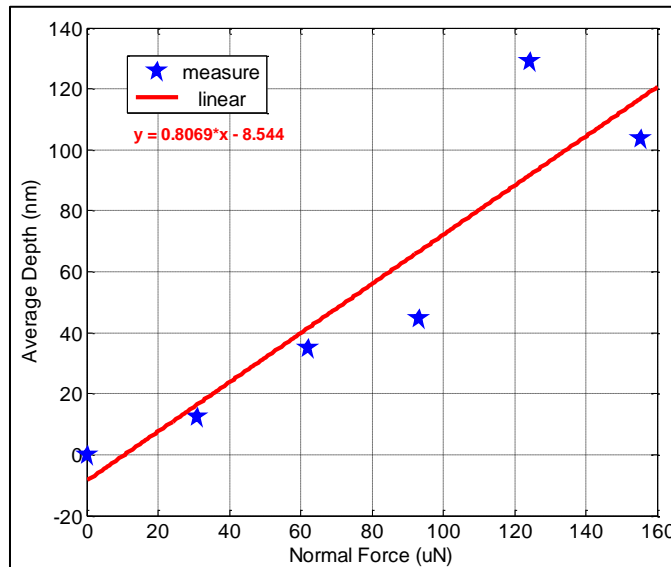
Figure 5.62: Linear relationship between depth and force for double-scratching.

143

As discussed previously, it is assumed the linear correlations between the nanochannel dimension and the normal force start at the origin (0, 0), which means a nanochannel appears no matter how small the normal force is. This assumption may not be completely precise. A more reasonable prospect is that a threshold of the normal force exists. No nanochannel can be fabricated unless the normal force exceeds this threshold, and this threshold should depend on material properties and geometry of both the surface and the AFM tip. However, the linear correlation cannot present the meaning in this level. In contrary, the linear correlation may mislead us to some confusion. Take Figure 5.60 for example, according to the linear correlation, a 0.4587-nm-deep channel will be fabricated with a normal force of zero magnitude which theoretically and physically cannot be true (a 0.9632-nanometer-deep channel would appear and the slope becomes 0.2357 according to the linear correlation obtained without the origin point). In addition, logarithmic correlations do possess a better coefficient of determination (R^2) [163][164]. Therefore, the logarithmic correlation as shown in Equation (5.9) and (5.10) is employed to represent the results on nanochannel depth and width, respectively.

$$d = \alpha_1 \ln\left(\frac{F_N}{F_{t1}}\right) \tag{5.9}$$

$$w = \alpha_2 \ln\left(\frac{F_N}{F_{t2}}\right) \tag{5.10}$$

where α_1 and α_2 are the scratching penetration depth and penetration width, respectively, and F_{t1} and F_{t2} are the threshold forces depending on the depth and width data, respectively.

Figure 5.63 shows both the linear and logarithmic correlations between the nanochannel depth and the normal force for single scratching. Hence, the scratching penetration depth is 18.421 nm, and the threshold force is 23.2992 µN. The logarithmic method possesses a better coefficient of determination (R^2) as expected. The same approach is used for the width as shown

in Figure 5.64, where the logarithmic method also has a better performance and the penetration width and the threshold force are 54.605 nm and 7.41889 µN, respectively. Figure 5.65 and Figure 5.66 illustrate the comparison between the linear and logarithmic correlations for the double-scratching, where neither of the two correlations possesses a good R^2 value. The main issue may lie in the experimental data collected from repeated scratching as the fourth channel (from left to right) in Figure 5.61 is fabricated beyond expected. The new results and data show that our experimental setup is correct and repeatable. The depth and width of the channel created with normal force of 124.44 µN are experimentally verified that they should be within the values of normal force of 93.33 µN and 155.55 µN. Also, the linear correlation possesses a higher coefficient of determination in repeatable scratching. Figure 5.67 and Figure 5.68 are one of the extra experimental results to illustrate the correlations between the channel dimensions and different normal forces with a constant scratching number of 2.
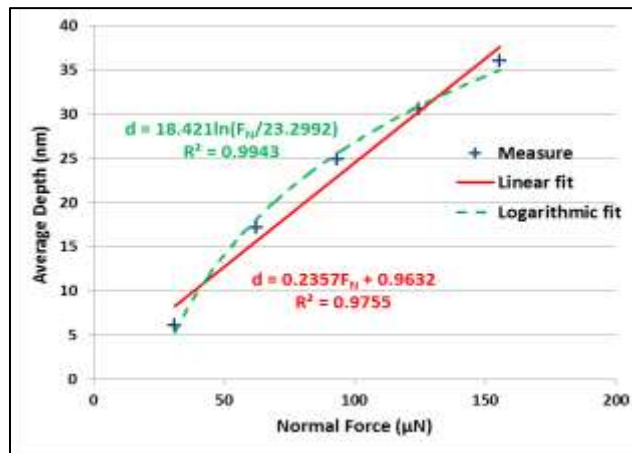
Figure 5.63: Linear and logarithmic correlations between channel depth and normal force for single scratching.
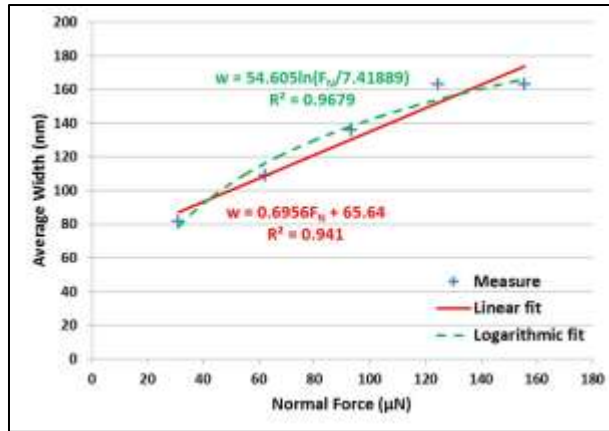
Figure 5.64: Linear and logarithmic correlations between channel width and normal force for
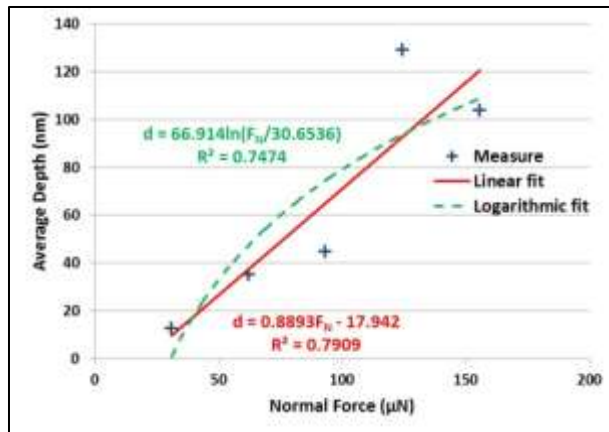
single scratching.

Figure 5.65: Linear and logarithmic correlations between channel depth and normal force for
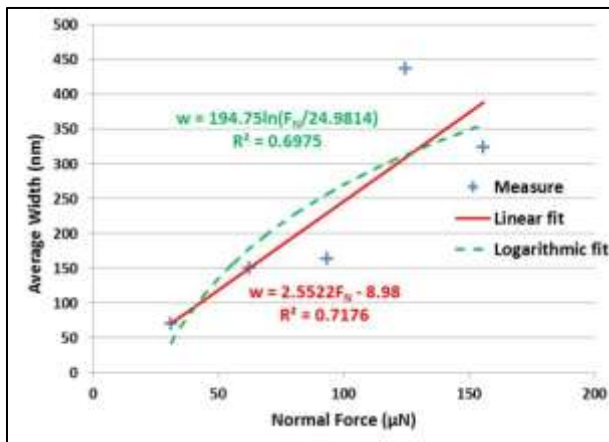
double scratching.

Figure 5.66: Linear and logarithmic correlations between channel width and normal force for
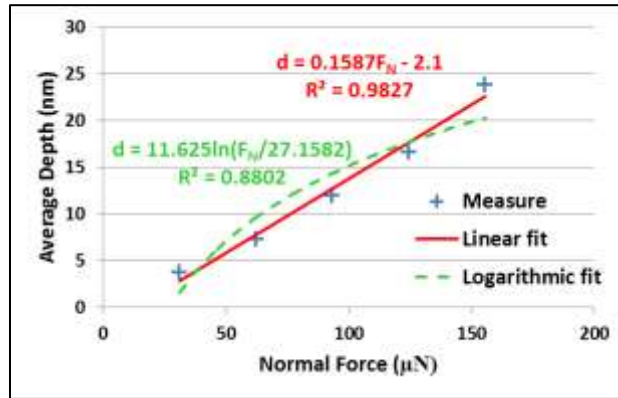
double scratching.

Figure 5.67: Additional linear and logarithmic correlations between channel depth and normal

force for double scratching.
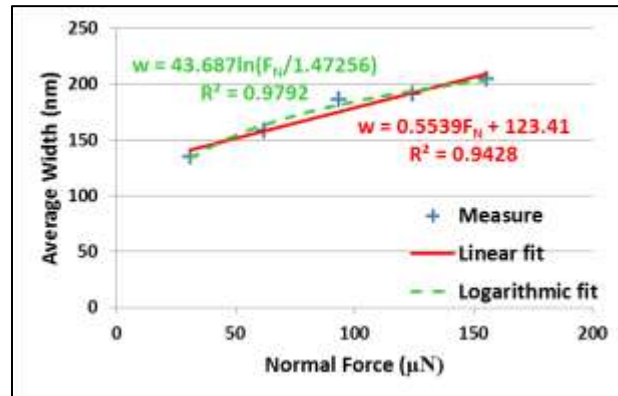
Figure 5.68: Additional linear and logarithmic correlations between channel width and normal

force for double scratching.

An experiment is conducted to conclude on the dimensional changes caused by an increasing

scratching number. Figure 5.69 (a) shows five 3 μm long nanochannels. Figure 5.69 (b) and (c)

are the height profiles. They are fabricated at constant speed (0.1 μm/s) and constant normal

force (31.11 μN) but with different scratching numbers from 1 to 5. Their mean depths are 0.837,

1.71, 2.45, 2.79 and 2.99 nm respectively, and the corresponding standard deviations are 0.141,

1.195, 0.141, 0.188, and 0.152 nm respectively. Although these five channels are still close to

each other spacing wise, they are scratched separately. Therefore, the diagonals no longer exist. As shown in Figure 5.70 and Figure 5.71, deeper and wider channels are fabricated as the scratching number is increased as expected. Additionally, the logarithmic correlation owns higher coefficient of determination especially for the depth. Furthermore, it is more logarithmic when scratching nanochannels at a constant normal force with increasing scratching number while it is more linear when scratching twice with increasing normal force.
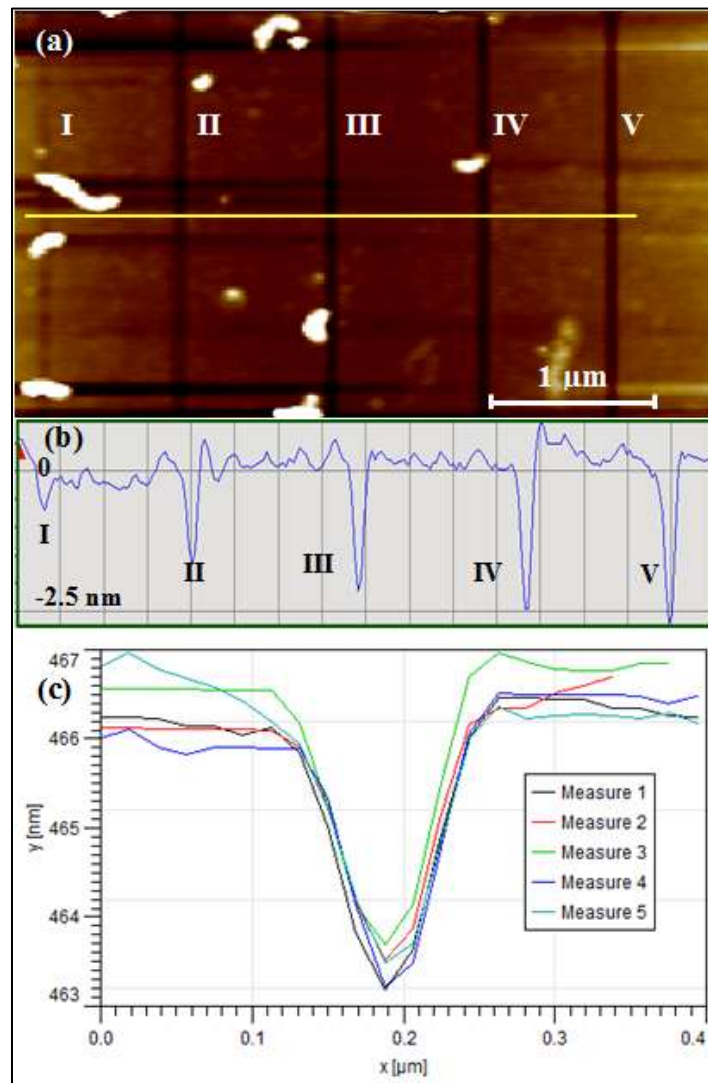
Figure 5.69: Test of varying scratching number 1-5 for channel I-V (a) topography, (b) height profile of yellow cross-section line, and (c) five height profiles of channel V.

148
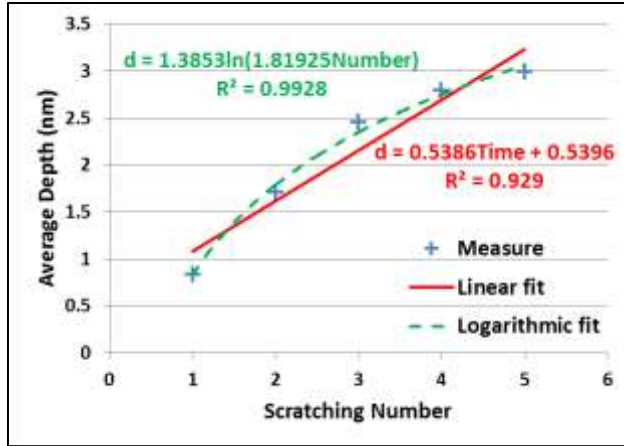
Figure 5.70: Linear and logarithmic correlations between channel depth and scratching numbers.
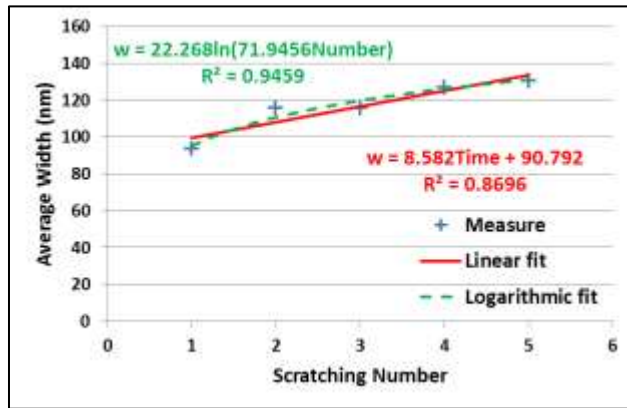
Figure 5.71: Linear and logarithmic correlations between channel width and scratching numbers.

After some careful comparison about the nanochannel depth between Figure 5.63 and Figure 5.70, Figure 5.65 and Figure 5.70, Figure 5.65 and Figure 5.67, it is obvious that the nanochannels become shallower when the results of first few nanoscratching represented in Figure 5.63 and Figure 5.65 are regarded as the reference even if the nanochannels are fabrication with the same parameter combinations. Thus, the diamond tip is imaged by SEM to examine its condition. Expectedly, the surface of the diamond tip is heavily contaminated as shown in Figure 5.72. The tip surface is covered by a layer of impurities and residuals from nanoscratching, which is supposed to be the major issue for repeatability. Besides the contamination, it has been confirmed the nanoscratching must be defined the same as in Figure

149

5.72 (a) in order to successfully fabricate nanochannels. Thus, since the diamond has to be loaded every time, a tiny geometry offset will also affect the performance of nanoscratching.
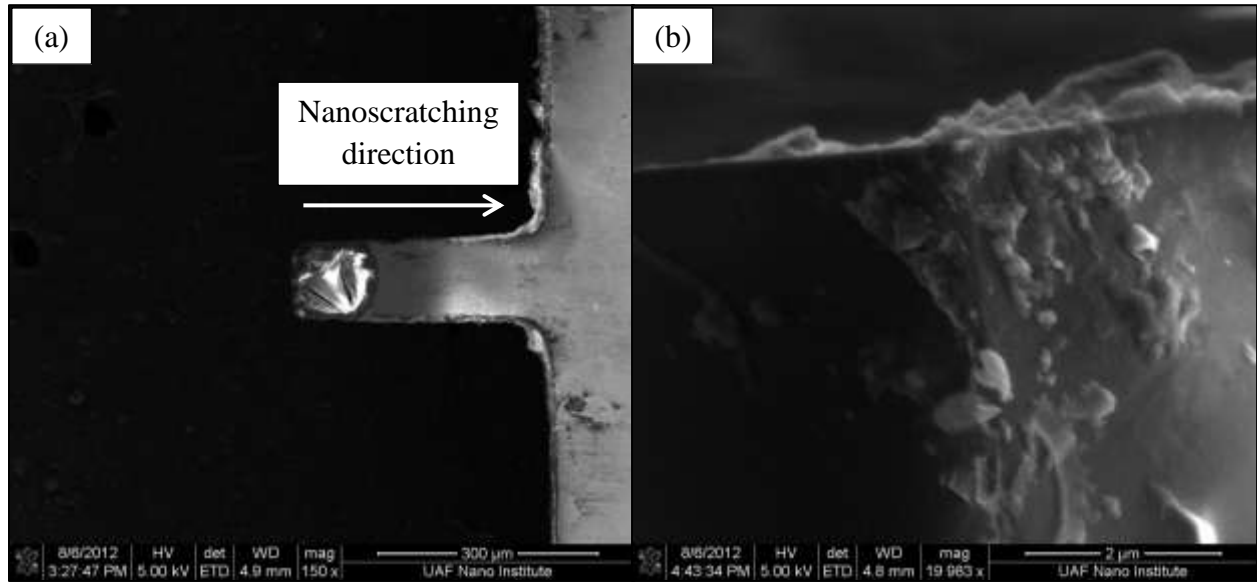
Figure 5.72: SEM images of diamond tip (a) overview and (b) zoomed-in tip.

5.9   Summary

A novel idea about CNT integrated ISFET has been proposed towards pH measurement of microliter/molecule scale solution samples. ISFET chips are fabricated in the cleanroom facility HiDEC, and the chip has been successfully used to measure the pH values of microliter level solutions. The fabrication involves major MEMS techniques including thermal oxidation, photolithography, diffusion, evaporation and lift-off. These MEMS techniques assure us that the ISFET chip is suitable for measuring tiny volume samples. Through Nernst Potential theory and proper experimental setup, the sensitivity of ISFET chip for pH testing is obtained. Some issues that may affect the sensor performance are discussed after comparing the current sensitivity to the ideal one from the Nernst mathematic model. CNT integrated ISFET is considered as a very promising solution to maintain an impressive sensitivity while scaling down sample volume. Besides MEMS fabrication techniques, other techniques and tools are involved in order to

integrate CNTs into ISFET. It is verified that CNT alignment by DEP is an effective method for connecting the source and drain in ISFET. Furthermore, the electrical property of single SWCNT and MWCNT is able to be characterized by current sensing AFM. At last, AFM based nanoscratching is proved as a simple and effective method to create nanochannels on substrates. The experimental results, especially the nanoscratching with diamond tip on silicon surface, encourage us to machine nanochannels in the inversion layer of ISFET and align CNTs inside the channel to seek for an improved performance in the future. All the experiments involved in this chapter make the feasibility of CNT integrated ISFET complete. It is believed that CNT integrated ISFET as next-generation ion concentration sensor is quite beneficial in various areas, such as engineering, biology, chemistry and medicine.

Chapter VI.   FUTURE WORK

6.1   Continuous Work on CNT-ISFET

Our ISFET has already been able to measure pH values for solution in microliter. However, although related preliminary testing has been carried to illustrate the methodology and prove the feasibility, CNT has not been integrated into ISFET to verify whether or not there is going to be any improvement. So, the first continuous work regarding CNT-ISFET is to integrate CNTs into the current ISFET chips. Those ISFET chips with triangle electrodes are designed to be used for CNTs' integration. The fourth mask (CNT), which is not involved in the previous fabrication process, will be needed. Besides testing the performance CNT-ISFET for pH sensing application, it is also very interesting and valuable to study the relation between the sensitivity and the size of ISFET. Therefore, another mask is designed as shown in Figure 6.1. In this design, there are two major types of ISFET both of which are larger than the design in **5.2.1**. One type is sized of 2 mm × 1.5 mm, and the other is sized of 12 mm × 9 mm. The corresponding fundamental gate areas are in 80 μm × 800 μm and 480 μm × 4800 μm respectively. We also make modifications to the base design, varying dimensions such as gate width, shape of metal electrodes, and gap between source and drain. The new ISFET chips sized of 2 mm × 1.5 mm are listed in Table 6.1. The wafer for these larger ISFETs is in the middle of fabrication using the same travelers as before. In the future, the Small Outline Integrated Circuit Package will be still suitable to package the new ISFET chips sized of 2 mm × 1.5 mm while the new chips of 12 mm × 9 mm can be fit into Hybrid Package Multi-Chip Module (HYB02806, Spectrum Semiconductor Materials Inc., USA). With conductive epoxy and wire bonding machine, the experiment for testing these larger ISFETs can be completed. If possible, a DC power supply with precision in 0.01/0.001 V should be employed to supply V_{ds} instead of the current one with precision in 0.1 V.

Electrode shape	Source/drain gap (μm)	Silicon dioxide gate width (μm)
Rectangular	80	80
Rectangular	40	30
		40
		50
Rectangular	60	50
		60
		70
Rectangular	70	60
		70
		80
Rectangular	80	70
		75
		85
		90
90-degree arrows (CNT)	80	70
		80
		90
	40	30
		40
		50
60-degree arrows (CNT)	80	70
		80
		90
	40	30
		40
		50
120-degree arrows (CNT)	80	70
		80
		90
	40	30
		40
		50
Flat (CNT)	80	70
		80
		90
	40	30
		40
		50

Table 6.1: Modifications made to ISFET base design (outline 2 mm × 1.5 mm).
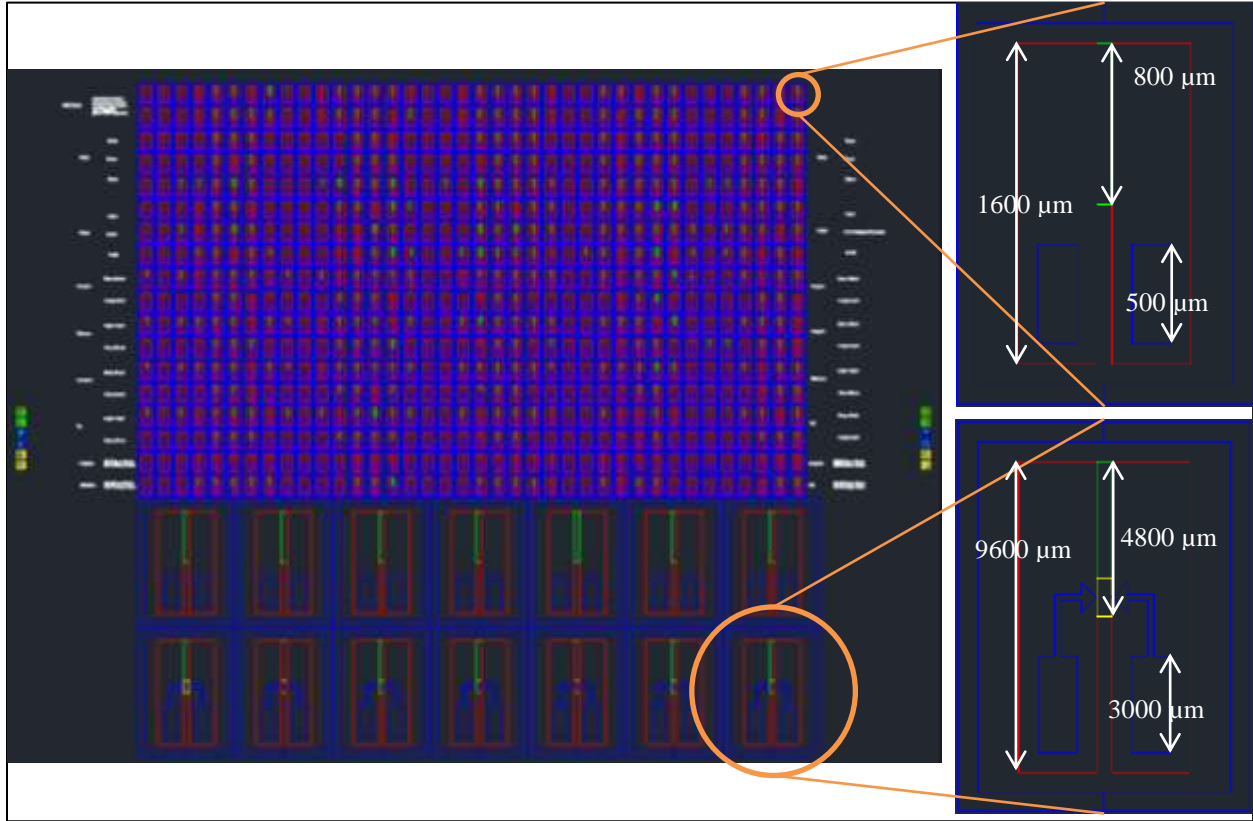
Figure 6.1: Multilayer mask design for fabricating larger ISFETs.

6.2 AFM Based Characterization and Related Application

As you have learned from the previous chapters in this dissertation, AFM is such a powerful tool that plenty of missions, which used to be impossible, are able to be carried out in order to learn and explore the nano world. Personally speaking, I enjoy very much when I work with AFM. I do believe AFM related manipulations and applications will be one of my major research interests in the future. I have accepted a job offer as a post-doctoral fellow in Notre Dame, where I will continue using AFM to characterize various nanomaterials. Right now, I am interested in the study of graphene. So far, I have obtained some encouraging preliminary results, and I would like to share it in this dissertation as the end of introducing my research work during my Ph. D.

student period. To work with AFM will never stop until the day more advanced nanotools take the place of it.

6.2.1   Nanomanipulation of Graphene by AFM

In recent years, significant attention has been paid to graphene, a monolayer structure nanomaterial, due to its excellent and unique physical, electrical and mechanical properties. The Nobel Prize in Physics 2010 was awarded jointly to Andre Geim and Konstantin Novoselov for groundbreaking experiments regarding the two-dimensional material graphene. Graphene also has shown its extraordinary performance in various nano devices. However, both theoretical and experimental studies have revealed that the electrical properties of graphene are closely related to its size, lattice orientation, geometry, and edge structures. Furthermore, graphene nanoribbons can possess metallic or semiconducting properties depending on their different edge structures (zigzag or armchair) with band gap tunable by width, which means graphene can be tailored into desired geometries and edge structures for generating expected and tunable band gaps. Therefore, an effective and reliable technique to study the structural characteristic of graphene in atom level and tailor the monolayer into desired shapes becomes necessary before properly using it in practical applications. Fortunately, we can realize all of them with AFM.

Figure 6.2 shows the graphene sample on silicon dioxide substrate. Then, the graphene sample is scanned under AC mode with a Tap300DLC AFM probe (BudgetSensors). In order to precisely tailor graphene, closed-loop is enabled all the time. Figure 6.3 shows two AFM images of graphene in an area of 1.5 nm × 1.5 nm. The AFM raw images, for example Figure 6.3 (a), are not sufficient in resolution to tell the lattice structure of the carbon atoms. Thus, the amplitude image is processed with FFT filtering technique to get rid of unnecessary period noises. As a result, the lattice structure shows up after a proper filtration. Figure 6.4 gives the corresponding

length of the lines drawn in Figure 6.3 (b) to represent the carbon-carbon bond in graphene. The mean length approximates the theoretical value 0.142 nm.
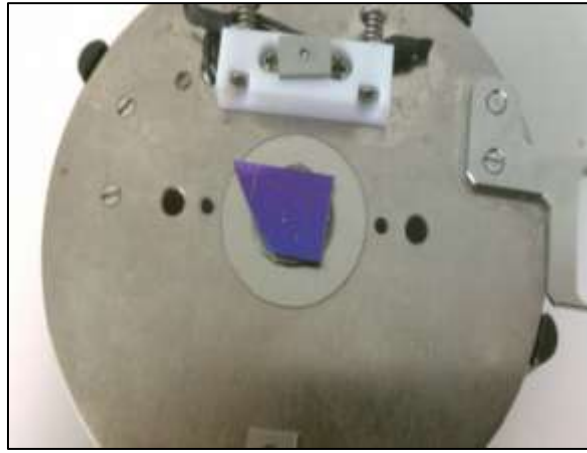
Figure 6.2: Graphene sample on silicon dioxide substrate.
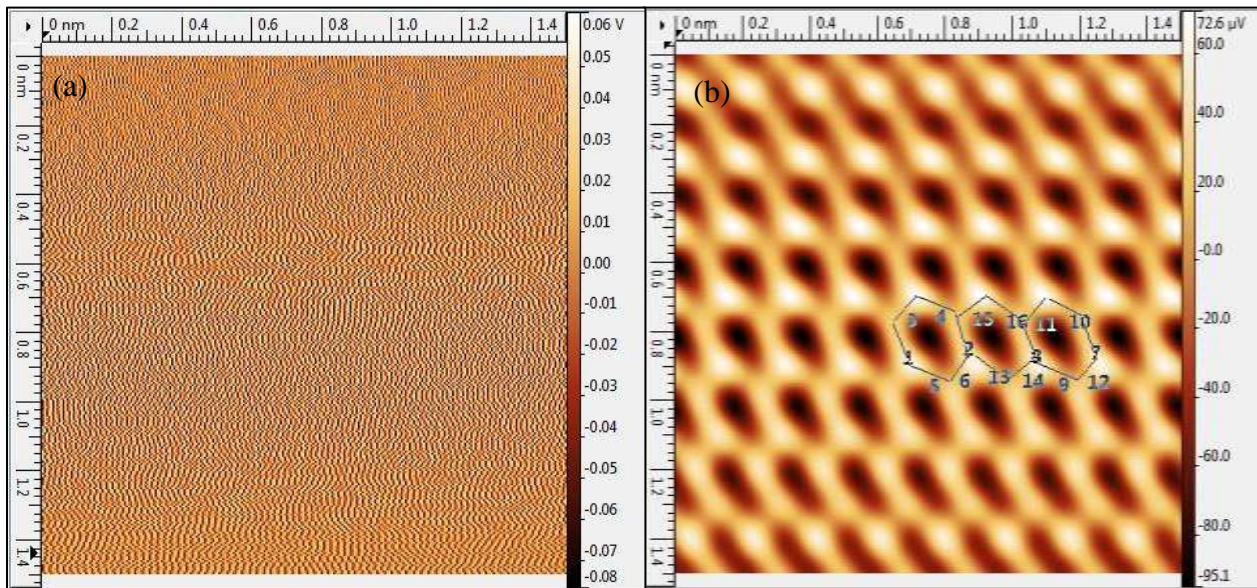
Figure 6.3: AFM images of graphene (a) amplitude and (b) FFT filtered.
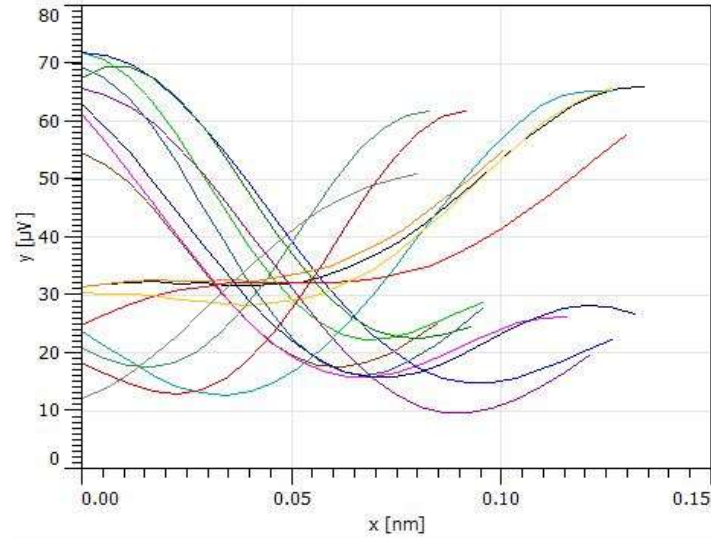
Figure 6.4: Corresponding line length of these drawn in Figure 6.3 (b).

After identifying appropriate parameters for nanoscratching on graphene with Tap300DLC tip, we are able to test the AFM lithographical capabilities by producing detailed, accurate, and clean shapes, and ultimately test the capability of tailoring graphene with this mechanical cutting method. For this, an electrode shape is drawn into the PicoLITH software Figure 6.5 (a) as an example of a possible application of this technique. With optimized parameters determined through previous tests on nanoscratching channels on graphene as shown in Figure 6.6, 2.5 μN, 7.5 μm/s, and scratching number 1 are applied to tailor the shape. The result for this test is seen in Figure 6.5 (b) verifying that it is indeed possible to produce a desired graphene shape through AFM based nanoscratching. This research also introduces some future areas of research in this field as to how thermal drift effects Z-axis positioning and varies with cutting speed. Another promising area of research for the future would be to produce a bias voltage across the graphene sample and to observe how that affects the efficiency parameters of such a mechanical cutting process. Then other methods such as electron beam or electrical force cutting methods could be explored and compared in order to identify the overall most efficient method for the tailoring and manipulation of graphene monolayers.
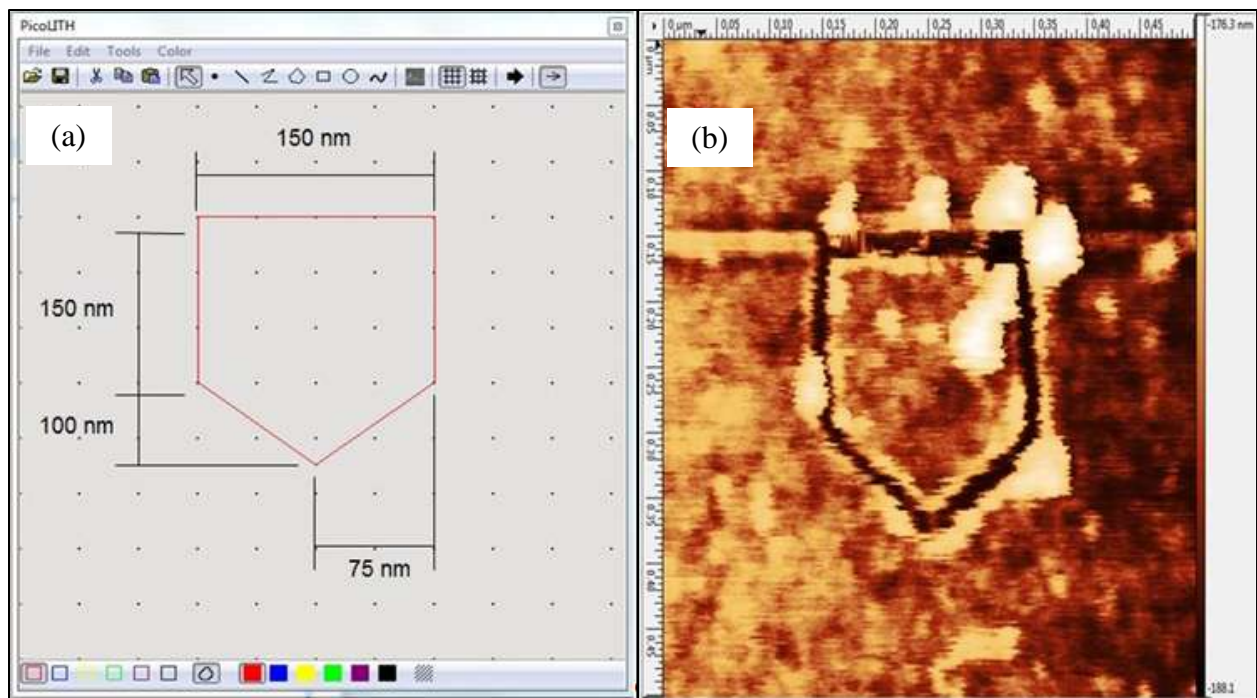
Figure 6.5: Tailor graphene to a desired shape (a) design and (b) result.
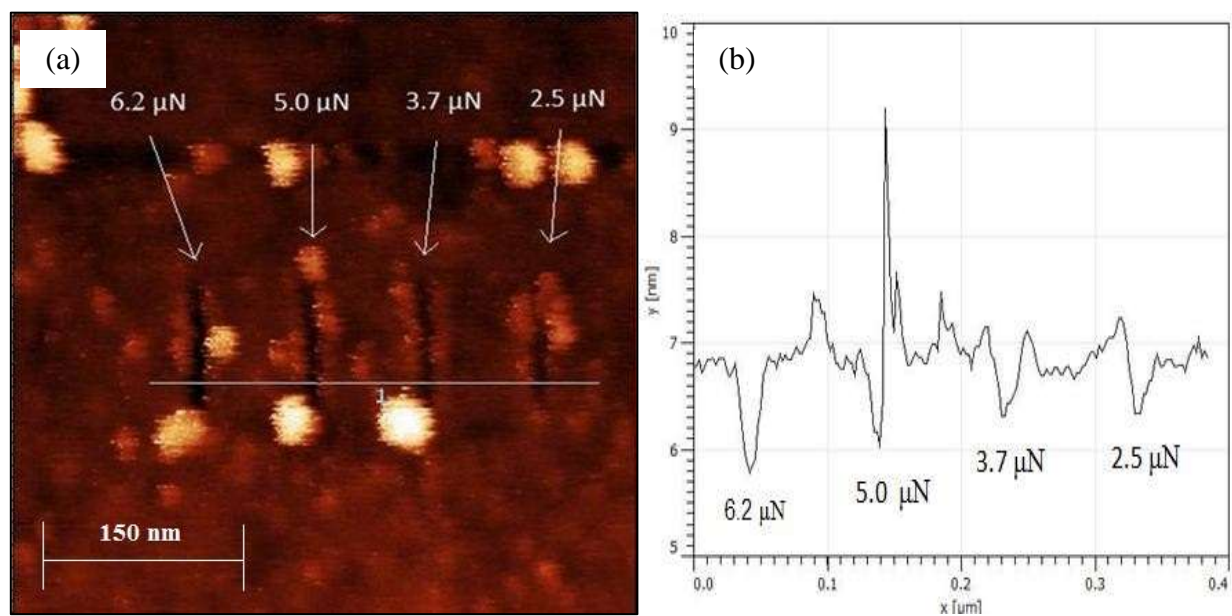
Figure 6.6: Nanoscratching on graphene (a) channels under different forces and (b) depth profile.

Chapter VII.   CONCLUSION

As introduced above, the goals of my research work involved in this dissertation include two major categories. One is to characterize nano or bio samples, and the other is to design, fabricate and test CNT integrated ISFET as the next generation pH sensor. The characterization results are important for studying related physical properties and quality control purpose, and the next generation pH sensor will be served for microliter or molecule level targets. As a matter of fact, the two researches are not completely independent to each other but closely connected through some nano technologies. For example, AFM is employed in both playing an important role. This phenomenon is not a coincidence but it is something inevitable as we have already entered the era of nanosystems. Fortunately, my research work has achieved its aims through the steps that I took during the research process.

Dimensional characterization of VACNF is a good example to present how to characterize nano samples in size using AFM. The characteristics of VACNFs, especially their height and density, determine the sensitivity of devices for which VACNFs work as the sensing elements. The experimental results not only verified the growth of these fibers but also provided us with accurate information in the level of 0.1 nm on the height and diameter. Furthermore, statistical analysis on the measurement made the results more complete and reliable.

AFM based nanoindentation is also an important technique to study mechanical properties of the materials/samples which are impossible to be tested unless the manipulation is precise-controlled in nanometer scale. The theory and a proper mathematical model for AFM based nanoindentation were introduced and applied to solve some practical issues. The behaviors of VACNFs in dimension and mechanical properties at subzero temperatures were observed. The Young's Moduli of VACNFs at different temperatures between -70 °C and 25 °C were

calculated by nanoindenting VACNFs after temperature treatment in a test chamber. We need to understand these behaviors within this temperature range before VACNFs are involved in any outer space missions.

Additionally, the Young's Modulus of soft tissue scaffold was also studied. The changes of Young's moduli were investigated when the scaffolds were made or treated differently. The Young's Moduli of scaffolds were obtained when they were in different combinations of ingredients and cell cultured. Mice heart and pancreas tissues were nanoindented as control to validate the experiment. Furthermore, the Young's Moduli of protein microbubbles in different sizes were estimated as their quality control process. Besides nanoindentation, the immobilization of microbubbles in liquid was the key to the success as clear AFM imaging of microbubbles was precondition of nanoindentation. Thus, the Young's Moduli of 1-µm-diameter and 3-µm-diameter bubbles were known by nanoindenting sufficient microbubbles. Hence, applications of the scaffolds for replacing human damaged tissues and the microbubbles for ultrasound imaging diagnose and drug delivery are able to be correctly realized only after their mechanical properties are known.

MEMS fabrication techniques and cleanroom facilities were employed to fabricate ISFET chips towards ion concentration sensing applications of extremely tiny solutions. Major steps during the fabrication process included multilayer mask design, oxidation, photolithography, diffusion and evaporation. With a proper packaging method, an ISFET chip was used to measure the pH values for 2.5 µL solutions in the range of pH 4 to 10, and the sensitivity was 10.7 mV/pH. Nernst Potential was adopted for mathematical modeling and result analysis. Promising strategies were proposed to improve the performance. Furthermore, related preliminary tests were completed to confirm the feasibility regarding integrating CNTs into the current ISFET

structure. When MEMS and CNT related nanotechnologies can be combined properly, the next generation product for ion concentration measurement will be available. It will be of great value and potential in various fields, such as biology, chemistry, medical and industry, as the new ion concentration sensor will be able sense samples in micron liter or molecule scale while maintain a high sensitivity. At the same, the mature MEMS technologies still guarantee low cost, massive productive, reliability, and repeatability.

In the future, I would like to continue developing CNT integrated ISFET. It is quite interesting to see how a CNT-ISFET would perform as a pH sensor for microliter scale solutions. Besides CNT, I am also willing to figure how the dimensions of ISFET affect its performance. I am currently fabricating larger ISFETs, which is almost done and would be used to measure relatively larger solution samples. Others will take over from here in the near future. On the other hand, I will focus on AFM based characterization and manipulation in my next research period. Most of the research results involved in this dissertation have been shared with others through publications and presentations. Hopefully, what I described could enlighten others in similar areas and we might keep contributing our own strength into the beloved micro/nano world.

REFERENCES

[1]   G. Binnig and H. Rohrer, "Scanning tunneling microscopy", *IBM Journal of Research and Development,* (1986) **30**:4.

[2]   S. Iijima, "Direct observation of the tetrahedral bonding in graphitized carbon black by high resolution electron microscopy", *Journal of Crystal Growth,* (1980) **50** (3), 675.

[3]   Mihail C. Roco, "Nanotechnology's future", *Sci. Am.,* (2006) **295**(2):21.

[4]   National Research Council and Committee on Indicators for Waterborne Pathogens, 2004. *Indicators for Waterborne Pathogens.* National Academies Press, Washington, DC.

[5]   K. Dill, D. D. Montgomery, A. L. Ghindilis, K. R. Schwarzkopf, S. R. Ragsdale and A. V. Oleinikov, "Immunoassays based on electrochemical detection using microelectrode arrays : Microarrays for Biodefense and Environmental Applications" *Biosens. Bioelectron.,* **20** (2004) 736-742.

[6]   O. Niwa and H. Tabei, "Voltammetric Measurements of Reversible and Quasi-Reversible Redox Species Using Carbon Film Based Interdigitated Array Microelectrode", *Anal. Chem.* **66** (2) (1994) 285-289.

[7]   J. Li, J. Koehne, A. M. Cassell, H. Chen, Q. Ye, H. T. Ng, J. Han and M. Meyyappan, "Miniaturized Multiplex Label-Free Electronic Chip for Rapid Nucleic Acid Analysis Based on Carbon Nanotube Nanoelectrode Arrays", *J. Mater. Chem.,* **14** (2004a) 676-684.

[8]   J. Li, J. Koehne, A. M. Cassell, H. Chen, Q. Ye, H. T. Ng, J. Han and M. Meyyappan, "Bio-Nano Fusion in Sensor and Device Development", *MCB 1* (1) (2004b) 69-80.

[9]   M. A. Guillorn, T. E. McKnight, A. Melechko, V. I. Merkulov, P. F. Britt, D. W. Austin, D. H. Lowndes and M. L. Simpson, "Individually Addressable Vertically Aligned Carbon Nanofiber Based Electrochemical Probes", *J. Appl. Phys.,* **91** (6) (2002) 3824-3828.

[10]   P. He and L. Dai, "Aligned Carbon Nanotube-DNA electrochemical Sensors", *Chem. Commun.,* (2004) 348-349.

[11]   Y. H. Yun, V. Shanov, M. J. Schulz, Z. Dong, A. Jazieh, W. R. Heineman, H. B. Halsall, D. K. Y. Wong, A. Bange, Y. Tuf and S. Subramaniam, "High Sensitivity Carbon Nanotube Tower Electrodes", *Sensors and Actuators B,* **120** (2006) 298-304.

[12]   P. V. Gerwen, W. Laureyn, W. Laureys, G. Huyberechts, M. O. D. Beeck, K. Baert, J. Suls, W. Sansen, P. Jacobs, L. Hermans and R. Mertens, "Nanoscaled Interdigitated Electrode Arrays for Biochemical Sensors", *Sensors and Actuators B,* **49** (1998) 73-80.

[13]   F. Patolsky, G. Zheng and C. M. Lieber, "Fabrication of Silicon Nanowire Devices for Ultrasensitive, Label-Free, Real-Time Detection of Biological and Chemical Species", *Nat. Protocols 1*, (2006) 1711-1724.

[14]   N. Yang, H. Uetsuka, E. Osawa and C. E. Nebel, "Vertically Aligned Diamond Nanowires for DNA Sensing", *Angew. Chem. Int. Ed.,* **47** (2008) 5183-5185.

[15]   J. Li and M. Meyyappan, *Carbon Nanotubes: Science and Applications,* 2004. CRC Press, Boca Raton, FL.

[16]   A. V. Melechko, V. I. Merkulov, T. E. McKnight, M. A. Guillorn, K. L. Klein, D. H. Lowndes and M. L. Simpson, 2003. "Large-Scale Synthesis of Arrays of High-Aspect-Ratio Rigid Vertically Aligned Carbon Nanofibers". *Nanotechnology,* **14** (2003) 1029-1035.

[17]   Prabhu U. Arumugam, Hua Chen, Shabnam Siddiqui, Jarret A. P. Weinrich, Ayodeji Jejelowo, Jun Li and M. Meyyappan, "Wafer-Scale Fabrication of Patterned Carbon Nanofiber Nanoelectrode Arrays: A Route for Development of Multiplexed, Ultrasensitive Disposable Biosensors", *Biosensors and Bioelectronics,* **24** (2009) 2818-2824.

[18]   E. Katz and I. Willner, "Biomolecule-Functionalized Carbon Nanotubes: Applications in Nanobioelectronics," *Chem. Phys. Chem.,* **5** (2004) 1084-1104.

[19]   A. Javey, J. Guo, Q. Wang, M. Lundstrom and H. Dai, "Ballistic Carbon Nanotube Field-Effect Transistors," *Letters to Nature,* **424** (2003) 654-657.

[20]   J. Clendenin, J. Kim, and S. Tung, "An aligned Carbon Nanotube Biosensor for DNA Detection." *Proceedings of the 2nd IEEE International Conference on Nano/Micro Engineering and Molecular Systems (NEMS)*, Jan. 16-19, 2007, Bangkok, Thailand.

[21]   L. Dong, A. Subramanian, B. Nelson, "Carbon nanotube for nano robotics," *Nano today*, Vol. 2 No. 6, December 2007.

[22]   K. Lai, N. Xi, U. Wejinya, Y. Shen, and W. J. Li, "Automated Robotic Deposition for Manufacturing Nano Devices," *Proceedings of the 2007 IEEE/RSJ International Conference on Intelligent Robots and Systems.* San Diego, CA, USA. 29 October – 2 November 2007.

[23]   H. B. Li and R. Bashir, "Dielectrophoretic separation and manipulation of live and heat-treated cells of Listeria onmicrofabricated devices with interdigitated electrodes," *Sensor Actuat. B –Chem.,* **86** (2002) 215-21.

[24]   R. Pethig, Y. Huang, X. B. Wang, and J. P. H. Burt, "Positive and negative dielectrophoretic collection of colloidal particles using interdigitated castellated microelectrodes," *J. Phys. D: Appl. Phys.,* **25** (1992) 881-8.

163

[25] D. F. Chen, H. Du, H. Q. Gong and W. H. Li, "A 3-D Microelectrode System for Dielectrophoretic Manipulation of Microparticles". *Journal of Physics: Conference Series,* **34** (2006) 1008-1013.

[26] Hywel Morgen and Nicolas G. Green, *AC Electrokinetics: colloids and nanoparticles.* Research Studies Press Ltd., Baldock, Hertfordshire, England, 2002.

[27] Anthony C. Fischer-Cripps, Nanoindentation, Second Edition, Mechanical Engineering Series, 2004.

[28] E.S. Berkovich, "Three-Faceted Diamond Pyramid for Studying Microhardness by Indentation," *Zavodskaya Laboratoria*, **13** 3 (1950) 345-347.

[29] M.M. Khrushchov & E.S. Berkovich, "Methods of Determining the Hardness of Very Hard Materials: The Hardness of Diamond," *Industrial Diamond Review,* **11** (1951) 42-49.

[30] W.C. Oliver and G.M. Pharr. "Measurement of hardness and elastic modulus by instrumented indentation: Advances in understanding and refinements to methodology." *J. Mater. Res.,* **19** (2004) 3.

[31] G. Binnig and H. Rohrer, "Scanning Tunneling Microscopy", *Surface Science,* **126** (1983) 236-244.

[32] G. Binnig, C. F. Quate and Ch. Gerber, "Atomic Force Microscope," *Physical Review Letters,* **56** (1986) 930-933.

[33] D. Tabor, The hardness of metals. Oxford: Oxford Univ. Press, 1951.

[34] B. Bhushan, Handbook of micro/nanotribology. 2nd Edition. Boca Raton (FL): CRC Press, 1999.

[35] D. Tabor, "Indentation hardness: fifty years on a personal view." *Philos Mag A,* **74** (1996) 1207-21.

[36] J. B. Pethica, R. Hutchings, and W. C. Oliver, "Hardness measurement at penetration depths as small as 20 nm." *Philos Mag A,* **48** (1983) 593-606.

[37] W. C. Oliver and G. M. Pharr, "An improved technique for determining hardness and elastic-modulus using load and displacement sensing indentation experiments." *J Mater Res,* **7** (1992) 1564-83.

[38] G. M. Pharr, "Measurement of mechanical properties by ultra-low load indentation." *Mater Sci Eng A,* **253** (1998) 151-9.

[39] S. I. Bulychev, V. P. Alekhin, M. Kh. Shorshorov, A. P. Ternovskii, and G. D. Shnyrev, "Determining Young's modulus from the indenter penetration diagram." *Zavod Lab,* **41** (1975) 1137-40.

[40] B. Bhushan, A. V. Kulkarni, W. Bonin, and J. T. Wyrobek, "Nanoindentation and picoindentation measurements using a capacitive transducer system in atomic force microscopy." *Philos Mag A,* **74** (1996) 1117-28.

[41] B. Bhushan, "Chemical, mechanical and tribological characterization of ultra-thin and hard amorphous carbon coating as thin as 3.5 nm: recent developments." *Diamond Relat Mater,* **8** (1999) 1985-2015.

[42] B. Bhushan, Mechanics and reliability of flexible magnetic media. 2nd ed., New York, Springer-Verlag, 2000.

[43] X. Li, D. Diao and B Bhushan, "Fracture mechanisms of thin amorphous carbon films in nanoindentation." *Acta Mater,* **45** (1997) 4453-61.

[44] X. Li and B. Bhushan, "Measurement of fracture toughness of ultra-thin amorphous carbon films." *Thin Solid Films,* **315** (1998) 214-21.

[45] X. Li and B. Bhushan, "Evaluation of fracture toughness of ultra-thin amorphous carbon coatings deposited by different deposition techniques." *Thin Solid Films,* **355-356** (1999) 330-6.

[46] B. Bhushan, B. K. Gupta, and M. H. Azarian, "Nanoindentation, microscratch, friction and wear studies of coatings for contact recording applications." *Wear,* **181-183** (1995) 743-58.

[47] B. Bhushan and X. Li, "Micromechanical and tribological characterization of doped single-crystal silicon and polysilicon films for microelectromechanical systems devices." *J Mater Res,* **12** (1997) 54-63.

[48] B. Bhushan, G. Theunissen and X. Li, "Tribological studies of chromium oxide films for magnetic recording applications." *Thin Solid Films,* **311** (1997) 67-80.

[49] X. Li and B. Bhushan, "Micromechanical and tribological characterization of hard amorphous carbon coatings as thin as 5 nm for magnetic recording heads." *Wear,* **220** (1998) 51-8.

[50] X. Li and B. Bhushan, "Micro/nanomechanical and tribological characterization of ultra-thin amorphous carbon coatings." *J Mater Res,* **14** (1999) 2328-37.

[51] X. Li and B. Bhushan, "Mechanical and tribological studies of ultra-thin hard carbon overcoats for magnetic recording heads." *Z Metallkd,* **90** (1999) 820-30.

[52]   X. Li and B. Bhushan, "Micro/nanomechanical characterization of ceramic films for microdevices." *Thin Solid Films,* **340** (1999) 210-7.

[53]   M. R. VanLandingham, S. H. McKnight, G. R. Palmese, R. F. Eduljee, J. W. Gillespie and Jr. R. L. McCulough, "Relating elastic modulus to indentation response using atomic force microscopy." *Journal of Materials Science Letters,* **16** (1997) 117-119.

[54]   Jan Domke and Manfred Radmacher, "Measuring the elastic properties of thin polymer films with the atomic force microscope." *Langmuir,* **14** (1998) 3320-3325.

[55]   W. Richard Bowen, Robert W. Lovitt and Chris J. Wright, "Application of atomic force microscopy to the study of micromechanical properties of biological materials." *Biotechnology Letters,* **22** (2000) 893-903.

[56]   Anshu B. Mathur, Amy M. Collinsworth, William M. Reichert, William E. Kraus and George A. Truskey, "Endothelial, cardiac muscle and skeletal muscle exhibit different viscous and elastic properties as determined by atomic force microscopy." *Journal of Biomechanics,* **34** (2001) 1545-1553.

[57]   Martin Stolz, Roberto Raiteri, A. U. Daniels, Mark R. VanLandingham and Werner Baschong, "Dynamic Elastic Modulus of Porcine Articular Cartilage Determined at Two Different Levels of Tissue Organization by Indentation-Type Atomic Force Microscopy." *Biophysical Journal,* **86** (2004) 3269-3283.

[58]   Marco P. E. Wenger, Laurent Bozec, Michael A. Horton and Patrick Mesquida, "Mechanical Properties of Collagen Fibrils." *Biophysical Journal,* **93** (2007) 1255-1263.

[59]   Laurel Ng, Han-Hwa Hung, Alexander Sprunt, Susan Chubinskaya, Christine Ortiz and Alan Grodzinsky, "Nanomechanical properties of individual chondrocytes and their developing growth factor-stimulated pericellular matrix." *Journal of Biomechanics,* **40** (2007) 1011-1023.

[60]   D. V. Lebedev, A. P. Chuklanov, A. A. Bukharaev and O. S. Druzhinina, "Measuring Young's Modulus of Biological Objects in a Liquid Medium Using an Atomic Force Microscope with a Special Probe." *Technical Physics Letters,* **35** (4) (2009) 371-374.

[61]   Zhao Gang, Qin Qi, Cui Jing and Chunyou Wang, "Measuring Microenvironment Mechanical Stress of Rat Liver During Diethylnitrosamine Induced Hepatocarcinogenesis by Atomic Force Microscope." *Microscopy Research and Technique,* **72** (2009) 672-678.

[62]   BoBae Lee, Lin Han, Eliot H. Frank, Susan Chubinskaya, Christine Ortiz and Alan J. Grodzinsky, "Dynamic mechanical properties of the tissue-engineered matrix associated with individual chondrocytes." *Journal of Biomechanics,* **43** (2010) 469-476.

[63]   H. W. Kroto, J. R. Heath, S. C. O'Brien, R. F. Curl and R. E. Smalley, "C_{60}: Buckminsterfullerene", *Nature,* **318**, 162 (1985).

166

[64]   J. Baggott, Perfect symmetry: the accidental discovery of buckminsterfullerene. Oxford University Press, 1994.

[65]   H. Aldersey-Williams, The most beautiful molecule. Aurum Press, London, 1995.

[66]   H. W. Kroto, "Symmetry, space, stars and C_{60}" (Nobel lecture), *Rev. Mod. Phys.,* **69** (1997) 703.

[67]   R. E. Smalley, "Discovering the fullerenes" (Nobel lecture), *Rev. Mod. Phys.,* **69** (1997) 723.

[68]   S. Iijima, "Helical microtubules of graphitic carbon", *Nature,* **354** (1991) 56.

[69]   S. Iijima and T. Ichihashi, "Single-shell carbon nanotubes of 1-nm diameter", *Nature,* **363** (1993) 603.

[70]   D. S. Bethune, C. H. Kiang, M. S. de Vries, G. Gorman, R. Savoy, J. Vasquez and R. Beyers, "Cobalt-catalysed growth of carbon nanotubes with single-atomic-layer walls", *Nature,* **363** (1993) 605.

[71]   M. Ge and K. Sattler, "Scanning tunneling microscopy of single-shell nanotubes of carbon", *Appl. Phys. Lett.,* **65** (1994) 2284.

[72]   Steve Tung, Husein Rokadia and Wen J. Li, "A Micro Shear Stress Sensor Based on Laterally Aligned Carbon Nanotubes", *Sensors and Actuators A: Physical,* **133** (2007) 431-438.

[73]   Mandy L. Y. Sin, Gary C. T. Chow, Gary M. K. Wong, Wen J. Li, Philip H. W. Leong and Ka Wai Wong, "Ultra-Low-Power Alcohol Vapor Sensors using Chemically Functionalized Multi-Walled Carbon Nanotubes", *IEEE Transactions on Nanotechnology,* May 01, 2007.

[74]   Peng Xiao, Wen J. Li and Ruxu Du, "Microbubble Generation Using Carbon Nanotubes Heating Elements", *IEEE Transactions on Nanotechnology,* **10** (3) (2011) 520-527.

[75]   Mengxing Ouyang, Yu Zhang and Wen J. Li, "Investigation on Optimizing Performance of Conductance-Based CNTs Chemical Sensors", *IEEE Nanotechnology Materials and Devices Conference (IEEE-NMDC),* October 12-15, 2010.

[76]   F. Kreupl, et al., "Carbon Nanotubes in Interconnect Applications", *Microelectronic Engineering,* **64** (99) (2002) 399-408.

[77]   J. Li, et al., "Bottom-up Approach for Carbon Nanotube Interconnects", *Applied Physics Letters,* **82** (15) (2003) 2491-2493.

[78]   S. Wind, J. Appenzeller and P. Avouris, "Lateral scaling in CNT field effect transistors", *Phys. Rev. Lett.,* **91** (2003) 058 301-1-058 301-4.

[79]   S. Hasan, S. Salahuddin, M. Vaidyanathan and M. A. Alam, "High-Frequency Performance Projections for Ballistic Carbon-Nanotube Transistors", *IEEE Transactions on Nanotechnology,* **5** (1) (2006) 14-22.

[80]   S. J. Wind, J. Appenzeller, R. Martel, V. Derycke and P. Avouris, "Vertical scaling of carbon nanotube field effect transistors using top gate electrodes", *Applied Physics Letters,* **80** (20) (2002) 3817-3819.

[81]   D. Kahng and M. M. Atalla, "Silicon-Silicon Dioxide Field Induced Surface Devices,"*IRE-AIEE Solid-State Device Res. Conf.,* Carnegie Inst. Of Tech., Pittsburgh, PA, 1960.

[82]   E. H. Snow, B. E. Deal, A. S. Grove and C. T. Sah, "Ion Transport Phenomena in Insulating Films Using the MOS Structure," *J. Appl. Phys.,* **36** (1965) 1664.

[83]   D. R. Kerr, J. S. Logan, P. J. Burkhardt and W. A. Pliskin, "Stabilization of SiO_2Passivated Layers with P_2O_5," *IBM J. Res. Develop.,* **8** (1964) 376.

[84]   J. B. Balk, "Effects of Hydrogen Annealing on Silicon Surfaces," *Electrochem. Soc. Meeting,* San Francisco, CA, 1965.

[85]   J. C. Sarace, R. E. Kerwin, D. L. Klein and R. Edwards, "Metal-Nitride-Silicon Field Effect Transistors with Self-Aligned Gates," *Solid-State Electron.,* **11** (1968) 653.

[86]   P. Bergveld, "ISFET, Theory and Practice," *IEEE Sensor Conference,* pp. 26, Toronto, Oct. 2003.

[87]   P. Bergveld, "Thirty years of ISFETOLOGY What happened in the past 30 years and what may happen in the next 30 years," *Sensors and Actuators B,* **88** (2003) 1-20.

[88]   S. C. Chen, Yan-Kuin Su and J. S. Tzeng, "The fabrication and characterization of ion-sensitive field effect transistors with a silicon dioxide gate," *J. Phys. D: Appl. Phys.,* **19** (1986) 1951-1956.

[89]   URL: http://www.microsens.ch/products/pdf/MSFET_datasheet%20.pdf

[90]   David Freedman, Robert Pisani and Roger Purves, *Statistics 4th Edition,* 2007. Publisher: Norton, W. W. & Company, Inc..

[91]   I. N. Sneddon, "The relation between load and penetration in the axisymmetric boussinesq problem for a punch of arbitrary profile". *Int. J. Engng. Sci.,* **3** (1965) 47-57.

[92]   A. L. Weisenhorn, M. Khorsandi, S. Kasas, V. Gotzos and H. J. butt. "Deformation and height anomaly of soft surfaces studied with an AFM". *Nanotechnology,* **4** (1993) 106-113.

[93]   M. Radmacher, M. Fritz, C. M. Kacher, J. P. Cleveland and P. K. Hansma. "Measuring the viscoelastic properties of human platelets with the atomic firce microscope". *Biophysical Journal,* **70** (1996) 556-567.

[94]   D. Shin and K. Athanasiou. "Cytoindentation for obtaining cell biomechanical properties". *Journal of Orthopaedic Reasearch,* **17** (1999) 1999.

[95]   J.W.G. Wildoer, L.C. Venema, A.G. Rinzler, R.E. Smalley, and C. Dekker, Electronic structure of atomically resolved carbon nanotubes, *Nature,* **391** (1998) 59–62.

[96]   T.W. Odom, J.L. Huang, P. Kim, and C.M. Lieber, Atomic structure and electronic properties of single-walled carbon nanotubes, *Nature,* **391** (1998) 62–64.

[97]   M. Burghard, Electronic and vibrational properties of chemically modified single-wall carbon nanotubes, *Surf. Sci. Rep.,* **58** (2005) 1–109.

[98]   F. Schedin, A. K. Geim, S. V. Morozov, E. W. Hill, P. Blake, M. I. Katsnelson, and K. S. Novoselov, "Detection of individual gas molecules adsorbed on graphene". *Nature Materials,* **6** (2007) 652-655.

[99]   Ulrike Tisch and Hossam Haick, "Nanomaterials for cross-reactive sensor arrays". *MRS BULLETIN,* **35** (2010) 797-803.

[100]   URL:http://www.nasa.gov/centers/ames/research/technology-onepagers/gas_detection.html, data retrieved on 07/06/2011.

[101]   Elizabeth Kolawa, "Extreme Environment technologies for future space science missions", *a report by NASA,* 09/19/2007.

[102]   Yu, Min-Feng; Lourie, Oleg; Dyer, Mark J.; Moloni, Katerina; Kelly, Thomas F.; Ruoff, Rodney S. "Strength and Breaking Mechanism of Multiwalled Carbon Nanotubes Under Tensile Load". *Science,* **287** (5453) (2000) 637–640.

[103]   B. Peng, M. Locascio, P. Zapol, S. Li, S. L. Mielke, G. C. Schatz, and H. D. Espinosa, "Measurements of near-ultimate strength for multiwalled carbon nanotubes and irradiation-induced crosslinking improvements," *Nature Nanotechnology,* **3** (2008) 626–631.

[104]   L. Ma, C. Y. Gao and Z. W. Mao et al., *Biomaterials,* **24** (2003) 4833. (doi: 10.1016/S0142-9612(03)00374-0)

[105]   Y. F. Zhang, X. R. Cheng and J. W. Wang et al., *Biochem. Biophys. Res. Commun.,* **344** (2006) 362. (doi: 10.1016/j.bbrc.2006.03.106)

[106]   R. N. Chen, G.M. Wang and C.H. Chen et al., *Biomacromolecules,* **7** (2006) 1058. (doi:10.1021/bm050754b)

[107]   J. Yan, X. Li and L. Liu et al., Artif. Cells Blood Substit. *Immobil. Biotechnol.,* **34** (2006) 27. (doi:10.1080/10731190500430024)

[108]   X. Wang, and K. Ye, "Three-dimensional differentiation of embryonic stem cells into islet-like insulin-producing clusters." *Tissue Eng Part A,* **15** (8) (2009) 1941-52.

[109]   D. Von Heimburg, S. Zachariah, I. Heschel, H. Kuhling, H. Schoof, B. Hafemann and N. Pallua, "Human preadipocytes seeded on freeze-dried collagen scaffolds investigated in vitro and in vivo." *Biomaterials,* **22** (5) (2001) 429-38.

[110]   S. P. Zustiak and J. B. Leach, "Hydrolytically degradable poly(ethylene glycol) hydrogel scaffolds with tunable degradation and mechanical properties." *Biomacromolecules,* **11** (5) (2010) 1348-57.

[111]   D. Discher, C. Dong, J. Fredberg, F. Guilak, D. Ingber, P. Janmey, R. Kamm, G. Schmid-Schonbein and S. Weinbaum, "Biomechanics: cell research and applications for the next decade." *Ann Biomed Eng.,* **37** (5) (2009) 847-59.

[112]   A. Engler, S. Sen, H Sweeney, and D. Discher, "Matrix elasticity directs stem cell lineage specification." *Cell,* **126** (4) (2006) 677-89.

[113]   P. C. Georges and P. A. Janmey, "Cell type-specific response to growth on soft materials." *J. Appl. Physiol.,* **98** (4) (2005) 1547-53.

[114]   I. Leventh, P. C. Georges and P. Janmey, "Soft biological materials and their impact on cell function." *Soft Matter,* **3** (2007) 299-306.

[115]   A. Mammoto, K. M. Connor, T. Mammoto, C. W. Yung, D. Huh, C. M. Aderman, G. Mostoslavsky, L. E. Smith and D. E. Ingber, "A mechanosensitive transcriptional mechanism that controls angiogenesis." *Nature,* **457** (7233) (2009) 1103-8.

[116]   J. P. Winer, S. Oake and P. A. Janmey, "Non-linear elasticity of extracellular matrices enables contractile cells to communicate local position and orientation." *PLoS One,* **4** (7) (2009) e6382.

[117]   M. Doube, E. C. Firth, A. Boyde and A. J. Bushby, "Combined nanoindentation testing and scanning electron microscopy of bone and articular calcified cartilage in an equine fracture predilection site." *Eur Cell Mater,* **19** (2010) 242-51.

[118] H. Isaksson, S. Nagao, M. Malkiewicz, P. Julkunen, R. Nowak and J. S. Jurvelin, "Precision of nanoindentation protocols for measurement of viscoelasticity in cortical and trabecular bone." *J Biomech,* **43** (12) (2010) 2410-7.

[119] A. C. Barone, M. Salerno, N. Patra, D. Gastaldi, E. Bertarelli, D. Carnelli and P. Vena, "Calibration issues for nanoindentation experiments: direct atomic force microscopy measurements and indirect methods." *Microsc Res Tech,* **73** (10) (2010) 996-1004.

[120] S. Chowdhury and M. T. Laugier, "The use of non-contact AFM with nanoindentation techniques for measuring mechanical properties of carbon nitride thin films." *Applied Surface Science,* **233** (1-4) (2004) 219-226.

[121] C. A. Clifford and M. P. Seah, "Modeling of nanomechanical nanoindentation measurements using an AFM or nanoindenter for compliant layers on stiffer substrates." *Nanotechnology,* **17** (21) (2006) 5283-5292.

[122] E. M. Darling, S. Zauscher, J. A. Block and F. Guilak, "A thin-layer model for viscoelastic, stress-relaxation testing of cells using atomic force microscopy: do cell properties reflect metastatic potential?" *Biophys J.,* **92** (5) (2007) 1784-91.

[123] Yanxia Zhu, Tianqing Liu and Kedong Song. "Collagen-chitosan polymeric scaffolds for the in vitro expansion of human adipose tissue-derived stem cells". *J Mater Sci: Mater Med,* **20** (3) (2009) 799-808.

[124] I. V. Yannas, D. S. Tzeranis, B. A. Harley and P. T. So, "Biologically active collagen-based scaffolds: advances in processing and characterization." *Philos Transact A Math Phys Eng Sci,* **368** (1917) (2010) 2123-39.

[125] S. F. Badylak, D. O. Freytes and T. W. Gilbert, 2009. "Extracellular matrix as a biological scaffold material: Structure and function." *Acta Biomater,* 5 (1), 1-13.

[126] Z. Gong, H. Xiong, X. Long, L. Wei, J. Li, Y. Wu and Z. Lin, "Use of synovium-derived stromal cells and chitosan/collagen type I scaffolds for cartilage tissue engineering." *Biomed Mater,* **5** (5) (2010) 055005.

[127] G. R. Ragetly, D. J. Griffon, H. B. Lee, L. P. Fredericks, W. Gordon-Evans and Y. S. Chung, "Effect of chitosan scaffold microstructure on mesenchymal stem cell chondrogenesis." *Acta Biomater,* **6** (4) (2010) 1430-6.

[128] Y. Zhu, T. Liu, H. Ye, K. Song, X. Ma, and Z.Cui, "Enhancement of adipose-derived stem cell differentiation in scaffolds with IGF-I gene impregnation under dynamic microenvironment." *Stem Cells Dev,* **19** (10) (2010) 1547-56.

[129] Y. C. Lin, F. J. Tan, K. G. Marra, S. S. Jan and D. C. Liu, "Synthesis and characterization of collagen/hyaluronan/chitosan composite sponges for potential biomedical applications." *Acta Biomater,* **5** (7) (2009) 2591-600.

[130] R. Howland, and L. Benatar, A Paractical Guide to Scanning Probe Microscopy. (2000), *ThermoMicroscopes,* Sunnyvale, CA.

[131] J. J. van der Loo, J. Jacot and P. H. M. Bovendeerd, "The Development in Cardiac Stiffness in Embryonic, Neonatal and Adult Mice Evaluated with Atomic Force Microscopy." University of California, San Diego, Technical University, Eindhoven, Internship 2008, San Diego.

[132] V. Serpooshan, M. Julien, O. Nguyen, H. Wang, A. Li, N. Muja, J. E. Henderson, S. N. Nazhat, "Reduced hydraulic permeability of three-dimensional collagen scaffolds attenuates gel contraction and promotes the growth and differentiation of mesenchymal stem cells." *Acta Biomater,* **6** (2010) 3978-3987.

[133] J. Zhu, T. Sabharwal, A. Kalyanasundaram, L. Guo, and G. Wang, "Topographic mapping and compression elasticity analysis of skinned cardiac muscle fibers in vitro with atomic force microscopy and nanoindentation." *J Biomech,* **42** (2009a) 2143-2150.

[134] E. J. Orwin, M. L. Borene and A. Hubel, "Biomechanical and optical characteristics of a corneal stromal equivalent." *J Biomech Eng,* **125** (2003) 439-444.

[135] S. Sakai, H. Masuhara, Y. Yamada, T. Ono, H. Ijima and K. Kawakami, "Transition of mechanical property of porous alginate scaffold with cells during culture period." *J Biosci Bioeng,* **100** (2005) 127-129.

[136] M. Levy-Mishali, J. Zoldan and S. Levenberg, "Effect of scaffold stiffness on myoblast differentiation." *Tissue Eng Part A,* **15** (2009) 935-944.

[137] Martin J. K. Blomley, Jennifer C. Cooke, Evan C. Unger, Mark J. Monaghan and David O. Cosgrove, "Microbubble contrast agents: a new era in ultrasound." *BMJ,* **322** (2001) 1222-5.

[138] Shashank Sirsi and Mark Borden, "Microbubble Compositions, Properties and Biomedical Applications." *Bubble Sci Eng Technol.,* **1** (1-2) (2009) 3-17.

[139] M. W. Miller, "Gene transfection and drug delivery." *Ultrasound Med Biol,* **26** (suppl 1) (2000) S59-62.

[140] S. J. Russell, "Science, Medicine, and the future: gene therapy." *BMJ,* **315** (1997) 1289-92.

[141] M. Postema and G. Schmitz, "Ultrasonic bubbles in medicine: Influence of the shell," *Ultrason. Sonochem.,* **14** (2007) 438-444.

[142] Abhay V. Patil, Paul Reynolds, and John A. Hossack, "A non-linear three-dimensional model for quantifying microbubble dynamics," *J. Acoust. Soc. Am,* **127** (2) (2010) EL80-EL86.

[143] Product data sheet of photoresist AZ 5214E. Available: http://groups.mrl.uiuc.edu/dvh/pdf/AZ5214E.pdf

[144] Uda Hashim, Mohd Khairuddin Md Arshad, Chin Seng Fatt, "Silicon Nitride Gate ISFET Fabrication Based on Four Mask Layers using Standard MOSFET Technology," *Proceedings of IEEE International Conference on Semiconductor Electronics (ICSE),* Nov. 25-27, 2008, Johor Bahru, Malaysia.

[145] Liming Yu, Ciprian Iliescu, Guolin Xu and Francis E. H. Tay, "Sequential Field-Flow Cell Separation Method in a Dielectrophoresis Chip with 3-D Electrodes". *Journal of Microelectromechanical Systems,* **16** (5) (2007).

[146] J. Haneveld, H. Jansen, E. Berenschot, N. Tas and M. Elwenspoek, "Wet anisotropic etching for fluidic 1D nanochannels". *Journal of Micromechanics and Microengineering,* **13** (2003) S62-S66.

[147] Arindom Datta, Shubhra Gangopadhyay, Henryk Temkin, Qiaosheng Pu, and Shaorong Liu, "Nanofluidic channels by anodic bonding of amorphous silicon to glass to study ion-accumulation and ion-depletion effect". *Talanta,* **68** (2006) 659-665.

[148] M. B. Stern, M. W. Geis and J. E. Curtin, "Nanochannel fabrication for chemical sensors". *Journal of Vacuum Scinece and Technology B,* **15** (6) (1997) 2887-2891.

[149] M. J. de Boer, R. W. Tjerkstra, J. W. Berenschot, H. V. Jansen, C. J. Burger, J. G. E. Gardeniers, M. Elwenspoek and A. van den Berg, "Micromachining of buried micro channels in silicon". *Journal of Microelectromechanical Systems,* **9** (2000) 94-103.

[150] Han Cao, Jonas O. Tegenfeldt, Robert H. Austin and Stephen Y. Chou, "Gradient nanostructures for interfacing microfluidics and nanofluidics". *Applied Physics Letters,* vol. **81** issue 16 (2002) 174-176.

[151] L. J. Guo, X. Cheng and C. F. Chou, "Fabrication of size-controllable Nanofluidic channels by nanoimprinting and its application for DNA stretching". *Nano Letters,* **4** (1) (2004) 69-73.

[152] J. O. Tegenfeldt, C. Prinz, H. Cao, R. L. Huang, R. H. Austin, S. Y. Chou, E. C. Cox and J. C. Sturm, "Micro- and nanofluidics for DNA analysis". *Analytical and Bioanalytical Chemistry,* **378** (7) (2004) 1678-1692.

[153] X. N. Xie, H. J. Chung, C. H. Sow and A. T. S. Wee, "Nanoscale materials patterning and engineering by atomic force microscopy nanlithography". *Materials Science and Engineering: R: Reports,* **54** (1-2) (2006) 1-48.

[154] Jie-Ming Chen, Shang-Wei Liao and Yu-Chen Tsai, "Electrochemical synthesis of polypyrrole within PMMA nanochaneels produced by AFM mechanical lithography". *Synthetic Metals,* **155** (1) (2005) 11-17.

[155] B. Cappella and H. Sturm, "Comparison between dynamic plowing lithography and nanoindentation methods". *J. Appl. Phys.,* **91** (2002) 506-512.

[156] M. Heyde, K. Rademann, B. Cappella, M. Geuss, H. Sturm, T. Spangenberg and H. Niehus, "Dynamic plowing nanolithography on polymethylmethacrylate using an atomic force microscope". *Rev. Sci. Instrum.,* **72** (2001) 136-141.

[157] Z. Kato, M. Sakairi and H. Takahashi, "Nanopatterning on aluminum surfaces with AFM probe". *Surface and coatings technology,* **169-170** (2003) 195-198.

[158] J. C. Rosa, M. Wendel, H. Lorenz and J. P. Kotthaus, "Direct patterning of surface quantum wells with an atomic force microscope". *Applied Physics Letters,* **73** (18) (1998) 2684-2686.

[159] J. Regul, U. F. Keyser, M. Paesler, F. Hohls, U. Zeitler, R. J. Haug, A. Malave, E. Oesterschulze, D. Reuter and A. D. Wieck," Fabrication of quantum point contacts by engraving GaAs/AlGaAs heterostructures with a diamond tip". *Applied Physics Letters,* **81** (2002) 2023-2025.

[160] P. A. Fontaine, E. Dubois and D. Stievenard, "Characterization of scanning tunneling microscopy and atomic force microscopy-based techniques for nanolithography on hydrogen-passivated silicon," *Journal of Applied Physics,* **84** (4) (1998) 1776-1881.

[161] Z. Q. Wang, N. D. Jiao, S. Tung and Z. L. Dong, "Atomic force microscopy-based repeated machining theory for nanochannels on silicon oxide surfaces," *Applied Surface Science,* **257** (2011) 3627-3631.

[162] B. Bhushan, Nanotribology and Nanomechanics, Springer-Verlag, Berlin, Heidelberg, 2008.

[163] Ampere A. Tseng, Jun-ichi Shirakashi, Shinya Nishimura, Kazuya Miyashita and Andrea Notargiacomo, "Scratching properties of nickel-iron thin film and silicon using atomic force microscopy". *Journal of Applied Physics,* **106** (2009) 044314.

[164] Ampere A. Tseng, "A comparison study of scratch and wear properties using atomic force microscopy". *Applied Surface Science,* **256** (2010) 4246-4252.

APPENDIX 1: Publication Related to Dissertation

Journal:

1. **Zhuxin Dong**, Uchechukwu C. Wejinya, Siva Naga Sandeep Chalamalasetty, and Meyya Meyyappan, "Dimensional Analysis and Mechanical Properties Characterization of Carbon Nanofibers under Subzero Temperatures." *IEEE Transactions on Nanotechnology,* July 2012, *in press*.
2. **Zhuxin Dong** and Uchechukwu C. Wejinya, "Atomic Force Microscopy Based Repeatable Surface Nanomachining for Nanochannels on Silicon Substrate." *Applied Surface Science,* **258** (2012) 8689-8695.
3. **Zhuxin Dong**, Uchechukwu C. Wejinya and Siva Naga Sandeep Chalamalasetty, "Development of CNT-ISFET based pH sensing system using atomic force microscopy." *Sensors and Actuators: A. Physical,* **173** (2012) 293-301.
4. Siva Naga Sandeep Chalamalasetty, Uchechukwu C. Wejinya, **Zhuxin Dong** and Meyya Meyyappan, "Synthesis and Electrical Properties Characterization of Conductive Polymer – Carbon Nanotubes Based Nanocomposites." *Journal of Nanostructured Polymers and Nanocomposites,* Vol. 7, Issue 04, 2011, pp. 112-116.
5. Uchechukwu C. Wejinya, Siva Naga Sandeep Chalamalasetty, **Zhuxin Dong**, Meyya Meyyappan and Sunny E. Iyuke, "Acid Etching Effects and Dimensional Analysis on Vertically Aligned Carbon Nanofibers Using Atomic Force Microscopy." *IEEE Transactions on Nanotechnology*, Oct. 2011, *in press*.
6. Uchechukwu C. Wejinya, Siva Naga Sandeep Chalamalasetty, **Zhuxin Dong**, Prabhu U. Arumugam and Meyya Meyyappan, "Carbon Nanofiber Nanoelectrode Array: Effect of Process Conditions on Reliability." *IEEE Transactions on Nanotechnology*, Oct. 2011, *in press*.
7. Yanxia Zhu, **Zhuxin Dong**, Uchechukwu C. Wejinya, Sha Jin and Kaiming Ye, "Determination of mechanical properties of soft tissue scaffolds by atomic force microscopy nanoindentation." *Journal of Biomechanics*, **44** (2011) 2356-2361.
8. **Zhuxin Dong** and Uchechukwu C. Wejinya, "Characterization of Vertically Aligned Carbon Nanofibers without Electrochemical Treatment Using Atomic Force Microscopy." *IEEE Transactions on Nanotechnology*, Vol. 10, Issue 3, pp. 639-646, 2011.
9. **Zhuxin Dong**, Uchechukwu C. Wejinya and Wen J. Li, "An Optical-Tracking Calibration Method for MEMS-Based Digital Writing Instrument." *IEEE Sensors Journal,* Vol. 10, No. 10, Oct. 2010, pp. 1543-1551.

Magazine:

1. Steve Tung, Michael B. Schulte, **Zhuxin Dong**, Jin-Woo Kim, Uche Wejinya, Hyung-Mo Moon and Byung-Whi Kong, "Electrical Properties of an Individual Chicken Infectious Laryngotracheitis Virus," *IEEE Nanotechnology Magazine,* vol. 4, issue 3, pp. 10-14, September 2010.

Conference Proceedings:

1. **Zhuxin Dong**, Uchechukwu C. Wejinya, John M. Vaughan, and Alan M. Albrecht, "Fabrication and Testing of ISFET Based pH Sensor for Microliter Scale Solution Targets". *Proceedings of IEEE Nanotechnology Materials and Devices Conference (NMDC 2012),* October 16-19, 2012, Waikiki Beach, Hawaii, USA.

2. **Zhuxin Dong** and Uchechukwu C. Wejinya, "Atomic Force Microscopy-Based Repeatable Surface Nanomachining for Nanochannels on Bare Silicon Substrates". *Proceedings of IEEE 12th International Conference on Nanotechnology (NANO 2012),* August 20-23, Birmingham, UK.

3. Siva Naga Sandeep Chalamalasetty, Uchechukwu C. Wejinya, **Zhuxin Dong** and Meyya Meyyappan, "A Study of Sulfuric and Acetic Acid Effect on Vertically Aligned Carbon Nanofibers for Bio/Chemical Sensors Development". *Proceedings of 11th IEEE International Conference on Nanotechnology (NANO 2011),* August 15-18, 2011, Portland, Oregon, USA.

4. **Zhuxin Dong**, Uchechukwu C. Wejinya, Siva Naga S. Chalamalasetty and Matthew Margis*, "Atomic Force Microscopy Based Nano Manipulation towards CNT-ISFET pH Sensing System". *Proceedings of IEEE 6th International Conference on Nano/Micro Engineered and Molecular Systems (NEMS 2011),* Feb. 20-23, Kaohsiung, Taiwan.

5. Siva Naga Sandeep Chalamalasetty, Uchechukwu C. Wejinya, **Zhuxin Dong**, Mathew R. Margis*, Theodore G. Duensing* and Trent Chudej*, "A Study of Temperature Effect on Unetched and Etched Vertically Aligned Carbon Nanofibers for Bio/Chemical Sensors Development". *Proceedings of the 2010 IEEE International Conference on Robotics and Biomimetics (ROBIO 2010),* December 14-18, Tianjin, China.

6. **Zhuxin Dong**, Uchechukwu C. Wejinya, Yanxia Zhu and Kaiming Ye, "Force Measurement Study of Engineered Collagen-Chitosan Scaffold Using Atomic Force Microscopy". *Proceedings of 2010 IEEE International Conference on Nano/Molecular Medicine and Engineering (NANOMED 2010),* Dec. 5-9, Hong Kong/Macau, China.

7. Siva Naga Sandeep Chalamalasetty, Uchechukwu C. Wejinya and **Zhuxin Dong**, "Characterization of Etched and Unetched Vertically Aligned Carbon Nanofibers (VACNFs) Using Atomic Force Microscopy". *Proceedings of the 2010 IEEE/RSJ International Conference on Intelligent Robots and Systems (IROS 2010),* Oct. 18-22, Taipei, Taiwan.

8. **Zhuxin Dong**, Uchechukwu C. Wejinya, Siva Naga Sandeep Chalamalasetty, Mathew R. Margis* and Theodore G. Duensing*, "Acid Etch Study of Vertically Aligned Carbon Nanofibers (VACNFs)". *Proceedings of 2010 IEEE Nanotechnology Materials and Devices Conference (NMDC 2010),* Oct. 12-15, Monterey, California, USA.

9. Siva Naga Sandeep Chalamalasetty, Uchechukwu C. Wejinya and **Zhuxin Dong**, "A study of Temperature Effect on Vertically Aligned Carbon Nanofibers for Bio/Chemical Sensors Development". *Proceedings of 10th IEEE International Conference on Nanotechnology Joint Symposium with Nano Korea 2010 (NANO 2010),* Aug. 17-20, KINTEX, Korea.

10. **Zhuxin Dong** and Uchechukwu C. Wejinya, "Electrical Property Measurement of Carbon Nanotubes Using Atomic Force Microscopy for Nano Sensor Applications," *Proceedings of the 5th IEEE International Conference on Nano/Micro Engineered and Molecular Systems (NEMS 2010),* Jan. 20-23, Xiamen, China, 2010.

11. **Zhuxin Dong**, Uchechukwu C. Wejinya and Wen J. Li, "Calibration of MEMS Accelerometer Based on Plane Optical Tracking Technique and Measurements," *Proceedings of the 4th IEEE International Conference on Nano/Micro Engineered and Molecular Systems (NEMS 2009),* Jan. 5-8, Shenzhen, China.

12. **Zhuxin Dong**, Uchechukwu C. Wejinya, Haibo Yu and Imad H. Elhajj, "Design, Fabrication, and Testing of CNT-Based ISFET for Nano pH Sensor Application: A Preliminary Study", *Proceedings of IEEE/ASME International Conference on Advanced Intelligent Mechatronics (AIM 2009),* July 14-17, Singapore.

13. **Zhuxin Dong** and Uchechukwu C. Wejinya, "Design, Fabrication, and Measurement of CNT-Based ISFET for Nano Devices", *Proceedings of IEEE Nanotechnology Materials and Devices Conference (NMDC 2009),* June 2-5, Traverse City, MI, USA.

14. **Zhuxin Dong**, Uchechukwu C. Wejinya, Imad H. Elhajj and Meyya Meyyappan, "Characterization of Vertically Aligned Carbon Nanofibers Grown on Ni Dots Nanoelectrode Array Using Atomic Force Microscopy", *Proceedings of the 2009 IEEE/RSJ International Conference on Intelligent Robots and Systems (IROS 2009),* Oct. 11-15, St. Louis, MO USA.

15. Michael B. Schulte, **Zhuxin Dong**, Steve Tung, Jin-Woo Kim, Uche Wejinya, Hyung-Mo Moon and Byung-Whi Kong, "Impedance Spectroscopy of Chicken Infectious Laryngotracheitis Virus Based on Atomic Force Microscopy". *Proceedings of the 2009 IEEE 3rd International Conference on Nano/Molecular Medicine and Engineering (NANOMED 2009),* Oct. 18-21, Tainan, Taiwan.

16. **Zhuxin Dong**, Uchechukwu C. Wejinya, Holly D. Tourtillott*, Imad H. Elhajj and Meyya Meyyappan, "Scanning and Measurement of Carbon Nanofiber Nanoelectrode Arrays Using Atomic Force Microscopy". *Proceedings of the 2009 IEEE International Conference on Robotics and Biomimetics (ROBIO 2009),* Dec. 19-23, Guilin, China.

17. **Zhuxin Dong**, Uchechukwu C. Wejinya, Shengli Zhou, Qing Shan and Wen J. Li, "Real-Time Written-Character Recognition Using MEMS Motion Sensors: Calibration and Experimental Results". *Proceedings of the 2008 IEEE International Conference on Robotics and Biomimetics (ROBIO 2008),* Feb. 21-26, 2009, Bangkok, Thailand.

APPENDIX 2: Datasheet of AFM Probe Tap190Al-G

Budget Sensors

AFM probe Model: Tap190Al-G

- Tapping Mode, Intermittent Contact Mode, Long Cantilever
- Rotated Monolithic Silicon Probe
  Symmetric Tip Shape
  Chipsize: 3.4 x 1.6 x 0.3 mm
- Coating: Aluminium reflex coating, 30 nm thick
- This probe uses an "on scan angle" symmetric tip to provide a more symmetric representation of features over 200 nm.

This probe has alignment grooves on the backside of the holder chip.

	Typical Values	Range
Resonant Frequency	190 kHz	+/- 60 kHz
Force Constant	48 N/m	20 - 100 N/m
Cantilever Length	225 μm	+/- 12 μm
Mean Width	38 μm	+/- 9 μm
Thickness	7 μm	+/- 1 μm
Tip Height	17 μm	+/- 2 μm
Tip Set Back	15 μm	+/- 5 μm
Tip Radius	< 10 nm	
Coating	Aluminium Reflex	
Half Cone Angle	20º - 25º along cantilever axis 25º - 30º from side 10º at the apex	

Order Code	Units in Package	Coating	Price
Tap190Al-G-10	10 pieces	Aluminium Reflex	$210
Tap190Al-G-50	50 pieces	Aluminium Reflex	$890
Tap190Al-G-380	380 pieces	Aluminium Reflex	$3900

www.budgetsensors.com

APPENDIX 3: Datasheet of AFM Probe Tap190DLC

Budget Sensors

AFM probe Model: Tap190DLC
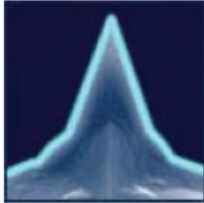
- Tapping Mode, Intermittent Contact Mode, Long Cantilever
- Rotated Monolithic Silicon Probe
  Symmetric Tip Shape
  Chipsize: 3.4 x 1.6 x 0.3 mm
- Diamond-Like-Carbon coating on tip side of the cantilever, 15nm thick;
  Aluminium Reflex coating on detector side of the cantilever, 30 nm thick
- This probe uses an "on scan angle" symmetric tip to provide
  a more symmetric representation of features over 200 nm.

This probe has alignment grooves on the backside of the holder chip.

	Typical Values	Range
Resonant Frequency	190 kHz	+/- 60 kHz
Force Constant	48 N/m	20 - 100 N/m
Cantilever Length	225 µm	+/- 12 µm
Mean Width	38 µm	+/- 9 µm
Thickness	7 µm	+/- 1 µm
Tip Height	17 µm	+/- 2 µm
Tip Set Back	15 µm	+/- 5 µm
Tip Radius	< 15 nm	
Coating	Diamond-Like-Carbon coating on the tip side of the cantilever, 15nm thick Aluminium Reflex coating on detector side of the cantilever, 30 nm thick	
Half Cone Angle	20º - 25º along cantilever axis 25º - 30º from side 10º at the apex	

Order Code	Units in Package	Coating	Price
Tap190DLC-10	10 pieces	DLC and Al Reflex	$240
Tap190DLC-50	50 pieces	DLC and Al Reflex	$1000

www.budgetsensors.com

APPENDIX 4: Datasheet of AFM Probe ContAl

Budget Sensors

AFM probe Model: ContAl
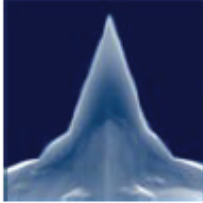
- Contact Mode
- Rotated Monolithic Silicon Probe
  Symmetric Tip Shape
  Chipsize: 3.4 x 1.6 x 0.3 mm
- Coating: Aluminium reflex coating, 30 nm thick
- This probe uses an "on scan angle" symmetric tip to provide a more symmetric representation of features over 200 nm.

	Typical Values	Range
Resonant Frequency	13 kHz	+/- 4 kHz
Force Constant	0.2 N/m	0.07 - 0.4 N/m
Cantilever Length	450 µm	+/- 10 µm
Mean Width	50 µm	+/- 5 µm
Thickness	2 µm	+/- 1 µm
Tip Height	17 µm	+/- 2 µm
Tip Set Back	15 µm	+/- 5 µm
Tip Radius	< 10 nm	
Coating	30 nm thick Aluminium coating	
Half Cone Angle	20° - 25° along cantilever axis 25° - 30° from side 10° at the apex	

Order Code	Units in Package	Coating	Price
ContAl-10	10 pieces	Aluminium Reflex	$210
ContAl-50	50 pieces	Aluminium Reflex	$890
ContAl-W	380 pieces	Aluminium Reflex	$3900

www.budgetsensors.com

APPENDIX 5: Datasheet of AFM Probe ElectriCont-G

Budget Sensors

AFM probe Model: *ElectriCont-G*

- Contact Mode and Electric Modes like:
  - Scanning Capacitance Microscopy (SCM)
  - Electrostatic Force Microscopy (EFM)
  - Kelvin probe Force Microscopy (KFM)
  - Scanning probe lithography
- Rotated Monolithic Silicon Probe
  Symmetric Tip Shape
  Chipsize: 3.4 x 1.6 x 0.3 mm
  Alignment Grooves

- Coating: Electrically conductive coating of 5 nm Chromium and 25 nm Platinum on both sides of the cantilever. This coating also enhances the laser reflectivity of the cantilever
- This probe uses an "on scan angle" symmetric tip to provide a more symmetric representation of features over 200 nm.

	Typical Values	Range
Resonant Frequency	13 kHz	+/- 4 kHz
Force Constant	0.2 N/m	0.07 - 0.4 N/m
Cantilever Length	450 μm	+/- 10 μm
Mean Width	50 μm	+/- 5 μm
Thickness	2 μm	+/- 1 μm
Tip Height	17 μm	+/- 2 μm
Tip Set Back	15 μm	+/- 5 μm
Tip Radius	< 25 nm	
Coating	Cr/Pt on both sides	
Half Cone Angle	20° - 25° along cantilever axis 25° - 30° from side 10° at the apex	
Contact Resistance	300 Ohms on platinum thin film surface	

Order Code	Units in Package	Coating	Price
ContE-G-10	10 pieces	Cr/Pt	$240
ContE-G-50	50 pieces	Cr/Pt	$1000

www.budgetsensors.com

181

APPENDIX 6: Datasheet of AFM Probe PPP-NCH

NANOSENSORS™
The World Leader in Scanning Probes
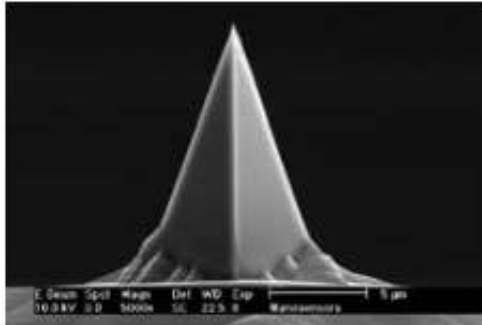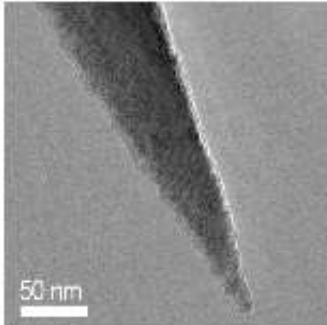
PPP-NCH

PointProbe® Plus Non-Contact / Tapping Mode - High Resonance Frequency

The new PointProbe® Plus (PPP) combines the well-known features of the proven PointProbe® series such as high application versatility and compatibility with most commercial SPMs with a further reduced and more reproducible tip radius as well as a more defined tip shape. The typical tip radius of less than 7 nm and the minimized variation in tip shape provide more reproducible images and enhanced resolution.

NANOSENSORS™ PPP-NCH AFM probes are designed for non-contact mode or tapping mode AFM (also known as: attractive or dynamic mode). This type of AFM probe combines high operation stability with outstanding sensitivity and fast scanning ability.

The probe offers unique features:
- guaranteed tip radius of curvature < 10 nm
- highly doped to dissipate static charge
- chemically inert
- high mechanical Q-factor for high sensitivity

Cantilever data:

Technical Data	Nominal Value	Specified Range
Thickness /μm	4	3.0 - 5.0
Mean Width /μm	30	22.5 - 37.5
Length /μm	125	115 - 135
Force Constant /(N/m)	42	10 - 130
Resonance Frequency /kHz	330	204 - 497

Order codes and shipping units:

Order Code	Quantity	Data Sheet	Coating
PPP-NCH-10	10	of all probes	without
PPP-NCH-20	20	of all probes	without
PPP-NCH-50	50	without	without
PPP-NCH-W	> 380	of up to 32 probes	without

For further information please contact your local distributor or NANOSENSORS™ directly.
NANOSENSORS™ is a trademark of NanoWorld AG / info@nanosensors.com / www.nanosensors.com

APPENDIX 7: Datasheet of AFM Probe DNISP

DNISP

Product Description:

A single probe of Indentation Probes Hand-crafted Natural Diamond Nano-indenting tip. Unmounted for all AFMs.
Quantity=1

Add To Cart

Model	Mount	Pack Size	Price	Pack Quantity
DNISP	Unmounted	1	$2,100.00 (USD)	

🛒 **Add to cart**

Shape	Resonant Freq. kHz			Spring Const. N/m			Length μm			Width μm		
	Nom.	Min.	Max.	Nom.	Min.	Max.	Nom.	Min.	Max.	Nom.	Min.	Max.
Rectangular	50	35	65	150	100	300	350	500	300	100	80	120

Tip Specification

The DNISP is a hand-crafted high force cantilever for nanoindenting/nanoscratching applications. The tip is designed to be ultra high strength and is fabricated by precision grinding of a solid diamond. These tips are not for use in general imaging. The diamond tip apex is the corner of a cube so that three right angle planes form the apex "A". To provide more symmetric dents, the diamond is mounted with the vertical axis of the tip approximately normal to the sample when mounted on the microscope. The nanoindenting probe is designed for use in air and is not recommended for liquid operation due to contamination & solvent incompatibility issues.

Geometry:	Rotated (Symmetric)
Tip Height (h):	50μm
Front Angle (FA):	55 ± 2°
Back Angle (BA):	35 ± 2°
Side Angle (SA):	51 ± 2°
Tip Radius (Nom):	40nm
Tip Radius (Max):	50nm
Tip SetBack (TSB)(Nom):	13μm
Tip Set Back (TSB)(RNG):	5 - 20μm

Tip Schematic

Cantilever Specification

Each cantilever individually qualified and is supplied with a calibration certificate. These probes can be repaired - contact Bruker.

Material:	Stainless Steel
Geometry:	Rectangular
Cantilevers Number:	1
Cantilever Thickness (Nom):	13μm
Cantilever Thickness (RNG):	11 - 15μm

Cantilever schematic

APPENDIX 8: Datasheet of Small Outline Integrated Circuit Package

APPENDIX 9: Datasheet of Hybrid Package Multi-Chip Module

185

APPENDIX 10: Fabrication Travelers for ISFET

Wafer ID: 125MM
Student: ISFET
Wafers: 411W1

SECTION I: FIELD OXIDATION

SUBSTRATE PREPARATION

		Initials	Class	Wafer
Scribe wafer				
Spin rinse dry				

SUBSTRATE RCA CLEAN

	Location	Volume	Units	H2O	Units	H2O2	Units	H2SO4	Units	Time	Units
Organic clean	ACID BENCH	1800	ml	600	ml	600	ml			10	min
Dump Rinse		Volume	Units	H2O	Units	HF	Units			Time	Units
Oxide strip	ACID BENCH	1500	ml	1471	ml	29	ml			15	sec
Dump Rinse		Volume	Units	H2O	Units	H2O2	Units	JBT100	Units	Time	Units
Ionic clean	ACID BENCH	1500	ml	1210	ml	48	ml	242	ml	10	min
Dump Rinse											
Spin rinse dry (SRD)											
Put away chemicals											
Rinse dishware											

SILICON OXIDE GROWTH

Prechecks	Bruce BDF4			LOAD		
Powerup		Supervisor		Timers	Gases	Bubbler	Boat loader
Powerup		Tube icon		ICCI GMI/r.bat	Tube	O2 open	
Build recipe				RMU	FILE	Manager	
Powerup						NEW	ICCI GMI Cell Manager	New number*
Recipe numbers		100's for tube 1	200's for tube 2	300's for tube 3		

EDIT MASTER TEMP TABLE — insert row — input temp — spikes zero — Select row #

EDIT MASTER TEMP TABLE

Temp #	LOAD	CENTER	SOURCE	P-LOAD	P-CENTER	P-SOURCE	Spike offsets
1	400	400	400	400	400	400	zero
2	750	750	750	750	750	750	zero
3	1100	1100	1100	1100	1100	1100	zero
4	20	20	20	20	20	20	zero
5							
6							
7							
8							

EDIT RECIPE TABLE: BOAT

		Segment 1		Segment 2		Segment 3	
		RATE	START	RATE	MID	RATE	END
		(%)	pos	(%)	pos	(%)	pos
Initial	LOAD 1	99	40	99	60	99	99
Subseque	LOAD 1	99	40	99	60	99	99
Initial	UNLOAD 1	99	60	99	40	99	0
Subseque	UNLOAD 1	99	60	99	40	99	0

EDIT RECIPE TABLE: GAS (actual flow, not percent)

Gas #	N2	O2	---	DCE	---	STEAM	Comments
1	1	0	---	0	---	0	Control-4: Profile
2	5	5		0		0	Control-1: Normal
3	3	0		0		0	Alarm-D: Disregard
4	0	3		0		0	
5	0	9.5		0.3		0	
6	8	0		0		0	
7	0	0		0		0	
8	0	0		0		0	
RNG	10	10	20	0	1	1	RNG: Max flow range

EDIT INTERVAL TABLE

Interval	Description	Time	Temp.	Cont.	Gases	Alarm	Boat	Valves	Comments
0 (idle)	IDLE	----	400	4	8	D		0000000	
1	RAMP	0:50:00	750	4	8	D		0000000	
2	DCE CLEAN	0:30:00	750	4	5	D		0101100	
3	DRY OX	0:40:00	1100	4	4	D		0100000	
4	WET OX	0:34:00	1100	4	8	D		0000001	
5	STOP OX	0:05:00	1100	4	2	D		0000000	
6	COOL TO 750	0:35:00	750	4	3	D		1000000	
7	PULL	0:20:00	750	4	2	D		1000000	

Step					
Recipe saving	Name	Verify	Save		
Load wafers	Dummies	Center Process wafers			
Load recipe	Tube icon (double click)	Select recipe (F4)			
Install tube	BOAT	Verify Boat Parameters	INTRVL	std_func	
	Boat in	Functions "On"		ENTER	
	STATUS	Wait till boat is completely in tube			
Run process	Ack alarms (F7)	Verify Boat in On	START (F5)	Verify Boat in On	
Monitor recipe					
Unload wafers					
Shutdown	Close Cell and then supervisor	Turn off breaker		O2 cylinder off	

SILICON OXIDE MEASUREMENT

NANOSPEC

Step		Ave.	Center	Left	Top	Right	Bottom
Measure thickness	Bare silicon wafer on left side of tray						
Nanospec Prechecks							
Power up	Light on				Focus	Laptop	
Calibrate	30.3	Photo-intensity			#1	#1	
Load sample	Major flat facing you					Sample #	
Measure sample							
Determine etch rate	C1						
Unload sample							
Shutdown	Light off						

SECTION II: PHOSPHOROUS SOURCE PREPARATION

	Bruce BDF4		Log		Bubbler:	
Prechecks						Boat loader
Powerup			Timers:			
Powerup		Supervisor	ICCI GMlfr.bat	Gases		O2 open
Build recipe		Tube icon	RMU	Tube	Manager	ICCI GMI Cell Manager
"Recipe numbers"		*100's for tube 1*	*200's for tube 2*	FILE	NEW	New number*
EDIT MASTER TEMP TABLE	insert row	input temp	spikes zero	*300's for tube 3*		
				400's for tube 4	Select row #	

EDIT MASTER TEMP TABLE

Temp #	LOAD	CENTER	SOURCE	P-LOAD	P-CENTER	P-SOURCE	Spike offsets
1	400	20	20	20	20	20	zero
2	750	400	400	400	400	400	zero
3	885	750	750	750	750	750	zero
4	1000	1100	1100	1100	1100	1100	zero
5	0	800	800	800	800	800	zero
6	0	900	900	900	900	900	zero
7	0	885	885	885	885	885	zero
8	0	0					

EDIT RECIPE TABLE: BOAT

		Segment 1		Segment 2		Segment 3	
		RATE	START	RATE	MID	RATE	END
		[%]	pos	[%]	pos	[%]	pos
(In)	Initial	LOAD1	[99]	[30]	[10]	[30]	[30]	[50]
(In)	Subsequen	LOAD1	[99]	[30]	[60]	[30]	[99]	[99]
(Out)	Initial	UNLOAD1	[30]	[60]	[30]	[30]	[50]	[0]
(Out)	Subsequen	UNLOAD1	[30]	[60]	[10]	[30]	[50]	[0]

EDIT RECIPE TABLE: GAS (actual flow, not percent)

Gas #	N2	O2	=	DCE	=	STEAM
1	1	0	=	0	=	0
2	9	0	=	0	=	0
3	0	9	=	0	=	0
4	9.199	2	=	0	=	0
5	0	0	=	0	=	0
6	0	0	=	0	=	0
7	0	0	=	0	=	0
8	0	0	=	0	=	0
RNG	10	10	=	10	=	1

RNG: Max flow range

EDIT INTERVAL TABLE

Interval	Description	Time	Temp. Row	Center (=Profile)	Gas Row	Alarm	Boat	Valves	Comments
0	IDLE	0:00:00	1	400	1	D	0	1000000	Control-4: Profile
1	Dry in N2	1:00:00	1	400	2	D	0	1000000	Control-1: Normal
2	Ramp to 885	0:50:00	3	885	2	D	0	1000000	Alarm-D: Disregard
3	Age in N2/O2	18:00:00	3	885	4	D	0	1100000	
4	Cool to 400	1:00:00	1	400	2	D	1	1000000	

Recipe saving	Name	Verify	Save	
Load Sources	Load Controls	Dummies	Center Process wafers	
Load recipe	Tube icon (double click)		Select recipe (f4)	
Install tube	BOAT	Verify Boat Parameters	INTRVL	std_func
	Boat in	Functions "On"	Verify Boat in On	ENTER
	STATUS	Wait till boat is completely in tube		
Run process	Ack alarms (F7)		START (F5)	
Monitor recipe				
Unload control wafers				
Shutdown		Close Cell and then supervisor	Turn off breaker	O2 cylinder off

SECTION III: EMITTER DIFFUSION - PRE DEP

Wafer ID: 125MM
Student: ISFET
Wafers: 411W1

PHOTOLITHOGRAPHY

Step	Equipment	Temp								
Photolithography Prechecks			HMDS						Resist	Bake
Photolithography Prechecks			Developer						Mask	Exposure
Prep Etch BOE 5:1	ACID BENCH	25°C	PRS1000	6000ml	BOE 5:1	In-bench tank	3500ml			Plastic beaker
Prep Strip PRS1000	SOLVENT WET BENCH	85°C						PWR	HOLD	Recipe
Resist apply frontside EATON			Resist	Recipe	Thickness		Speed	Time	Bake	Time
Bake			4110	3	1.25		3,000	30	110	2
Retrieve mask			Mask		Energy	Intensity	Time	Mode	Gap	Type
Align mask to wafer SUSS MA150			N DIFF							
Exposure			N DIFF		56.25		6	Align	65	SC
Develop DEVELOP WET BENCH			Sol	Conc.	Time	Units				
			TMAH	2.50%	180	sec				
Dump Rinse										
Spin rinse dry (SRD)										
Resist apply backside DESKTOP COATER			Recipe	Resist Apply						
Backside Oxide Bake BLUE M OVEN			110°C	20 MIN						
Oxide etch wafer 1 ACID BENCH	Volume	Units	Etch rate	units	Thickness		Act. Time	Time	Units	
Dump Rinse & SRD	2500	ml	1000	A/min	5000		7	5	min	
Wafer inspection NIKON										
Strip resist SOLVENT WET BENCH			Sol	Temp	Time	Units				
Dump Rinse			PRS1000	85C	10	min				
Spin rinse dry (SRD)										

SUBSTRATE RCA CLEAN

Step	Location	Volume	Units							
Organic clean	ACID BENCH	1800	ml	600	ml	600	ml	666	ml	O2 open
Dump Rinse		Volume	Units	H2O	Units	HF	Units	Manager		
Oxide strip	ACID BENCH	1500	ml	1:65	ml	28	ml	666	ml	
Dump Rinse	Volume	Units	H2O	Units	H2O2	Units				
Ionic clean	ACID BENCH	1500	ml	1210	ml	48	ml	242	ml	
Dump rinse & SRD								10	ml	
Put away chemicals & Rinse dishware										

PHOSPHOROUS PREDEP

Step	Equipment					
Prechecks	Bruce BDF4	Log	Gases	Bubbler		Boat loader
Powerup		Timers	Tube	O2 open		
Powerup		Supervisor	ICCI GMI/r.bat	FILE	Manager	ICCI GMI Cell Manager
Build recipe		Tube icon	RMU		NEW	New number*
EDIT MASTER TEMP TABLE		insert row	input temp	spikes zero	Select row #	New number*

Temp #	LOAD	CENTER	SOURCE	P-LOAD	P-CENTER	P-SOURCE	Spike offsets
1	20	20	20	20	20	20	zero

189

EDIT RECIPE TABLE: BOAT

2	700	885	700	885	700	885	700	885	zero
3	885	885	700	885	700	885	700	885	zero

		Segment 1		Segment 2		Segment 3	
		Speed 1	Dist. 1	Speed 2	Dist. 2	Speed 3	Dist. 3
Initial	LOAD 1	99	30	10	60	99	99
Subseque	LOAD 1	99	30	60	60	99	99
Initial	UNLOAD 1	99	60	10	30	0	0
Subseque	UNLOAD 1	99	60	10	30	0	0

EDIT RECIPE TABLE: GAS (actual flow, not percent)

Gas #	N2	O2	---	DCE	---	STEAM	
Range	10.00	10.00	20.00	0.00	1.00	0.00	1.00	RNG: Max flow range
1	1.00						
2	9.00						

EDIT INTERVAL TABLE

Recipe: **PH900 Dep**

Interval	Descriptio	Time	Temp.	Cont.	Gases	Alarm	Boat	Valves	Comments
0	IDLE	----	700	1	1	D		1000000	Control-4: Profile
1	HOLD	0:30:00	700	1	9	D		1000000	Control-1: Normal
2	Ramp to 885	0:20:00	885	1	9	D		1000000	Alarm-D: Disregard
3	Soak @885	0:45:00	885	1	9	D		1000000	
4	Ramp to 700	0:35:00	700	1	9	D		1000000	Alarm-D: Disregard

PHOSPHOROUS PREDEP

	Name	Verify	Save	INTRVL	std_func
Recipe saving	LOAD C1	Dummies	Center Process wafers		ENTER
Load wafers					
Load recipe	Tube icon (double click)		Select recipe (F4)		
Install tube	BOAT	Verify Boat Parameters			
	Boat in	Functions "On"		Verify Boat in On	
	STATUS	Wait till boat is completely in tube			
Run process	Ack alarms (F7)		START (F5)		
Monitor recipe					
Unload wafers					
Shutdown		Close Cell and then supervisor	Turn off tube breaker		O2 cylinder off

DEGLAZE

Prep Etch	10:1 HF	**ACID BENCH**	25°C		50% Hydrofluoric acid		6000ml		Plastic TANK
Oxide etch C1		**ACID BENCH**	Volume	Units	H2O	Units	HF	Units	Time	Units
			1800	ml	1636	ml	164	ml		2	min
Dump Rinse & SRD									
Wafer inspection		**NIKON**							
Oxide etch W1		**ACID BENCH**	Volume	Units	H2O	Units	HF	Units	Time	Units

190

Dump Rinse & SRD | 1800 ml | 1636 ml | 164 ml | | 2 min

Wafer inspection | NIKON

DESKTOP RECIPE #3

STEP DESCRIPTION		PARAMETERS				
		RAMP	RPM	DWELL	DISPLAY	TIME
1	CONFIGURATION STEP	0	0	0	4	0.1
2	COAT STEP	0	0	2	0	0
3	SPREAD STEP	0.5	500	2	0	0
4	COVERAGE STEP	0.5	1000	2	0	0
5	SETTLE STEP	0.5	500	2	0	0
6	FINAL SPIN STEP	3	3000	30	0	0

PHOSPHOROUS DRIVE IN   Bruce BDF4   (1 µm Junction Depth)

Wafer ID: 125MM   Student: ISFET   Wafers: 411W1

- Prechecks — Log — Gases — number — Boat loader
- Powerup — Computers — Timers — Tube — O2 open
- Build recipe — Tube icon — RMU — FILE — NEW — New number*
- EDIT MASTER TEMP TABLE — insert row — input temp — spikes zero — Select row zero — Select row #

EDIT MASTER TEMP TABLE

Temp #	LOAD	CENTER	SOURCE	P-LOAD	P-CENTER	P-SOURCE	Spike offsets
1	750	750	750	750	750	750	zero
2	1000	1000	1000	1000	1000	1000	zero

EDIT RECIPE TABLE: BOAT

		Segment 1		Segment 2		Segment 3	
		Speed 1	Dist. 1	Speed 2	Dist. 2	Speed 3	Dist. 3
Initial	LOAD 1	99	30	10	60	99	99
Subseque	LOAD 1	99	30	10	60	99	99
Initial	UNLOAD 1	30	60	10	30	30	0
Subseque	UNLOAD 1	30	60	10	30	30	0

EDIT RECIPE TABLE: GAS (actual flow, not percent)

Gas #	N2	O2	---	---	DCE	STEAM	
Range	10.00	10.00	20.00	0.00	1.00	1.00	RNG: Max flow range
1	1.00	0.00	---	---	1.00		
2	9.00	0.00					
3	0.00	9.00					
4	9.199	2.00					
5	0.00	0.00					
6	0.00	0.00					
7	0.00	8.00					
8	0.00	0.00					

EDIT INTERVAL TABLE

Recipe: BN975 Dep 100ohm/sq

Interval	Description	Time	Temp.	Cont.	Gases	Alarm	Boat	Valves	Comments
0	IDLE	----	750	1	1	D	D	1000000	Control-4: Profile
1	Ramp to 1000	0:30:00	1000	1	2	D	D	1000000	Alarm-D: Disregard
2	DRY OX	0:30:00	1000	1	3	D	D	0100000	
3	WET OX	0:20:00	1000	1	8	D	D	0000001	Control-1: Normal
4	Ramp to 750	0:35:00	750	2	2	D	D	1000000	Alarm-D: Disregard

	Name	Verify	Save	
Recipe saving				
Load wafers	Load C1, W1	Dummies	Center Process wafers	
Load recipe	Tube icon (double click)		Select recipe (f4)	
Install tube	BOAT	Verify Boat Parameters	INTRVL	std func

OPTIONAL MEASUREMENT PROCESS ON CONTROL WAFER

Run process	STATUS	Functions "On"	Verify Boat in On
Boat in	Wait till boat is completely in tube	ENTER
Monitor recipe		
Ack alarms (F7)	START (F5)	
Unload wafers		
Shutdown		

SILICON OXIDE MEASUREMENT — NANOSPEC

Shutdown	Close Cell and then supervisor	Turn off breaker	O2 cylinder off
Load sample		
Calibrate	30.3	Photo-intensity	#1	Choose program	Sample #
Power up	Light on	Focus	Laptop	#1
Nanospec Prechecks	Bare silicon wafer on left side of tray
Measure thickness	Major flat facing you

Measure sample	Ave.	Center	Left	Top	Right	Bottom
METAL OXIDE REMOVAL	C1					
GATE OXIDE REMOVAL	W1					

Shutdown	Light off

OPTIONAL MEASUREMENT PROCESS ON CONTROL WAFER   Wafer C1

OXIDE REMOVAL

| Prep Etch   BOE 5:1 | ACID BENCH | | 25°C | | BOE 5:1 | | 2000ml | Plastic beaker |

Oxide etch C1	ACID BENCH	Volume	Units	Etch rate	units	Thickness		Act. Time	Time	Units
Dump Rinse & SRD	2000	ml	1000	A/min	2500			3	min

SILICON RESISTIVITY AND TYPE

Measure thickness 4-point probe						
Power up	Power switch		Clear			Sheet
Load sample	Install on base		Install 100mm ring			

Measure sample	Ave.	Center	Left	Top	Right	Bottom	Type
Unload sample	C1						

Shutdown	Power switch

SILICON JUNCTION DEPTH

Measure thickness Wafer groover			
Power up	Hookup	Water flow check	Test
Disengage holder	Check pressure	Set time	
Clean mandrill	Press Start	Wipe mandrill	
Load sample	Install in clamp		
Run mandrill	Set time to 2 min.		
Engage holder	Press START		

193

Groove silicon

MEASURE GROOVE DEPTH — *Dektak 3030*

- Dektak Prechecks
- Power up
- Load sample
- Focus
- Review recipe
- Align needle — Needle down?
- Scan and evaluate
- Shutdown

C1	Pressure	Units	Time	Units	Depth	Units
	On the line	NA	5	min	16	um

PREP JUNCTION STAIN

Prep Stain — ACID BENCH — N-type stai... — 25°C — $CuSO_4*5H_2O$ — 47% Hydrofluoric acid — 100mL — Plastic beaker

Volume	Units	$CuSO_4*5H_2O$	Units	HF	Units		Time	Units
1000	ml	4	g	3	ml		5	sec

APPLY JUNCTION STAIN

- Stain Prechecks — 500ml Beaker — Plastic eye dropper — 250ml Stain
- Photolithography Prechecks — Wafer — Blank mask — Exposure
- Prep Aligner — Short Program — Dummy wafer — Blank mask
- Apply droplet of stain
- Install mask holder — Clamping On — START — Minutes
- START — **SUSS 125MM**

Mask	Energy	Intensity	Time	Mode	Gap	Type
N/A	3900	10	390 s	Align	65	SC

- Deinstall mask holder — Clamping Off
- Retrieve wafer — Rinse off stain — Blow dry w/ N2

MEASURE STAIN PROFILE

- Inspect copper plating — **Nikon Microscope**
- Measure sample — *Micromeasure* — C1

C1	R	Units	W1	Units	W2	Units
	19885	um	$(W_1/2)^2$	um	$(W_2/2)^2$	um
	R²	Units		Units		Units
Depth	4E+08	um	0	um	0	um
	SQRT (R² - (W₁/2)²)		SQRT (R² - (W₂/2)²)			
Depth	19885		19885			Units

Depth	SQRT (R² - (W₁/2)²) - SQRT (R² - (W₂/2)²)	µm

SECTION V: GATE OXIDE

Wafer ID: 125MM **Student:** _____ ISFET **Wafers:** 411W1

OXIDE REMOVAL

Step	Location							
Photolithography Prechecks	HMDS	Resist	107.8	Bake		Recipe		
Photolithography Prechecks	Developer	Mask		Exposure				
Prep Etch BOE 5:1	ACID BENCH	25°C	BOE 5:1	3500ml	Plastic beaker			

Step	Location	Resist	Recipe	Thickness	Speed	Time	Bake	Time
Resist apply	EATON	4110	1		1,000	30	110	2
Bake								

Step	Location	Mask		Energy	Intensity	Time	Mode	Gap	Type
Retrieve mask		GATE							
Align mask to wafer	SUSS 100MM								
Exposure		GATE		112.5	10	11	Align	65	SC

Step	Location	Sol	Conc.	Time	Units
Develop	DEVELOP WET BENCH	TMAH	2.50%	180	sec
Dump Rinse					
Spin rinse dry (SRD)					

Step	Location	Volume	Units	Etch rate	units	Thickness	Act. Time	Time	Units
Oxide etch C2	ACID BENCH	1000	ml	1000	A/min	5500	6.0	6	min
Dump Rinse & SRD	NIKON								
Wafer inspection									
Oxide etch W1	ACID BENCH	1000	ml	1000	A/min	4000	5	4	min
Dump Rinse & SRD	NIKON								
Wafer inspection	NIKON								

Step	Location	Sol	Temp	Time	Units	Act. Time	Time	Units
Strip resist	DEVELOP WET BENCH	L 2 AB	225	10	23	Align	65	SC
Exposure	SUSS 100MM							
Develop	DEVELOP WET BENCH	TMAH	2.50%	180	sec			
Dump Rinse								
Spin rinse dry (SRD)								

SUBSTRATE RCA CLEAN

Step	Location	Volume	Units	H2O	Units	H2O2	Units	H2SO4	Units	Time	Units
Organic clean	ACID BENCH	1800	ml	600	ml	600	ml	600	ml	10	min
Dump Rinse		Volume	Units	H2O	Units						
Oxide strip	ACID BENCH	1500	ml	1765	ml	29	ml			15	sec
Dump Rinse		Volume	Units	H2O	Units						
Ionic clean	ACID BENCH	1500	ml	1210	ml	48	ml	JBT100 242	ml	10	min
Dump Rinse		Volume	Units	H2O	Units	H2O2	Units	JBT100	Units	Time	Units
Spin rinse dry (SRD)											

SILICON OXIDE GROWTH 800 Angstroms

Bruce BDF4

THIS STEP CAN BE SKIPPED WHEN DCE IS INCLUDED IN NEXT OXIDATION PROCESS

Wafer ID: 125MM **Student:** _____ ISFET **Wafers:** 411W1

Step				Wafers
Prechecks				
Powerup	Log	Gases	Bubbler	Boat loader
Build recipe	Tube icon	Timers	Tube	O2 open	15	sec
	RMU		FILE	NEW	New number*
EDIT MASTER TEMP TABLE	insert row	input temp	spikes zero	Select row #	

Temp #	LOAD	CENTER	SOURCE	P-LOAD	P-CENTER	P-SOURCE	Spike offsets

EDIT RECIPE TABLE: BOAT

		Segment 1		Segment 2		Segment 3		
1		400	400	400	400	400	400	zero
2		750	750	750	750	750	750	zero
3		1100	1100	1100	1100	1100	1100	zero
		RATE	START	RATE	MID	RATE	END	
		(%)	pos	(%)	pos	(%)	pos	
Initial	LOAD 1	[99]	[40]	[10]	[60]	[30]	[60]	
Subseque	LOAD 1	[99]	[40]	[10]	[60]	[30]	[99]	
Initial	UNLOAD 1	[30]	[60]	[10]	[40]	[30]	[0]	
Subseque	UNLOAD 1	[30]	[60]	[10]	[40]	[30]	[0]	

EDIT RECIPE TABLE: GAS (actual flow, not percent)

Gas #	N2	O2	---	---	DCE	---	STEAM
1	1	0			0		0
2	5	5			0		0
3	3	0			0		0
4	0	3			0		0
5	0	9.5			0.3		0
6	8	0			0		0
7	0	8			0		0
8	0	0			0		0
RNG	10	10	20		1		1

RNG: Max flow range

EDIT INTERVAL TABLE

Interval	Descriptior	Time	Temp.	Cont.	Gases	Alarm	Boat	Valves	Comments
0 (idle)	IDLE	----	750	1	1	D	0	1000000	Control-4: Profile
1	DCE CLEAN	0:35:00	750	1	5	D	0	0101100	Control-1: Normal
2	DRY OX	0:40:00	1100	1	4	D	0	0100000	Alarm-D: Disregard
3	STOP OX	0:05:00	1100	1	6	D	0	1000000	
4	COOL TO 40(	3:00:00	400	1	1	D	0	1000000	
5	Hold @ 400	10:00:00	400	1	1	D	0	1000000	

Action							
Recipe saving	Name	**W1**	Verify	**C2 (gate thickness)**	Save	**C1 (metalization etch)**	**Center Process wafers**
Load wafers							**(Two dummies on edges)**
Load recipe		Tube icon (double click)			Select recipe (f4)		
Install tube		BOAT	Verify Boat Parameters			INTRVL	std_func
		Boat in	Functions "On"			Verify Boat in On	ENTER
Run process		STATUS	Wait till boat is completely in tube				
		Ack alarms (F7)				START (F5)	
Monitor recipe		Press F7 when recipe is done					
Unload wafers		Uninstall tube					

GATE OXIDE MEASUREMENT

NANOSPEC

| | | Close Cell and then supervisor | Turn off breaker | | | | | O2 cylinder off |

Shutdown

Measure thickness
Nanospec Prechecks
Power up
Calibrate
Load sample
Measure sample

					Bare silicon wafer on left side of tray			
			Light on		Focus			Laptop
30.3		Photo-intensity	#1		Choose program		#1	Sample #
		Major flat facing you						

GATE OXIDE DIF. AREA

| | C2 | | | | | | |
| | C1 | Ave. | Center | Left | Top | Right | Bottom |

Unload sample
Shutdown

| | | | Light off | | | |

SECTION VII: BACKSIDE OXIDE ETCH

SILICON OXIDE MEASUREMENT (Optional) — *NANOSPEC*

Step						
Measure thickness						
Nanospec Prechecks						
Power up	Light on					
Calibrate	30.3	Photo-intensity	#1	Focus	Laptop	
Load sample	Major flat facing you			Choose program	#1	Sample #
Measure sample						

Bare silicon wafer on left side of tray

	Ave.	Center	Left	Top	Right	Bottom
Determine etch rate	C1					

- Unload sample
- Shutdown — Light off

BACKSIDE OXIDE REMOVAL

Step				Mask		Recipe
Photolithography Prechecks		HMDS	Resist		Bake	
Photolithography Prechecks		Developer			Exposure	
Prep Etch	BOE 5:1	**ACID BENCH**	25°C	BOE 5:1	3500ml	Plastic beaker
Prep Strip	PRS1000	**SOLVENT WET BENCH**	85°C	PRS1000	6000ml	In-bench tank / PWR / HOLD

Resist apply frontside — EATON

	Resist	Recipe	Thickness	Speed	Time	Bake	Time	Units
	4110	3	1.25	3,000	30	110	2	

- Bake

Oxide etch 10 wafers — ACID BENCH

	Volume	Units	Etch rate	units	Thickness	Act. Time	Time	Units
	2500	ml	1000	A/min	5000	7	5	min

- Dump Rinse & SRD
- Wafer inspection — **NIKON**
- Strip resist — **Developer** — ~3 mins
- Dump Rinse
- Spin rinse dry (SRD)

198

SECTION VII: LIFT-OFF PATTERNING

Au Lift-off Patterning

Wafer ID: 125MM

	Resist	Bake 1	Bake 2	Mask	Expose	Developer
Prechecks						
Prep Ultrasonic bath **SOLVENT**	Add water			Waste	Bottles	Funnel
	IPA					
Acetone clean glass wafer	Acetone					

	Solvent	Recipe	Thickness	Speed	Time	Bake	Time
	Acetone	18	N/A	500	10	None	:45

Resist apply **Desktop**	Resist	Recipe	Thickness	Speed	Time	Bake 1	Time
Pre-exposure bake	5214E	4	2	4,000	30	88	:45

Expose **ALIGNER (100MM, DOUBLE BLUE TAPE)**	Energy	Intensity	Time	Type	SP	GAP	Mode	Hours
	60	10	6.0	SC	N	65	First Mask	

Image reversal bake	Resist	Recipe	Thickness			Bake 2	Time
						106	:45

Flood-expose **ALIGNER (100MM, DOUBLE BLUE TAPE)**	Energy	Intensity	Time	Type	SP	GAP	Mode	Hours
	450	10	45.0	SC	N	65	First Mask	

Develop **DEVELOP BENCH**	Developer	Dilution					Time
Dump Rinse & SRD	MF-CD-26	100%					:45

Scope inspection **NIKON**	Photo name			
	Capture photos			

Au Lift-off PRECLEAN (ONLY WHEN THE OPENING IS UNCLEAR)

RIE Prechecks	RIE	FILL out process log	CHECK cabinet	FLIP status card to IN USE
Powerup	MONITOR	TURN monitor - ON	CHECK utilities green, Lock & Chamber under Vacuum	
Vent LOCK	KEYBOARD	PRESS the **ALT** key	PRESS the letters **U** then **L** then **V**	
Edit/Review process	MONITOR	CHECK - ON and STANDBY are lit	CLICK ON - System Monitor toolbar	
	KEYBOARD	PRESS the **ALT** key	PRESS the letters **P** then **C** then **Q** then *resistrm* then **OK**	

Recipe Name	Step		Gas flow (sccm)				Pres.	Power	Time
		Desc.	Ar	CF4	O2	SF6	mTorr	(W)	(Min:sec)
resistrm.PRC	Etch	--	--	--	60	--	200	100	00:30
resistrm.BCH	Stability	--	--	--	60	--	200	0	00:10

Load wafer	LOAD LOCK	LEAVE alumina wafer	REMOVE aluminum wafer	INSTALL process wafer
	MONITOR	CHECK - ON and STANDBY are lit		
Pumpdown	LOAD LOCK	PRESS DOWN on LOADLOCK lid WHILE performing the ne CLICK ON - System Monitor toolbar		
	KEYBOARD	PRESS the **ALT** key	PRESS the letters **U** then **L** then **P**	
	MONITOR	PRESS DOWN on LOADLOCK lid WHILE performing the ne CLICK ON - System Monitor toolbar		
Load batch	KEYBOARD	LOAD batch recipe THEN WAIT until Lock and Chamber pump to 0mTorr		
	MONITOR	PRESS the **ALT** key	PRESS the letters **U** then **L** then **P**	
Run recipe	MONITOR	SELECT - READY & RUN	PRESS **P** & **B** then CLICK ON - System Monitor toolbar	
Unload wafer	LOAD LOCK	REMOVE processed wafer	INSTALL new wafer	
	LOAD LOCK	PRESS DOWN on LOADLOCK lid WHILE performing the next step	WAIT until alarms indicates process is complete	
Shutdown	LOAD LOCK	PRESS the **ALT** key	PRESS the letters **U** then **L** then **P**	
	KEYBOARD	WAIT until lock reads 0 Torr	TURN monitor - OFF	
	MONITOR	FILL out process log	FLIP status card to FREE	
	RIE			

EDWARDS TURBO CHECKLIST

EDWARDS TURBO CHECKLIST	Date	Wafer ID:	Time	Operator

METALLIZATION — Edwards 306 TURBO

LEGEND	CONTROL PANEL [CP]	CURRENT CONTROL [CC]	TURRET ROTATION CONTROL [TRC]

PRECHECKS

POWER UP	[CP]	Water Open	FILL LN Trap	Logbook	Crystal Light ON
POWER FAILURE	[CP]	If it reads 'Power fail', press RESET		Verify Power On (Switch from 0 to 1)
	[CP]	Press START		Wait until Turbo Start appears

Vent	[CP]	Press "VENT"	When Vented (1E+3MB) Press "SEAL"
Load source	Chamber	Trim 0.5cm off boat(s)	Install boats/rods then source metal
	Chamber	Install shutter over metal (black knob near LN2 fill tube)	
TURRET ROTATION		Rotate turret to 1st source to be evaporated. Match source material w/ turret position.	

SET DENSITY

Metal Type	Turret pos.	Density (g/cc)	Tooling factor	Boat Type	Thickness (nm)	Pellet Quantity (no.)
Cr	1	7.2	0.3	W-rod	15	1-chrome plate rod
Au	2	19.3	0.3	Mo-boat		4
Au	3	19.3	0.3	Mo-boat	backup	4

SET DENSITY	FTM6	Set LAYER to [1] and [2] to correct density {see table above}	
	FTM6	Press DATA and up/down keys together to change density quickly	
Load wafer	Chamber	Attach glass wafers to 100mm silicon wafers w/ Kapton tape around edges	
	Chamber	Slide wafer(s) over C-clips on holder WHILE IN CHAMBER	
	Workholder	Press Start	Press ON
Pumpdown	[CP]	Close door	Press 'CYCLE'
	[CP]	Display will read: (1) "Roughing, (2) "PumpDown", (3) "Fine Pumping"	Adjust speed
	[CP]	Until pressure ~2e-6 MB	
WAIT	[CP]	Wait until pressure ~2e-6 MB	
METALLIZE 1			
Set Monitor to 1	FTM6	Set LAYER to [1]	Set TERMINATION to **Desired Thickness**
	FTM6	Press **RUN** to reset monitor thickness to "0"	
	[CC]	Push in "RESET"	Switch to "LT"
Evaporate	[CC]	Increase current by "0.25A" every 5 seconds until max current then remove shutter	Close Shutter

Metal	Layer	[CP] Dial Setting		Measured	Rate
Type	#	Actual	Max	Thickness	(nm/s)
Au	2		4		0.4

METAL THICKNESS ACHIEVED		SET [CC] dial to "0"	SWITCH LT to "0"	Push in "TRIP"
SHUTDOWN				
WAIT		Allow sources to cool for ~10 minutes under vacuum		
Press "VENT"	[CP]	When Vented (1E+3MB)	Press "SEAL"	
Unload source	Chamber	Remove boats/rods		
Unload wafer	Chamber	Slide wafer(s) away from C-clips on holder WHILE IN CHAMBER		
Pumpdown	[CP]	Close door	Press "CYCLE"	
	[CP]	Display will read: (1) "Roughing, (2) "PumpDown", (3) "Fine Pumping"		
WAIT	[CP]	Until pressure ~1e-4 MB	Press "SEAL"	
	[CP]	Press "STOP"	Display should read "TURBO STOP" then "STANDBY"	
LIFT OFF METAL				
Prep Ultrasonic bath SOLVENT	Add water	Acetone	IPA	
Remove resist	Start sonics (5 minutes)			
Rinse wafer	Acetone	IPA		
Measure Thickness				
Review recipe	Use FOCUS to find shadow of needle			
Focus	Adjust focus so shadow just dissappears			
Load sample	Drive stage forward	Place sample in front of stage		
Power up	Red button	PRGM		
Dektak Prechecks	DEKTAK	Needle down?	Camera	Printer paper?
			Brightness	
				Waste

Description	Default parameter
Scan Prg	Select Prog. #9
Scan ID	todays date i.e. 111011
Scan length	500um
Auto level	Ref.
Speed	Med
Profile	50/50
Meas. Range	1310KA (Max)
Display Range	Auto
Ref cursor	200
Meas. Cursor	350
Stylus force	20 mg

Lower needle	Press blue Δ key to lower needle	
Align & Scan	Needle to be 1-1/2 squares from Au image	Press FUNC. - 5 (obtain horz. Bar)
Scan		Press blue scan key
Measure	Average HT	
Print results	Press PT	
Shutdown		

Ave.	Center	Left	Top	Right	Bottom